Mid-Infrared Integrated Devices for Optical Chemical Sensing

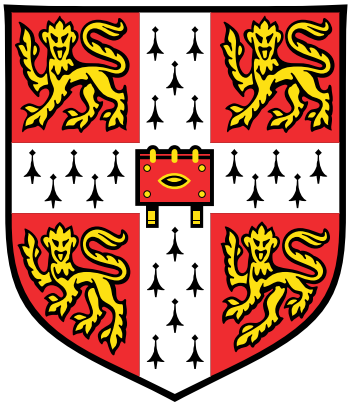

Farah Christina Alimagham

Lucy Cavendish College
University of Cambridge

This dissertation is submitted for the degree of
Doctor of Philosophy

May 2020

Dedicated with love to my parents, Linda and Farshad.

Declaration

I hereby declare that this thesis is the result of my own work and includes nothing which is the outcome of work done in collaboration, except as declared in the preface and specified in the text. It is not substantially the same as any work that has already been submitted before for any degree or other qualification, except as declared in the preface and specified in the text. It does not exceed the prescribed word limit for the Degree Committee of the Faculty of Physics & Chemistry.

Farah Christina Alimagham
May 2020

Abstract

Mid-Infrared Integrated Devices for Optical Chemical Sensing

Farah Christina Alimagham

The mid-infrared (MIR) spectral range is of special interest for establishing optical chemical sensor technologies by allowing specific molecular identification and quantification, whether the sample is in a liquid, gas or solid form, in addition to providing highly sensitive, rapid, reagent-free and non-destructive detection.

This thesis explores four different liquid- and gas- sensing applications and methods using MIR spectroscopy by integrating it with other technologies, such as microfluidics and fibre-optics.

Firstly, fibre-optic integrated microfluidic devices were developed and tested for continuous fluid monitoring. These showed good sensing capabilities for online, continuous and real-time liquid sensing in hard-to-reach locations.

Next, this thesis presents the establishment and clinical testing of a novel method for continuous monitoring of the brain chemistry of traumatically brain-injured patients by MIR transmission spectroscopy. Here, the outlet of a cerebral microdialysis catheter is coupled to a micro flow-cell and the flowing microdialysate is continuously analysed. Clinical studies were carried out and showed the capability of this system for performing continuous patient monitoring over several hours. With further optimisation, the implementation of this system could lead to improved patient outcome.

This thesis also presents a novel method and system based on MIR fibre-optic evanescent-wave spectroscopy, which enables enhanced detection of volatile organic compounds (VOCs). Here, a nanoporous silicon cladding was used to reversibly concentrate molecules close to the fibre surface, thus enhancing VOC detection. A significant increase in sensitivity was seen compared to that of an uncoated fibre and successful detection of three different VOCs, both independently and in binary mixtures, was achieved.

Finally, this thesis introduces a simple and relatively low-cost fibre-optic sensor for in-line, real-time bioprocess monitoring. The sensor was successfully able to monitor varying concentrations of product (sophorolipids) in fermentation broth and was able to distinguish between the two types of generated product (acidic and lactonic sophorolipids).

The work presented in this thesis showed that MIR-integrated sensors have great potential to provide novel and/or enhanced sensing solutions in a wide range of applications, including medical, industrial and environmental.

Acknowledgements

I would like to take this opportunity to express my deepest gratitude to all the people who, in so many ways, supported me throughout this fascinating journey.

First and foremost, I would like to thank my supervisor, Professor Stephen Elliott, for giving me the opportunity to undertake this research and for being incredibly supportive and helpful whenever needed. I am especially thankful to Dr Tanya Hutter for the exceptional mentoring, exciting discussions, for sharing her knowledge and experience and for supporting me through my research adventures.

I am very grateful to all the members of the Chemical Physics group for providing a pleasant and supportive environment. I owe many thanks to the Sensor CDT, for providing me with the initial opportunity to carry out a PhD in sensor technologies and for the brilliant sensor community it has allowed me to be a part of. The Engineering and Physical Research Council (EPSRC) is greatly thanked for the financial support (grant number: EP/L015889/1) for the past three years.

I would like to thank all the people who collaborated with me on the various projects, with special thanks to: Professor Hutchinson, Dr Keri Carpenter and Dr Susan Giorgi-Coll who provided me with essential knowledge and support to conduct research on the traumatic brain injury monitoring sensor; Professor Abraham Katzir and key members of his research group from whom I learnt a lot about mid-infrared optical fibre sensors; Dr Ben Dolman, who provided helpful insight on bioreactor processes as well as samples for my experiments; and Mr Dan Hutter, for providing help and support on multivariate data analysis methods.

I would also like to thank the mechanical workshop of the Department of Chemistry, particularly Ollie Norris and Simon Dowe, who manufactured many of the prototypes for my experiments. Many thanks are owed to Dr Mike Casford, for providing access to the FTIR spectrometers and for the helpful discussions on IR spectroscopy. Thank you very much to the members of the Department of Chemistry who always provided incredible support and guidance, particularly Dr Deborah Longbottom, Dr Howard Jones, Dr Nick Bampos and Rachel MacDonald.

An enormous and heart-felt thanks goes to my dear family and friends for their care and support throughout the years and for all the wonderful and happy memories. To my amazing and incredible friends (you know very well who you are!), thank you for your optimism

and positivity and for some of the best moments of my life, before and during the PhD. I cannot go without giving a special thanks to my wonderful friend Jane and her family, whom I consider my 'Cambridge family', for all the kindness and happy moments. I am so grateful for everything. To nana, thank you for always being there for me from near or far away. To Christopher and Kamran, thank you for being the most awesome brothers one could ask for and for all the fun times we have shared.

An infinitely huge thank you goes to Guillermo for being by my side through some of the toughest times of this journey and for all your incredible patience, care and love.

Last but not least, to my amazing mum and dad, Linda and Farshad, I can't even begin to express how grateful I am for all the love, support and guidance you have always given me and for encouraging me to pursue my dreams. I am blessed to have you as my parents and as my best friends.

Table of contents

*F. Alimagham, T. Hutter, **Integration of IR fiber optics and microfluidics for sensing applications**, Accepted for publication in *OSA Optical Sensors and Sensing Congress Proceedings*, **2020**

[†]F. Alimagham, K. Carpenter, P. Hutchinson and T. Hutter, **Detector assembly and method**, Patent no. GB1916168.6, **2019**

[‡]F. Alimagham, M. Platkov, J. Prestage, S. Basov, G. Izakson, A. Katzir, S. R. Elliott and T. Hutter, **Mid-IR evanescent-field fiber sensor with enhanced sensitivity for volatile organic compounds**, *RSC Advances*, 9, 21186, **2019**

List of figures

List of tables

List of Abbreviations

AgX	Silver halides
AlGaAs	Aluminium Gallium Arsenide
ANOVA	Analysis of variance
ATR	Attenuated total reflection
BiSb	Bismuth Antimonide
CaF_2	Calcium Fluoride
CMD	Cerebral microdialysis
DI	Deionised
DLaTGS	Deuterated and L-alanine-doped TriGlycine Sulfate
DoF	Degrees of freedom
DTGS	Deuterated Triglycine Sulfate
ECF	Extracellular fluid
EFSW	Electric-field standing waves
FT-IR	Fourier-Transform Infrared
FEWS	Fibre-optic evanescent-wave spectroscopy
GaAs	Gallium Arsenide
Ge	Germanium
ID	Inner diameter
ICP	Intracranial pressure
IR	Infrared
KBr	Potassium Bromide

KCl	Potassium Chloride
LoD	Limit of detection
LoQ	Limit of quantification
LPR	Lactate-to-pyruvate ratio
MCT	Mercury-Cadmium-Telluride
MD	Microdialysis
MIR	Mid-infrared
MWCO	Molecular weight cut-off
NA	Numerical aperture
NCCU	Neuro-critical care unit
NIR	Near-infrared
OD	Outer diameter
PAT	Process analytical technology
$PbtO_2$	Brain tissue oxygen pressure
PEEK	Polyether ether ketone
PF	Perfusion fluid
PLSR	Partial least squares regression
PSi	Porous-silicon
PTFE	Polytetrafluoroethylene (Teflon)
QCL	Quantum cascade laser
RMSE	Root mean square error
RMSECV	Root mean square error of cross validation
RMSEP	Root mean square error of prediction
SEM	Scanning electron microscope
SL	Sophorolipid
SNR	Signal-to-noise ratio
Si	Silicon

TBI	Traumatic brain injury
TIR	Total internal reflection
VOC	Volatile organic compound
ZnSe	Zinc Selenide
ZnS	Zinc Sulfide

Chapter 1

Introduction

1.1 Aim & motivation

Spectroscopy in the mid-infrared (MIR) spectral region, extending from 4000 to 400 cm^{-1} (2.5 to 25 μm) provides highly discriminatory and quantitative information on the composition, chemistry and structure of a wide range of constituent molecules in the gas, liquid, and solid phases [1]. As well as molecular sensitivity and selectivity, it also provides label-free and reagent-less analysis and fast acquisition times, enabling real-time and continuous monitoring. These features make it an attractive tool for a variety of sensing applications, ranging from medicine (e.g. point-of-care devices and biomedical diagnostics/monitoring), biotechnology, environmental analysis and industrial production monitoring [2, 3]. The introduction and development in recent years of advanced light sources, sophisticated detection schemes and innovative waveguide/transducer materials and structures, has allowed the use of the MIR spectral window to evolve from a routine laboratory technique into a state-of-the-art spectroscopy and sensing tool, enabling the emergence and adoption of new application areas. For instance, the high intensity of advanced MIR light sources, such as quantum cascade lasers (QCLs), which can be tunable across broad spectral ranges, has led to a significant decrease in achievable limits of detection (LoD) in modern IR spectroscopy, mainly due to allowing larger optical path-lengths, and consequently, increased light-sample interaction [1]. Moreover, with the escalating adoption of micro- and nano-fabricated optical components (e.g. light sources, waveguides, detectors) along with novel system-integration strategies, the MIR spectral region also benefits in cost, sample volume and compactness from substantially decreasing overall system dimensions [2].

The wide range of optical components and different configurations in which they can be used, as well as the easy integration with other systems (e.g. microfluidics [4]), makes MIR spectroscopy a highly versatile technique. This allows the development of sensor

systems customised for particular applications, depending on the specific requirements in each case, which may include detection of molecules in different phases (solid, liquid or gas), the sensing parameters (sensitivity, real-time, continuous, etc.), and the overall system configuration (*in-situ*, on-chip, remote, etc.), as well as dimensions. Figure 1.1 shows the most prevalent optical components used in MIR-sensing systems. For each particular application, careful design considerations must be taken into account in order to achieve optimum sensor performance [5].

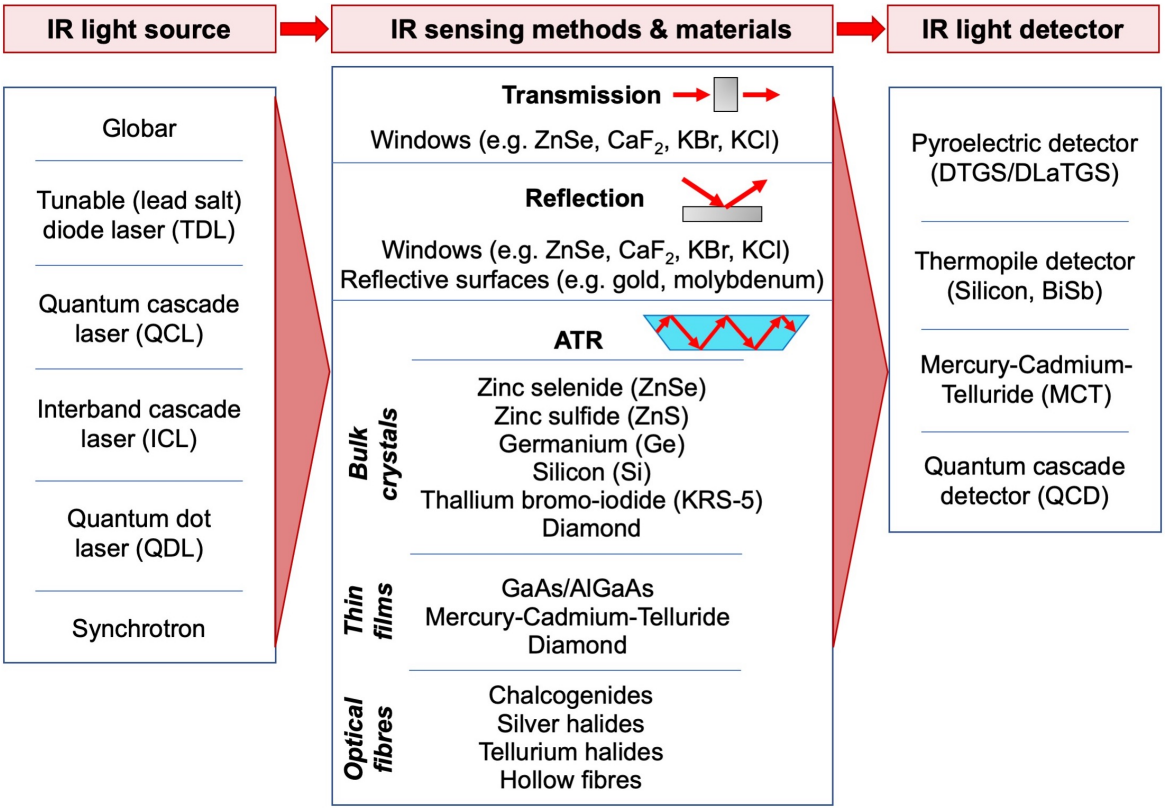

Fig. 1.1 Summary of the most common MIR light sources, sensing methods (transmission, reflection and ATR), materials and light detectors, which can be combined differently to best suit the requirements for specific applications. Pyroelectric detectors and QCDs are operated at room temperature while thermopile and MCT detectors can either be operated at room temperature or can be thermoelectrically or liquid-nitrogen cooled, respectively, to achieve higher sensitivities. Adapted from [2].

The aim of this thesis was to explore and expand the use of MIR spectroscopy for different sensing applications to solve real-world problems, with focus on the following four topics:

1. **The integration of IR spectroscopy with microfluidic systems for continuous monitoring of fluids** (Chapter 3). While MIR spectroscopy provides access to the chemical

composition of samples, microfluidics provides miniaturised flow-cells and continuous flow of small sample volumes. The combination of these two approaches opens several opportunities in the analytical field. In this thesis, microfluidic chips were developed and integrated with IR spectroscopy via optical fibres in both transmission and transfection-mode configurations, and their performance for continuously measuring compounds of interest in fluids was assessed. This research was accepted for publication in the OSA Optical Sensors and Sensing Congress Proceedings 2020, entitled **"Integration of IR Fiber Optics and Microfluidics for Sensing Applications"**[*].

2. **MIR sensor for continuous chemical monitoring of traumatic brain injury (TBI) patients** (Chapter 4). MIR spectroscopy was investigated as a tool for the identification and continuous monitoring of dynamic changes in physiologically-relevant compounds (glucose, lactate and pyruvate) in the extracellular brain fluid of patients suffering from TBI, sampled via cerebral microdialysis. The performance of standard transmission-mode spectroscopy and of a QCL-system with an integrated micro flow-cell were assessed and compared. Upon system optimisation, clinical studies were carried out using the QCL-system. Multivariate data analysis methods were then implemented in an attempt to quantify the compounds present in patient samples. This work resulted in a patent, entitled **"Detector assembly and method"**[†].

3. **MIR evanescent-field fibre-optic sensor with enhanced sensitivity for volatile organic compounds (VOCs)** (Chapter 5). The development and testing of a novel sensor system for increased sensitivity and selectivity of VOCs based on MIR evanescent-wave fibre-optic spectroscopy was carried out. The sensing principle is based on using porous silicon as a fibre cladding to concentrate volatile molecules near the surface (within the evanescent field) of a tapered (U-bent) optical fibre. The sensor's performance to detect different VOCs individually and as mixtures was assessed. This research was published in a journal article, entitled **"Mid-IR evanescent-field fiber sensor with enhanced sensitivity for volatile organic compounds"**, RSC Advances, 2019[‡] [6].

4. **Development of an in-line MIR optical fibre sensor for bioprocess monitoring** (Chapter 6). Here, MIR spectroscopy and fibre-optics were explored for the detection

[*]F. Alimagham and T. Hutter, **Integration of IR fiber optics and microfluidics for sensing applications**, *Accepted for publication in OSA Optical Sensors and Sensing Congress Proceedings*, **2020**

[†]F. Alimagham, K. Carpenter, P. Hutchinson and T. Hutter, **Detector assembly and method**, Patent no. GB1916168.6, **November 2019**

[‡]F. Alimagham, M. Platkov, J. Prestage, S. Basov, G. Izakson, A. Katzir, S. R. Elliott and T. Hutter, **Mid-IR evanescent-field fiber sensor with enhanced sensitivity for volatile organic compounds**, *RSC Advances*, 9, 21186, **2019**

and real-time, in-line monitoring of different compounds relevant to a particular bioprocess for sophorolipid production. This work was carried out in collaboration with fermentation technology companies (primarily, Holiferm Ltd., UK) with a particular interest in such sensor, who provided insight into the sensor requirements as well as bioreactor samples for sensor development and performance assessment.

1.2 Thesis outline

The following paragraphs provide a brief guide to the contents of each chapter of this thesis. The literature review of the background work is provided separately at the beginning of each Chapter due to the different topics presented in each one.

Chapter 2 provides the theoretical background that is relevant for the understanding of the main concepts in this thesis. The fundamentals of vibrational spectroscopy with a particular focus on the MIR region is provided along with the principles and methods associated with MIR absorption spectroscopy relevant to this thesis.

Chapter 3 presents the work carried out to integrate MIR spectroscopy with microfluidic chips for continuous fluid monitoring. A brief overview on the relevance and potential applications of MIR-integrated fluidic systems is provided. The development of four devices (three in transmission mode and one transflection mode) are described and the results from their assessment for continuous monitoring of fluids are presented and discussed.

Chapter 4 starts by providing an introduction to the principles and mechanisms of TBI, as well as a description of the current techniques used for metabolic profiling of the injured brain. A study of the main metabolites of interest (glucose, lactate and pyruvate) using standard transmission Fourier-Transform infrared (FT-IR) spectroscopy is presented, followed by measurements acquired of both synthetic and patient samples using a QCL-system with an integrated flow-cell. The clinical studies carried out using this technique upon optimisation are shown and discussed. Finally, the multivariate data-analysis methods to predict compound concentrations from patient sample spectra are presented and discussed.

In **Chapter 5**, the fabrication of a MIR evanescent-field fibre-optic sensor with enhanced sensitivity for VOCs is presented. Firstly, the importance of VOC monitoring is discussed, followed by a literature review on current VOC detection methods. The fabrication methods of the sensor are described and the results obtained from measurements of different VOCs (individually and in binary mixtures) are discussed.

Chapter 6 describes the development and assessment of an in-line MIR optical fibre sensor for bioprocess monitoring. Current methods of bioprocess monitoring and the importance of continuous real-time sensors for process optimisation are initially discussed. This is

followed by a description of the fabrication and experimental methods implemented in this work along with a discussion of measurements acquired from bioreactor samples.

In **Chapter 7**, the general conclusions of the thesis and potential future work are presented. Specific conclusions for each chapter are presented individually.

Chapter 2

Theoretical Background

This chapter focuses on introducing the main theoretical principles relevant for an understanding of the work carried out in this thesis. Here, the theory behind vibrational spectroscopy, with particular focus on mid-infrared (MIR) spectroscopy, as well as the operating principles and methods of the spectroscopic techniques used in this work, will be provided.

2.1 Fundamentals of vibrational spectroscopy

Molecular vibrational spectra arise from different types of molecular energy changes. The total change in molecular-energy is made under the Born-Oppenheimer approximation as $\Delta E = \Delta E_e + \Delta E_v + \Delta E_r(+\Delta E_t{}^*)$, where E_e is the electronic energy, E_v the interatomic vibrational energy, E_r the molecular rotational energy and E_t the translational energy. More energy is required to raise an electron from the ground state to an excited state than raising the vibrational state of a molecule, which in turn, requires more energy than raising energy for a rotational energy state ($\Delta E_e > \Delta E_v > \Delta E_r$). While for a given electronic energy level many possible vibrational energy levels exist, for a vibrational energy level there are also multiple possible rotational levels [7].

Vibrational spectroscopy is based on measuring the vibrational and rotational energy levels of molecules. The number of vibrational modes of a molecule (i.e. the number of different ways in which a molecule can vibrate), depends entirely on the structure and the number of atoms of that particular molecule and is indicated by the number of internal degrees of freedom (DoF) it possesses. For a diatomic molecule, only one vibrational mode corresponding to the stretching and compression of the bond is possible, and it accounts for one degree of vibrational freedom. Each atom within a molecule has three DoF (in the x, y

*E_t is usually omitted as it is negligibly small.

and z directions) in terms of its motion, and therefore, polyatomic molecules containing N atoms, will have 3N DoF. A linear molecule (e.g. CO_2) has 3N-5 vibrational DoF, while a non-linear molecule (e.g. H_2O) has 3N-6 vibrational DoF [8]. Two main modes of vibrations are commonly known: stretching (where the distance between the two atoms and hence the bond length are affected) and bending (where the angle between the two bonds is altered). Further classification of these types of motions include two stretching modes: symmetric (where the two atoms simultaneously move toward and away from the central atom) and anti-symmetric (where one of the atoms moves toward the central atom while the other moves away from the central atom). Bending vibrations include four types of motions: rocking (two atoms moving in-plane either clockwise or anti-clockwise), scissoring (in-plane, both atoms simultaneously moving either toward each other or away from each other), wagging (out-of-plane, where both atoms simultaneously move like a V sign back and forth), and twisting (out-of-plane, where one atom moves forward while the other moves backward) [9]. The vibrational energy levels range from relatively simple bands for di-atomic molecules to complicated patterns for larger molecules. The atomic displacement behaviour can be approximated as a harmonic oscillator, where the atoms vibrate at a characteristic frequency, ν_i, for each particular mode i. The potential energy of a harmonic oscillator is shown by the green line in Figure 2.1 as a function of the distance between the atoms, r.

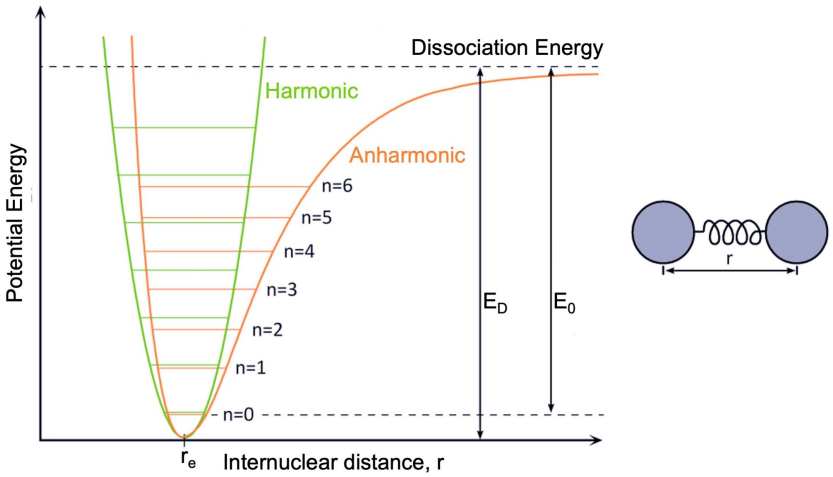

Fig. 2.1 Potential energy of a diatomic molecule as a function of the atomic displacement during a vibration for a harmonic oscillator (green line) and an anharmonic oscillator (orange line). The discrete energy levels are labelled with quantum numbers, n, starting from the ground state ($n = 0$). E_D describes the depth of the potential well for the anharmonic oscillator and r_e is the equilibrium bond distance. Adapted from [10].

For any mode in which the atoms vibrate with simple harmonic motion (i.e. obeying Hooke's law), the vibrational energy states E_n can be described by Equation 2.1 [11].

$$E_n = h\nu(n+\frac{1}{2}) \tag{2.1}$$

Here, h is Planck's constant[†], n is the vibrational quantum number, and the frequency ν is given by $\nu = \frac{1}{2\pi}\sqrt{\frac{k}{\mu}}$, where μ is the reduced mass of the molecule[‡] and k is the spring constant. This harmonic approximation is valid for lower vibrational quantum numbers and transitions are restricted to the fundamental $\Delta n = \pm 1$. When higher energy levels are reached and the displacement of atoms is larger, the anharmonic oscillator model (e.g. Morse-potential - see Figure 2.1) describes the energy levels more accurately, as shown in Equation 2.2.

$$E_n = h\nu(n+\frac{1}{2}) - h\nu\chi(n+\frac{1}{2})^2 \tag{2.2}$$

Here, χ represents the anharmonicity constant. The anharmonic model reflects the fact that, if the internuclear distance between two bonded nuclei becomes too great, the bond will eventually break, which is not the case for the simple harmonic oscillator. In this case, transitions with $\Delta n = \pm 1, \pm 2, \pm 3, ...$ are permitted, giving rise to overtone bands and combination transitions. A transition between two vibrational states can be induced by absorption of electromagnetic radiation, if the energy difference between these two states corresponds to the energy E of the incident radiation. The energy of an electromagnetic wave depends on its frequency, ν, multiplied by Planck's constant, h (Equation 2.3).

$$E = h\nu \tag{2.3}$$

While the frequency, ν is given in units of Hertz (Hz, s^{-1}), vibrational energies are usually given in wavenumbers, $\widetilde{\nu}$. Wavenumbers correspond to wavelengths, λ, per unit length. In vibrational spectroscopy, centimetres are typically the unit length, and therefore, the units are provided in cm^{-1}. Knowing this, one can rewrite Equation 2.3 as Equation 2.4:

$$E_n = h\frac{c}{\lambda} = hc\widetilde{\nu} \tag{2.4}$$

where c is the speed of light (c = 2.99792458 x 10^{10} cm s^{-1}). The energy difference of fundamental vibrations (from the ground state, n = 0, to the first excited state, n =1) corresponds to electromagnetic radiation in the MIR range (4000 - 400 cm^{-1} or 2.5 - 25 μm, i.e. 50 - 500 meV) for most vibrational modes. The overtone and combination bands correspond to energies in the near-infrared (NIR) spectrum (14000 - 4000 cm^{-1} or 0.8

[†] $h = 6.62607004 \times 10^{-34}\ J\ s\ (m^2\ kg\ s^{-1})$

[‡] The reduced mass allows both nuclei to be represented by a single mass which reflects the relative masses of each nucleus.

- 2.5 μm, i.e. 500 - 1500 meV) and are typically (much) less intense than fundamental transitions [7]. Therefore, in the MIR range, functional groups of molecules have unique, characteristic absorption bands, allowing the fingerprint identification of compounds and structural characterization of molecules.

For there to be IR absorptions of a molecule, it must possess a specific feature: an electric dipole moment μ of the molecule must change during the vibration (unless the molecule has a permanent dipole moment). This is the 'selection rule' for IR spectroscopy. A molecule in which the dipole moment changes as the bond expands and contracts, is termed 'IR-active'. By comparison, a molecule is deemed 'IR-inactive' if its dipole moment remains at zero, no matter how long the bond (as in homonuclear diatomic molecules) [8]. Vibrational spectroscopy is the communal label given to describe measurements involving both IR and Raman spectroscopies. While Raman spectroscopy also probes vibrational levels of molecular bonds, it does so by inelastic scattering of high-energy photons (from the UV to NIR). For Raman scattering, a change in the polarizability[§] α of the molecule is necessary. IR and Raman spectroscopy complement each other in the way that, under the particular condition that the molecule has a centre of symmetry, transitions that are forbidden in Raman scattering are allowed in IR absorption and vice-versa. In general, IR spectroscopy, which is active for polar bonds such as O–H, N–H or C-O, is used for the identification of functional groups of molecules, while Raman spectroscopy, active for bonds such as C=C, S–S, or C–S, is used for the identification of skeletal structures [12]. Since the work carried out in this thesis was predominantly based on MIR vibrational spectroscopy, only MIR-related methods, materials and techniques will be subsequently addressed and described in detail.

2.2 MIR absorption spectroscopy

The observation of spectral features in specific wavenumber regions of the IR absorption spectrum can be associated with modes characteristic of specific functional groups in organic molecules (e.g. -OH, -CH_2, C=O, etc.). These modes originate from large displacements of only a few atoms, while the rest of the molecule is almost stationary. Other modes involve the motion of several atoms in the molecule and lead to absorption bands characteristic of the molecule itself. These bands allow one to distinguish between molecules which contain similar functional groups and the frequencies are typically located in the region between 1500 and 600 cm^{-1} (or 6.66 and 16.66 μm), known as the *fingerprint region*, as shown in Figure 2.2 [11]. For different applications, different wavenumber regions are considered the most interesting (exhibiting characteristic peaks for the particular molecules of interest).

[§]The measure of the tendency of a molecule's electron cloud to be distorted by an external electric field.

Therefore, in this thesis, different wavenumber regions were considered according to each specific application.

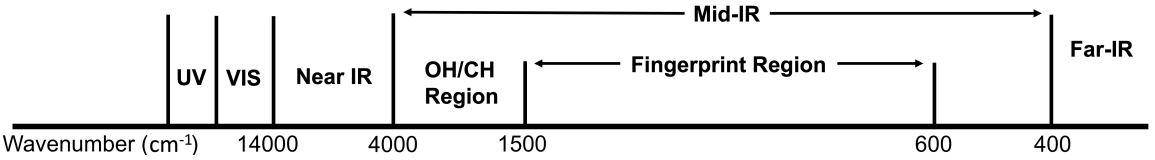

Fig. 2.2 Portion of the electromagnetic spectrum highlighting the MIR region and its fingerprint region.

2.2.1 Quantitative considerations

As a type of absorption spectroscopy, IR spectra can be evaluated quantitatively. The Beer-Lambert law[¶] is the fundamental law of quantitative spectroscopy. The *transmittance* of any sample at wavenumber $\widetilde{\nu}$ is given by the ratio between the intensity of light $I(\widetilde{\nu})$ that reaches the detector when the sample is in place (i.e. the sample (channel)), and the intensity of light $I_0(\widetilde{\nu})$ that reaches the detector without the sample in place (i.e. background or reference channel[‖]) - Equation 2.5. These intensity spectra are typically referred to as single-beam spectra.

$$T(\widetilde{\nu}) = \frac{I(\widetilde{\nu})}{I_0(\widetilde{\nu})} \tag{2.5}$$

The Beer-Lambert law relates the transmittance of light to the *absorbance A* by taking the negative logarithmic function (base 10) of the transmittance for a sample, which results in a linear relationship between the molar decadic absorption coefficient ε ($m^2\ mol^{-1}$), the concentration c (mol m^{-3}) of the sample and the length d (m) of the light interaction with the sample. The absorbance of a sample consisting of only one molecular species is given by Equation 2.6. While for low concentrations and assuming no interaction between molecular species, the Beer-Lambert law is additive, for N-component mixtures where more than one component absorbs at $\widetilde{\nu}$, the absorbance is given by the sum of the respective absorbances of each molecular species (Equation 2.7) [11].

$$A(\widetilde{\nu}) = -log_{10}T(\widetilde{\nu}) = \varepsilon(\widetilde{\nu}) \cdot c \cdot d \tag{2.6}$$

[¶]The Beer-Lambert law is a combination of two different laws: (1) Beer's law, which states that concentration of a chemical solution is directly proportional to its absorption of light; and (2) Lambert law, which states that absorbance of a sample is directly proportional to the path-length of light.

[‖]The reference channel (reference single-beam spectrum) takes into account the transmission characteristics of the spectrometer and the measurement set-up itself.

$$A_N(\tilde{\nu}) = \sum_{i=1}^{N} \varepsilon_i(\tilde{\nu}) \cdot c_i \cdot d \tag{2.7}$$

The IR absorption bands for small molecules in the gas phase at low densities consist of many narrow lines, which originate from a large number of transitions between rotational-vibrational energy levels. In the condensed phase, these bands are broadened due to intermolecular interactions [8, 11]. Therefore, for liquid samples, it is sufficient to record spectra with a resolution of 4 or 8 cm^{-1}. However, this broadening of the bands can sometimes make it difficult to distinguish between different molecules with similar spectral features in a mixture since these bands may overlap. In these cases, multivariate approaches, such as partial least squares regression (PLSR), which allows quantification of analytes of interest within mixtures, should be implemented. A brief introduction to PLSR is provided in Section 2.5.

2.3 MIR spectroscopic measurement principles

MIR spectra can be acquired via the following different techniques/configurations: transmission mode, transflection (double transmission) mode, reflection mode, or by attenuated total reflection (ATR) spectroscopy. The following paragraphs focus on providing an overview of transmission, transflection and ATR spectroscopy principles (Figure 2.3) since these were the main techniques used in this thesis.

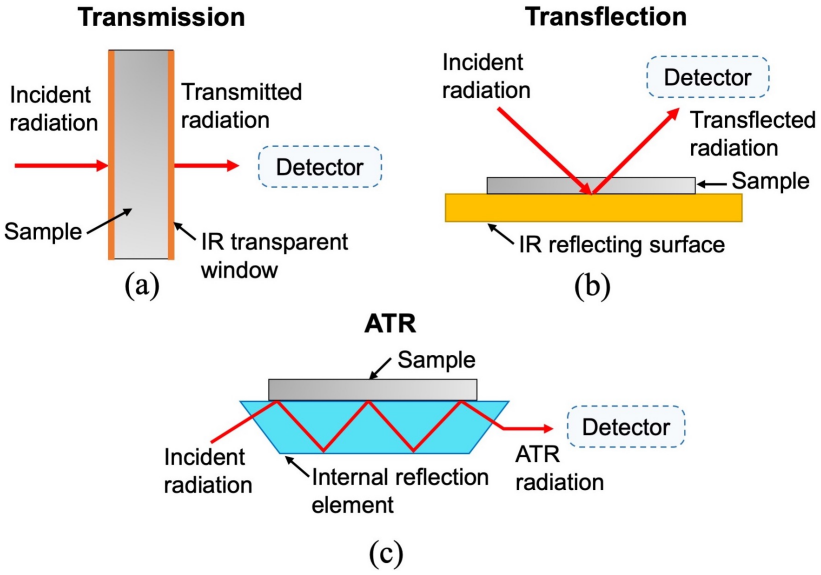

Fig. 2.3 Overview of three sampling methods commonly used for MIR spectral acquisition: (a) transmission; (b) transflection; and (c) attenuated total reflection (ATR).

2.3.1 Transmission mode

Transmission-mode measurements are the most simple form of IR spectroscopy, where the sample is held between two windows, which must be composed of an IR-transparent material, e.g. calcium fluoride (CaF_2) or zinc selenide (ZnSe), and placed directly in the light path of the spectrometer. Incident light enters the cell through one window, passes through the sample and, the remaining (non-absorbed) light exits the cell via the second window (Figure 2.3a). Apart from the selection of the IR-transparent window material, which should be transparent to IR-radiation over the wavelength range of interest and inert to the constituents of the sample, another important parameter to consider when carrying out transmission-mode measurements is the distance between the two windows, which essentially determines the optical path-length [8]. Longer path-lengths increase the amount of light-sample interaction, leading to increased absorption and stronger IR spectral peaks. However, if the optical path-length is too large, then the sample absorbs all the energy and the resulting spectrum will contain distorted or saturated peaks. Determining the optimum optical path-length depends on the nature of the sample (whether it contains a strong IR-absorber, e.g. water) and on the intensity of the MIR light source used, and therefore it will vary for different applications and setups. While the main advantage of transmission-mode MIR spectroscopy is its simplicity and the fact that it is a well-established technique, transmission measurements often provide spectra which are easy to interpret with good signal-to-noise ratio (SNR), and show an accurate correlation between molecular structures and spectral features.

2.3.2 Transflection mode

To measure a sample in transflection mode, the sample is placed on a window comprising an IR-reflective surface. The incident beam focused onto the sample transmits through the sample and the beam then bounces off the IR-reflective window surface (e.g. gold-coated silica), transmitting back through the sample and up into the detector, located on the same side as the IR-source (Figure 2.3b). The technique is termed transflection rather than reflection, as the measured spectrum is closely equivalent to a transmission spectrum recorded from a sample of approximately double the section thickness [7].

An advantage of a transflection-mode configuration system, and the main reason for its exploration in this thesis, is that both the light source and detector can be located close together, allowing the potential fabrication of a more compact and miniaturised IR-sensing system/device, unlike transmission-mode configurations where the source and detector are conventionally located on opposite sides of the system. However, a disadvantage of this method is that transflection spectra can be distorted non-linearly as a function of wavenumber

with respect to sample thickness, due to electric-field standing waves (EFSW) [13] which arise due to the reflection from the metallic surface of the reflective window.

2.3.3 Attenuated total reflectance

ATR spectroscopy is based upon the principle of total internal reflection (TIR). For incident angles θ_i greater than a critical incident angle θ_c, light is totally reflected at the interface between an optically dense medium, with high refractive index n_1, and an optically rare medium, with low refractive index n_2, (Figure 2.4). The critical angle θ_c can be derived from Snell's law (Equation 2.8) by setting the angle of the transmitted beam θ_t to 90^o ($\sin\theta_t = 1$) and solving for θ_c (Equation 2.9). The higher n_1 is in relation to n_2, the smaller θ_c becomes, and total internal reflection can be achieved over a broader range of incident angles.

$$n_1 sin\theta_i = n_2 sin\theta_t \tag{2.8}$$

$$\theta_c = sin^{-1}\frac{n_2}{n_1} \tag{2.9}$$

Although the incident beam is confined to the optically dense medium upon total reflection, since a photon has an electromagnetic field perpendicular to its path, its field also extends from the interface into the optically rare medium at the point of contact. This field is referred to as the evanescent field, also called evanescent wave (shown in Figure 2.4).

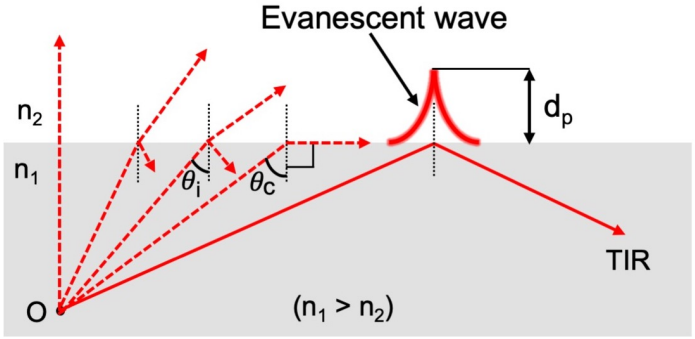

Fig. 2.4 IR light is refracted at the interface of an optically dense medium n_1 and an optically rare medium n_2 (dashed lines, Snell's law - Equation 2.8). Once a critical angle θ_c is exceeded, the incident light is totally reflected at the interface (solid line), generating an evanescent wave which extends into the optically rare medium, with a penetration depth d_p (Equation 2.10).

The evanescent field decays exponentially with distance into the optically rare medium and the decay rate depends directly on the wavelength of the radiation [14]. The effective

distance from the surface over which the evanescent wave interacts with the optically rare medium is known as the penetration depth, d_p, and can be approximated as the distance from the surface at which the strength of the field has decayed to e^{-1} of its intensity at the surface. It can be calculated from the wavelength of the incident radiation, λ, the refractive index of the ATR element and the sample, n_1 and n_2 respectively, and the angle of incidence, θ_i [14]:

$$d_p = \frac{\lambda}{2\pi n_1 \sqrt{sin^2\theta_i - (\frac{n_2}{n_1})^2}} \tag{2.10}$$

Typical materials used in ATR elements for MIR spectroscopy are germanium (Ge), ZnSe and diamond. Since the d_p is affected by θ_i and the refractive index of the ATR element, one can select the material of the ATR element and set the θ_i accordingly, to achieve a higher or lower d_p (to probe further into the sample or closer to the surface, respectively). However, this depth will always be limited by the wavelength of the incident radiation. In the MIR spectral range, the penetration depth of many common and relevant materials is of the order of microns. For instance, for total reflection at the interface of diamond (n_1 = 2.41) and water (n_2 = 1.34) and for a typical incidence angle $\theta_i = 50^o$, the penetration depth of the evanescent field into water ranges between 3.13 μm for a wavelength of 25 μm ($\widetilde{\nu}$ = 400 cm^{-1}) and 0.313 μm for a wavelength of 2.5 μm ($\widetilde{\nu}$ = 4000 cm^{-1}). While ATR elements having single reflections are used for a wide range of applications, particularly those where miniaturization is key, multiple internal reflections can be used to enhance the interaction of the sample with the IR beam, allowing higher sensitivities. The cumulative path-length obtained can be compared with the absorbance values of transmission measurements [14].

2.4 MIR optical fibres

IR fibres provide the capability of "taking the spectrometer to the sample" instead of the traditional method of taking the sample to the spectrometer. The transfer of IR signal between the spectrometer and sensing location via optical fibres offers several advantages, such as the measurement of samples in remote or hard-to-reach locations and the ability to perform real-time measurements of reactions and media of interest by direct insertion of fibre-optic probes. Moreover, optical fibres are typically flexible up to a certain degree, making their connection between the spectrometer and sample relatively easy. The guidance of a light beam through an optical fibre takes place due to the phenomena of TIR, described previously. Figure 2.5 shows a diagram of an optical fibre which consists of a cylindrical core (refractive index n_{co}) clad by a material of lower refractive index (n_{cl}). When shining light on the end of a fibre, ray optics define which rays may be guided. The largest angle incident on the end

of a fibre below which light may be guided, denoted θ_a^{max}, corresponds to an internal angle θ which is equal to θ_c. By applying Snell's Law, the *Numerical Aperture* (NA) of an optical fibre can be determined:

$$NA = n_a sin\theta_a^{max} = \sqrt{n_{co}^2 - n_{cl}^2} \tag{2.11}$$

where n_a is the refractive index beyond the end of the fibre, usually air ($n_a \approx 1.0$) [15]. In practical terms, the NA is a measure of the light-gathering ability of a fibre and it also indicates how easy it is to couple light into a fibre. A larger difference between the refractive indices (n_{cl} and n_{co}) leads to a smaller value of the critical angle for total internal reflection and therefore a higher flexibility in coupling in and out of the optical fibre. On the other hand, losses due to reflections at the core ends are higher for fibres with high refractive indices. In ideal cases (i.e. when there is no bending or scattering), optical fibres tend to preserve the angle of incidence during transmission (i.e. if a ray is incident at angle θ_a, it will ideally emerge from a fibre at angle θ_a).

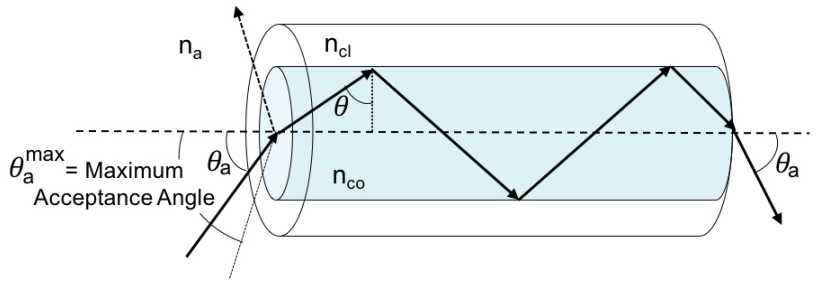

Fig. 2.5 Acceptance angle and light propagation in an optical fibre.

Fibre-optic sensors can be constructed using a variety of configurations, including transmission, transflection, reflection, and ATR [16]. The fibre-optic sensing configurations used in this thesis were transmission and ATR, and therefore these will be discussed in the following paragraphs in more detail. For the transmission and transflection configurations, the same principles as described in Section 2.3 are applied, but using optical fibres to guide light to and from the sample of interest. Typically, in these cases, two fibres are used: one to transmit the IR beam to the sample (illuminating fibre) and the other to collect the IR beam resulting from the interaction with the sample (detection fibre). In the ATR configuration, the sensing region of the fibre is core-only (unclad) in order to allow the interaction of the propagating evanescent field (generated by TIR, as described in Section 2.3.3) with the surrounding medium. In fact, sensors based on fibre-optic evanescent-wave spectroscopy (FEWS) can be considered as an advancement of the ATR technique, where the sensitivity can be enhanced by the increased number of internal reflections [17]. Since the intensity of

the evanescent field strongly depends on the waveguide geometry, tapering a section of the fibre, or bending it, significantly increases both the number of internal reflections and the penetration depth d_p of the evanescent field at each reflection into the measured sample, thus improving the sensitivity of detection. Fibre tapering has been extensively explored in recent years for a wide range of applications [18–20]. The use of U-bent fibres has been explored in this thesis for two different sensing applications. By bending a cylindrical fibre to form a U-shaped element, during the propagation of the beam within the U-bend, the angle θ_i decreases and becomes closer to θ_c. It has been found that the sensitivity increases with the increase in refractive index of the surrounding medium and also is roughly proportional to $1/R$, where R is the diameter of the bend (see Figure 2.6) [19, 21, 22].

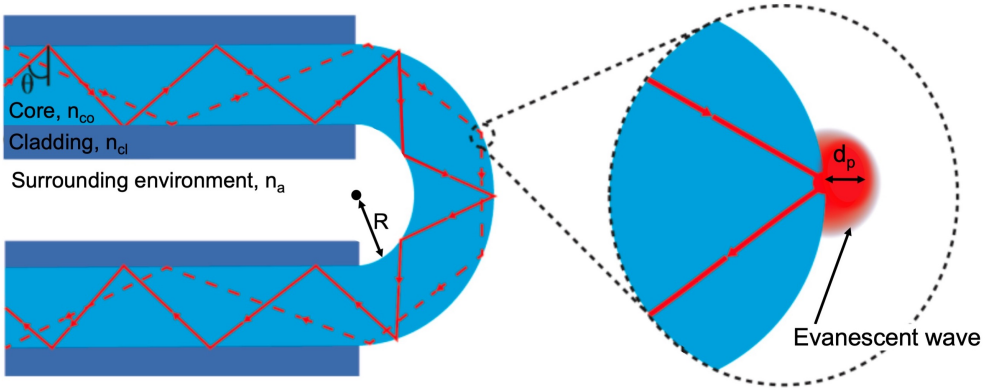

Fig. 2.6 Geometry of a U-bent fibre illustrating the penetration depth d_p of the evanescent wave in the sensing region. Adapted from [23].

The IR transmission (i.e. intensity and ranges) through a fibre is governed by the material properties but is also affected by other factors, such as scattering losses within the material, impurities, material defects and excessive bending. The losses that occur when the light travels through a fibre or waveguide are called propagation losses and the loss coefficient per unit length of an optical fibre is termed the *attenuation* and is typically measured in decibels (dB) per metre. For an input power P_{in} resulting in an output power P_{out}, the power loss, α, in dB is given by:

$$\alpha[dB] = 10log(\frac{P_{in}}{P_{out}}) \tag{2.12}$$

MIR-transmitting fibres are typically fabricated from a variety of materials, such as polycrystalline silver halides (AgX), most commonly chloride (Cl) and bromide (Br), amorphous chalcogenide glasses, fluoride glasses and tellurium halides. Silver halide fibres are flexible, non-toxic, and non-hygroscopic, and they are transparent in the spectral range 500 - 2500

cm^{-1} (4 – 20 μm) with a minimum loss of 0.2 dB/metre between 666 and 1111 cm^{-1} (9 and 15 μm). Figure 2.7 shows a typical typical transmission curve of an unclad silver halide (AgClBr) fibre.

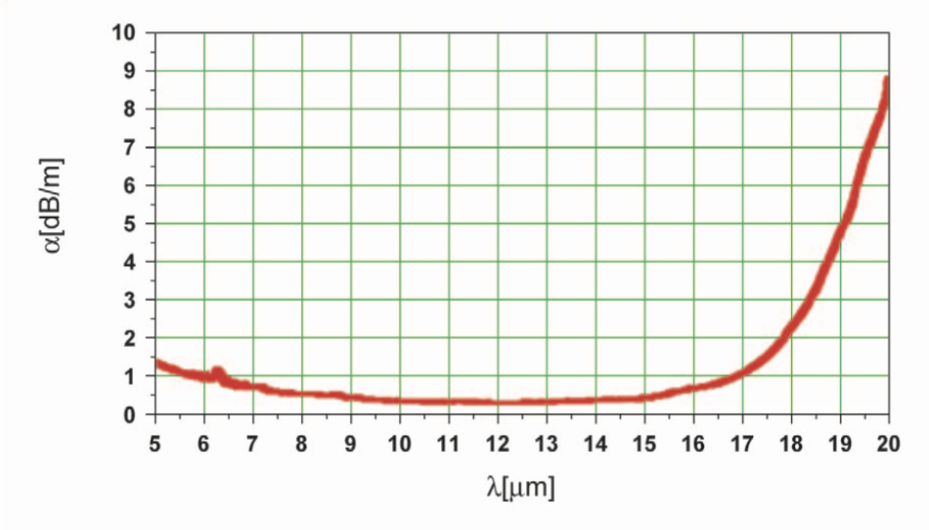

Fig. 2.7 Transmission losses of an unclad silver halide (AgClBr) fibre with a length of 7 m and a diameter of 0.9 mm [22].

2.5 Multivariate data analysis: PLSR

Data analysis is of great importance when handling MIR spectra of multicomponent systems. Typically, in order to obtain quantitative information on target analytes, multivariate regression methods need to be implemented. Since multivariate analysis was not the primary focus of this work, but rather a tool used to analyse the acquired data, the following paragraphs provide only a brief introduction to the multivariate analysis method used in this thesis, namely Partial Least Squares Regression (PLSR), highlighting the general basic principles and terminologies. A more in-depth description of this method is provided elsewhere [24–26]. PLSR is known to be a suitable technique to correlate, noisy, numerous and strongly correlated (co-linear) **X** data (i.e. IR spectra) with dependent response data, **Y** (i.e. concentration values), by a linear multivariate model. The independent **X** data are projected onto a set of components ("latent variables") which are good predictors of **Y**. Prior to building a model, the reference data **Y** must be known, either predefined by measuring standards of known concentration (i.e. synthetic standards), or determined by a reference technique. For PLSR, the **X** data are decomposed into a score matrix **T**, a loadings matrix **P**, and an error matrix **E** (external relation, Equation 2.13). A similar external relation can also be calculated for the

dependent (reference) data, **Y** (Equation 2.14). A regression model can then be iteratively calculated using scores matrices of the **X** and **Y** data (**T** and **U**), the inner relation (Equation 2.15), under the condition to minimise the error matrix **F**. Figure 2.8 shows a schematic representation of a PLSR model.

$$\mathbf{X} = \mathbf{TP^T} + \mathbf{E} \tag{2.13}$$

$$\mathbf{Y} = \mathbf{UQ^T} + \mathbf{F} \tag{2.14}$$

$$\mathbf{U} = \mathbf{BT} \tag{2.15}$$

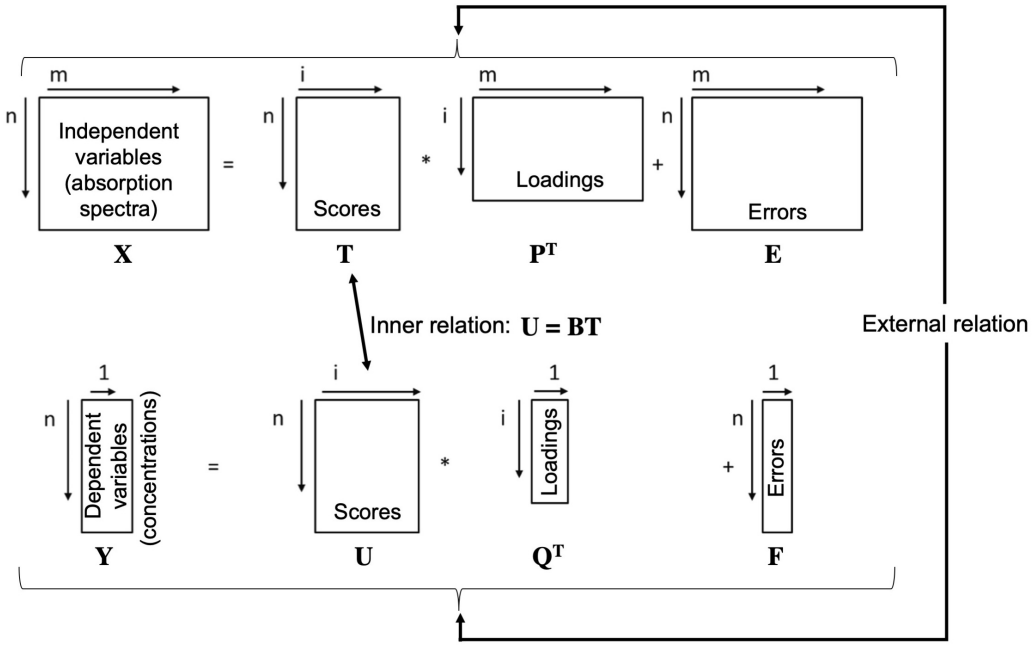

Fig. 2.8 Schematic representation of a PLSR model. Adapted from [26].

The result is a number of PLSR components or "latent variables" that best describe the variation of the dependent variables. The choice of an optimum number of components is a crucial step in model development, since PLSR models can suffer from over-fitting if the number of components are not selected objectively. This can be done by internal or external validation of the model and evaluation of the root-mean-square error (RMSE), calculated using equation 2.16, where y_i are the measured **Y** values, $\hat{y}_i$ are the predicted values and n is the number of samples (i.e. number of spectra).

$$RMSE = \sqrt{\frac{\sum_{i=1}^{n}(y_i - \hat{y}_i)^2}{n}} \tag{2.16}$$

The lower the RMSE, the more accurate is the predictive ability of the model. When performing internal validation, it is referred to as the root-mean-square error of cross-validation (RMSECV), while when using external validation, it is referred to as the root-mean-square error of prediction (RMESP). For internal or cross-validation, the **X** data are divided into smaller subsets and one of the subsets (the test-set) is used to test the predictive quality of the model built using the remaining subsets. Depending on the size and nature of the data set, different algorithms can be used to choose the subsets. The most straight-forward method is the "leave-one-out" cross-validation method, where one sample is left out one after another. This method, however, often leads to overly optimistic results. Another, more robust form of cross-validation, is the k-fold cross-validation method. This was the method used in this thesis to build the PLSR model and calibrate the number of components. In k-fold cross validation, the data are randomly divided into k segments, commonly referred to as folds. Subsequently, k iterations of training and validation are performed so that, for each iteration, one fold of data is removed for validation whilst the remaining k-1 folds are used for training the model. The RMSE is then the mean prediction error (RMSEP) for each fold of data removed during cross validation. The number of components that give the lowest RMSEP are considered optimal for the model [27]. Although many other methods are available for building PLSR models, such as the method based on independent test sets, they will not be discussed here since they were not implemented. In the present thesis (Chapter 4), a PLSR model was developed to quantify the clinically relevant compound concentrations from acquired MIR spectra of brain-trauma patient microdialysis samples.

2.6 Summary

This Chapter has provided the relevant theory and principles which form the basis of the work carried out in the different chapters presented in this thesis. The principles of transmission-mode and transflection-mode measurements are explored and assessed in Chapter 3 for infrared liquid sensing applications. In Chapter 4, mid-infrared transmission-mode absorption spectroscopy is explored as a technique to continuously monitor cerebral dialysate of traumatic brain injury patients. It is also in this Chapter that PLSR is implemented to perform multivariate analysis on acquired data. Chapters 5 is based on the principles of fibre-optic evanescent-field spectroscopy, where a U-bent fibre with a porous silicon cladding is used to enhance the detection of volatile organic compounds. Finally, Chapter 6 assesses the use of standard ATR spectroscopy and fibre-optic evanescent-field sensing for bioprocess monitoring.

Chapter 3

Integration of infrared spectroscopy and microfluidics for liquid sensing*

3.1 Introduction and literature review

Infrared (IR) spectroscopy has emerged in recent years as the preferred analytical method for quantitative and qualitative analysis due to it being rapid, non-destructive, reproducible, cost-effective and reagent-free [4]. In particular, it is an ideal tool for performing *in situ* and real-time monitoring of the evolution of reactive fluidic media, such as bio-fluids and micro-reactors [28]. In order to achieve this and to take full advantage of the benefits of IR spectroscopy, additional techniques which enable the handling of small sample volumes at controlled and reproducible flow-rates can be implemented. Microfluidics has become a fundamental tool in chemistry and biology and is typically used to manipulate small amounts of fluid within channels of dimensions of tens to hundreds of micrometers [4]. Moreover, the operation of microfluidic devices can be fully automated, thus improving ease of use, repeatability and reducing the element of human error and labour [29]. The coupling of microfluidic platforms with IR spectroscopy enables the sensitive analysis of micro- and nano-litre volumes, opening doors to multiple novel chemical and biochemical sensor concepts and applications from biosensing, catalytic process monitoring, lab-on-a-chip devices, and biochemical analysis [4]. However, this combination may give rise to additional challenges, such as the on-chip integration of light sources, the need for specific fabrication materials/components with IR-transparency and also optimum chip geometries (e.g. fluid-channel dimensions), which have an effect on the overall performance of the system. Challenges associated with fabrication materials, such as IR-transparency and

*F. Alimagham, T. Hutter, **Integration of IR fiber optics and microfluidics for sensing applications**, Accepted for publication in *OSA Optical Sensors and Sensing Congress Proceedings*, **2020**

chemical/biological compatibility arise since traditional microfluidic device-fabrication materials (e.g. glass, polymers) cannot always be easily implemented due to their IR absorption, reflection and scattering effects. Therefore, either IR-transparent materials or optical-integration methods which avoid this are required. Several strategies to integrate IR light sources into microfluidic systems have been implemented and reported, such as the integration of miniature ATR elements [30, 31] and waveguides [32, 33] directly into the microfluidic architecture, as well as the coupling of optical fibres [34, 35]. While the direct integration of ATR elements and waveguides typically involves complex integration and fabrication processes, optical fibres can be simply coupled directly to the microfluidic device, allowing beam delivery and collection at a single location with high precision. Moreover, the coupling of optical fibres to microfluidic structures typically avoids major adaptations to current microsystems and, in some cases, may not require the use of special IR-transparent components, since optical fibre tips can be designed to accommodate contact with various substances. An added advantage of using fibre-optics is that it allows miniaturizing the sensor to the size of a wearable device, which can be placed in remote locations (e.g. hard-to-reach or unfavourable locations or on/close to a patient for continuous monitoring applications). The fact that the IR equipment is maintained at a distance from the sensing location also eliminates the risk of on-chip interference from the light source/detector, allowing increased spectral stability and quality [36].

In this chapter, the development of four microfluidic device prototypes with integrated optical IR fibres is described. Section 3.2 focuses on the fabrication and testing of three devices in transmission-mode configuration while Section 3.3 describes a device fabricated in transflection-mode configuration. All devices were assessed in terms of their hardware performance and chemical-compound sensing capabilities in aqueous media. Preliminary optical measurements to test the hardware were carried out using near-infrared (NIR) optical fibres, given their lower cost, wider availability and easier handling compared to MIR fibres. All subsequent measurements were carried out using MIR optical fibres.

3.1.1 Device design, configuration and functional principle

Standard configurations for performing infrared measurements include transmission-mode, transflection-mode and ATR (see Figure 2.3), as previously described in Chapter 2. In this chapter, transmission and transflection-mode devices were considered due to their simple and straight-forward assembly and easy device integration. Three fibre-optic integrated microfluidic device prototypes in transmission-mode configuration were developed and tested. Figure 3.1a shows the general configuration of such a device, which consists of a microfluidic platform, to enable the flow of a given liquid sample through a channel, which

is coupled to optical fibres, to remotely provide a source of IR light on one side of the channel (via the illumination fibre) and detect the transmitted signal on the other (via the detection fibre). The design, characteristic features and performance of these devices are fully described in Section 3.2. A fourth fibre-optic integrated microfluidic device prototype in transflection-mode was developed and tested. The general configuration of such a device is shown in Figure 3.1b, which equally consists of a microfluidic platform, with the main difference being the angle at which the fibres attach to the device. In transflection-mode, both fibres (illumination and detection) can be attached from the same side of the device, where a reflective surface is placed on the far side of the fluidic channel to reflect the incident light into the detecting fibre after passing through the channel. This arrangement can result, overall, in a less bulky, more compact and robust system. Since the light interacts with the sample twice (before and after reflection), the optical path-length of this system can be made half the size of the required path-length (e.g. if the required path-length is 50 μm, a path-length of 25 μm can be used). Section 3.3 describes the fabrication process and performance of this device. All four devices were tested in terms of their performance for aqueous sample-handling and sensing capabilities for different organic compounds.

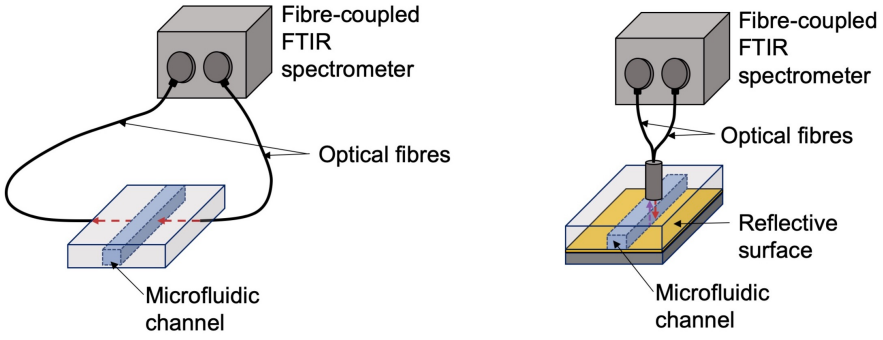

Fig. 3.1 Schematics of fibre-coupled microfluidic devices in (a) transmission-mode; and (b) transflection-mode.

3.2 Transmission-mode devices

Three devices of different materials and specifications were designed, fabricated and tested for suitability for IR spectroscopic analysis of aqueous samples. The devices were built in transmission-mode configuration with a flow-through channel that is perpendicular to the optical path-length defined by two fibres. The generic configuration is illustrated in Figure 3.2. When a given sample flows through the channel and across the beam of light between

the fibres (sensing region), part of the light is absorbed by the sample, part is scattered and the remaining light is transmitted to the receiving fibre. The absorbed and scattered light vary with the analyte concentration of the sample (i.e. the higher the concentration, the higher the absorption), and it is the variation in amplitude of the light transmitted to the detection fibre that can be used to determine the sample concentration. An attractive feature of this design is that it allows the light to interact directly with the sample, without the need for IR-transparent windows. The main components of the devices were fabricated out of two different polymers (devices 1 and 3) and stainless-steel (device 2) by the workshop of the Department of Chemistry.

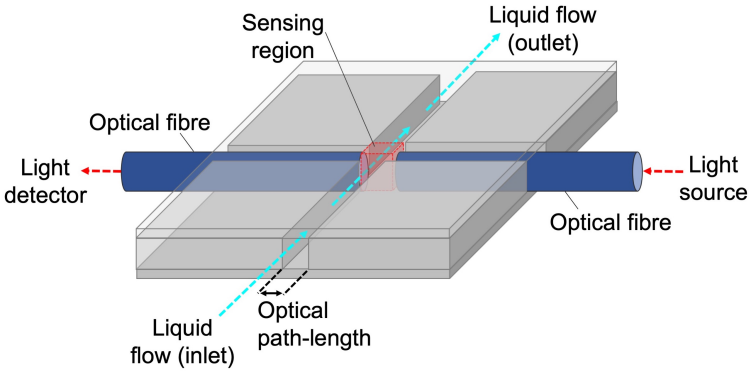

Fig. 3.2 Illustration of a transmission-mode sensing configuration using optical fibres to carry light to and from a fluidic platform, where the delivered light interacts with a continuously flowing liquid sample.

As well as the three fabricated transmission-mode devices (devices 1, 2 and 3), measurements using a standard quartz transmission cell of 1 mm path-length were also taken as a means of comparison. Given the higher cost and limited availability of MIR fibres and components, preliminary measurements of ethanol and glucose solutions were carried out using NIR fibres in conjunction with the standard cell and devices 1 and 2. Both ethanol and glucose were chosen as test molecules, given their relevance and well-studied IR spectra. Once an optimised system was achieved (device 3), MIR fibres were implemented and used to detect different concentrations of glucose.

3.2.1 Device 1: fibre-coupled PTFE microfluidic flow-cell

3.2.1.1 Design and fabrication

Device 1 comprises two machined layers of polytetrafluoroethylene (PTFE), a synthetic fluoropolymer, which are stacked and tightly assembled using four bolts and nuts, as presented

in the CAD models of Figure 3.3. The general specifications of device 1 are presented in table 3.1 and the respective engineering designs can be found in Figure A.1 (Appendix A).

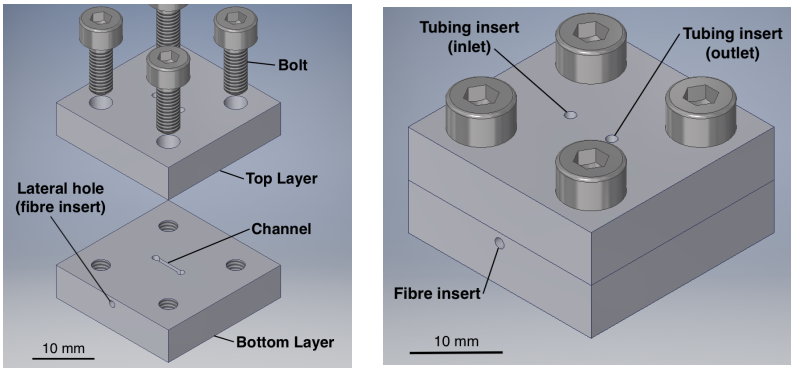

Fig. 3.3 CAD models of device 1. (a) Unassembled; and (b) assembled.

Table 3.1 Specifications of device 1.

Material	PTFE
Path-length	Adjustable (0 - 500 μm)
Channel volume	2.5 μL
Fibre coupling	Bare fibre terminations

The fluidic channel is located in the bottom layer through which the sample flows. Two aligned holes are located on either side of the channel for insertion of the optical fibres. These holes have the same diameter as the outer diameter of the fibre cladding to ensure a tight fit and thus prevent leakage. The fibres are pushed in until reaching the channel and their surfaces are flush with the channel walls, as shown in Figure 3.4a.

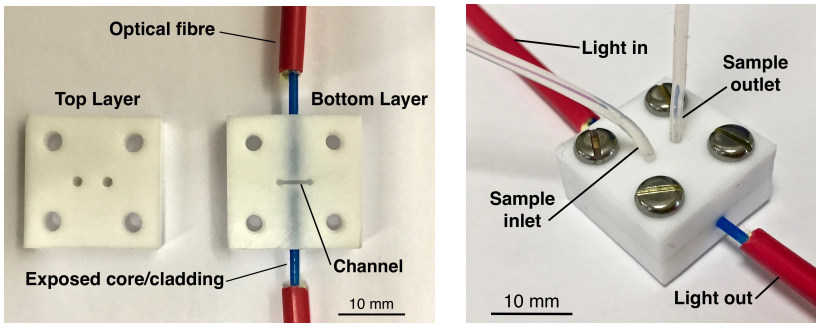

(a) (b)

Fig. 3.4 Images of device 1 with connected optical fibres. (a) Unassembled; and (b) assembled with connector tubing.

A NIR fibre (1 m, 0.5 numerical aperture (NA), 1000/1030 μm core/cladding, FP1000ERT, Thorlabs), was cleaved using a diamond cutter and stripped from its coating to expose the core/cladding before being inserted into the lateral holes. The top layer has two holes on the surface (see Figure 3.4a - top layer), into which tubing (008T16-030-200 PTFE tubing 1.6 mm OD x 0.3 mm ID, Cole-Parmer Ltd., UK) is inserted to be used as the sample inlet/outlet, as shown in Figure 3.4b.

3.2.1.2 Fibre preparation

Device 1 was built to incorporate two terminations on either side of the channel. For this, the NIR fibre was cut in two equal parts and a small section (approx. 2 cm) of the fibre coating was stripped from each end using standard electrical cable-stripping tools. Since the end surface quality is one of the most important factors affecting fibre losses, preparing good quality end-faces which are smooth and flat is crucial. This can be achieved by polishing and/or using a fibre cleaver. A custom-made clamp was developed to secure the fibres in place for the cleaving and polishing processes (Figure 3.5a). Two bolts were used to secure and clamp the fibre in place and can be adjusted for fibres of different diameters. A diamond blade was used to scribe and cleave the end of each fibre. Figure 3.5 shows a silica fibre cleaved using the diamond blade (3.5b) and using a carbon steel blade (3.5c). As shown, the diamond cutter provides a far better quality cleave, given its suitable material properties and ability to "scratch" the silica surface, while the steel blade provides an uneven and highly-scattering surface. The fibre-cleaving is followed by a step-by-step polishing process, where the fibre end-face is positioned at the same level as the clamp surface and lapping films of 5, 3, 1 and 0.3 μm grit sizes (LF5P, LF3P, LF1P and LF03P, Thorlabs) are used (in this particular order) by making circular "figure 8" paths on the fibre end-face until no scratching is visible. The cleaved fibres were finally observed under a low magnification (6 - 10x) microscope to inspect the quality of the end-face.

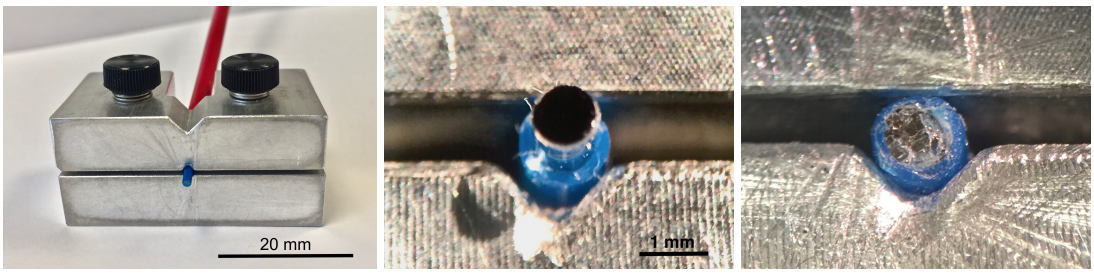

(a) (b) (c)

Fig. 3.5 (a) Custom-built clamp for fibre-cleaving and polishing. (b) Good quality end-face, cleaved using a diamond blade; (c) bad quality end-face, cleaved using a carbon steel blade.

3.2.1.3 Optical setup and calculations

Optical calculations were carried out in order to determine the theoretical light throughput from the illumination fibre to the detection fibre. The fibres used in device 1 have an NA of 0.5 and a silica core (refractive index n_c = 1.458) of 1000 μm diameter. From Equation 2.9, the critical angle θ_c was calculated as 30^o. Since optical fibres tend to preserve the angle of incidence during transmission, if a light ray enters the fibre at $\theta_c = 30^o$, it will reach the illuminating fibre end-face with the same angle. Since these flow-cells are most suitable for aqueous samples, the refractive index of water (n_m = 1.33) was used to estimate the amount of light that would reach the detection fibre. Knowing n_c, n_m and the estimated angle of the light emerging from the fibre (30^o), from Equation 2.8, the refracted angle that the light will acquire when entering the aqueous medium was calculated as being 33.29^o. Considering all possible directions of the light exiting the fibre core simultaneously at this angle and from different points (i.e. centre, extremities, etc.), a light cone is obtained (see Figure 3.6) which will expand towards the receiving fibre whose base dimensions after a certain optical path-length, l, and through a particular medium, can be calculated by applying basic trigonometry. The total cone-base area reaching the detection fibre for the optical path-length of device 1 ($l_{device1}$ = 500 μm), was determined as 2.154 mm^{2*}.

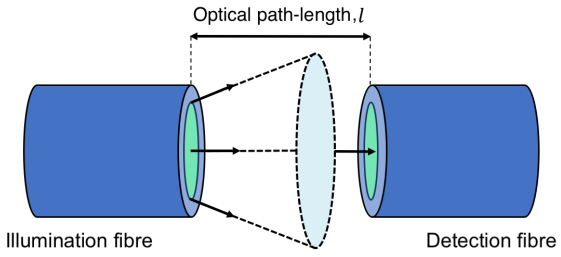

Fig. 3.6 Schematic of optical path-length, l, between illumination and detection optical fibres.

Finally, the percentage of transmitted light reaching the detection fibre can be determined from the ratio between the accepting fibre surface area (0.785 mm^2) and the calculated cone-base area (2.154 mm^2). For device 1, the theoretical percentage of light (considering the fibre surface is of acceptable quality) reaching the detection fibre is $\sim$ 36 %.

*Since light emerges from many points of the transmitting fibre surface (including extremities), the total area of light reaching the receiving fibre is determined by the sum of the overlapping cone-base areas resulting from the centre and the extremities of the fibre core.

3.2.1.4 Hardware performance

The general experimental arrangement for testing the device in terms of hardware performance is shown in Figure 3.7, where two fibres (illumination and detection) were connected to each side of the device and coupled to a fibre-coupling spectrometer. PTFE tubing was used to carry the sample to and from the device channel. A controlled and constant flow-rate was provided by a high-precision syringe pump (SPM 100, SIMTech Microfluidics Foundry, South Korea). After flowing through the channel, the sample was collected in a beaker via the outlet tubing.

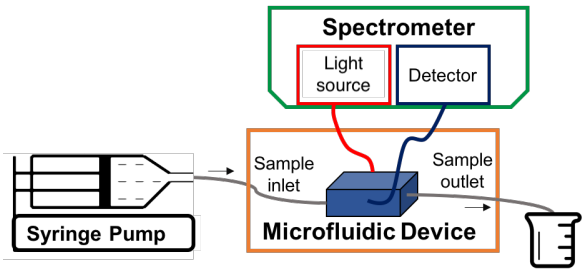

Fig. 3.7 Schematic of experimental setup to test devices for continuous fluid analysis.

Testing for leakage is a crucial part of the operation of fluidic devices and systems. Device leakage was tested by pumping DI water at a constant flow-rate of 0.5 mL min^{-1} through the channel for several hours. This device showed no signs of leakage, which is likely due to the material it is made out of (PTFE), which acts as a sealant when tightly clamped. Device 1 has an easily adjustable path-length determined by the distance between the end-faces of the cleaved fibres (0 - 500 μm). However, this distance cannot be accurately controlled. It is possible to manually calculate the path-length for a fixed fibre position using a fluid of a known composition and IR attenuation but this is impractical and time consuming. The device has a total channel volume of 2.5 μL, which is suitable for some applications, but might be too large in instances where sample volumes are very small (e.g. biofluid monitoring). Overall, the material and simple design of device 1 make it lightweight and very easy to handle and assemble, without mentioning its low-cost and easy fabrication. However, the inaccurate control of path-length and the need to cleave fibres makes it non-ideal for particular applications where highly accuracy and reproducibility are crucial.

3.2.2 Device 2: fibre-coupled stainless-steel microfluidic flow-cell

3.2.2.1 Design and fabrication

Device 2 comprises three machined stainless-steel layers which are stacked and fastened together using four bolts, as shown in Figure 3.8a. The general specifications of device 2 are presented in Table 3.2 and the respective engineering designs can be found in Figure A.2 (Appendix A).

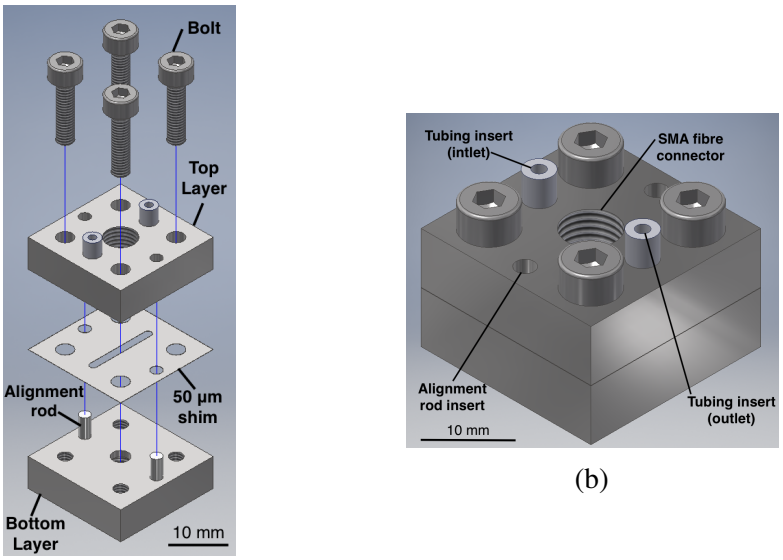

(a) (b)

Fig. 3.8 CAD models of device 2. (a) Unassembled and (b) assembled.

Table 3.2 Specifications of device 2.

Material	Stainless steel
Path-length	50 μm
Channel volume	1.6 μL
Fibre coupling	SMA connectors

The layers are carefully aligned during assembly using two alignment rods. In this apparatus, the fibres do not need to be cleaved and are directly coupled to the device using their standard SMA connectors. The top and bottom layers provide a central threaded hole for connecting the optical fibres in a two-step process: 1. Connecting SMA adapters (T4286, Thorlabs), which were modified to match the exact depth of the holes, to one of the SMA connectors of each fibre; and 2. connecting this set to the top and bottom layers of the device,

as shown in Figure 3.9. In order to prevent leakage, a rubber O-ring (RS Pro Nitrile) of 2 mm inner diameter (ID) was initially placed in the SMA connector insert. The middle layer consists of a 50 μm stainless-steel shim and provides a fluidic channel of 1.6 μL volume. Two holes on the top layer were used as the channel inlet and outlet, where hollow PTFE cylinders are inserted to provide a snug fit for the sample-carrying tubing (see Figure 3.8b). For NIR measurements, two 0.39 NA NIR fibre cables (FT1000EMT, Thorlabs) were used. As for device 1, one fibre is used as the light source and the other as the light detector. Before device assembly, each layer was cleaned with Kimtech wipes (7552, Kimberly-Clark) and isopropanol (437522, Sigma-Aldrich), to eliminate any dust particles that could cause internal leakage.

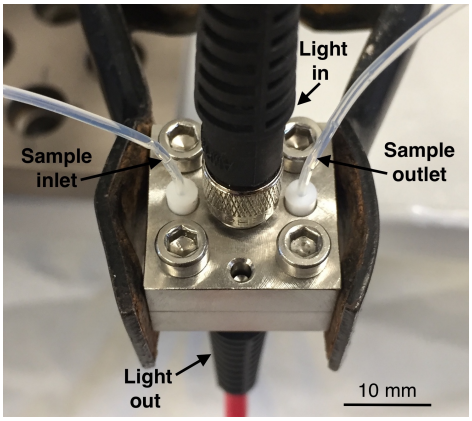

Fig. 3.9 Image of assembled device 2 with connected optical fibres and tubing.

3.2.2.2 Optical calculations

The NIR optical fibres used here have an NA of 0.39, with a 1000 μm diameter silica core. Following the same logic and considerations as for the calculations of device 1, the refracted angle entering the medium and the total light cone-base area reaching the receiving fibre were calculated to be 22.95^o and 0.861 mm^2, respectively, considering the reduced optical path-length of device 2 ($l_{device2}$ = 50 μm). The resulting light throughput for device 2 was therefore determined as being $\sim$ 91 %.

3.2.2.3 Hardware performance

In order to test this device, the same experimental arrangement, instrumentation and conditions as described for device 1 in Figure 3.7 was used. While device 1 showed no signs of leakage, device 2 showed small signs of leakage after four hours of flowing DI water. Device 2 is made entirely from stainless steel, which proved to not provide a tight seal. In order to

correct for this, two 50 μm-thick PTFE layers were cut in the same shape as the 50 μm-thin stainless steel shim and bonded to either side of the shim. In addition, all internal stainless steel surfaces were micro-roughened to ensure an enhanced, air-tight grip. After several uses of device 2, small amounts of leakage were also noted at the tubing inserts of the inlet and outlet, which are likely due to the their soft material properties which deform over time. Increasing the length of the tubing inserts helped solve this issue. The optical path-length of device 2 is provided by the 50 μm-thick shim, where the optical fibres do not need to be cleaved and are connected to the top and bottom layers through SMA adaptors. In this case, although the path-length is not adjustable (custom-made shims of different thicknesses would have to be made), the shim acts as a spacer to accurately control the distance between fibres (i.e. once each fibre end-face reaches the stainless steel shim, it cannot be pushed any further, leaving an exact 50 μm gap between the two). The smaller channel volume of 1.6 μL means that it can be used for smaller sample volumes compared to device 1. Although device 2 is heavier and more complicated to assemble in comparison to device 1 (due to the three layers and additional PTFE to prevent leakage), it is far more stable, robust and allows better reproducibility.

3.2.3 Device 3: fibre-coupled PEEK microfluidic flow-cell

3.2.3.1 Design and fabrication

Device 3 comprises two layers of polyether ether ketone (PEEK) which sandwich a PTFE spacer (of a given thickness) to establish the required optical path-length, as shown in Figure 3.10.

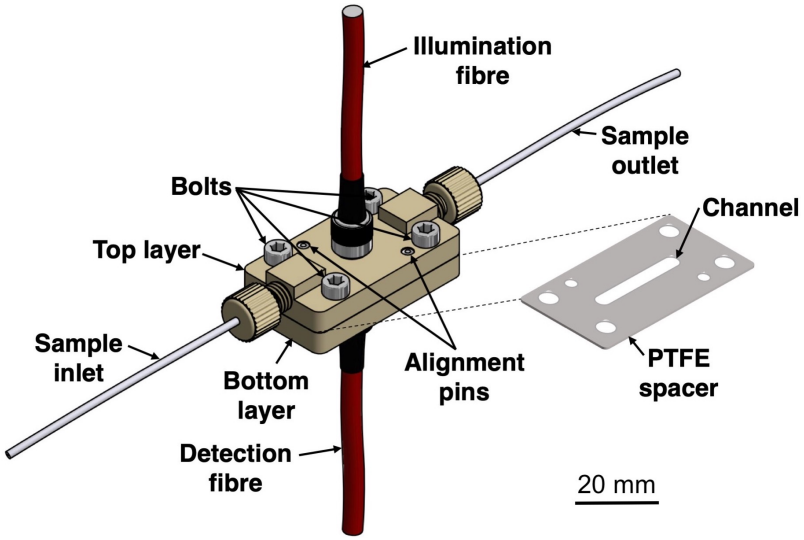

Fig. 3.10 CAD model of device 3 with connected optical fibres and tubing.

The general specifications of device 3 are presented in table 3.3 and the respective engineering designs can be found in Figure A.3 (Appendix A). The top and bottom layers provide a central threaded hole carefully designed to allow direct connection of the fibres via their SMA connectors while keeping the fibre tip flush with the inner surface of each layer, as can be seen in Figure 3.11a.

Table 3.3 Specifications of device 3.

Material	PEEK
Path-length	Adjustable (25, 50 or 100 μm)
Channel volume*	0.3, 0.65 or 1.3 μL
Fibre coupling	SMA connectors

*Dependent on PTFE spacer thickness

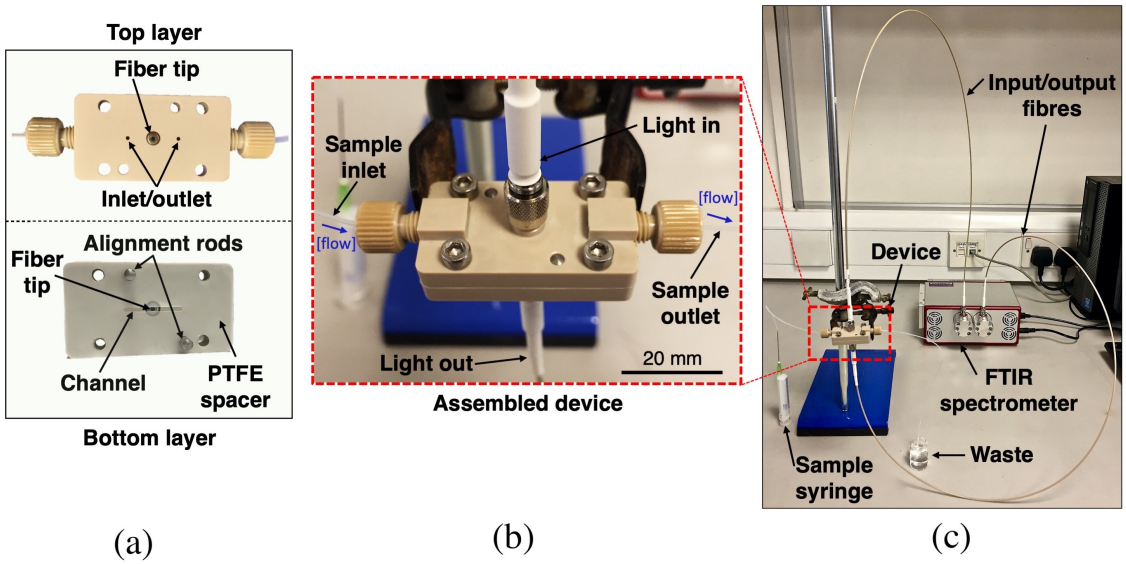

(a) (b) (c)

Fig. 3.11 Images of device 3. (a) Unassembled; (b) assembled and with connected optical fibres and tubing; and (c) coupled to a portable FT-IR spectrometer via the two (illuminating and detection) fibres.

Two threaded lateral holes on the top layer were made to connect off-the-shelf tubing connectors (PEEK gripper fitting nut and ferrule, 1.6 mm OD Tubing, 1/4-28 flat bottom, Kinesis) to provide the inlet and outlet of the device. The tubing was first attached to the connectors and only then were the connectors inserted into the device. During assembly, two alignment rods on either side of the device were used to secure the PTFE spacer and top layer in place before tightening.

Devices 1 and 2 were tested using NIR fibres, given their reduced cost and wide availability, while device 3, as the improved system, was tested using two hermetically-sealed MIR fibres (PIR AgCl:AgBr polycrystalline, core/clad 900/1000 μm, NA: 0.3, length: 0.5 m, Art Photonics, GmbH, Germany). The hermetic seal was only required on one end of each fibre (the end that would connect to the device) in order to prevent any leakages through the fibre. Figure 3.11b shows the final assembled device and Figure 3.11c shows the device connected to a fibre-coupled FT-IR spectrometer via the two fibres, ready for the spectral acquisition of an injected sample.

3.2.3.2 Transmission study and selection of optimum optical path-length

The optical path-length of device 3 is determined by the thickness of the PTFE spacer used in the assembly. Therefore, it was necessary to determine the optimum optical path-length for operation. For this, PTFE spacers of different thicknesses (25, 50 and 100 μm) were machined into the required shape and inserted into the device.

In order to give insight into the accessible wavenumber ranges using the different optical path-lengths and water as a solvent, single beam spectra (i.e. the intensity of light that reaches the detector at each wavenumber) were acquired with water being injected into the channel at a constant flow-rate of 0.2 mL min^{-1} using a fibre-coupled spectrometer (as shown in Figure 3.11c). These single beam spectra take into account the transmission characteristics of the measurement set-up itself. Figure 3.12 shows the single-beam (intensity) spectra of the setup of device 3 between 833 to 5000 cm^{-1} with water in the channel using each optical path-length, revealing the wavenumber regions where very little or no IR light reaches the detector.

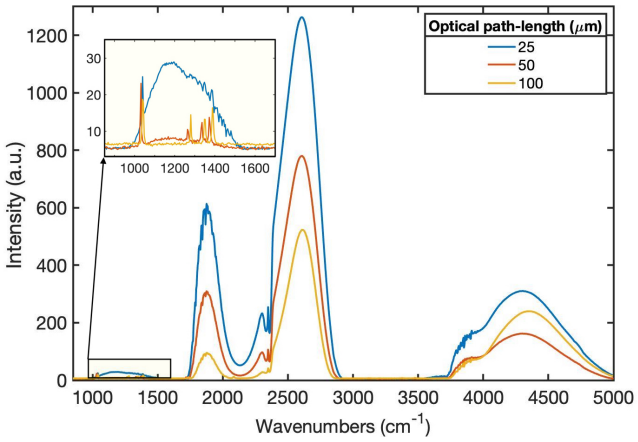

Fig. 3.12 Single-beam spectrum of water measured using device 3 coupled to the FT-IR spectrometer at different optical path-lengths: 25, 50 and 100 μm.

Water shows very intense and broad bands over the full MIR region: (i) a strong broad band centred near 3400 cm^{-1} caused by the O-H stretching; (ii) a medium band near 1635 cm^{-1} caused by the O-H-O scissors bending; and (iii) a small band at 2120 cm^{-1} resulting from the coupling of the scissors bending and broad liberation band in the NIR [37]. Due to the strong absorbance of water in this region, sufficient transmission was seen only in certain wavelength ranges, namely between 1700-2900 and 3600-5000 cm^{-1}. At an optical path-length of 25 μm, it is possible to measure between 1000 and 1500 cm^{-1}. While larger path-lengths allow for a greater interaction with the sample (and higher detection limits), the region of interest for many analytes lies within the IR fingerprint region (500-1500 cm^{-1}). Previous work suggests that the optimum path-length (out of 25, 50 and 100 μm available path-lengths) for transmission-mode measurements of compounds in aqueous solutions was 50 μm, since they yield results with the lowest limit of detection [38]. In this case, however, only the smaller path-length of 25 μm allows enough transmission, which is likely due to the added losses induced by the optical fibres; therefore, it was selected as the optimum path-length for the subsequent measurements. The use of higher intensity light sources such as quantum cascade lasers (QCLs) should allow longer path-lengths. The direct measurement of light transmitted through the channel to the detection fibre eliminated the need for optical calculations concerning light throughput.

3.2.3.3 Hardware performance

The experimental arrangement of Figure 3.7 was used once again to characterize the hardware performance of device 3. Device 3, made out of PEEK and a PTFE spacer, provides a leak-proof system after prolonged and repeated use. PEEK is a robust and reliable material typically used in demanding applications due to its resistance to chemicals, wear, fatigue and creep as well as exceptionally high temperature resistance [39]. In addition, the use of standard medical-grade inlet/outlet tubing connectors provides an air-tight seal. The optical path-length of device 3 is established by a PTFE spacer (of a given thickness), meaning that it can be easily adjusted for applications which may require specific path-lengths or to be used in conjunction with light sources of higher/lower intensities. The reduced channel volume of 0.3 μL (for a PTFE spacer thickness of 25 μm) allows very small sample volumes to be monitored continuously (i.e. at a flow-rate of $\sim$ 1 μL min^{-1}, the sample in the channel is "renewed" every 18 seconds), which for certain applications, particularly medical ones, can be very attractive. The direct SMA fibre connection without the need for cleaving or SMA adaptors (as previously) and the requirement of only one PTFE spacer makes it easy to assemble due to the reduced number of components. Overall, on top of being compact and light-weight, device 3 has a number of added improvements over devices 1 and 2.

3.2.4 NIR measurements: Devices 1 and 2

NIR measurements were performed using a FT-NIR Antaris MX spectrometer (Thermo Scientific) along with the previously specified NIR fibres. Aqueous solutions of ethanol and glucose were inserted into devices 1 and 2, in order to test their sensing capabilities. As a means of comparison, measurements were taken using a standard quartz transmission cell (100-OS, Hellma Analytics) of 1 mm path-length and 350 μL volume by pipetting the samples in the cell, and placing that cell into a fibre-coupled cell holder. The measurements were performed at room temperature and all spectra (including the reference) were acquired in triplicate to avoid errors and ensure repeatability. Raw spectra were obtained using the spectral-processing functions from the Thermo RESULT Integration Spectra Software and typical parameters such as 25 scans and a resolution of 16 cm^{-1} were applied. Absorbance spectra were computed from Equation 2.6 by ratioing raw sample spectra to reference spectra, acquired prior to the measurement of every sample. No spectral pretreatment (smoothing, noise reduction) was employed during data analysis.

3.2.4.1 NIR measurements of ethanol

Aqueous ethanol solutions of the following concentrations (% by vol.), 9%, 11%,14%, 20%, 33%, and 50%, were prepared using volumetric glassware and a 100-1000 μL pipette (728070, Biohit Proline Plus). Figures 3.13a, 3.13b and 3.13c show the NIR spectra of ethanol, relative to air, for all concentrations using the standard cell, device 1 and device 2 respectively, in the spectral range from 7250 to 4000 cm^{-1}. The range from 12,000 to 7250 cm^{-1} is not shown since it did not reveal any particular absorption features, explained by the fact that NIR bands occurring at longer wavelengths (lower wave frequency) are stronger, sharper, and better resolved than their corresponding higher overtone bands which occur at shorter wavelengths (higher wave frequencies). It was observed in all cases that the absorbance in several regions of the spectra changes with the ethanol concentration. Increasing the concentration of ethanol leads to a relatively large decrease in absorption in the 7150-6600 cm^{-1} region and an even larger decrease in the 5300-4800 cm^{-1} region. The peaks in these regions correspond to distinct absorption bands of water and are attributed to the O-H group, namely the first overtone transition for the first region and the stretching combination for the second. In the O-H combination stretch region (5300-4800 cm^{-1}) of the spectra acquired from device 1 and the standard cell, spectral spikes were observed, which correlate with increased water absorption. This phenomenon is commonly referred to as spectral saturation and is a result of the limited dynamic range of the detector. With increased water absorption, the transmitted signal reaching the detector is very low (i.e. the detector is

"starved" of light). After a certain level of absorbance, the detector's output signal no longer increases proportionally to its input signal, resulting in the observed spectral features.

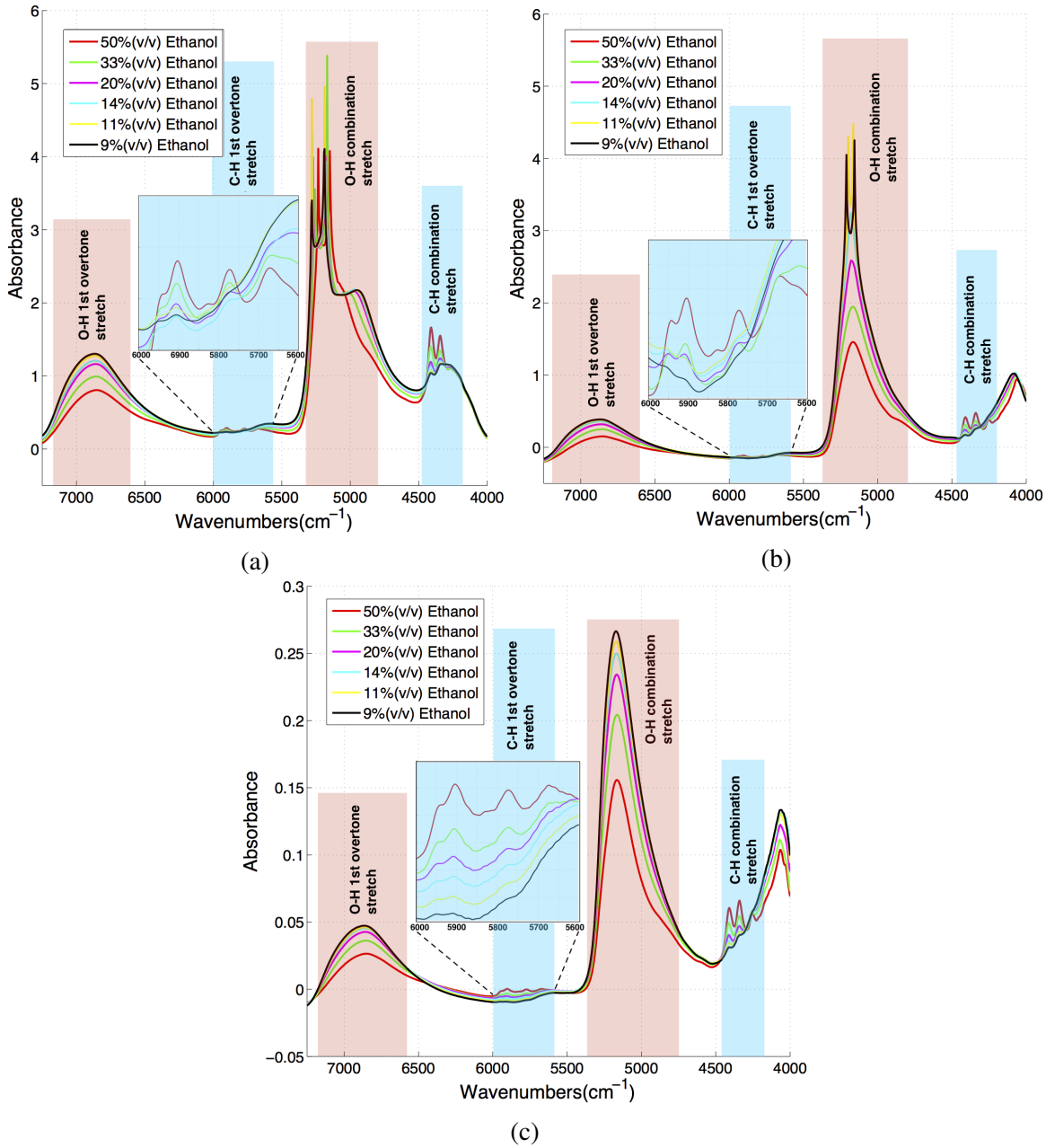

Fig. 3.13 NIR absorbance spectra (4000 to 7250 cm^{-1}) of ethanol concentrations between 9 and 50 % (v/v) in DI water on: (a) the standard cell, d = 1 mm (a); (b) device 1, d = 500 μm; and (c) device 2, d = 50 μm.

Spectral saturation in this region for the standard-cell measurements are significant and occurs for all the spectra. This can be explained by the large (1 mm) optical path-length

(i.e. distance between the light source and detector) which leads to a higher interaction with the sample, and thus, a greater absorption. The spectra acquired using device 1, with a smaller path-length of 500 μm, only saturate for the lower ethanol concentrations (9 and 11%) due to the higher water content in these samples. Another potentially contributing factor to this phenomenon occurring in the spectra of device 1 is the use of bare fibres, which were manually cleaved and polished. The resulting surface non-uniformities compared to industrially cleaved fibres likely induces further light scattering and losses. On the other hand, device 2, with an even smaller path-length of 50 μm and intact fibre surfaces, does not show saturation in any region of any of the acquired spectra. Typically, there is a trade-off between the amount of sample interaction (absorption) and the amount of light reaching the detector (signal), and therefore, for liquid sensing applications, an optimum optical path-length needs to be established.

In theory, the O-H vibrational mode for water and ethanol is different in terms of both frequency and oscillator strength, causing a slight shift between their peaks [40]. However, the very high absorption peaks of water in these regions usually overlap entirely and dampen the ethanol O-H peaks. For instance, according to the literature [41], at $\sim$ 5200 cm^{-1} the absorbance of water is around fifty times higher than the absorbance of ethanol, and thus it can be assumed that the absorbance of mixtures at this frequency depends mainly on the weight fraction of water. Since the fraction of ethanol correlates to that of water, the absorbance at 5200 cm^{-1} can be used for measuring the variation in the fraction of ethanol as long as there is no saturation. In the spectra of the standard cell (Figure 3.13a), the small band around 4900 cm^{-1} was believed to be caused by O-H residues in the quartz windows of the 1 mm cell (likely due to water impurities), and was assigned to a combination of an O-H stretching vibration and one of the SiO_2 fundamental vibrations [42]. This phenomenon is not seen in the spectra of devices 1 and 2 given the inexistence of windows. Two major absorption bands of ethanol were observed in the spectra from all devices in the frequency ranges of 6000-5600 cm^{-1} (highlighted in each graph) and 4490-4150 cm^{-1}, which increase with an increasing concentration of ethanol. These correspond to the first overtone of the C-H stretching mode and the combination C-H stretching mode, respectively [8, 43, 44]. In the highlighted 6000-5600 cm^{-1} region, clear differences were observed between the spectra taken on each device and on the standard cell. The C-H first overtone band is partially overlapped by the nearby O-H combination band in the device 1 spectra and even more significantly for the standard cell, while for device 2, no overlap is observed in this region. Additionally, the absorbance difference between ethanol concentrations is greater in this region for the measurements of device 2. This is a result of the decreasing path-length from the standard cell to device 1, and from device 1 to device 2, where a larger path-length leads

to higher water absorption, which in turn results in broader O-H bands, and hence, a higher overlap between these and the nearby ethanol-specific C-H absorption bands. These results indicate that device 2 appears to be the most promising for these measurements, likely owing to its shorter path-length (less water absorbance) and the fact that no optical windows (as in the standard cell) or manually cleaved/polished fibres (as in device 1) are used.

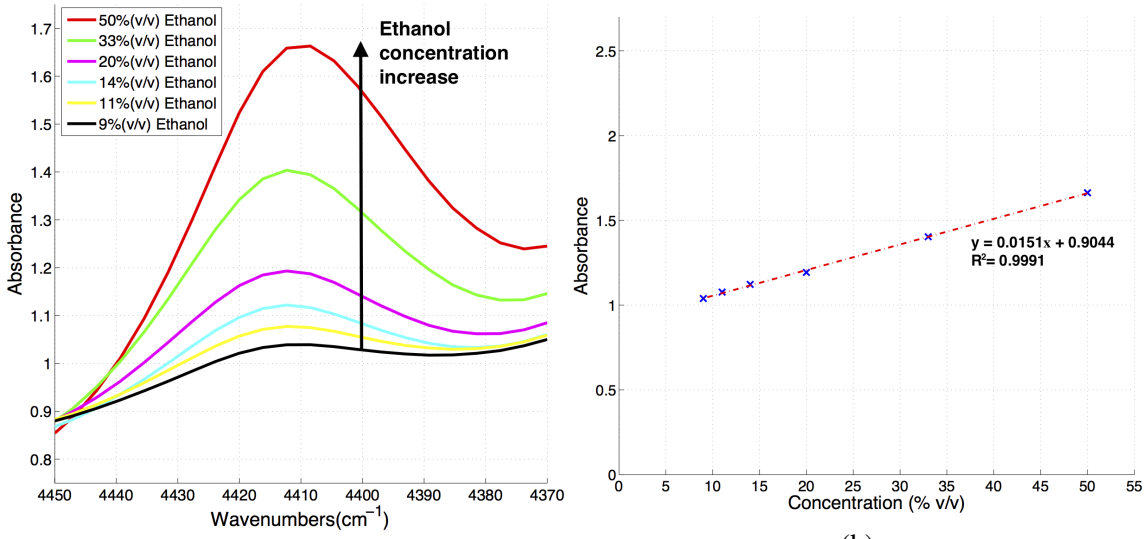

(a) (b)

Fig. 3.14 (a) NIR spectra (4450 to 4370 cm^{-1}) of ethanol in DI water using the standard cell; and (b) absorbance at 4410 cm^{-1} with increasing ethanol concentrations.

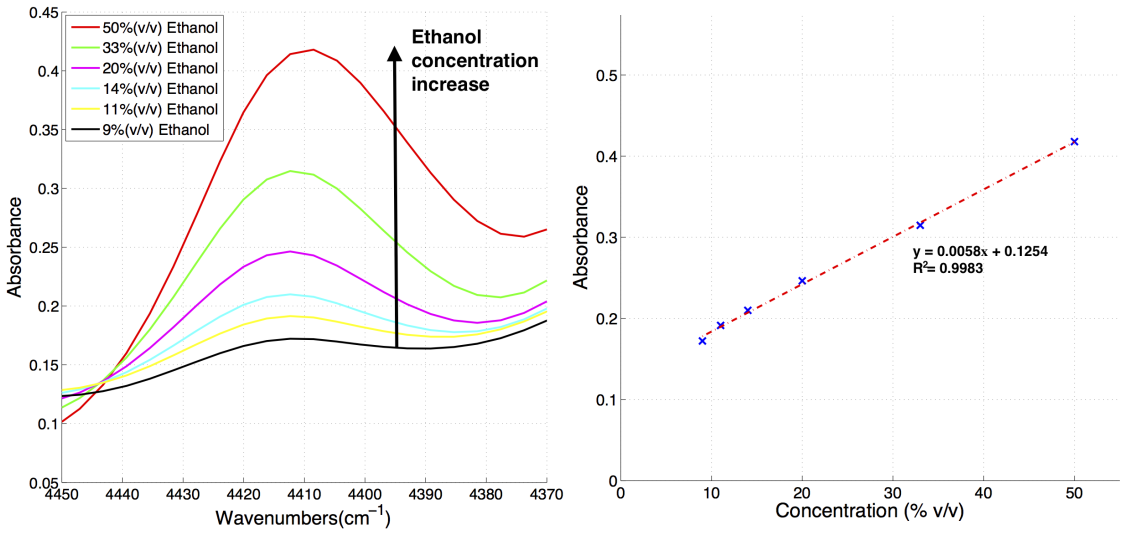

(a) (b)

Fig. 3.15 (a) NIR spectra (4450 to 4370 cm^{-1}) of ethanol in DI water using device 1; and (b) absorbance at 4410 cm^{-1} with increasing ethanol concentrations.

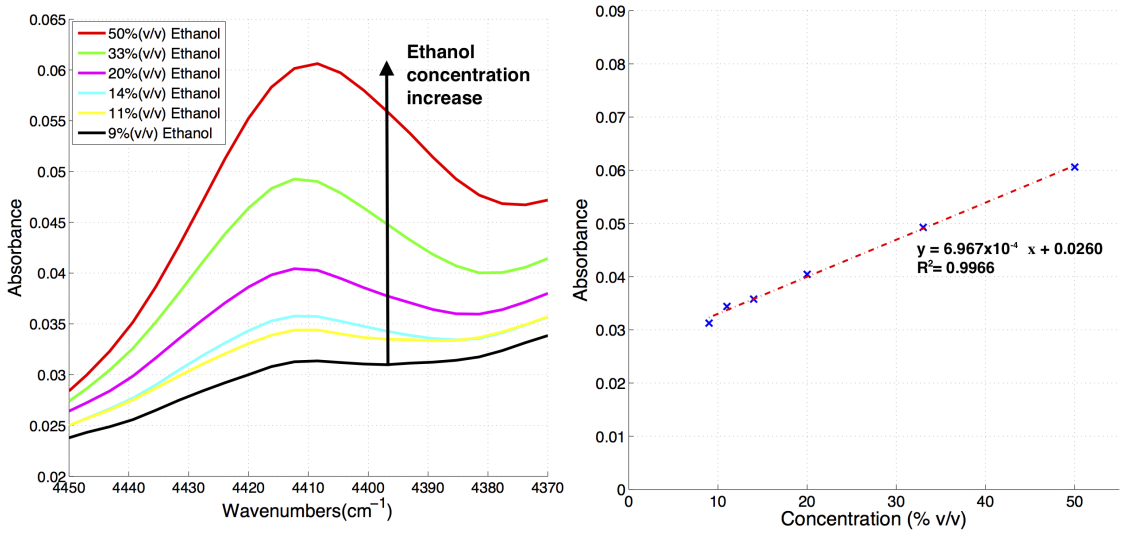

(a) (b)

Fig. 3.16 (a) NIR spectra (4450 to 4370 cm^{-1}) of ethanol in DI water using device 2; and (b) absorbance at 4410 cm $^{-1}$ with increasing ethanol concentrations.

Calibration curves for both devices and the standard cell were plotted in the spectral region from 4450 to 4370 cm^{-1} (within the first overtone C-H combination stretch region), and a linear regression analysis was applied, where the absorbance maxima ($\sim$ 4410 cm^{-1}) are plotted against the different ethanol concentrations, as shown in Figures 3.14, 3.15 and 3.16. The regression results for each device are shown in Table 3.4. The slope of the graphs (absorbance over concentration) equals the molar absorptivity coefficient times the path-length, ε *x* *l*, according to the Beer-Lambert law (Equation 2.6). Accordingly, since the slope is proportional to the optical path-length, the systematic changes in slope values observed between the standard cell, device 1 and device 2 could be explained by the large differences in optical path-lengths in each case. The non-zero y-intercept observed in the case of the standard cell may be due to noise levels and/or interfering compounds or materials. The R^2 values were high in all three cases, which reflects the linear correlation observed between the absorbances and corresponding concentrations.

Table 3.4 Regression results for standard cell, devices 1, and device 2.

	Standard cell	Device 1	Device 2
Slope	0.0151	0.0058	6.967x10^{-4}
y-intercept	0.9044	0.1254	0.0260
R^2	0.9991	0.9983	0.9966

3.2.4.2 NIR measurements of glucose

Aqueous glucose solutions of 0.5 M (5.8 % (v/v)) and 1 M (11.7 % (v/v)) concentrations were prepared by adding glucose (D-Glucose, Sigma-Aldrich) to DI water and measured on both devices (1 and 2) and on the standard cell. The same parameters as for the ethanol measurements in the previous section were applied. Figures 3.17a, 3.17b and 3.17c show the NIR spectra, relative to air, acquired for 0.5 M and 1 M glucose in water on the standard cell, device 1 and device 2, respectively.

Only the spectra between 4600 and 7500 cm^{-1} are shown since the absorption of glucose in the first overtone band (5400-6400 cm^{-1}) is higher than in the combination band (4300-4800cm^{-1}) [45]. The arrows in the Figures indicate the direction of glucose increase. In accordance with the previous ethanol measurements, water bands are observed in regions 7150-6600 cm^{-1} and 5300-4800 cm^{-1}, corresponding to the O-H first overtone stretch and the O-H combination (of bending and antisymmetric) stretch, as specified in each Figure. With the increase in glucose concentration, there is a decrease in absorption in these regions, apart from the 5300 - 4800 cm^{-1} region for device 1 and the standard cell, which shows the same spectral saturation as for the ethanol measurements, as explained in the previous section. Also, as previously noted, the small band at 4900 cm^{-1} for the standard-cell spectra is probably due to O-H residues in the quartz windows of the 1 mm cell and was assigned to a combination of an O-H stretching vibration and one of the SiO_2 fundamental vibrations [42]. The rest of the spectral regions do not show significant variations for all three device measurements since glucose absorption at these concentrations is very weak compared to the water absorption. For device 1 and the standard cell, the higher absorption of water, due to the larger path-lengths, dampens the entire spectra. On the other hand, the measurements taken by device 2 show a region at frequencies between 6710 and 5340 cm^{-1} where the measured absorbance increases as a function of glucose concentration, in accordance with the Beer-Lambert law (Equation 2.6). This region corresponds to glucose absorption bands in the first overtone where there are two broad glucose peaks assigned to the C-H first overtone bands [42]. At frequencies greater than 6710 cm^{-1} and less than 5340 cm^{-1}, however, the absorbance decreases as a function of glucose concentration. This apparent inversion of the Beer-Lambert law is explained by the relative magnitude of the molar absorptivity of water and glucose and the displacement of water molecules by the dissolution of glucose. The highlighted regions (B and C) of Figure 3.17c show the isobestic points at 6710 cm^{-1} (B) and 5340 cm^{-1} (C), which correspond to the points where the absorptivity of glucose equals the product of the absorptivity for water and the water-displacement coefficient for glucose ($\varepsilon_s = \varepsilon_w \cdot f_w^s$). For all the frequencies in between, the glucose absorptivity is greater than the

product of water absorptivity and the water-displacement coefficient ($\varepsilon_s > \varepsilon_w \cdot f_w^s$), resulting in a net positive absorption of the incident light as a function of glucose concentration.

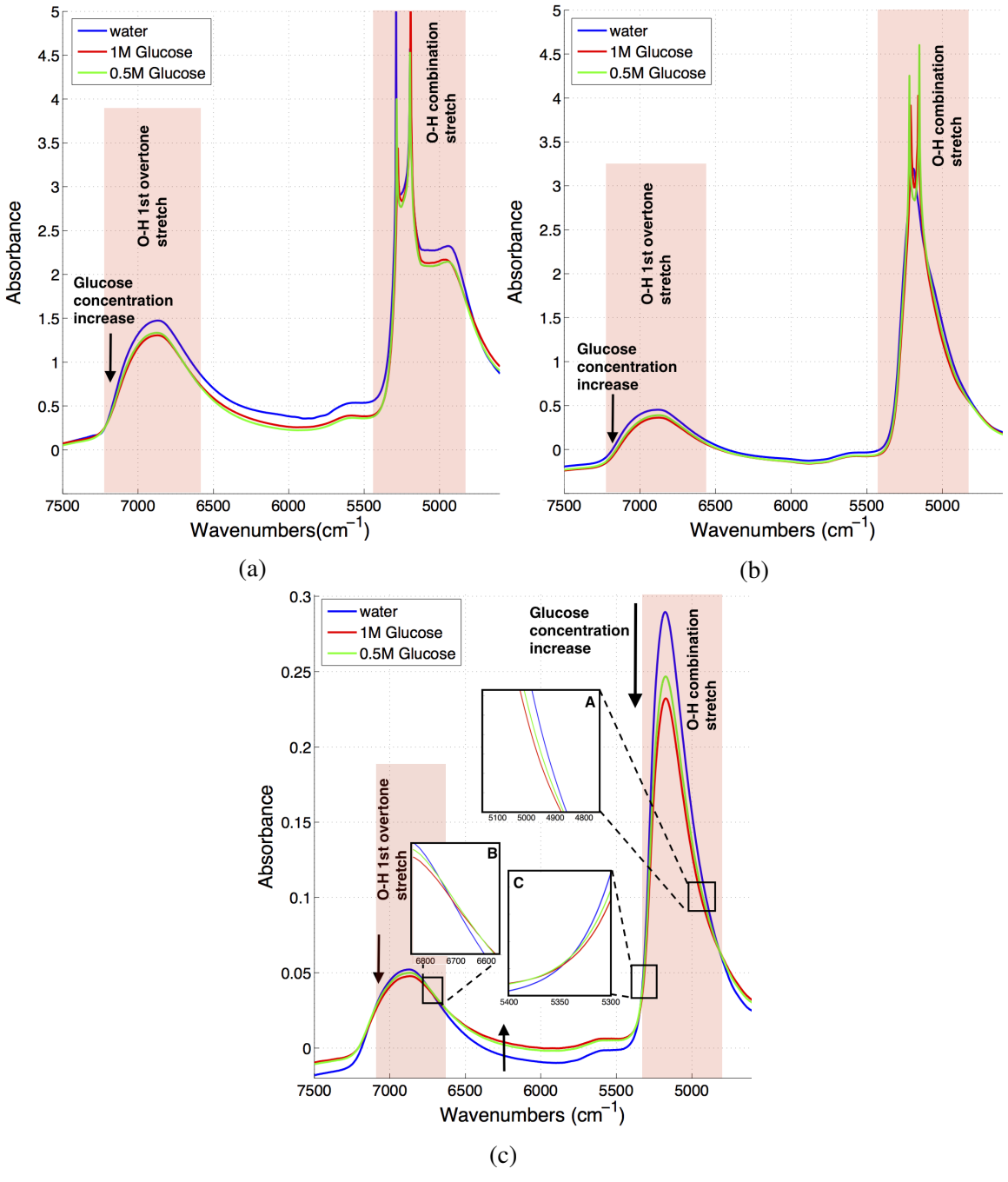

Fig. 3.17 NIR (4000 to 7500 cm^{-1}) absorbance spectra of glucose concentrations between 0.5 M and 1 M in DI water using: (a) the standard cell, d = 1 mm; (b) device 1, d = 500 μm; and (c) device 2, d = 50 μm. Inserts A, B and C highlight the isosbestic points of the spectra.

For higher and lower frequencies, the absorptivity for glucose is less than the product of the water absorptivity and the water-displacement coefficient ($\varepsilon_s < \varepsilon_w \cdot f_w^s$), thereby resulting in the observed net decrease in the absorbance with an increase in glucose concentration [46]. Another interesting point worth considering is the water displacement due to the glucose presence in solution which can be observed in the expanded view of Figure 3.17c (A).

When glucose is dissolved in water, the water volume of the solution is altered because each molecule of glucose takes up a finite space. Additionally, the water molecules around solute molecules are not free; they interact with solute molecules, causing the observed shift in the peaks. While no specific peaks of glucose can clearly be identified from the measured spectra, it is possible to observe changes correlated to its concentration, and therefore to perform qualitative glucose measurements, particularly for measurements obtained from device 2 where no saturation was observed. However, in order to extract the quantitative information contained in NIR spectra, multivariate data-analysis tools would need to be implemented [42]. Moreover, quantitative analysis in the NIR gets even more complicated when complex fluids are involved.

3.2.5 MIR measurements: Device 3

MIR measurements were carried out on device 3 using a FT-IR Rocket spectrometer (ArcOptix) and two MIR fibres (previously specified in subsection 3.2.3). The previously determined optimum optical path-length of 25 μm, defined by a PTFE spacer, was used for all measurements. Glucose is a relevant molecule for a wide range of clinical conditions and has well-defined specific peaks (1036, 1080, 1106, 1152 cm^{-1}) in the fingerprint region of the MIR [47, 48]. In order to test particular sensing capabilities of device 3, a 1 M solution of glucose in DI water was injected into the flow-cell at 0.2 mL min^{-1}, followed by pure DI water. Spectra were acquired every minute with an accumulation of 10 scans. Figure 3.18a shows the absorbance spectra over a period of 11 minutes, within which the glucose levels decreased from 1 M to 0 M. The absorbance at the specific glucose peak at 1080 cm^{-1} was plotted as a function of time, as shown in Figure 3.18b. Device 3 showed a very good performance in detecting and monitoring changes in glucose concentration over time and with a very good response time, meaning that it could be an ideal tool for continuous monitoring of compounds within liquid samples, which has relevant applications in a wide range of areas, from biofluid monitoring to water-pollution management.

Once the device was tested in terms of its response time and continuous monitoring capabilities, it was important to study its sensitivity for glucose at levels within the physiological range. Therefore, different concentrations of glucose within the physiological range (0, 1.5, 3, 6, 12 and 24 mM) were prepared in DI water and measured on the device. Each sample

was measured with an accumulation of 150 scans, given the higher noise levels at these lower concentrations.

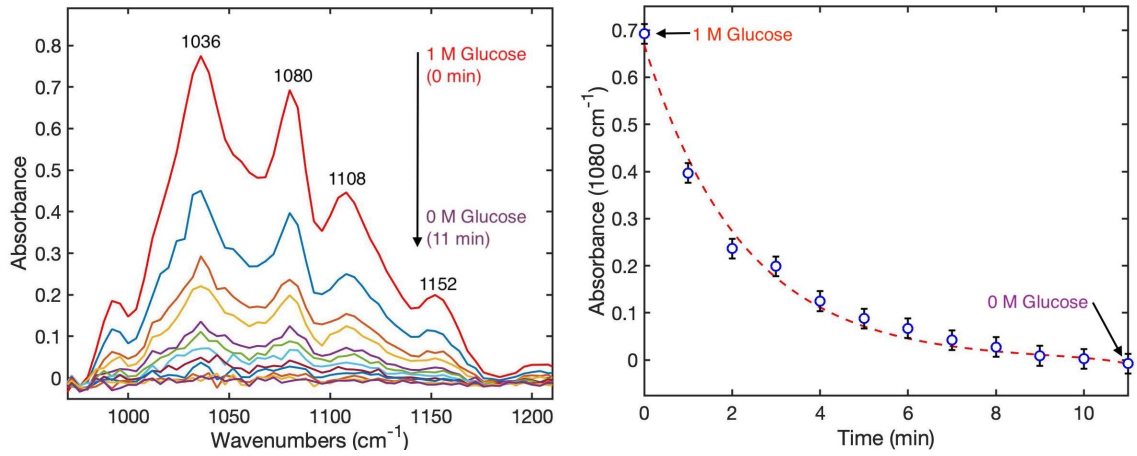

(a) (b)

Fig. 3.18 MIR absorbance spectra of aqueous glucose solutions at varying concentrations (between 1 M and 0 M) over time acquired using device 3. (a) All absorbance spectra; (b) Relative peak intensities at specified glucose peak (1036 cm^{-1}) for each concentration as a function of time.

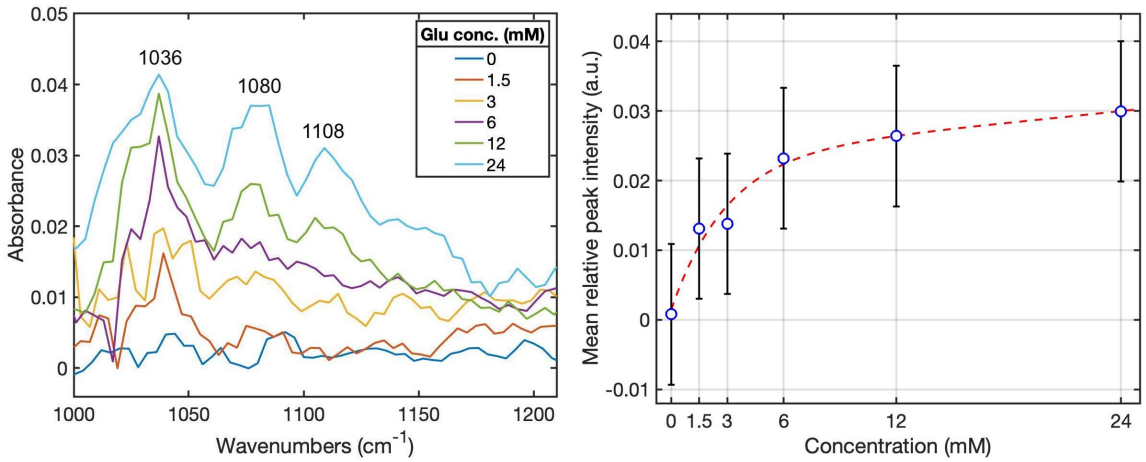

(a) (b)

Fig. 3.19 MIR absorbance spectra of aqueous glucose solutions at varying concentrations (between 0 - 24 mM) acquired using device 3. (a) All absorbance spectra; (b) Relative peak intensities at specified glucose peak (1036 cm^{-1}) for each concentration.

The device was flushed with pure DI water in between measurements to avoid any contamination from previous samples. Figure 3.19a shows the glucose absorbance spectra at each concentration and, for each of these, the peak intensity at 1036 cm^{-1} was plotted, as

shown in Figure 3.19b. Since there was a slight vertical offset between spectra, the relative peak intensities were calculated (from the measured difference in transmission between a peak maximum and a baseline point in a stable region of the spectrum) and compared for each spectrum. Although glucose peaks can be observed from 1.5 mM concentrations upwards, the noise level at this range is high and, as a result, produce measurements with a large error with a non-linear trend. While differences can be seen between each spectrum, it is not possible to accurately distinguish these low concentrations from each other and provide precise quantitative information, as can be seen by the overlapping error bars in Figure 3.19. The 25 μm optical path-length only allows a certain amount of light-sample interaction, which in this instance could not be increased due to the use of a standard FT-IR spectrometer. The use of fibres is also a contributing factor to the decreased sensitivity due to their inherent losses while light propagates through the fibre.

3.2.6 Transmission-mode devices: conclusions

Three low-cost and easy-to-make microfluidic device prototypes with integrated IR fibres were developed, tested and discussed. Preliminary measurements of ethanol and glucose were conducted in the NIR region on devices 1 and 2 due to the practicality and reduced cost of NIR components and equipment compared to the ones used in the MIR. Ethanol was successfully detected and specific ethanol peaks were observed at different concentrations on both devices (and standard cell, used for comparison). Although the NIR glucose spectra presented no glucose-specific peaks, it was possible to determine relative variations in glucose concentration by observing changes in the corresponding spectra. Based on the positive aspects of devices 1 and 2, device 3 was developed as the more optimised, robust and reliable version. With a simple assembly and no need for fibre preparation, device 3 allowed a leak-proof and controlled flow of fluid. The easily adjustable path-lengths is also an added advantage since it can be optimised to be used for different applications and in conjunction with specific IR equipment. MIR measurements, which provide higher specificity, were therefore carried out on glucose solutions using device 3. The successful detection of 1 M glucose and of the gradual changes in concentration over time was shown. Although detection of glucose within the physiological range was possible, the resulting spectra were noisy, which limited the ability of accurate quantification. Improved spectra and lower detection limits can be achieved by using high-intensity light sources, such as QCLs, which will enable the use of larger path-lengths, and thus, greater light-sample interaction. In addition, the use of shorter fibres can provide an improved signal due to the reduction of losses during light transmission through the fibre core. With further improvements, this could be an ideal tool

for continuous monitoring of chemical compounds within liquid samples for a wide range of applications.

3.3 Transflection-mode device

Transmission-mode device configurations have numerous advantages. However, when coupled to optical fibres, this often results in a bulky overall system, since a fibre typically needs to sit on either side of the device channel, as shown in Figure 3.11b. Therefore, in parallel to further development and testing of the transmission-mode devices, an attempt to develop a transflection-mode device was carried out, where both illumination and detection fibres connect from only one side of the device. The following section describes the design and fabrication of such a device, as well as discusses the results and challenges faced.

3.3.1 Device 4

3.3.1.1 Design and fabrication

A transflection-mode device was designed and developed with the aim of achieving a more simple, compact and robust system. The initial conceptual idea was based around having a single component, which would contain both illumination and detection fibres and would attach to only one side of the microfluidic device. Based on the work achieved for the previous transmission-mode devices, similar principles of having a PTFE spacer sandwiched between two layers of material to form a channel were applied. The concept of such a device is shown in Figure 3.20, where a PTFE spacer is sandwiched between a zinc selenide (ZnSe) window and a silica plate coated with gold (Au) on the side that interacts with the channel.

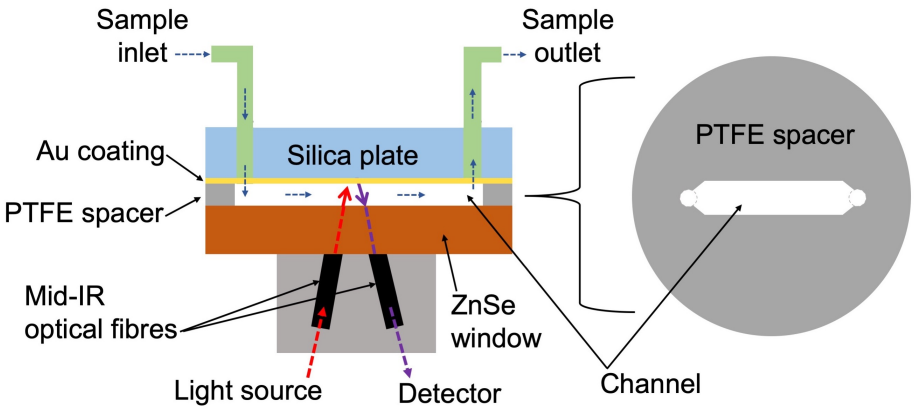

Fig. 3.20 Conceptual schematic of device 4 operation.

The gold coating is used as a mirror to reflect the incident light from the illuminating fibre into the detecting fibre, whilst also being chemically inert. The PTFE spacer forms the fluidic channel to which an inlet and outlet tubing are connected via two holes through the above silica plate. The fibre-optic cables are to be attached immediately below the ZnSe plate, at an angle such that the incoming light, from the illumination fibre, will be reflected (by the Au surface) into the detection fibre. In practical terms, it was necessary to build a mount to insert and enclose the several plates while holding them firmly together in order to avoid leakage. As an initial proof-of-concept, the design shown in Figure 3.21 was developed in collaboration with Knight Photonics Ltd. Referring to this Figure, two metalwork levels (A and B) were sandwiched with precision location pins (C). These levels are secured by four vertical Allen bolts and tightened together by four butterfly bolts. Two rods (D) connect a simple outer structure to support the general inner assembly and to allow for height to enable optical fibres to enter and exit the assembly with a low bend radius. All metallic framework components were provided by Knight Photonics Ltd. Components E and F are the gold-coated silica plate and ZnSe windows, respectively, between which the PTFE spacer of desired thickness is located. This general arrangement allows for a micrometer (G) to be mounted above the assembly to measure the path-length gap. Here, a T-piece end was used to measure between the top of the silica plate and the top of the ZnSe so that, when subtracting the thickness of the silica plate, the optical path-length can be obtained. Although the PTFE spacer is used to define the path-length, it can be slightly compressed when tightened down with Allen screws. Therefore, the micrometer is used to measure the actual distance with a high degree of precision. The hole in the PTFE (Figure 3.22b-3) allows the micrometer stylus to go through to the ZnSe. The fluid sample enters and exits the channel through the inlet and outlet tubing (J) connected via the silica plate.

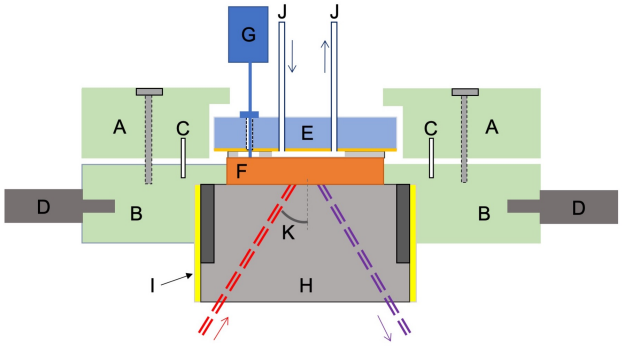

Fig. 3.21 Schematic of device 4 highlighting main components for its fabrication.

Two slot holders (I) with locking screws are used to insert the stainless steel fibre-optic plate (H), which has engraved angular guides for inserting the optical fibres. The fibre-

optic plate is replaceable with plates of guides at different angles and for fibres of different ferrule diameters. In this case, the illumination and detection ends of each of the fibres were terminated with a customised ferrule (instead of an SMA connector) so that these tips could be easily fitted and secured into the fibre-optic plate (H). The angle setting of the fibres (K) was set to 45^o to the ZnSe surface. In place of performing complex multilayer calculations (taking into account the absorption of light at each layer, the light reflected off each layer and the refraction of light within each layer), preliminary tests showed that the light reflected into the detection fibre was maximized at a 45^o angle. Figure 3.22 shows the silica plate (E), the ZnSe window (F) and PTFE spacer in more detail. The silica window (fused silica, UV grade) with holes was custom-made and supplied by Cystran Ltd. Its thickness was set at 4 mm ±0.1 to allow enough depth for securing the inlet/outlet tubing and its diameter was set to 30 mm ±0.1. A 300 nm-thick gold layer was deposited onto one side of the silica plate using electron-beam (e-beam) deposition at the Nanoscience Centre of the University of Cambridge. Holes 1 in Figure 3.22a are for inlet and outlet liquid tubing, with a 1.5 mm nominal diameter, toleranced against insert PTFE tubing diameter of 1.6 mm for a snug fit. Hole 2 is for the micrometer probe (approx. 5 mm diameter). A PTFE sheet was machined into a circular shape of 25 mm diameter by the workshop of the Department of Chemistry. The thickness of the PTFE layer in this 'double-pass' configuration is equivalent to half of the optical path-length since the light-beam passes through the channel twice (before and after being reflected).

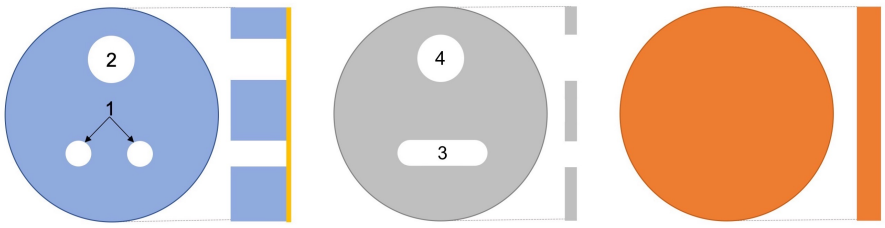

(a) (b) (c)

Fig. 3.22 Flow-cell components of device 4: (a) Silica plate; (b) PTFE spacer and (c) ZnSe window.

For preliminary tests, the PTFE spacer thickness was set to 25 μm, allowing a 50 μm optical path-length. Slot 3 in Figure 3.22b is a 1 mm wide liquid flow line and length of 7 mm. Hole 4 is for the micrometer probe (approx. 5 mm diameter). The ZnSe window was supplied by Crystran Ltd. Its diameter and thickness were set to 25 mm ±0.05 and 2 mm ±0.1, respectively. The diameters of the silica and ZnSe are different to allow close proximity

without using a more costly optic design. In order to support the several components of this preliminary system, a multi-purpose robust stand was used, as shown in Figure 3.23a.

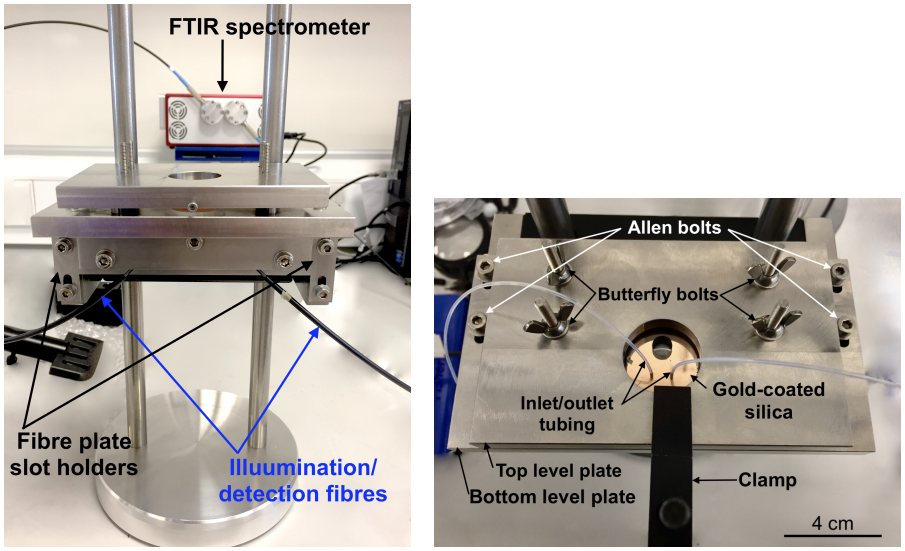

(a) (b)

Fig. 3.23 Images of device 4 highlighting main components. (a) Side-angle view; (b) top view.

The 14 mm diameter stainless steel upright poles of the stand were used to secure the bottom metalwork level in place, in which the flow-cell layers (ZnSe, PTFE and gold-coated silica) were aligned and assembled. The top plate was then secured firmly on top of these, using butterfly bolts in order to seal the flow-cell layers tightly together. A clamp was used to maintain the top metalwork plate levelled. PTFE tubing was inserted into the inlet and outlet ports provided by the silica plate. With the intention of comparing the performance of this system to that of device 3, MIR fibres were used (PIR AgCl:AgBr polycrystalline, core/clad 900/1000 μm, NA: 0.3, length: 1 m, Art Photonics, GmbH, Germany) with specifications as similar as possible to previously. However, this particular setup required the use of customised ferrules (on one termination of each fibre) as well as fibres of an increased length of 1 m (as opposed to 0.5 m used in the previous system) in order to minimize the bending radius needed for insertion into the fibre-optic plate.

3.3.1.2 Hardware performance

As performed for the previous systems, this device was also assessed in terms of its mechanical and fluid flow performance. As described in section 3.2.1.4, a syringe pump was used to inject DI water into the inlet of the fluidic channel at a constant flow-rate of 0.5 mL min^{-1}.

Although an air-tight seal was provided by the internal layers (PTFE spacer sandwiched between the ZnSe window and silica plate), signs of leakage were noticed at the inlet and outlet of the system, where the PTFE tubing connects to the silica plate, as can be seen in Figure 3.24a. In order to solve this, press-fit tubing connectors (460003, Grace Biolabs) were used to provide a leak-proof seal, which is created by pressing the adhesive-coated connector against the inlet/outlet ports of the silica plate. One of the connectors had to be adjusted slightly using a scalpel due to the close proximity of the ports, as shown in Figure 3.24.

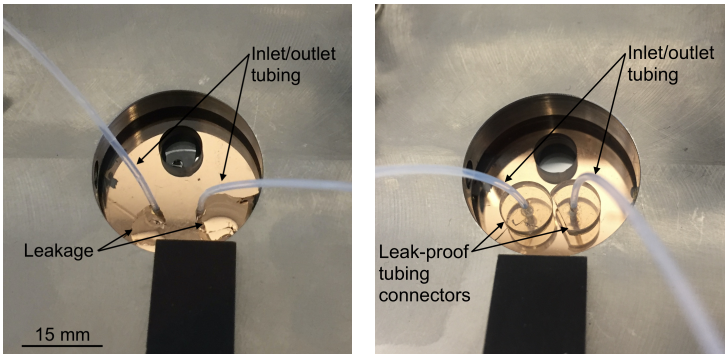

(a) (b)

Fig. 3.24 (a) Image showing leakage at the inlet and outlet ports of device 4. (b) leakage corrected by using leak-proof press-fit tubing connectors.

Regarding the materials comprising the flow-cell, both the ZnSe window and silica plate proved to be fragile when sealed together by the two levels of metallic framework. Moreover, the risk of damaging the plates was increased by the uncontrolled tightening of the bolts. After some usage, small cracks were seen at the edges of these, meaning that these would need replacing after repeated and prolonged use. The optical path-length of device 4 results from a double-pass of the light through the channel, which is defined by the PTFE spacer. The internal volume of the channel, also defined by the PTFE spacer, was 0.175 μL, which is suitable for very small sample volumes. In order to couple fibres to the system so that they are in contact with the bottom of the ZnSe window, a fibre-optic plate was used to attach and lock them into place. The insertion of the fibres into the plate requires them to be bent upwards. In order to minimize the bending radius (and hence minimize fibre losses), fibres of 1 m length were required. Finally, the angle at which the reflected signal was maximized was found to be 45^o, meaning that a relatively large component is needed to secure both fibres into place at this angle.

3.3.2 MIR measurements: Device 4

In order to test the sensing performance of device 4, similarly to device 3, MIR measurements were carried out using the FT-IR Rocket spectrometer and two MIR ferruled fibres (previously specified). A 1 M solution of glucose in DI water was injected into the flow-cell of device 4 at 0.2 mL min^{-1}, followed by pure DI water. Spectra were acquired every minute with an accumulation of 10 scans. Figure 3.25a shows the absorbance spectra over a period of 5 minutes, within which the glucose levels decreased from 1 M to 0 M. The absorbance at the specific glucose peak at 1080 cm^{-1}, plotted as a function of time, is shown in Figure 3.25b.

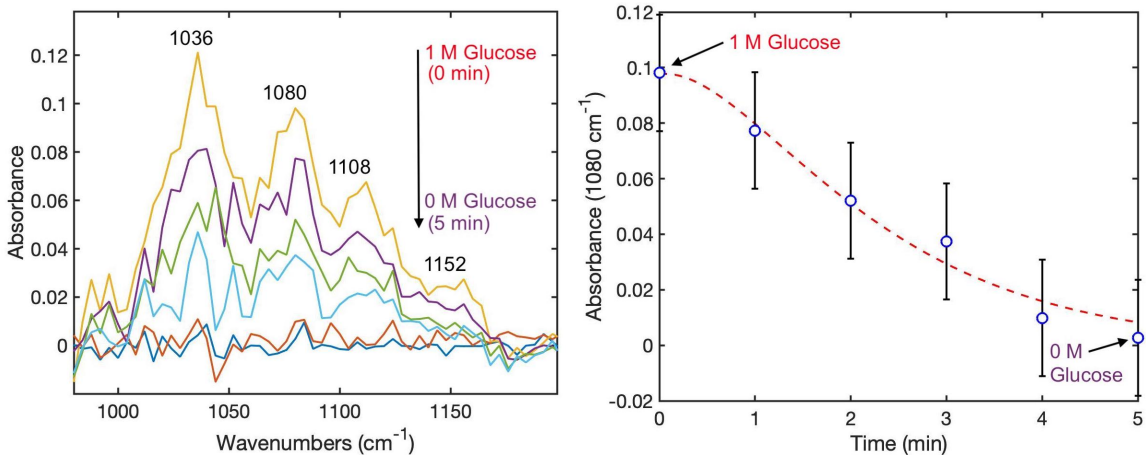

(a) (b)

Fig. 3.25 MIR absorbance spectra of varying concentrations of glucose (between 1 M and 0 M) acquired using device 4. (a) All spectra; and (b) Relative peak intensities at specified glucose peak (1036 cm^{-1}) as a function of time.

Specific glucose absorbance peaks are clearly visible at the initial 1 M concentration, and quickly decrease in a matter of minutes as the glucose solution becomes diluted with pure water. However, the noise levels are very high and it would be challenging to obtain accurate quantitative information from the spectra. In this case, the total path-length was 50 μm due to the 'double-pass' reflection through the channel, defined by a 25 μm PTFE spacer. As shown in section 3.2.3.2, the transmission of light through an aqueous medium of 50 μm results in an almost negligible signal. Given the non-availability of thinner PTFE spacers, it was not possible to test smaller path-lengths for potentially higher signals. In addition, in this configuration, it proved to be very challenging to accurately align the illumination and detection fibres to maximize the detected signal. A slight μm-shift in any direction would cause misalignment and reduce the signal significantly. Finally, the configuration of the setup requires the use of longer fibres and adds an additional bend to each fibre which naturally

increases the light losses throughout the fibre core significantly. Although a transflection-mode configuration may be advantageous in certain aspects, significant improvements are needed in this system in order to achieve reliable and quantitative measurements.

3.3.3 Transflection-mode device: conclusions

A microfluidic device with combined fibre-optics in transflection-mode was developed and tested. The primary aim for developing such system was to achieve a more compact and robust device in comparison to the previously developed transmission-mode setups. While the proof-of-concept system offered a reliable flow and an exceptionally small channel volume, which is ideal for small samples and flow-rates, it required several components and a delicate assembly. Moreover, the optimum angle of the fibres required to maximize the signal was such that it did not provide significant improvements to the compactness of the overall system. Although the fibres could now be located on only one side of the device, a relatively large optical plate was required to secure both fibres in place at a 45^o angle. The development of device 4 required a large number of components, from the different layers comprising the flow-cell, to the several metallic structures holding these together and securing the fibres. Alternative options for reducing the angle of the fibres (i.e. using cell components of different thicknesses and adjusting the distance of the fibres to each other) and improving the overall setup of the device could, however, be implemented with time and at a cost. Regarding its capabilities for performing MIR measurements, device 4 was able to detect 1 M levels of glucose in DI water and monitor the decrease in concentration to O M glucose over time. Although a significant amount of noise was observed and detecting lower concentrations of glucose in the physiological range with the current system would be challenging, certain adaptations to the system (i.e. adjustment of optical path-length and reduced fibre length), in combination with the use of a higher intensity light source, could allow a significantly improved signal.

3.4 Conclusions

This chapter describes the development and performance assessment of four microfluidic devices with integrated fibre-optics: three in transmission-mode configuration (devices 1, 2 and 3) and one in transflection-mode configuration (device 4). All devices were thoroughly tested in terms of their hardware performance in handling a continuous flow of liquids as well as their sensing capabilities. All three transmission-mode devices were easy to fabricate, compact and low-cost. Successful NIR measurements were carried out using devices 1 and 2

by coupling them to a FT-NIR spectrometer via NIR fibres, where different concentrations of ethanol and glucose were detected. Although NIR components and equipment are more affordable and widely available, obtaining quantitative information is complex in the NIR and calibration procedures are typically time consuming. This is primarily due to the fact that the absorption bands occurring in the NIR are the overtones of the fundamental bands residing in the MIR region, making them weak and not clearly defined. Out of the three transmission-mode devices, device 3 was the most optimised version, with a smaller channel volume, adjustable optical path-length and improved overall compactness. Therefore, device 3 was coupled to MIR fibres and assessed in terms of its continuous monitoring and detection capabilities for glucose, a clinically relevant molecule. Device 3 was able to continuously monitor varying levels of glucose over time, and the resulting spectra exhibited glucose peaks down to the physiologically relevant concentration of 1.5 mM. Despite the increased noise level at lower concentrations, improved sensitivity can be achieved by the use of a higher power light source (e.g. a QCL) in conjunction with an increased path-length. The main aim for developing a device in transflection-mode configuration was to attempt to achieve a more compact system by enabling both fibres (illumination and detection) to be integrated into the device through one direction (as opposed to two opposing directions inherent to the transmission-mode configurations). While device 4 enabled the integration of fibres to only one side of the device, the improvements in compactness were not significant as an optical plate was required to secure both fibres at a particular angle to the ZnSe window. Although successful glucose measurements were possible using device 4, the noise levels were higher in comparison to device 3, which could be due to a number of reasons. Firstly, for the same transmitting light intensity, the optical path-length of device 4 is double the optical path-length of device 3 due to the "double-pass" of the beam before and after reflection. Moreover, the addition of a ZnSe window (compared to the windowless transmission-mode systems) creates another medium in which the light is partially absorbed, scattered and reflected. Finally, the setup of device 4 required fibres which were double the length to those used in the transmission-mode measurements, which increase the propagation losses within the fibre significantly. All these factors could contribute in part to the increased noise levels observed for device 4. Although this could be improved in a similar way to device 3, the preliminary work carried out on device 4 showed that far more work would be needed to achieve desirable results using a transflection-mode configuration. In summary, device 3 was able to provide the best overall performance and results. This study showed the feasibility of integrating microfluidic systems with fibre-optics which opens doors to a wide range of applications from continuous biofluid analysis to water pollution monitoring over extended periods of time.

Chapter 4

MIR sensor for continuous chemical monitoring of TBI patients[†]

4.1 Introduction and literature review

Head injury is the single largest cause of death in those aged under 40 years in the developed world, typically resulting from road and sporting accidents, falls, violence, etc. [49]. Approximately every 90 seconds, an individual in the United Kingdom sustains a traumatic brain injury (TBI), with 10,000-20,000 people sustaining a serious brain injury requiring hospitalization and intensive therapy each year [50]. In addition to the high mortality, approximately 60% of survivors have significant ongoing deficits [51]. Following the initial traumatic event, complex changes evolve in the injured brain which may result in secondary damage in the following hours and days, leading to unfavourable outcomes, such as severe disability, vegetative state or death [52]. These processes are potentially amenable to intervention, and therefore, close monitoring is a key element in the management of the injured brain [50, 53]. Significant advances in monitoring and treatment of the past two decades for TBI has led to more patients surviving with far better outcomes. Among these is the direct monitoring of the intracranial pressure (ICP), brain tissue oxygen ($PbtO_2$) and the cerebral extracellular chemistry. While the ICP and $PbtO_2$ are both monitored in real-time, allowing a rapid response to any dangerous changes in these, the brain chemistry is monitored using a technique called cerebral microdialysis (MD), which requires the collection of microdialysate into vials and their manual transfer into the bedside analyser on an hourly basis [54]. Not only is the current microdialysate monitoring system labour-intensive and costly (to purchase and to maintain), it is also limited to hourly readings, meaning that any rapid changes in

[†]F. Alimagham, K. Carpenter, P. Hutchinson and T. Hutter, **Detector assembly and method**, Patent no. GB1916168.6, **2019**

brain chemistry are overlooked and opportunities for timely intervention are lost. Moreover, since it is based on enzymatic colorimetric assays, it requires a range of consumables and reagents, and the microdialysate is consumed/modified during measurements, meaning that it cannot be re-used for other relevant studies.

There is a clear need to design and develop a sensor system which would allow continuous online monitoring of glucose, lactate and pyruvate, the three most clinically relevant substances in TBI patient microdialysate, over several hours and days at the patient bedside, using methods which would eliminate the need for expensive consumables and manual labour. Based on existing evidence, such a system would be of great value and highly beneficial for clinicians, nurses and most importantly TBI patient outcome [55, 56]. Abundant research has already been carried out towards developing a real-time microdialysate analysing sensor [56–59] and a new product for real-time microdialysis monitoring, LOKE (M dialysis AB, Aurora Borealis Control BV, The Netherlands), has recently been developed. However, all these studies and developments are based on enzymatic assays, which, despite providing a good sensitivity, present the disadvantages of frequently requiring a number of fresh reagents and consumables for each analyte, having a relatively complex fabrication process and also alter/consume the sample of interest. Light-based techniques, such as absorption spectroscopy, polarimetry, linear scattering spectroscopy and Raman spectroscopy, can generally provide access to the microscopic chemical composition of samples. Previous work carried out in our research group [38] has shown that, among them, MIR absorption spectroscopy appears to be the most promising, that would enable monitoring the characteristic molecular-vibration spectral features of the molecules of interest to develop a practical, robust and clinically accurate device. Moreover, MIR spectroscopy, being a non-destructive, label-free and rapid-detection technique, would allow continuous monitoring and post-utilisation of the sample for further studies, if necessary. Meanwhile, dealing with small sample volumes and flow-rates can be achieved using microfluidics. Therefore, the combination of these two approaches (MIR spectroscopy and microfluidics) creates a major opportunity for this particular application, and was selected as the method of choice for this project. Successful work on combining MIR spectroscopy and microfluidics for continuous dialysate monitoring has been carried out where compounds, such as glucose and lactate (but not pyruvate), have been detected [60–62]. However, these studies have primarily focused on diabetic patient monitoring by skin, blood and extracorporeal dialysis, while none have demonstrated or focused on the challenges of TBI monitoring.

The purpose of this work was, therefore, to combine MIR spectroscopy and microfluidics and assess its feasibility for the continuous monitoring of glucose, lactate and pyruvate in TBI patient microdialysate in the neuro-critical care unit (NCCU) of Addenbrooke's

Hospital, to ultimately improve patient management and outcome. This work was completed in collaboration with the research team of Prof. Peter Hutchinson and Dr. Keri Carpenter from the Department of Clinical Neurosciences, University of Cambridge. Figure 4.1 shows a schematic illustration of the conceptual continuous monitoring IR sensor, connected to a patient in the NCCU, together with the other monitoring systems, where the data are being acquired in real-time and uploaded to a PC or online. Moreover, this technology could enable remote monitoring of several patients at once.

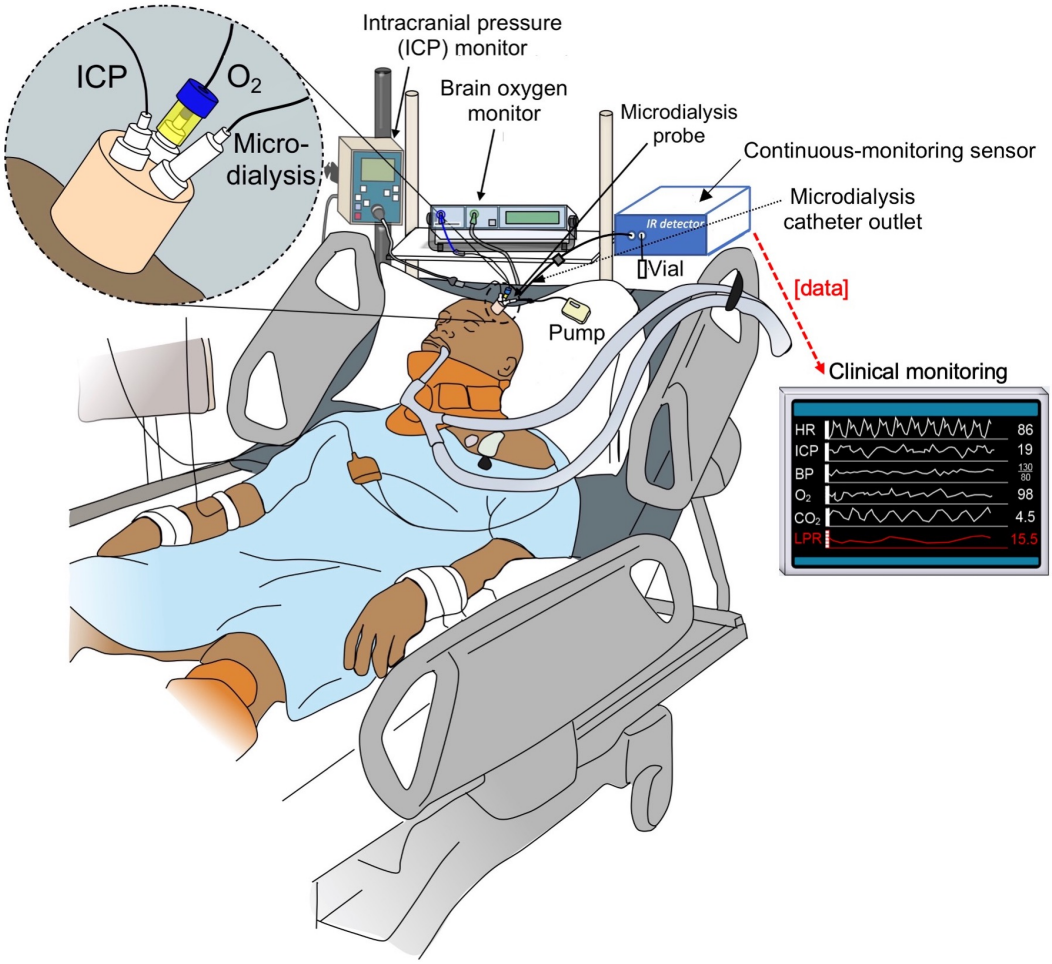

Fig. 4.1 Schematic illustration of the concept of an IR-based sensor for continuous monitoring of the brain chemistry of TBI patients in the neurocritical care unit, where the monitoring of intracranial pressure, brain oxygen and brain chemistry changes, using the proposed device, are being carried out simultaneously. Figure adapted from an illustration by Dr.Susan Giorgi-Coll.

Section 4.2 provides an insight into the pathophysiology of TBI and brain metabolism, as well as a description of the roles of glucose, lactate and pyruvate in TBI and the currently

implemented TBI-patient monitoring techniques. This is followed by a description of the requirements for a device based on IR spectroscopy and microfluidics capable of performing continuous microdialysis monitoring, provided in Section 4.3. Sections 4.4 and 4.5 focus on the identification of the MIR spectral features of glucose, lactate and pyruvate, as well as studying the suitability of transmission-mode FT-IR spectroscopy for this particular application. Further work, described in Section 4.6, was carried out to assess the performance of a MIR quantum cascade laser (QCL) system to provide higher sensitivities than that which was achievable using FT-IR spectroscopy. Clinical samples were measured using this system and a clinical-simulation setup was developed and tested in sections 4.7 and 4.8, respectively. Clinical studies were carried out on TBI patients using the QCL sensor system, as described in Section 4.9. In Section 4.10, a multivariate-analysis method (PLSR) was implemented to predict the concentrations of glucose, lactate and pyruvate in patient microdialysis samples. Section 4.11 presents the conclusions drawn from this work and discusses steps for future optimisation of this method and its translation into the clinic.

4.2 TBI principles and mechanisms

TBI is a term designating a wide range of pathology that results from an external mechanical force to the cranium and underlying brain. TBI poses a significant healthcare concern from the moment of initial insult until potentially many years later if long-term conditions manifest [63]. It is a major cause of mortality, especially among young adults, and lifelong disability is common in those who survive. Moreover, the incidence of TBI around the world is rising sharply, mainly due to increasing use of motor-vehicles in low and middle-income countries. In addition, it poses a major socio-economic burden and it is among the top three causes of injury-related medical costs [64, 65]. Therefore, effective management and treatment of TBI cases is of critical importance on a global level. The principal mechanisms of TBI are classified as: (a) focal brain damage, owing to contact injury and resulting in contusion, laceration, and intracranial haemorrhage; and (b) diffuse brain damage, owing to acceleration/deceleration injury and resulting in diffuse axonal injury or brain swelling [66]. TBI patient outcome is typically determined by two significantly distinct mechanisms/stages: (a) the primary insult (primary or mechanical damage); and (b) the secondary insult (secondary or delayed non-mechanical damage). Primary damage occurs at the moment of the impact and is solely sensitive to preventative measures but not therapeutic measures. On the other hand, secondary injury consists of consecutive pathological processes initiated at the instant of the injury with delayed clinical presentation [66, 67]. Secondary insults may include cerebral ischaemia, hyperglycemia, the imbalance between energy expenditure/supply and

intracranial hypertension and, in treatment terms, these types of injury are sensitive to therapeutic interventions. In fact, the evolving secondary injury may often predominate as the most significant determinant of neurological outcome [68].

4.2.1 TBI monitoring

The leading cause of in-hospital deaths that occur following a TBI is secondary brain injury, and even the most attentive clinicians can often be in the dark about evolving secondary neurological injury since it often does not exhibit any obvious clinical symptoms [68, 69]. Therefore, advanced monitoring of the cerebral variables during secondary injury is paramount in order to proceed with appropriate intervention as early as possible and to monitor patient progression. The information gathered from clinical monitoring can then be for treatment decision-making which can significantly improve patient outcome. In patients with severe TBI, the brain condition is currently monitored via the insertion of a cerebral microdialysis catheter (CMD), which monitors the brain biochemistry (i.e. metabolite concentration), alongside two probes, which monitor the ICP and $PbtO_2$. For the purpose of this work, further details on ICP and $PbtO_2$ monitoring and how these can be used, both independently and in combination with microdialysis, to guide treatment will not be discussed but can be found extensively in the literature [67–70]. The primary focus will be on brain-chemistry monitoring via microdialysis, since it is directly linked to the aim of this work.

4.2.1.1 Cerebral microdialysis

Cerebral microdialysis (CMD) is a well-established tool for sampling the brain extracellular fluid (ECF) via a thin (0.5 mm diameter) catheter that is inserted into the interstitium of the brain. The catheter consists of two concentric tubes, where the outer tube is connected to a syringe pump (MD pump) that continuously infuses a perfusate to the tip of the catheter, which consists of a "physiological" salt solution (i.e. 147 mM NaCl, 2.7 mM KCl, 1.2 mM $CaCl_2$ and 0.85 mM $MgCl_2$, available as “CNS perfusion fluid” from CMA Microdialysis AB, Solna, Sweden) that resembles the composition and pH of brain ECF [67, 71, 72]. The catheter receives the perfusate at a typical flow-rate of 0.3 μL min^{-1} and its semi-permeable membrane, which constitutes the outer wall at the end of the catheter (i.e. 10 mm length) and typically has a 100 kDa molecular weight cut-off, allows the perfusate to be exposed to the ECF of the surrounding brain tissue. Endogenous molecules present in the brain ECF diffuse through the membrane from the interstitium into the perfusate. The "enriched" perfusate then enters the inner concentric tube where it flows out of the brain and the emerging fluid,

termed microdialysate, is collected into a vial [71]. This vial is typically changed hourly and the microdialysate is currently analysed via enzyme-catalysed colorimetric assays using a commercially-available bedside analyser (ISCUS Flex Microdialysis Analyser, M Dialysis AB, Sweden) to quantify the concentrations of glucose, lactate and pyruvate, the three main clinically monitored molecules. The process of cerebral microdialysis, as well as the components used, are summarised in Figure 4.2.

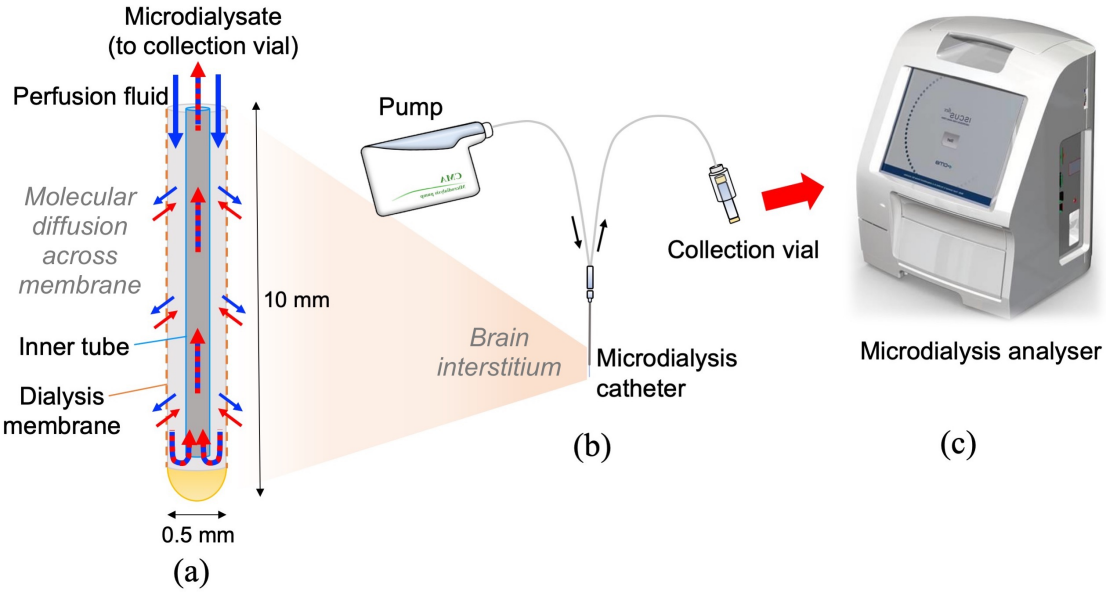

Fig. 4.2 Components and procedure of cerebral microdialysis: (a) microdialysis catheter tip showing exchange of molecules across the dialysis membrane; (b) microdialysis pump, microdialysis catheter and microvial for collection of the microdialysate; (c) bedside analyser (ISCUS Flex Microdialysis Analyser).

Clearly, the concentration of a given molecule in the dialysate will be lower than its concentration in the brain ECF unless there is total equilibrium across the dialysis membrane. The proportion of the true ECF concentration collected in the dialysate is termed the relative recovery and is dependent on membrane pore size, membrane area, rate of flow of perfusate and diffusion speed of the substance [71, 73]. Representative mean values for relative recovery *in vitro* with the commonly-used flow-rate of 0.3 μL min^{-1}, in combination with a 100 kDa molecular weight cut-off (MWCO) microdialysis catheter with a 10 mm length membrane, generates a mean recovery* of 101.3 $\pm$ 5.5 %, 88.3 $\pm$ 2.3 % and 101.0 $\pm$ 3.6 % for glucose, lactate and pyruvate, respectively [71]. Since the dialysis membrane is selective only for size, any compound smaller than 100 kDa can be collected, including compounds

*Recovery (%) is expressed as the concentration of analyte in the microdialysate, divided by the concentration of analyte in the external solution, multiplied by 100%.

other than the main ones of interest, such as drug molecules (e.g. anti-seizure medication, administered as part of the TBI treatment), cytokines, nitric oxide products, glutamate and glycerol) [74]. The conventional and clinically relevant MD variables, such as glucose, lactate, pyruvate and lactate:pyruvate ratio (LPR), will be discussed further in Section 4.2.2.

4.2.2 TBI metabolism and CMD markers

Energy metabolism in the human brain is not entirely understood, even in the normal uninjured state. Glucose, lactate and pyruvate are key compounds in the process of cellular respiration, by which glucose is metabolised to produce adenosine triphosphate (ATP) - the source of chemical potential energy used by all cells for intracellular energy transfer [75]. Figure 4.3 summarizes the key reactions of cellular respiration.

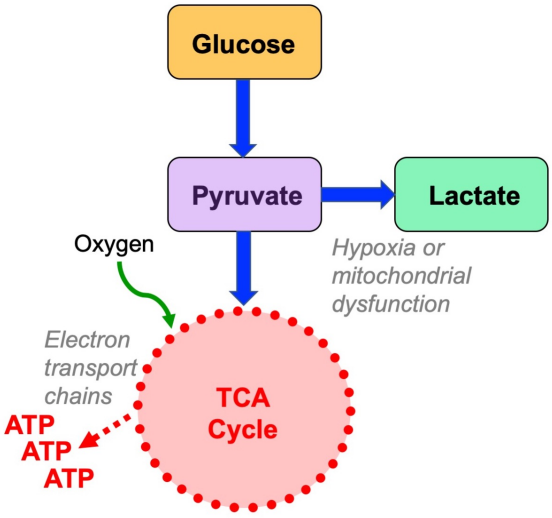

Fig. 4.3 Simplified schematic highlighting the roles of glucose, lactate and pyruvate within the major energy pathways in the brain. (Adapted from [76]).

Glycolysis is the first stage of cellular respiration, where glucose is converted into pyruvate through a series of enzyme-catalysed reactions, producing a net yield of two ATP molecules and two pyruvate molecules for each molecule of glucose. The produced pyruvate is then used as a substrate for one of two reaction pathways, depending on the availability of oxygen. If enough oxygen is available, pyruvate is converted into acetyl coenzyme A, which in turn is used as an initial substrate for the Tricarboxylic Acid (TCA) cycle, where the mitochondrial respiratory chain uses oxygen to produce 36 molecules of ATP for each originally oxidised glucose molecule. In the absence of oxygen, pyruvate is converted into lactate via the anaerobic respiration pathway [72].

Glucose in TBI

Glucose is the main substrate used by the brain under normal conditions and brain-glucose levels are dictated by a balance between glucose supply and demand. Normal MD brain glucose levels, measured using a 0.3 μL min^{-1} flow of perfusate, was determined as 1.7 $\pm$ 0.9 mM [77]. If brain glucose increases or decreases disproportionally, then changes in blood flow or metabolism may be the reasons responsible for it. MD glucose levels may be affected by a number of reasons: ischaemia, hyperaemia, hyperglycaemia, hypermetabolism or hypometabolism [72]. Table 4.1 summarizes the conditions that may lead to low or high MD glucose levels [72, 78].

Table 4.1 Conditions associated with low or high microdialysate glucose levels [78].

Low MD glucose	**High MD glucose**
Ischaemia - due to insufficient blood flow, causing decreased levels of tissue glucose	***Hyperemia*** - due to increased blood flow, causing increased glucose delivery
Hypoglycemia - due to decreased blood glucose, which decreases MD glucose	***Hyperglycemia*** due to increased blood glucose, which increases MD glucose
Hypermetabolism - causes an increase of glucose uptake into the cells, leading to low extracellular glucose	***Hypometabolism*** - causes a decrease of glucose uptake into the cells, leading to high extracellular glucose

Lactate and Pyruvate in TBI

An increase in lactate and decrease in pyruvate indicates decreased oxygen availability, which may be due to ischaemia or hypoxia. In acutely brain-injured patients, however, increased extracellular lactate can also be associated with hyperglycolysis. Normal values of lactate and pyruvate, obtained at a flow-rate of 0.3 μL min^{-1} from an uninjured brain are 2.9 $\pm$ 0.9 mM and 166 $\pm$ 47 μM, respectively [77]. The relative proportion of lactate and pyruvate (LPR) is used as a marker of aerobic vs. anaerobic metabolism within the brain. The normal LPR is approximately 20 and, while a value greater than 25 is considered abnormal (impaired cerebral oxidative metabolism), a LPR greater than 40 is the critical level above which brain metabolic crisis is defined [79]. LPR increase can essentially be categorised into two types: (a) Type 1, indicating ischaemia, where lactate is increased and pyruvate is decreased; and (b) Type 2, non-ischaemic, where both lactate and pyruvate are increased, as a result of mitochondrial dysfunction [54, 72]. Therefore, the monitoring of other parameters, such as oxygen levels, in conjunction with LPR monitoring is crucial in interpreting the condition of the injured brain. Table 4.2 summarizes the conditions associated with increased extracellular LPR.

Table 4.2 Conditions associated with increased LPR [72].

Lactate	Pyruvate	LPR	Conditions
High	Low	High	Ischaemia
High	High	Normal	Hyperglycolysis
Very high	Normal to high	High	Mitochondrial dysfunction

LPR = lactate:pyruvate ratio

CMD variables to guide intervention and therapy

Before considering the use of CMD for clinical monitoring and intervention, it is important to understand that there are broad variations in MD variables over time after injury, not only between different subjects but also within individuals. The elevated and dynamic levels of metabolic activity within the injured brain make it challenging to interpret 'one-off' MD measurements in isolation. Therefore, it is essential that the data are interpreted in combination with other measured variables. According to the current trends in multimodal monitoring, in order to direct individualized intensive-care therapy, it is essential to consider the LPR rather than lactate alone, to look for dynamic changes and trends of both LPR and glucose, and finally to take into account additional monitored modalities, such as ICP and $PbtO_2$ [79]. There is an extensive body of literature suggesting combinations of different variables and modalities to assist clinical decision-making to guide treatment, such as drug administration and surgical procedures [54, 73, 74, 79]. Figure 4.4 presents a method for interpretation of CMD abnormalities, based on low CMD glucose (typically < 0.8 mM) [79].

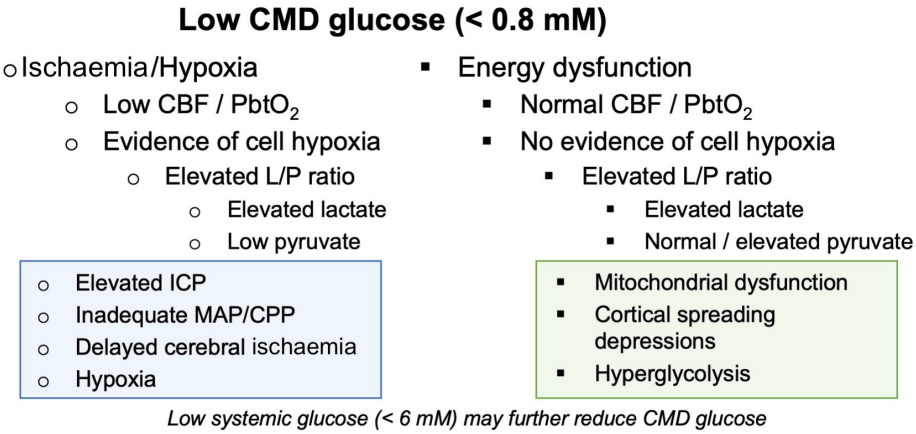

Fig. 4.4 Method to guide interpretation and diagnosis of cerebral metabolic abnormalities based on cerebral microdialysis. Abbreviations: CBF, cerebral blood flow; CMD, cerebral microdialysis; CPP, cerebral perfusion pressure; ICP, intracranial pressure; L/P, lactate/pyruvate; MAP, mean arterial pressure; $PbtO_2$, brain tissue oxygen pressure. Adapted from [79].

4.3 Device considerations and requirements

As mentioned, the aim of this work is to develop a MIR spectroscopy and microfluidic-based sensor capable of performing continuous measurements of TBI-patient microdialysate. The development of such a system is not trivial and many considerations should be taken into account.

Firstly, it was important to pin down the performance requirements of the sensor, including sensitivity and selectivity for the compounds of interest: glucose, lactate and pyruvate. The sensor should be able to detect compounds within their physiologically relevant concentrations, namely, between 0.1-24 mM for glucose and lactate, and between 0.01-1.5 mM for pyruvate [53, 80]. Moreover, the Limit of Quantification (LoQ) of the sensor, defined as the smallest concentration of analyte that can be detected and differentiated from other concentrations of that analyte [81], should be comparable to the LoQ provided by the standard microdialysis analyser (ISCUS Flex Microdialysis Analyser). According to the literature [82], the LoQ provided by the ISCUS (measured as the last concentration with coefficient of variation below 20 %) for glucose, lactate and pyruvate are 0.10 mM, 0.20 mM and 0.016 mM, respectively. Regarding the selectivity, it was paramount that the sensor was capable of accurately measuring the individual concentrations of all three compounds, regardless of interference with one another and with other potential molecules present in the microdialysate. As previously detailed in Chapter 2, the MIR fingerprint region allows the identification of specific compounds within a complex medium, due to the unique spectral vibrations in this region. Therefore, ranges within the fingerprint region of the MIR spectrum were selected for this study and efforts were made to reach the proposed detection limits of the compounds of interest.

Secondly, the operational and hardware requirements of the sensor were considered and defined. The size of the sensor was a key factor to take into account, given that many other parameters depend on it. Since the sensor is to be connected to the outlet of the MD catheter in place of the vial (see Figure 4.2), a small, miniaturised sensor would be ideal in order to sit close to or on the patient, while a larger sensor would require a bedside trolley and consequently longer tubing to deliver the sample, which may have implications on the time-response. In Chapter 3, efforts were made towards developing miniaturised microfluidic sensing devices coupled to IR fibre-optics for continuous fluid monitoring. Although these showed good potential for this application, the sensitivities were insufficient and would require further work with higher power light sources. Therefore, at this stage, priority was given to achieving better detection limits using high-power light sources, rather than to device miniaturisation, which can be later implemented. Other than the size, the ability to measure small volumes of liquid, flowing at 0.3 μL min^{-1}, was crucial for the application at hand.

Microfluidic techniques, small inner-diameter (ID) tubing and appropriate connectors were considered for this reason. Moreover, the ability to perform continuous or semi-continuous monitoring (i.e. measurements at least once every 5 minutes) of all compounds of interest, simultaneously, was one of the most crucial considerations during this work. Finally, another criterion of the sensor was for it to be user-friendly for the clinical staff, including nurses and clinicians, and also easily implementable into a clinical setting. Easy operation of the sensor and interpretation of data, as well as its clinical-translation methods, were also considered and taken into account.

4.4 MIR spectra of glucose, lactate and pyruvate and spectral interference

This section aims to characterise the MIR absorbance spectra of glucose, lactate and pyruvate, both individually and in a mixture, in order to determine the unique peaks of each compound and ensure that these are not affected by the presence of the other two analytes. Pure 100 mM solutions of each compound were prepared by dissolving pure compounds D-(+)-glucose, sodium L-lactate and sodium pyruvate (all $\geq$ 99 %, Sigma Aldrich) in perfusion fluid (PF). A high concentration of 100 mM was used to ensure clear absorbance peaks. PF was used as a solvent to better approximate microdialysis samples. For this, a stock solution of PF was prepared to the identical recipe as the PF used in the NCCU (CNS Perfusion Fluid, M Dialysis AB, Sweden): 147 mM NaCl, 2.7 mM KCl, 1.2 mM $CaCl_2$ and 0.85 mM $MgCl_2$ in DI water, with all compounds purchased from Sigma Aldrich. The resulting PF was stored at 4^oC and used for up to one month before being replaced by fresh PF. All measurements were taken using a standard IR spectrometer (Perkin Elmer Spectrum 100 FT-IR), using a Specac Pearl liquid-transmission accessory coupled with a Specac Oyster cell assembly, which was mounted into the sample compartment of the Perkin Elmer instrument. The spectrometer was operated via the Perkin Elmer 'Spectrum' Software and was equipped with a SiC hot spot-stabilised IR light source, a KBr beam-splitter, a Michelson interferometer and a liquid nitrogen-cooled mercury cadmium telluride (MCT) detector. The Oyster cell is manufactured with Zinc Selenide (ZnSe) windows at a fixed path-length and is used as the sample holder during measurements, allowing the transmission of IR light through a given sample. For these measurements, a 50 μm path-length cell was used, into which 20 μL of each sample was pipetted to be measured. The cell was cleaned between each sample using deionised (DI) water. Prior to the measurements, a spectrum of pure PF was acquired and used as a background reference for all absorbance spectra. The spectra were generated

via the accumulation of 150 scans with a resolution of 4 cm^{-1} and acquired in the spectral range between 400 and 4500 cm^{-1}, although a smaller range between 900 and 1800 cm^{-1} was presented in the results for easier interpretation and due to the irrelevance of spectral features in the remaining range. Finally, the potential presence of other interfering species in the microdialysate was also considered to ensure that these will not affect the concentration read-outs of glucose, lactate and pyruvate.

4.4.1 MIR spectra of glucose

The MIR absorbance spectrum of the 100 mM glucose solution in PF and its associated peak assignments are shown in Figure 4.5 and Table 4.3, respectively.

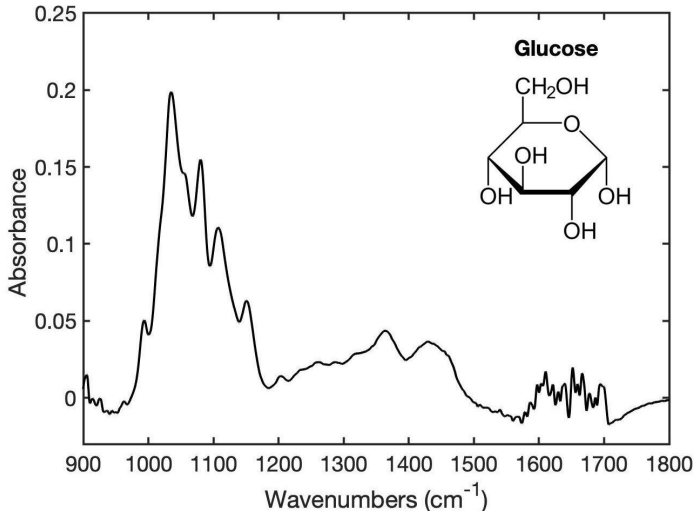

Fig. 4.5 MIR spectrum of a 100 mM solution of glucose in perfusion fluid, acquired using standard transmission-FTIR and a 50 μm path-length.

The most distinctive feature of the spectrum is the collection of strong peaks in the region between 950 and 1200 cm^{-1}, which correspond to the C-O vibrations (at 1036 and 1080 cm^{-1}) and the C-C vibrations (at 994, 1108 and 1152 cm^{-1}) [83]. According to the literature, these are the most significant peaks for glucose identification in MIR spectroscopy [84]. Noise was observed between 1600 and 1700 cm^{-1}, which was believed to be caused by the strong IR absorption of water which caused detector saturation.

4.4.2 MIR spectra of lactate

Table 4.3 Peak assignments associated with the spectrum of a 100 mM solution of glucose in perfusion fluid shown in Figure 4.5 [83].

Peak position (cm^{-1})	Description	Assignment
994	medium	C-C (alicyclic) vibration
1036	strong	C-O stretch
1080	strong	C-O stretch
1108	medium	C-C (alicyclic) vibration
1152	medium	C-C (alicyclic) vibration
1204	weak	C-C (alicyclic) vibration
1262	weak	C-C (alicyclic) vibration
1288	weak	C-C (alicyclic) vibration
1364	medium	C-O-H bend
1432	medium	CH_2 bend

The MIR absorbance spectrum of the 100 mM lactate solution in PF and its associated peak assignments are shown in Figure 4.6 and Table 4.4, respectively.

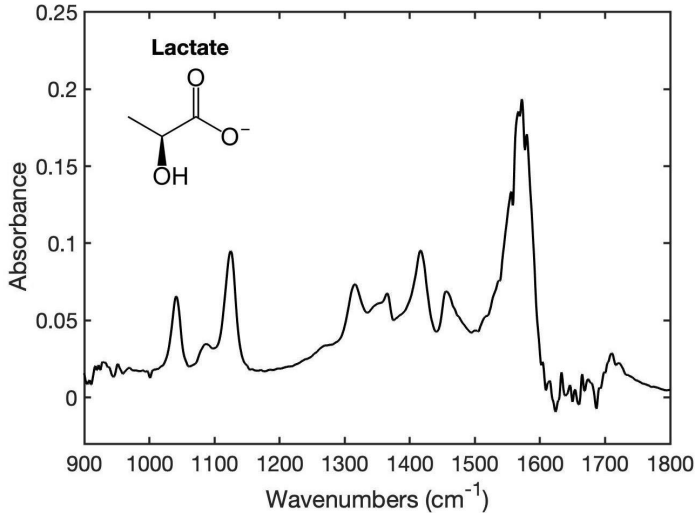

Fig. 4.6 MIR absorbance spectrum of a 100 mM solution of lactate in perfusion fluid, acquired using standard transmission-FTIR and a 50 μm path-length.

A cluster of strongly absorbing and overlapping peaks were observed between 1556 and 1580 cm^{-1}, which correspond to the stretching vibration of the CO_2^- functional group. Despite producing the strongest peaks of the lactate spectrum, these peaks are not a specific

indicator for the presence of lactate when used in isolation, since all molecules with a carbonyl group are known to absorb strongly in that region of the spectrum. Two other groups, of mostly medium-intensity peaks, were also observed in the regions 1042-1124 cm^{-1} and 1315-1456 cm^{-1}. However, according to the literature, the peaks at 1042 cm^{-1} and 1124 cm^{-1}, corresponding to the C-O stretches, have been shown to be the most useful for identifying lactate [84]. As before, water-induced noise was also observed between 1600 and 1700 cm^{-1}.

Table 4.4 Peak assignments associated with the spectrum of a 100 mM solution of lactate in perfusion fluid shown in Figure 4.6 [83].

Peak position (cm^{-1})	**Description**	**Assignment**
928	weak	C-C (aliphatic) vibration
1042	medium	C-O stretch
1086	weak	C-O stretch
1124	medium	C-O stretch
1315	medium	C-O-H bend
1365	medium	CH_3 bend
1417	medium	CO_2^- stretch (sym.)
1456	medium	CH_3 bend
1556	medium	CO_2^- stretch (asym.)
1567	strong	CO_2^- stretch (asym.)
1572	strong	CO_2^- stretch (asym.)
1580	strong	CO_2^- stretch (asym.)

4.4.3 MIR spectra of pyruvate

The MIR absorbance spectrum of the 100 mM pyruvate solution in PF and its associated peak assignments are shown in Figure 4.7 and Table 4.5, respectively. Essentially, three groups of peaks with similar intensity were observed in the regions 1356-1424 cm^{-1}, 1572-1586 cm^{-1} and 1711 cm^{-1}, while a notably stronger peak was observed at 1176 cm^{-1}, corresponding to C-C vibrations. Once again, water-induced noise was present between 1600 and 1700 cm^{-1}.

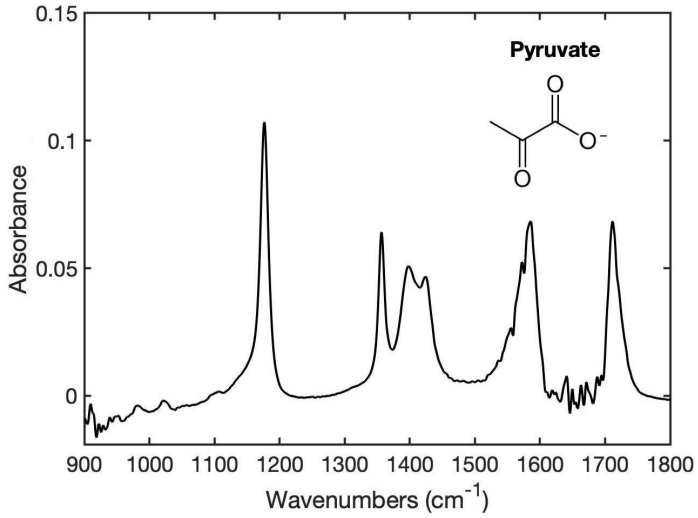

Fig. 4.7 MIR absorbance spectrum of a 100 mM solution of pyruvate in perfusion fluid, acquired using standard transmission-FTIR and a 50 μm path-length.

Table 4.5 Peak assignments associated with the spectrum of a 100 mM solution of pyruvate in perfusion fluid shown in Figure 4.7 [83].

Peak position (cm^{-1})	**Description**	**Assignment**
1022	weak	C-C (aliphatic) vibration
1176	strong	C-C (aliphatic) vibration
1356	strong	CH_3 bend
1398	medium	CO_2^- stretch (sym.)
1424	medium	CO_2^- stretch (sym.)
1572	medium	CO_2^- stretch (asym.)
1586	strong	CO_2^- stretch (asym.)
1711	strong	C=O stretch

4.4.4 MIR spectra of a mixture of glucose, lactate and pyruvate

A solution containing a mixture of 100 mM of all three compounds, glucose, lactate and pyruvate, was prepared in perfusion fluid and analysed in the same way as the pure compounds. This small study was carried out in order to compare the spectrum of the pure compounds with the mixture of all three for two main reasons: (1) to identify any specific peaks for each compound, which remain noticeable in the mixture spectrum; and (2) to identify any peaks which may be hindered due to the overlap of peaks from another compound. By doing this, specific peaks, which could be used to identify each individual compound from a mixture of

the three, could be identified. To help visualise the contribution of each compound to the mixture spectrum, Figure 4.8 presents the overlay of the pure compound spectra (of 100 mM glucose, lactate and pyruvate) with the spectrum of a mixture containing 100 mM of all three. From here, it was evident that a number of compound-specific peaks remain visible when all three compounds are mixed in solution.

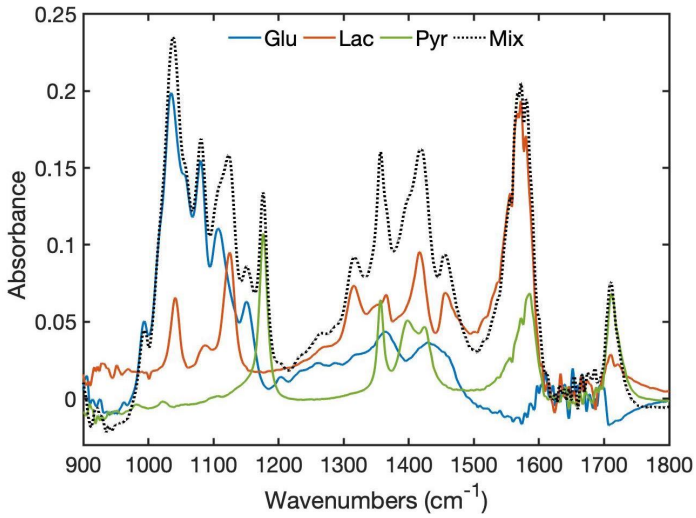

Fig. 4.8 Absorbance spectra of 100 mM solutions of pure glucose, lactate and pyruvate in perfusion fluid overlaid with the absorbance spectrum of a mixture containing 100 mM of each compound showing the individual contribution of each compound. Spectra acquired using transmission-FTIR and an optical path-length of 50 μm.

Specific glucose peaks could be seen at 1080 cm^{-1} and 1152 cm^{-1}, with the strongest of the two being the one at 1080 cm^{-1}, corresponding to a C-O stretching vibration. The strong glucose peak at 1036 cm^{-1}, previously recognized as one of the main peaks for glucose identification, overlaps considerably with the lactate C-O stretching peak at 1042 cm^{-1}, resulting in a single strong 'mixture peak' at 1038 cm^{-1}. Although this peak cannot be considered specific to either compound, based on the spectra, it is evident that, when glucose and lactate are present at similar concentrations in a mixture, glucose has a far greater contribution to this peak compared to lactate. The specific peaks only for lactate were found at 1315 cm^{-1} (C-O-H bend) and 1456 cm^{-1} (CH_3 bend), while the two absorption bands at 1042 cm^{-1} and 1124 cm^{-1}, typically used for lactate identification, overlap with the glucose C-O stretching vibrations, and thus could not be deemed specific to lactate when glucose is present in the mixture. Therefore, in order to identify and quantify glucose and lactate independently in microdialysis samples, the implementation of multivariate-analysis methods will be required. The following three specific pyruvate peaks could be seen in the mixture

spectrum: 1176 cm^{-1} (C-C vibration), 1356 (CH_3 bending mode) and 1711 cm^{-1} (C=O stretch), all of which are of medium/strong intensity.

4.4.5 Spectral interference of other compounds

As previously discussed in Subsection 4.2.1, there are a number of other compounds which may be present in clinical microdialysis samples, such as drug molecules, cytokines, nitric oxide products, glutamate and glycerol. A previous study within our research group analysed the extent to which each of these compounds may interfere with the detection and quantification of glucose, lactate and pyruvate, the main compounds of interest [38]. This analysis concluded that many of these molecules, primarily the non-specific ones, such as the drug molecules and nitric oxide products, are difficult to account for at this stage and their investigation should be highly considered during clinical studies. In addition, it was seen that both glutamate and glycerol exhibit unique MIR spectral features in relation to glucose, lactate and pyruvate when present at equimolar concentrations within a mixture of all five in perfusion fluid. Moreover, the concentrations of glycerol and glutamate are expected to be present in clinical microdialysates at significantly lower concentrations than both glucose and lactate, and therefore their interference with the latter may be considered negligible. Finally, studies have shown that cytokine molecules are present in microdialysates at picomolar concentrations [85], and therefore, are highly unlikely to have any effect on the final spectra. Although some measurements to confirm these findings were also carried out during this work, they will not be presented or discussed here due to lack of priority.

4.4.6 Conclusions

The MIR spectra of glucose, lactate and pyruvate were analysed and the characteristic peaks for each of these were determined. The mixture study concluded that each compound exhibited unique peaks, primarily in the MIR fingerprint region, which would allow them to be detected and individually quantified within an equimolar mixture of all three. However, it was shown that the two most relevant absorbing bands of lactate at 1040 cm^{-1} and 1124 cm^{-1} overlap with the glucose peaks in that region, specifically at 1036 cm^{-1} and 1108 cm^{-1}, respectively. This phenomenon is common in MIR spectroscopy of complex liquid samples and therefore standard procedures to resolve analyte-specific information hidden in the acquired spectra, such as multivariate data analysis, have been developed and can be implemented successfully. Since the primary peaks for each compound were seen between 950 and 1200 cm^{-1}, this will be the main wavelength range used for subsequent spectral analysis. Finally, the interference of other compounds within the microdialysate was taken

into account, and it was concluded that, while there is no risk of interference by any of the known compounds (cytokines, glutamate and glycerol), further analysis should be carried out during clinical studies to assess the interference of unspecified compounds, such as drugs and nitric oxide products.

4.5 Assessment of standard transmission-mode FTIR

Previous collaborative work carried out in our research group compared two methods of FT-IR spectroscopy, namely ATR-FTIR and transmission-FTIR, for this particular application in terms of specific peak determination, sensitivity for the compounds of interest, water interference, simplicity, and practical aspects of device design and miniaturisation [38]. Out of these, transmission-FTIR was deemed to be the most suitable for the application in question due to easily allowing a larger sample interaction, an increased signal-to-noise ratio (SNR) and simple configuration, rendering it likely to be the most straightforward approach for device development and miniaturisation. The preferred use of transmission-FTIR over ATR for similar applications has also been confirmed in the literature [86, 87].

This section was aimed at assessing the use of transmission-FTIR spectroscopy for the detection and quantification of the compounds of interest at clinically relevant concentrations, using a standard FT-IR instrument, as well as determining the optimum optical path-length to be used when developing a miniaturised sensing device. Firstly, the optimum optical path-length was determined, after which, pure solutions of pure glucose at varying concentrations were prepared and measured using the selected path-length in order to determine the achievable sensitivities. For the experiments in the following section, glucose was selected as the test analyte as it is often used as a bench-mark for MIR spectroscopy on which there is extensive literature [88], although any of the three could have been used.

4.5.1 Optimum optical path-length selection

In order to determine the optimum optical path-length for the detection of the compounds of interest, the same instrument, accessory and parameters, as described in Section 4.4, were used. In addition to using a cell with a 50 μm optical path-length, cells with a smaller and longer optical path-lengths were also used, of 25 μm and 100 μm, respectively. These two path-lengths were selected since they were the only other available Oyster-cell options for the Specac Pearl liquid-transmission accessory. For this study, a 24 mM glucose solution in PF was prepared and used to test the three optical path-lengths and to determine which of these provides the best SNR. To maximise the chance of visualising clear peaks in this experiment,

a glucose concentration of 24 mM was selected since it was the highest value within the physiological range. A spectrum of pure PF was used as a background reference for all absorbance spectra and the spectra were presented within the range containing the primary glucose peaks, 1036, 1080, 1108 and 1152 cm^{-1}. Figure 4.9a presents the absorbance spectra of a 24 mM glucose solution for the 25, 50 and 100 μm optical path-lengths and Figure 4.9b shows the SNR and relative absorbance-peak intensity at 1036 cm^{-1} for the spectra at each path-length. The SNR values were determined by dividing the difference between the peak signal and background by the root mean square of the noise of the background signal, while the relative peak intensities were determined from the difference in absorbance between the peak maximum and a baseline point of the spectrum, selected at 1180 cm^{-1} from an examination of the spectra. The peak at 1036 cm^{-1} was selected for determining the peak absorbance since it is the most prominent glucose peak.

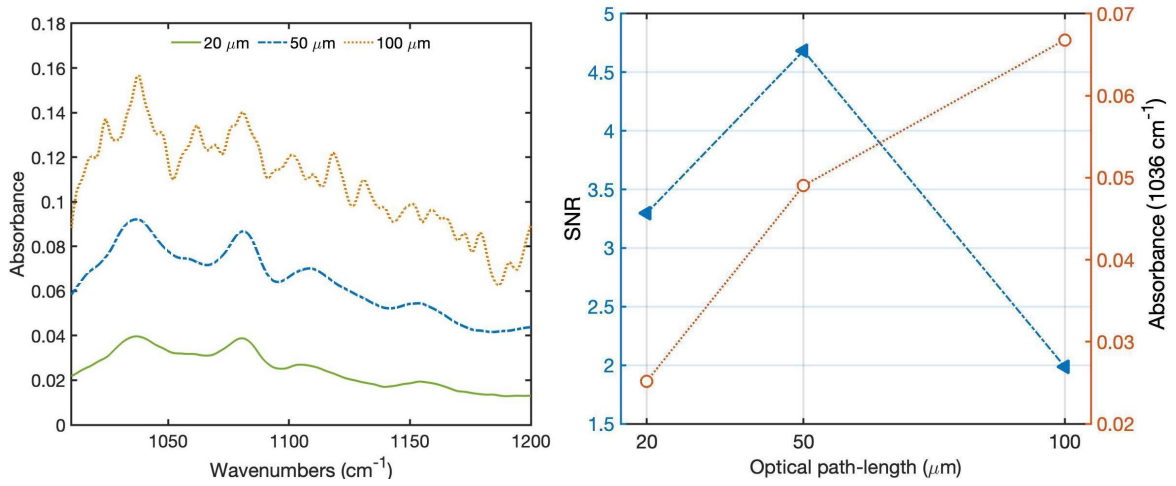

(a) (b)

Fig. 4.9 (a) Absorbance spectra of 24 mM glucose in perfusion fluid, acquired using a standard FT-IR system and different cell path-lengths: 20, 50 and 100 μm. Note: spectra plotted with a vertical offset for clarity. (b) SNR and relative absorbance peak-height at the 1036 cm^{-1} glucose peak corresponding to each path-length. The results obtained with a path-length of 50 μm showed the best SNR.

Although the highest relative peak absorbance was seen for the 100 μm optical path-length, the SNR for the same path-length was by far the lowest. This could be explained by the fact that most of the solvents - and especially water - exhibit strong absorptions in the IR wavelength range which limits the penetration depth of incoming light, resulting in a more noisy signal. On the other hand, the lowest relative peak absorbance was seen for the 25 μm path-length, since the interaction of IR radiation with the sample is reduced. The highest overall SNR was observed for the 50 μm path-length, despite the slightly lower peak

absorbance compared to the 100 μm path-length, since it allows sufficient light to reach the detector and sufficient light-sample interaction. For this reason, the 50 μm path-length was selected to carry out the subsequent studies on the sensitivity using the standard FT-IR spectrometer.

4.5.2 Sensitivity study

In order to study the detection sensitivity (ratio between the output signal and measured property) for glucose using the standard FT-IR spectrometer and the selected 50 μm path-length, pure solutions of glucose in PF at different concentrations were prepared to cover the clinical range: 0.05 mM, 0.1 mM, 0.2 mM, 0.4 mM, 0.75 mM, 1.5 mM, 3 mM, 6 mM and 12 mM. A measurement of pure PF, representing 0 mM glucose, was also taken. The measurement of 24 mM glucose was deemed unnecessary since it had been previously measured and was at a clearly detectable concentration. Each concentration was measured three times using three separate samples of each solution. For all absorbance spectra, pure perfusion fluid was used as a reference. The LoQ, defined in Section 4.3, is an important parameter used to describe the performance of sensors. Due to the known relationship between IR absorption, peak intensity and analyte concentration, expressed by the Beer-Lambert law (Equation 2.6), the comparison of peak intensities was considered a valid method for determining the LoQ of glucose provided by an optical path-length of 50 μm, and is described in further detail in the following paragraphs. Figure 4.10 shows the absorbance spectra of the glucose concentrations from 0 to 12 mM, including all repeats.

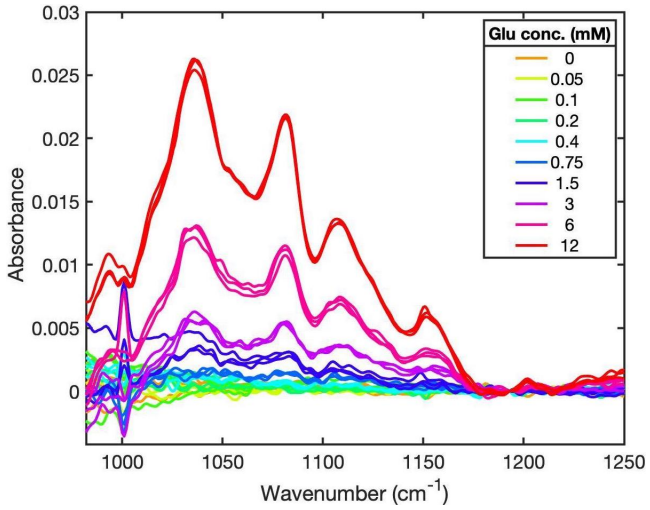

Fig. 4.10 Absorbance spectra of glucose in perfusion fluid at a range of clinically relevant concentrations, acquired using standard transmission-FTIR and a 50 μm path-length. Note: spectra normalised to a baseline point at 1180 cm^{-1}.

Clear glucose peaks at the expected frequencies were observed, especially for the higher concentrations. Although the spectra showed relatively flat baselines, a slight vertical offset was sometimes observed with respect to one another, and therefore, all spectra were normalised to a baseline point, selected at 1180 cm^{-1}. Subsequently, the relative peak intensities were calculated at each concentration for the two strongest unique glucose absorption peaks, at 1036 and 1080 cm^{-1}. Figures 4.11a and 4.11b show the analysis of relative peak intensities at varying concentrations for the peaks at 1036 cm^{-1} and 1080 cm^{-1}, respectively. In both cases, the relationship between the relative peak intensity and concentration was linear and a trend-line (line of best fit) was fitted to the data.

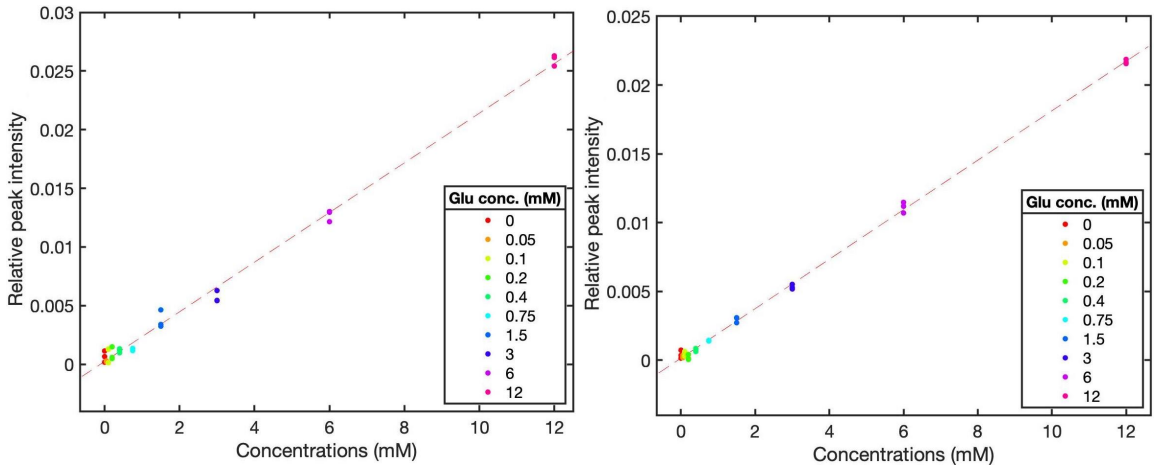

(a) (b)

Fig. 4.11 Relationship between different glucose concentrations and the corresponding relative peak intensities measured using a 50 μm path-length on a standard FT-IR spectrometer at: (a) 1036 cm^{-1} ($R^2 = 0.995$, $m = 0.0021$); and (b) 1080 cm^{-1} ($R^2 = 0.999$, $m = 0.0018$). The results of each repeat are included here.

In order to assess the performance of these measurements, two parameters were extracted from the data: (1) the coefficient of determination, R^2, which is a measure of the linearity of the relationship; and (2) the gradient of the fitted line, m, which represents the sensitivity of response of the peak intensity to a change in concentration. The R^2 value ranges between 0 and 1, and the closer the value is to 1, the higher the linearity of the relationship, which is ultimately a desirable feature for a sensor. On the other hand, the magnitude of the gradient of the line of best fit is a representation of the strength of the relationship, where a greater gradient value indicated a greater increase in the peak intensity for an increase in concentration, making a high gradient also a desirable sensor characteristic. The R^2 values for the glucose peaks at 1036 cm^{-1} and 1080 cm^{-1} were 0.995 and 0.999, respectively, meaning that a highly linear relationship was observed for both, but with the peak at 1080

cm^{-1} exhibiting a slightly higher value. This could be explained from analysing the spectra in Figure 4.10, where despite the peak at 1036 cm^{-1} being more prominent, the noise level seems to increase for the lower frequencies. The exact cause for this is unclear but could be due to an inconsistency in the intensity of the light source throughout the entire spectral range and due to the detector sensitivity, resulting in a slightly higher noise level at particular frequencies. Furthermore, the gradient values for the glucose peaks at 1036 cm^{-1} and 1080 cm^{-1} were 0.0021 and 0.0018, respectively, meaning that the highest gradient was observed for the trend-line of the 1080 cm^{-1} glucose peak. The R^2 and gradient values corresponding to the above glucose measurements are summarised in Table 4.6.

To identify which of the mean values of relative peak intensity within a dataset were statistically significantly different from others, a one-way ANOVA test was performed for both glucose peaks (1036 cm^{-1} and 1080 cm^{-1}) using the Statistics and Machine-Learning toolbox for Matlab (MathWorks Inc., USA). A multicomparison *post-hoc* test was then carried out using the the 'multicompare' function, also included in the Statistics and Machine-Learning toolbox, where the mean relative peak intensities at each particular concentration were compared with those at all other concentrations. This process enabled the determination of the LoQ. Figures 4.12 and 4.13 illustrate the multicomparison test for both glucose peaks, where the blue bar represents the comparison interval for a particular mean relative peak intensity group at the corresponding glucose concentration, which was selected for analysis. This process was repeated for each concentration to compare the relative peak intensities at all concentrations until the statistically significantly different one was determined. The group means with which the blue bar overlaps are shown in grey, meaning that these are not significantly different from each other, while the group means with which the blue bar does not overlap are shown in red, meaning that these groups are significantly different form each other. For the glucose peak at 1036 cm^{-1}, two examples are shown, where the first one (Figure 4.12a) shows the mean relative peak intensity at a concentration of 0.75 mM, which overlaps with all the lower concentrations and is only statistically different from the 1.5 mM, 3 mM and higher concentrations. For a more clear visualization of this analysis, and since all concentrations above 3 mM did not overlap, the concentrations above 3 mM were not included in the plots. The second example (in Figure 4.12b) shows that the mean relative peak intensity for the 1.5 mM concentration is significantly different from those of all other concentrations. Therefore, the LoQ for glucose using the peak at 1036 cm^{-1} was determined to be between 0.75 and 1.5 mM. This process was repeated for the glucose peak at 1080 cm^{-1}, shown in figure 4.13.

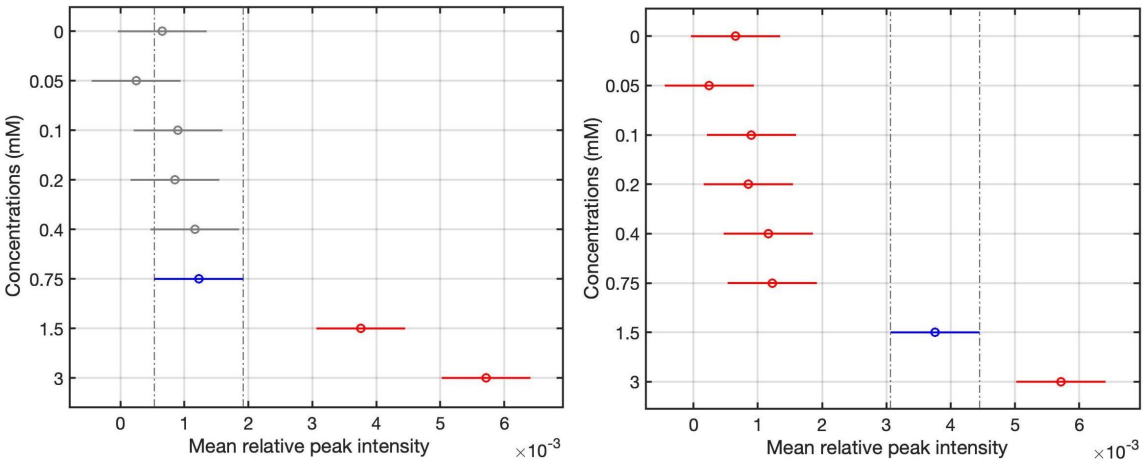

(a) (b)

Fig. 4.12 One-way ANOVA and multicomparison test for the glucose peak at 1036 cm^{-1}. (a) The mean relative peak intensity at 0.75 mM (blue bar) is not statistically significantly different to all those at lower concentrations (grey bars) but is statistically different from those at all higher concentrations. (b) The mean relative peak intensity at 1.5 mM (blue bar) is statistically significantly different to those at all other concentrations (red bars). The LoQ for the 1036 cm^{-1} glucose peak is between 0.75 and 1.5 mM. Note: the entire range of concentrations is not shown here for clarity.

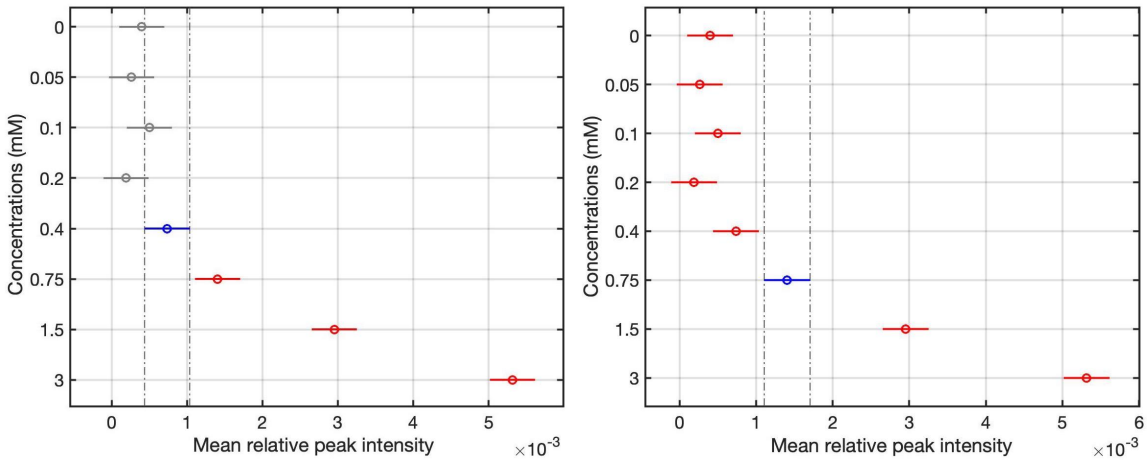

(a) (b)

Fig. 4.13 One-way ANOVA and multicomparison test for the glucose peak at 1080 cm^{-1}. (a) The mean relative peak intensity at 0.4 mM (blue bar) is not statistically significantly different to all those at lower concentrations (grey bars) but is statistically different from those at all higher concentrations. (b) The mean relative peak intensity at 0.75 mM (blue bar) is statistically significantly different to those at all other concentrations (red bars). The LoQ for the 1080 cm^{-1} glucose peak is between 0.4 and 0.75 mM. Note: the entire range of concentrations is not shown here for clarity.

Here, the mean relative peak intensities at a 0.4 mM glucose concentration overlapped with the ones at all concentrations below this one (Figure 4.13a) while the 0.75 mM glucose concentration was significantly different for all peaks (4.13b), and thus, the LoQ when using the 1080 cm^{-1} glucose peak, was determined as being between 0.4 and 0.75 mM. This means that, between the two peaks at 1036 cm^{-1} and 1080 cm^{-1}, the one which would provide a higher LoQ for glucose is the peak at 1080 cm^{-1}. The results of the multi-comparison *post-hoc* test are summarised in Table 4.6.

These overall results show the great capability of transmission-mode FT-IR for developing a continuous monitoring sensor for TBI patients, after the integration of microfluidics to allow a continuous flow of sample, and the determined LoQ for glucose (between 0.4 and 0.75 mM) shows that this method is potentially capable of detecting concentrations almost within the entire physiological range of glucose (0.1 - 24 mM), and probably also of lactate (0.1 - 24 mM), given their similar absorbance intensities. However, in order to conclude this, a study of mixture samples containing at least all three compounds of interest would have to be carried out. On the other hand, the physiological range of pyruvate (0.01 - 1.5 mM) is an order of magnitude lower than that of glucose and lactate, and the LoQ achieved here for glucose conveys that the detection of pyruvate using the method used in this chapter would be remarkably challenging. The LoQs obtained here were significantly higher that the LoQs achievable by the standard ISCUS Analyser (0.10, 0.20 and 0.016 for glucose, lactate and pyruvate, respectively). Therefore, alternative means for achieving increased sensitivities were explored and these will be later discussed in Section 4.6.

Table 4.6 Summary of results obtained for glucose measured using standard transmission-FTIR, namely: the R^2 value of the linear relationship between concentration and relative peak intensities; the gradient of the resulting line of best fit; and the LoQ within the range of analysed concentrations.

Compound	**Peak (cm^{-1})**	**Gradient, m**	**R^2**	**LoQ (mM)**
Glucose	1036	0.0021	0.995	0.75-3
	1080	0.0018	0.999	0.4-1.5

4.5.3 Conclusion

This section was aimed, essentially, at assessing the performance of standard transmission-mode FT-IR for the development of a sensor to continuously monitor the brain chemistry of TBI patients. Firstly, in order to optimize its performance, an optimum optical path-length for carrying out the measurements had to be selected. Different optical path-lengths within the

25 μm - 100 μm range were therefore tested to determine which of these would provide the best SNR, and thus, the most sensitive measurements. The path-length which provided the best results was 50 μm and was consequently used to perform the subsequent measurements, which included the study of the sensitivity and determination of the LoQ of glucose using transmission-mode FT-IR.

The LoQ for glucose was determined to be between 0.4 and 0.75 mM, which means that this method shows promising potential to provide enough sensitivity to almost cover the entire physiological range of glucose and potentially also of lactate (both between 0.1 - 24 mM), given their comparable absorbance intensities. However, since this study was only carried out for solutions of pure compounds, a study of mixtures including at least all three molecules of interest, would be essential to confirm this since an increase of complexity of the medium tends to decrease the accuracy of MIR-based measurements. Moreover, the detection of pyruvate, which is present at significantly lower concentrations in microdialysates (0.01 - 1.5 mM) compared to glucose and lactate, would remain a great challenge. A reason for this challenge is the limitation provided by the standard FT-IR light source, which does not provide sufficient intensity to enable the use of larger path-lengths. Increasing the path-length would enable a greater interaction with the analytes of interest, and thus yield higher sensitivities, but this is only possible if high-power light sources are used. Therefore, it was necessary to explore other light-source alternatives, such as Quantum Cascade Lasers (QCLs), which is the focus of Section 4.6.

4.6 Assessment of QCL-integrated microfluidics

In transmission-mode liquid MIR spectroscopy, the use of larger optical path-lengths increases the light-sample interaction, and therefore, should in theory lead to increased SNR and sensitivities. However, the transmission path-length is often limited, and needs to be selected, based on a trade-off between analyte absorbance signal and the noise level, as observed in the study of Section 4.5, where a standard light source was used. It is here where the use of high-power light sources, such as quantum cascade lasers (QCLs), can make a big difference. In recent years, the high spectral power density provided by QCLs (up to hundreds of mW/cm^{-1}) compared to that of an FT-IR spectrometer (in the range of μW/cm^{-1}) [89], has opened up access to the use of significantly increased optical path-lengths for transmission measurements and faster measurement times. While QCLs typically emit light at a single specific frequency, the increasing development of QCL technology has lead to the appearance of external cavity-QCLs (EC-QCLs), which combine a broad spectral tuning range with high spectral power densities [90]. Moreover, novel QCL technologies exhibit

laser elements of only several millimetres in size, which is a key feature for the development of a miniaturised sensor system [91].

This section focuses on investigating the use of a QCL system with integrated microfluidics for continuous monitoring of TBI patients. The initial aim was to purchase a QCL/EC-QCL and integrate it with in-house built microfluidics, either via direct transmission-mode or via fibre-optic coupling. One option would have been to optimise the work on fibre-optic coupled microfluidic devices carried out in Chapter 3, by coupling optical fibres to a QCL for increased sensitivities, which would potentially yield an ideal configuration for the application at stake. However, since the main priority of this work was to assess the feasibility of MIR spectroscopy for TBI patient monitoring, rather than to develop a system from scratch, a recent commercially-available EC-QCL system with an integrated microfluidic flow-cell for liquid analysis (ChemDetect Liquid Analyzer, Daylight Solutions Inc., USA) was purchased and thoroughly tested for its potential use in the continuous monitoring of the dynamic chemical changes in the brains of TBI patients. As a first step, a study on the relevant ChemDetect components (i.e. flow-cell) and parameters (i.e. flow-rate and averaging effect) was carried out. This was then followed by the selection of the optimum optical path-length as well as a sensitivity study, analogous to what was done in Subsection 4.5.2, but for all three compounds of interest, glucose, lactate and pyruvate, in order to determine the LoQ for each compound using ChemDetect.

4.6.1 Instrument operation and relevant components

The ChemDetect Analyzer is a compact and portable instrument which allows the continuous analysis and identification of chemical compounds within fluids and comprises, essentially, of a tunable QCL light source, a microfluidic flow-cell and a thermoelectrically-cooled InAsSb (indium arsenide antimonide) detector, as shown in Figure 4.14a. The emerging QCL beam is directed (via coupling optics and a mirror) into the flow-cell, where it interacts with a flowing sample, and the non-absorbed light is then directed into the detector, resulting in absorbance spectra for the sample. The QCL is broadly tunable within the MIR fingerprint region between 982 and 1258 cm^{-1}, and sweeps were made with 0.2 cm^{-1} steps, and averaged to 2 cm^{-1} resolution. A single sweep was taken in approximately 1 second, but several sweeps can be averaged for an increased SNR in the final spectrum (e.g. four sweeps result in a 5 second spectral acquisition). A cooling system (UC160-190, Solid State Cooling Systems, USA) was used in conjunction with ChemDetect to ensure temperature stability during measurements by recirculating a mixture of chilled water and liquid coolant (702 Liquid Coolant, Koolance, South Korea) in the bottom plate of the instrument via two rear

inlet/outlet connectors. The ChemDetect comes with its own software which allows for acquiring and saving measurements as well as controlling its operation.

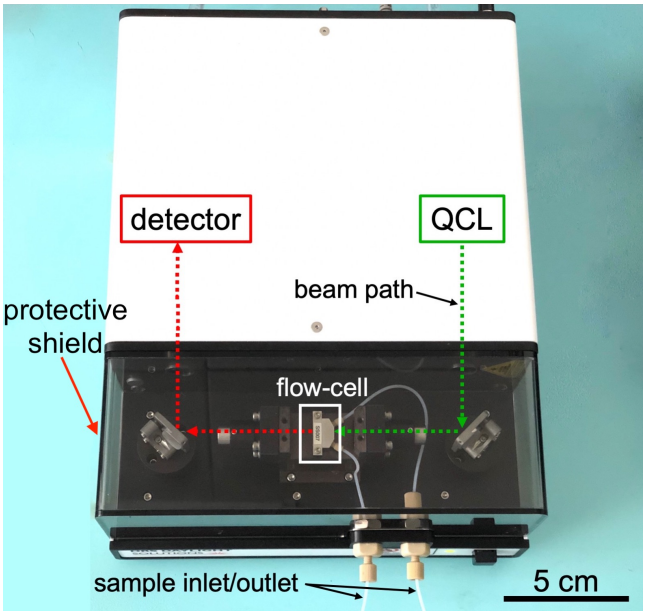

(a)

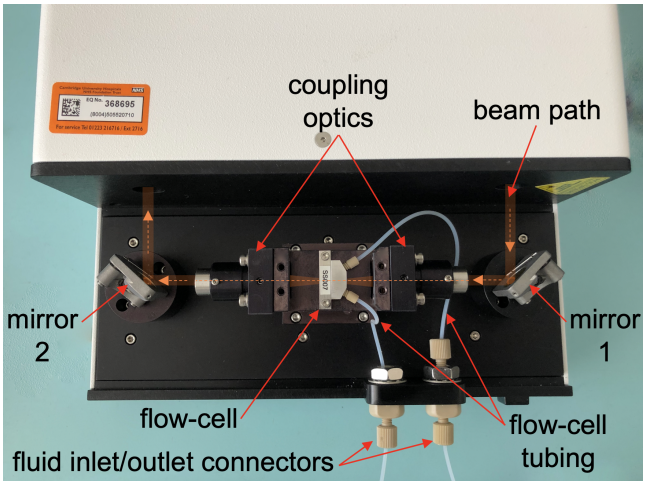

(b)

Fig. 4.14 (a) Image of the QCL-system (Chemdetect Analyzer), where the initial IR light beam (green line) emerges from the QCL and is directed into the sample-containing flow-cell where a portion will be absorbed, after which the remaining (non-absorbed) light (red line) is directed into the detector. Note: the positioning of QCL and detector are not exact. (b) Open sample compartment and its main components.

Sample compartment and flow-cell

The ChemDetect sample compartment is where the liquid samples flowing through the flow-cell are probed by the laser beam. During measurements, the sample compartment is enclosed by a protective shield which prevents interfering absorptions from atmospheric gases and which also contains a safety interlock, which stops the laser from operating when the shield is removed. Figure 4.14b shows the open sample compartment with all its components, including the flow-cell, its inlet/outlet tubing, and inlet/outlet connectors, and which contains the sample, as well as the coupling optics and turning mirrors, which guide the laser beam path, highlighted in the figure.

The flow-cell of ChemDetect is the centre of the sample interface and is shown in Figure 4.15. It has a small channel volume of 1 μL and a path-length which can be adjusted through the selection of different PTFE-gasket thicknesses. The gasket is sandwiched between the top and bottom pieces, which are assembled using alignment pins and attachment screws. The flow-cell incorporates two diamond windows through which the laser beam transmits to interact with the flowing sample. Inlet and outlet tubing are then connected to the flow-cell using appropriate connectors (M660 Nut and super flangeless M650 Ferrule for 1.6 mm OD tubing, Cole-Parmer Ltd., UK). The flow-cell is mounted into the sample compartment using alignment pins and attachment screws, and two coned 10-32 ports are used to connect external sample-carrying tubing to the ChemDetect, allowing the sample to enter/exit the inlet/outlet tubing of the flow-cell. The cell can easily be disassembled for cleaning and/or gasket changing if different optical path-lengths are required.

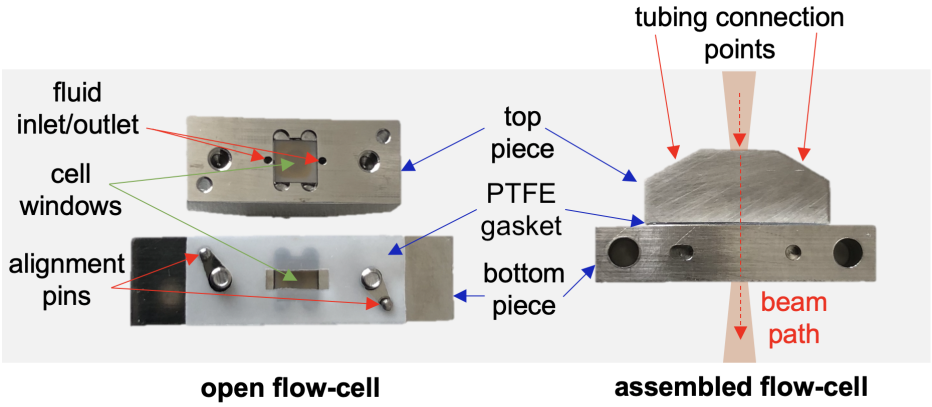

Fig. 4.15 ChemDetect flow-cell components. Open flow-cell showing the top and bottom halves of the cell with diamond windows and a fitted PTFE gasket (left side). Assembled flow-cell showing tubing connector points and laser-beam path (right side).

Sample injection and flow control

For the most accurate results, it is critical to connect the ChemDetect to a liquid system which provides a constant flow-rate and pressure. By simply injecting sample into the flow-cell, bubbles and pressure variations arise, making it challenging to generate accurate measurements. This setup also allows to flow solvent (i.e. PF) through the system for an accurate baseline acquisition before the introduction of the sample, and in between measurements if desired. This setup can be achieved in different ways, but in this work a precision dual-syringe precision pump (SPM 100, SIMTech Microfluidics Foundry, South Korea) was used to pump the fluid in conjunction with an auto-injector six-port valve (MVP, RS-232, Hamilton, USA). Figure 4.16 shows a diagram of the type of auto-injector used in this work, which presents two positions for operation. Two syringes are used for each set of measurements, where the first (syringe 1) contains the sample and the second (syringe 2) contains the solvent (e.g. PF). With the auto-injector in "load" position, syringe 1 introduces the sample into the sample loop, while syringe 2 injects the solvent directly into the flow-cell. When switched to "inject" position, solvent is injected into the end of the sample loop, where it sends a portion of sample into the flow-cell for analysis. The constant switching between solvent and sample means that, between each measurement, the flow-cell is cleaned out and a fresh baseline can be acquired. After the flow-cell, waste tubing directs the sample/solvent to a waste container.

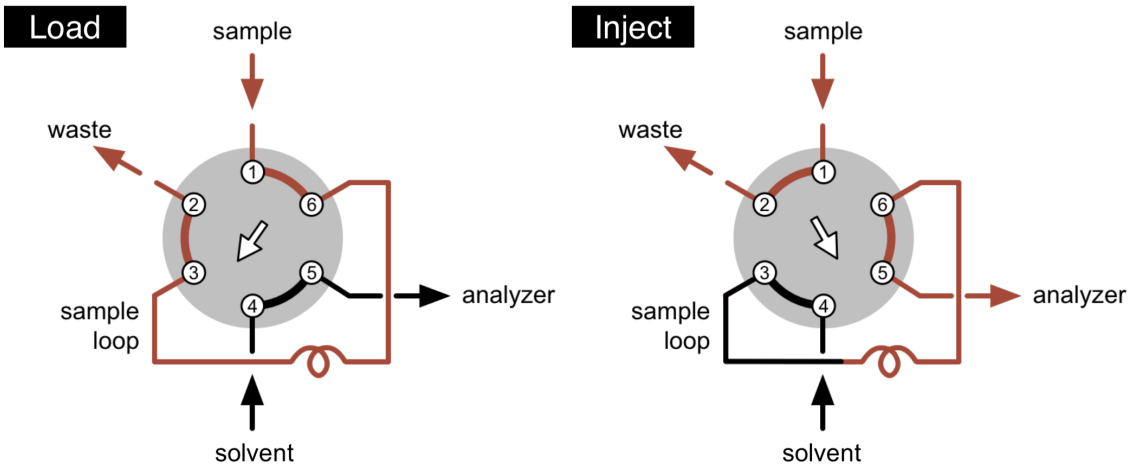

Fig. 4.16 Diagram of sample injector valve. With the valve in "load" position, sample flows through the external loop while the solvent flows directly to the flow-cell. When the valve is switched to "inject" position, the sample contained in the sample loop is injected into the flow-cell for analysis. Image adapted from VICI, Valco Instruments Co. Inc.

For cases in which the sample volume is very small and irreplaceable (i.e. patient microdialysate samples, approximately 10 μL), the samples can be introduced into the sample loop through manual withdrawal directly from the microdialysate vials using a small 1 mL volume syringe. This sample loop can then be carefully connected to syringe 1, now containing PF, so that it is pushed into the flow-cell when the auto-injector is in "inject" position. In this case, the syringe 1 is only activated once the auto-injector is in "inject" position so as to not lose the sample. This method ensures that one-off samples are not mistakenly lost. This method is used in Section 4.7 and Subsection 4.10.3 for the patient-sample measurements.

Fluid connections between the syringes, auto-injector and ChemDetect were made using syringe needles (27G, 305109, BD PrecisionGlide Needle, Becton Dickinson, USA), standard PEEK connectors (002122S Flat bottom Nut 1/16" and 008FTK16 PEEK-cased Ferrule 1/16", Kinesis, UK) and 1.6 mm outer diameter (OD) tubing. The flow-rate and sample loop volumes can be adjusted according to the particular need. For the majority of this work, 0.3 μm inner diameter (ID) tubing (PTFE, X53PT055, Diba, Sweden) was used, apart from certain pre-clinical tests and clinical studies where 0.15 ID tubing (18115659 PEEK tubing KIT 0.15 mm, 2m, GE Healthcare Life Sciences) was used for increased response time, as will be later discussed. The typical flow-rates used in this work are discussed in Subsection 4.6.2.

The auto-injector setup presented here was used for most measurements in this work, apart from those which require the use of the standard MD pump (P000127, CMA 107 Microdialysis Pump, M Dialysis AB, Sweden) in conjunction with the MD catheter, such as for the pre-clinical testing and clinical studies discussed in Sections 4.8 and 4.9. In these cases, a baseline of sterile PF is first acquired by flowing it through the ChemDetect flow-cell at the standard 0.3 μL min^{-1} flow-rate using the precision syringe pump, before the outlet of the MD catheter is connected to the flow-cell. Once a stable baseline is acquired, the outlet of the MD catheter is connected to the inlet of the flow-cell and the CMA 107 pump is activated to start the flow of sterile PF through the catheter and then into the flow-cell.

4.6.2 Parameter study: optical path-length, number of QCL sweeps and sample flow-rate

To achieve the best results when using the ChemDetect, it was necessary to carry out a study on the relevant adjustable parameters, such as the optical path-length, number of QCL sweeps and sample flow-rate, and select the optimised ones for our particular application.

Optimum optical path-length selection

Similarly to what was done for the path-length selection in Section 4.5, a study to determine the optical path-length which would yield the best SNR for detection of the compounds of interest using the ChemDetect was carried out. PTFE gaskets of different thicknesses were assembled in the flow-cell for each set of measurements. The available gasket thicknesses were: 76 μm, 127 μm, 152 μm and 200 μm, which are larger than the ones used for the transmission-FTIR measurements, given the increased spectral power density of the QCL light source. A 1.5 mM pyruvate solution in PF was prepared and used to test the different optical path-lengths. In this case, pyruvate was used as the test analyte, given its single unique peak in the available spectral range. For all absorbance spectra, a spectrum of pure PF was used as a background reference. The flow-rate was set to 10 μL min^{-1} on the syringe pump and spectra were acquired using an average of 25 sweeps. Figure 4.17a shows the absorbance spectra of 1.5 mM pyruvate for the different optical path-lengths and Figure 4.17b shows the SNR and relative absorbance peak intensity at 1176 cm^{-1} for the spectra at each path-length.

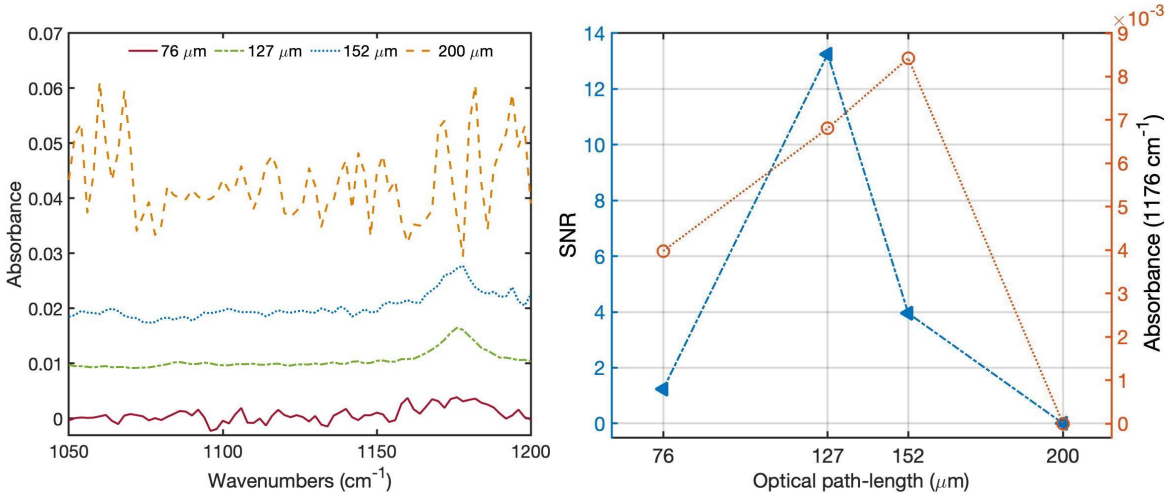

(a) (b)

Fig. 4.17 (a) Absorbance spectra of 1 mM pyruvate in perfusion fluid acquired using ChemDetect and different optical path-lengths: 76, 127, 152 and 200 μm, which are defined by PTFE gaskets of different thicknesses. Note: spectra plotted with a vertical offset for clarity. (b) SNR and relative absorbance peak-height at the 1176 cm^{-1} pyruvate peak corresponding to each path-length. The results obtained with a path-length of 127 μm showed the highest SNR.

The SNR and relative peak intensities were determined as previously described in Section 4.5, with the exceptions that the analysed peak was the specific pyruvate peak at 1176 $^{-1}$

and the baseline point was selected at 1200 cm^{-1} after an analysis of the spectra. From the analysis of the figures, it is clear that, although the highest relative peak intensity was seen for an optical path-length of 152 μm, the highest SNR was achieved for the 127 μm path-length. As previously observed, while an increase in path-length causes a linear increase in the analyte response, it simultaneously decreases the light power to a far greater degree due to water absorption. Therefore, all subsequent assessments and measurements were carried out using an optical path-length of 127 μm.

Number of sweeps and SNR

Due to the swept-wavelength operation of the QCL, its wavelength is rapidly swept over a broad bandwidth. One QCL sweep has a duration of $\approx$ 1 second and several sweeps can be averaged to achieved an increased SNR in the final spectrum. However, the larger the number of averaged sweeps, the longer the spectral acquisition times. Therefore, a study of the SNR and spectral acquisition time as a function of the number of sweeps was performed in order to determine the optimum number of sweeps for the highest SNR within an acceptable time-frame. For this study, a pure solution of 1 mM pyruvate in PF was measured on the ChemDetect system using a fixed path-length of 127 μm at several different averaged sweeps, from 1 to 160. Figure 4.18 shows the variation in SNR as well as the spectral acquisition times of each measurement of 1 mM pyruvate for increasing averaged sweeps.

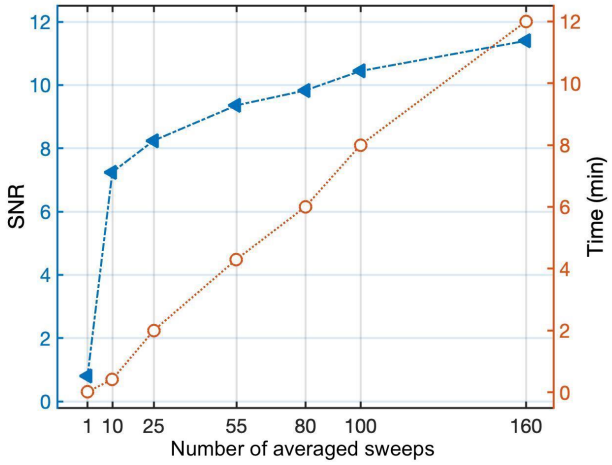

Fig. 4.18 SNR (left axis) and spectral acquisition times (right axis) for measurements of 1 mM pyruvate in perfusion fluid for increasing averaged sweeps.

It was seen that the SNR obtained for one sweep is low, but that increasing the number of averaged sweeps to 10 increases the SNR drastically, whilst maintaining a reduced acquisition time of approximately 48 s. It was also seen that beyond 10 averaged sweeps,

a further increase of number of sweeps does not cause significant changes in SNR, but significantly increases the acquisition time to beyond the requirements of the TBI monitoring system ($\leq$ approximately 5 minutes). Therefore, subsequent measurements were taken with a number of averaged sweeps between 10 and 80, depending on the nature of the measurements, ensuring that a sufficiently high SNR could be achieved under 6 minutes. While for some measurements, a higher SNR was paramount, for others (i.e. continuous monitoring), minimum acquisition times were prioritized.

Flow-rate study

Given the large number of measurements required for testing the ChemDetect system, it would be impractical and time-consuming to run all measurements at the cerebral micro-dialysis standard flow-rate of 0.3 μL min^{-1}. Therefore, the effect of the flow-rate on the absorbance was studied in order to determine which was the maximum flow-rate which could be used without affecting the absorbance measurements. For this, a baseline of PF was injected into the flow-cell at a 0.3 μL min^{-1} flow-rate after which the flow-rate was gradually increased up to 100 μL min^{-1}. The absorbance spectra at each flow-rate were acquired and the results were plotted in Figure 4.19. It is worth noting the scale on which this graph was plotted and that only pure PF is being measured, which explains the non-flat appearance of the baseline. It can be seen that above a 12 μL min^{-1} flow-rate, the absorbance baseline is significantly shifted upwards.

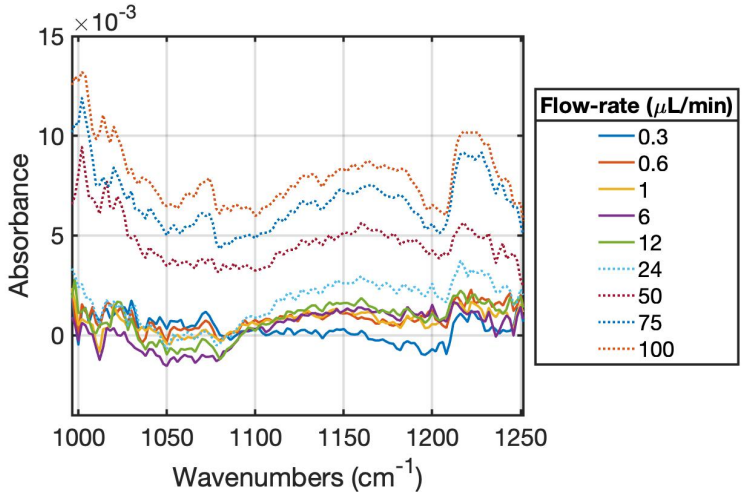

Fig. 4.19 Absorbance baseline variation with increasing flow-rates applied to the flow-cell.

This increase in absorbance is likely due to micro-expansions in the channel width, and thus, the optical path-length, caused by the increased pressure exerted on the flow-cell

windows. Therefore, for measurements which did not require a 0.3 μL min^{-1} flow-rate (i.e. primarily those which do not require the use of a microdialysis catheter or for testing the response time of the sensor), flow-rates between 0.3 and 10 μL min^{-1} were used.

4.6.3 Sensitivity study

To study the sensitivity provided by the QCL system for glucose, lactate and pyruvate, the same approach as in Subsection 4.5.2 was carried out. For this, pure samples of each compound in PF at known concentrations were prepared and measured, with an optical path-length of 127 μm, and each spectrum was generated from an average of 80 sweeps. The sample concentrations were selected to cover the physiological range of each compound (0.1-24 mM for glucose and lactate, 0.01 - 1.5 mM for pyruvate) and are listed in table 4.7. Lower concentrations of each compound were also measured to obtain more reference points for determining the LoQ and it was deemed unnecessary to measure high 24 mM concentrations as it would not provide useful information for the sensitivity study. The samples were injected into the flow-cell, as described in Section 4.6.1, and a baseline of PF was taken before and in-between measurements. Each sample was measured 3 separate times. The specific peaks used in this study were selected from those identified in Section 4.4.

Table 4.7 Concentrations of glucose, lactate and pyruvate used for the sensitivity study of the QCL system.

Glu (mM)	**Lac (mM)**	**Pyr (mM)**
0	0	0
0.02	0.02	0.005
0.05	0.05	0.01
0.1	0.1	0.02
0.2	0.2	0.05
0.4	0.4	0.1
0.75	0.75	0.15
1.5	1.5	0.2
3	3	0.4
6	6	0.75
12	12	1
-	-	1.5

Glucose

Figure 4.20a shows the absorbance spectra of the glucose concentrations including all repeats, where clear glucose peaks are observed at 1036, 1080, 1108 and 1152 cm^{-1}. As before, to avoid any slight vertical offsets, the spectra were normalised to a baseline point at 1180 cm^{-1}. The relative peak intensities were again calculated at each concentration for the glucose peaks at 1036 and 1080 cm^{-1} and analysed at each concentration, as shown in Figures 4.20b and 4.20c, respectively.

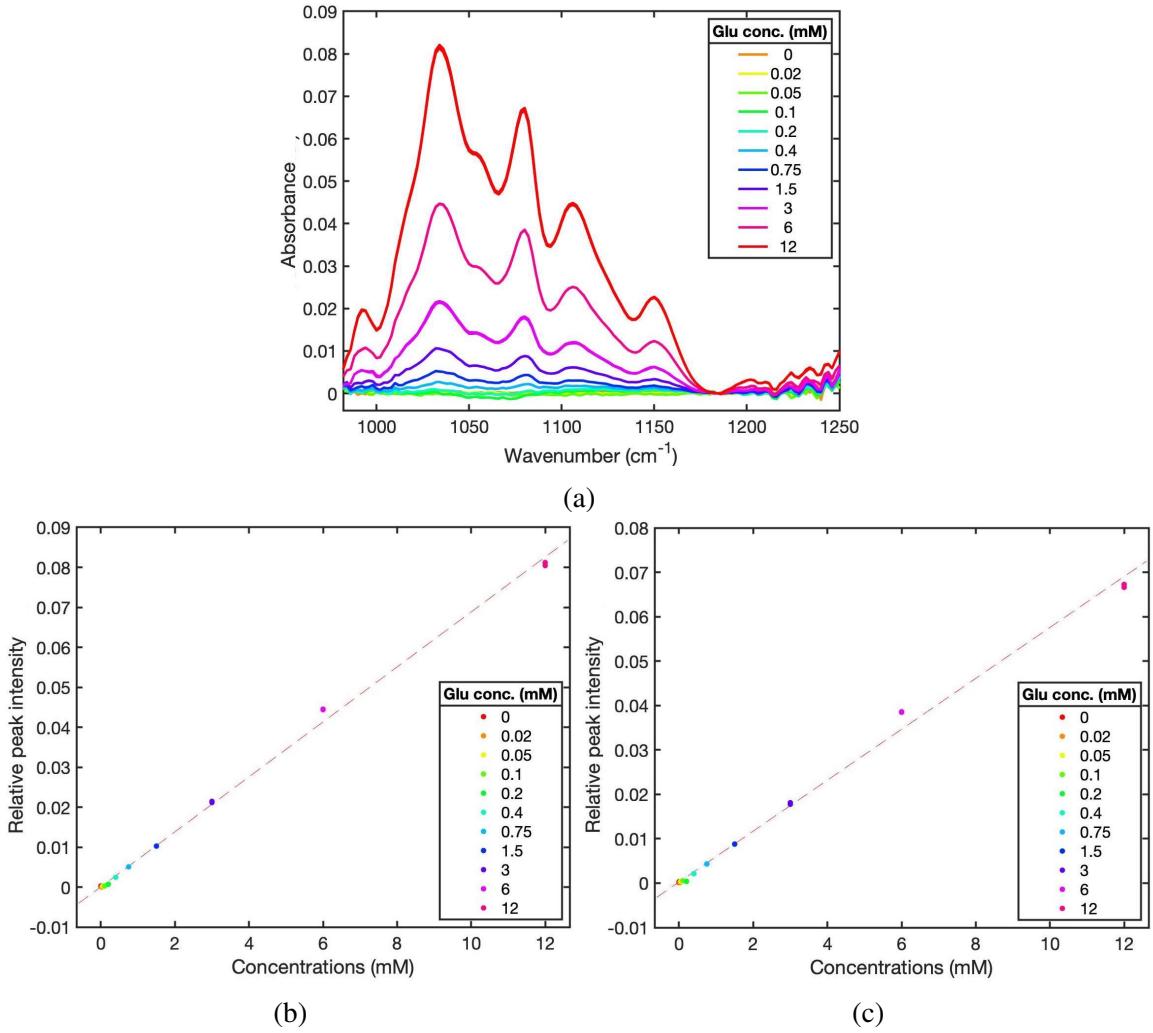

Fig. 4.20 (a) Absorbance spectra of glucose in perfusion fluid at clinically relevant concentrations, acquired using ChemDetect. Note: spectra normalised to a baseline point at 1180 cm^{-1}; (b) Relationship between different glucose concentrations and the corresponding relative peak intensities at 1036 cm^{-1} (R^2 = 0.998, m = 0.0069) and (c) 1080 cm^{-1} (R^2 = 0.996, m = 0.0057). The results of each repeat are included here.

From fitting the line of best fit to the data, the R^2 and gradient values were determined respectively as 0.998 and 0.0069 for the 1036 cm^{-1} glucose peak and as 0.0057 and 0.996 for the 1080 cm^{-1} glucose peak. The LoQs of glucose at each peak were then determined by comparison of the mean relative peak intensities at each concentration, via a one-way ANOVA test and multicomparison tests, as previously described in Subsection 4.5.2. The multicomparison tests for both glucose peaks at 1036 and 1080 cm^{-1} are illustrated in Figures 4.21 and 4.22, respectively.

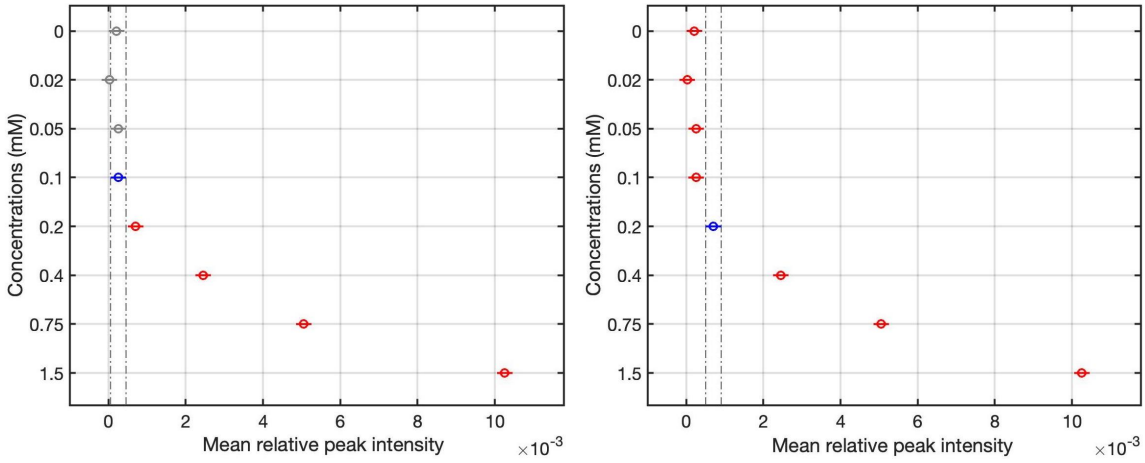

Fig. 4.21 One-way ANOVA and multicomparison test for the glucose peak at 1036 cm^{-1} using ChemDetect. The LoQ for the 1036 cm^{-1} glucose peak is between 0.1 and 0.2 mM. Note: the entire range of concentrations is not shown here for clarity.

Since it was clear that glucose was easily detectable up to 1.5 mM, the multicomparison tests were applied to the concentration range between 0 and 1.5 mM. The LoQs were determined between 0.1 and 0.2 mM for the 1036 cm^{-1} peak and between 0.2 and 0.4 mM for the 1080 cm^{-1} peak. Contrary to what was seen for the transmission-FTIR glucose measurements, the LoQ obtained for the 1036 cm^{-1} peak was greater than the LoQ achieved for the 1080 cm^{-1} peak. This could be expected given the larger absorbance of the 1036 cm^{-1} peak, and that in this case, potential interference from ZnSe windows is irrelevant. This same process was applied for determining the R^2, gradient and LoQ for lactate and pyruvate, and therefore a description of the process will not be repeated.

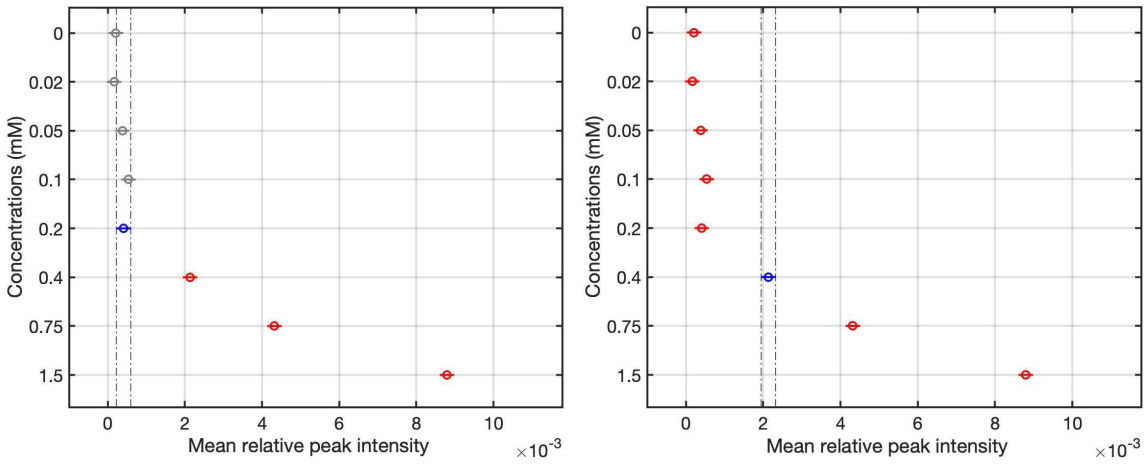

(a) (b)

Fig. 4.22 One-way ANOVA and multicomparison test for the glucose peak at 1080 cm^{-1} using ChemDetect. The LoQ for the 1080 cm^{-1} glucose peak is between 0.2 and 0.4 mM. Note: the entire range of concentrations is not shown here for clarity.

Lactate

The absorbance spectra for the lactate concentrations including all repeats are shown in Figure 4.23a, where the lactate peaks at 1042, 1086 and 1124 cm^{-1} are clearly visible.

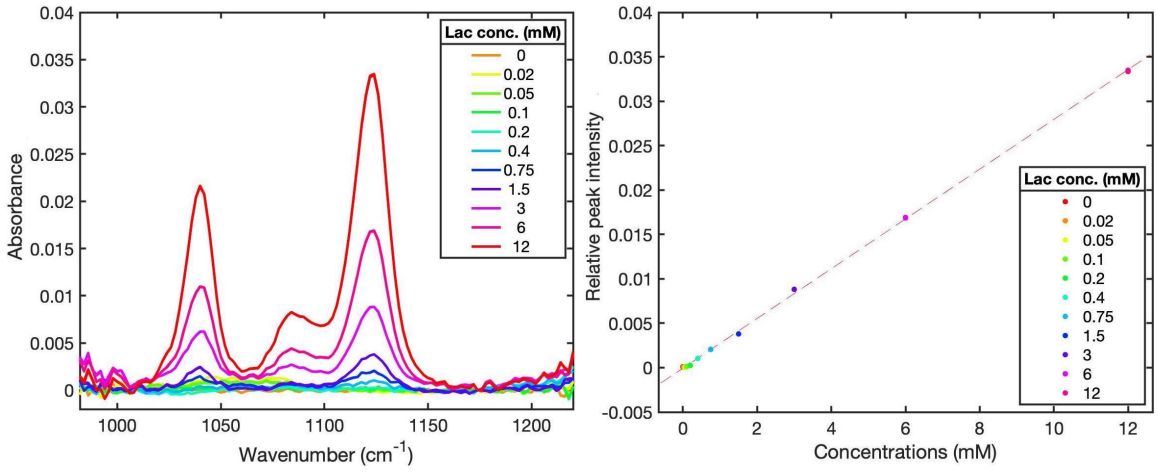

(a) (b)

Fig. 4.23 (a) Absorbance spectra of lactate in perfusion fluid at clinically relevant concentrations, acquired using ChemDetect. Note: spectra normalised to a baseline point at 1200 cm^{-1}; (b) Relationship between different lactate concentrations and the corresponding relative peak intensities at 1124 cm^{-1} ($R^2 = 0.999$, $m = 0.0028$). The results of each repeat are included here.

The spectra were normalised to a baseline point at 1200 cm^{-1} and the relative peak intensities were determined at each lactate concentration for the most prominent peak at 1124 cm^{-1}, as shown in Figure 4.23b. From here, the R^2 and gradient were extracted as 0.999 and 0.0028 respectively. The multicomparison test for the lactate peak is illustrated in Figure 4.24, where the mean relative peak intensity corresponding to the 0.1 mM concentration overlaps with those corresponding to the 0.02 and 0 mM concentrations. The mean relative peak intensity corresponding to the 0.2 mM concentration, however, does not overlap with any of those corresponding to other spectra and therefore was determined as statistically significantly different. The LoQ of lactate therefore lies between 0.1 and 0.2 mM.

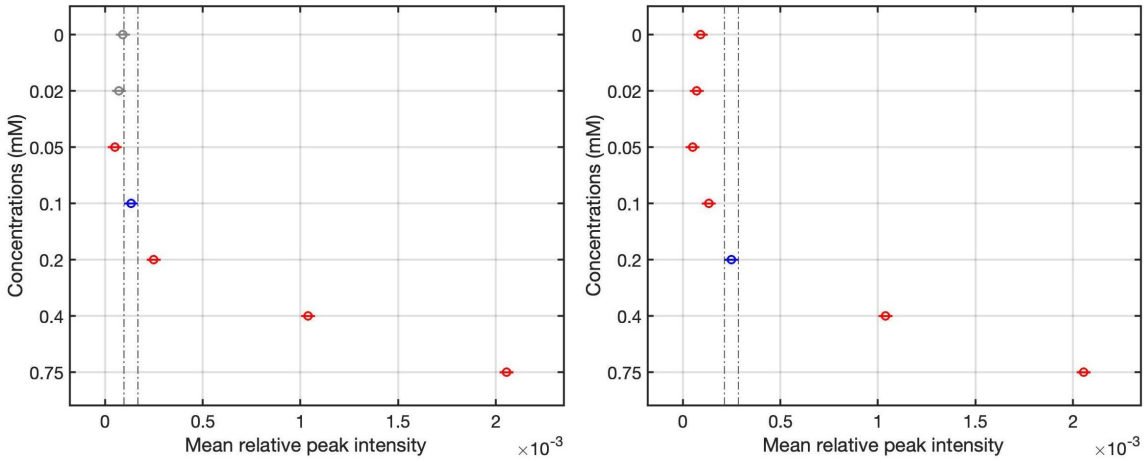

Fig. 4.24 One-way ANOVA and multicomparison test for the lactate peak at 1124 cm^{-1} using ChemDetect. The LoQ for the 1124 cm^{-1} lactate peak is between 0.1 and 0.2 mM. Note: the entire range of concentrations is not shown here for clarity.

Pyruvate

The absorbance spectra for pyruvate, including all repeats, are shown in Figure 4.25a, where the only pyruvate peak in the QCL's tunable range is visible at 1176 cm^{-1}. All spectra were normalised to the selected baseline point at 1200 cm^{-1} and Figure 4.26 shows the calculated relative peak intensities corresponding to each concentration. From applying a linear fit, the R^2 and gradient for the 1176 cm^{-1} pyruvate peak were determined as 0.994 and 0.0058, respectively. From the one-way ANOVA test and multicomparison analysis illustrated in Figure 4.26, the pyruvate exhibits a LoQ between 0.2 and 0.4 mM.

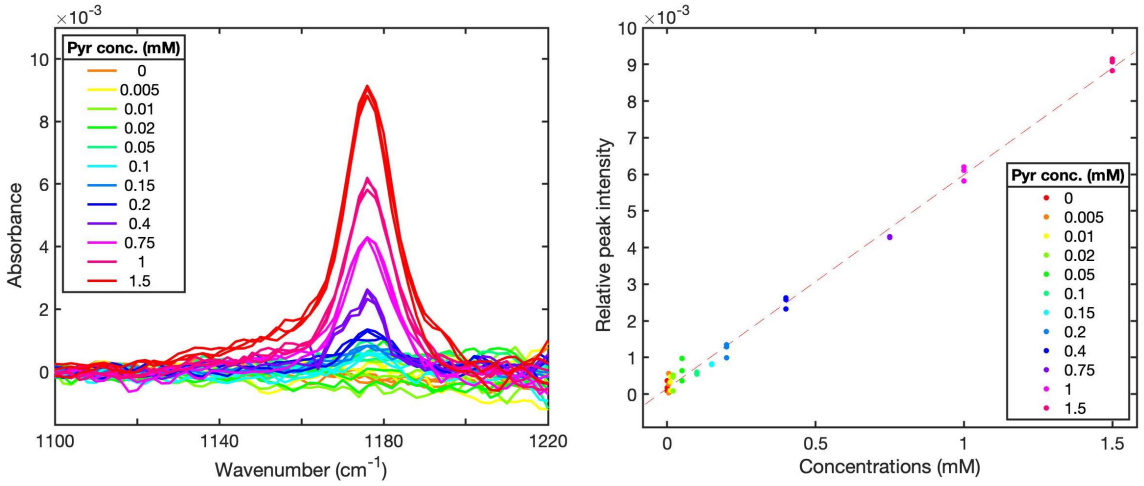

(a) (b)

Fig. 4.25 (a) Absorbance spectra of pyruvate in perfusion fluid at clinically relevant concentrations, acquired using ChemDetect. Note: spectra normalised to a baseline point at 1200 cm^{-1}; (b) Relationship between different pyruvate concentrations and the corresponding relative peak intensities at 1176 cm^{-1} (R^2 = 0.994, m = 0.0058). The results of each repeat are included here.

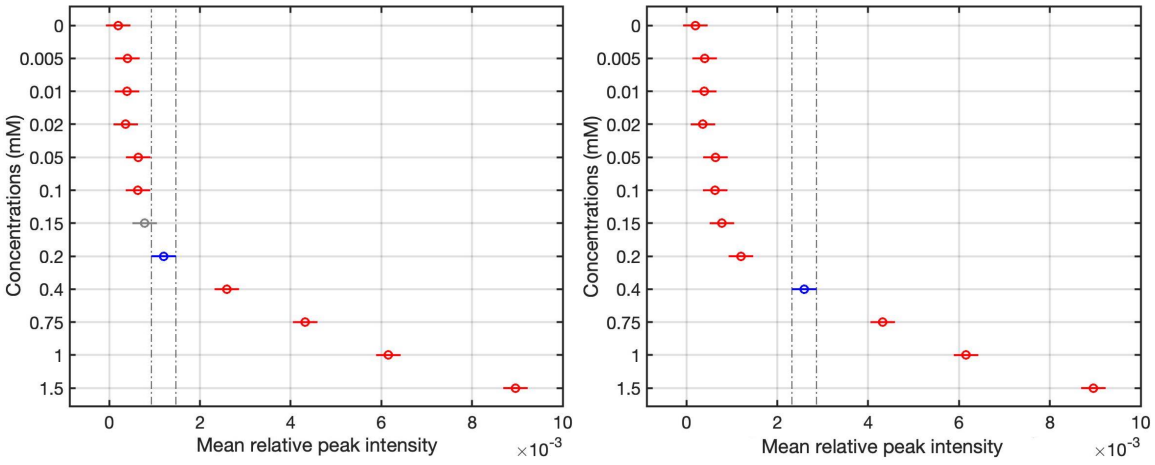

(a) (b)

Fig. 4.26 One-way ANOVA and multicomparison test for the pyruvate peak at 1176 cm^{-1} using ChemDetect. The LoQ for the 1176 cm^{-1} pyruvate peak is between 0.2 and 0.4 mM. Note: the entire range of concentrations is not shown here for clarity.

Summary

All the determined R^2, gradient and LoQ values for all three compounds are summarised in Table 4.8. The R^2 values for all peaks of all compounds reflected a high linearity between

the relative peak intensities and varying concentrations. The lowest R^2 value was seen for pyruvate, which was likely due to the smaller concentrations measured for this compound, respective to its presence at physiological levels. The gradient for the lactate peak was approximately half of the gradient values seen for both glucose peaks, which was probably due to its weaker absorbance for the same concentrations. Moreover, the gradient obtained for the pyruvate peak, measured at lower concentrations, was comparable to those obtained for glucose, which was promising. The LoQs obtained using the ChemDetect are far superior to those obtained using standard transmission-FTIR. In the case of glucose and lactate, the achieved LoQs allow for coverage of the entire physiological range and are comparable to the LoQs provided by the standard ISCUS Analyser (0.10 mM for glucose and 0.20 mM for lactate). While the LoQ obtained for pyruvate is not quite sufficient to quantify concentrations within the lower end of its physiological range (0.01-0.15 mM) and is almost an order of magnitude larger than that provided by the ISCUS Analyser (0.016 mM), it is able to detect concentrations above 0.2 mM, which will still yield valuable information.

Table 4.8 Summary of results obtained for each compound using the QCL-system, namely: the R^2 value of the linear relationship between concentration and relative peak intensity; the gradient of the resulting line of best fit; and the LoQ within the range of analysed concentrations.

Compound	**Peak (cm^{-1})**	**Gradient, m**	**R^2**	**LoQ (mM)**
Glucose	1036	0.0069	0.998	0.1-0.2
	1080	0.0057	0.996	0.2-0.4
Lactate	1124	0.0028	0.999	0.1-0.2
Pyruvate	1176	0.0058	0.994	0.2-0.4

4.6.4 Conclusions

This section was aimed at assessing and optimising the performance of a QCL-based microfluidic system (ChemDetect Analyzer) for detection of glucose, lactate and pyruvate in a physiological range. After a thorough analysis of the system hardware, components and operation, several parameters, such as the optical path-length, number of averaged sweeps and sample flow-rate, were studied and optimised for our particular application. It was found that the optimum path-length to be used in this study was 127 μm, while the number of averaged sweeps should be applied between 10 and 80 for a good trade-off between SNR and acquisition time. Moreover, it was found that flow-rates larger than 12 μL min^{-1} should be avoided and that they should be kept between 0.3 and 10 μL, depending on the specific experimental

needs. The sensitivity study, performed for all three compounds, confirmed that the use of a QCL-based system yields far better results that the standard transmission-FTIR, as expected. By comparing the R^2, gradient and LoQ values obtained for glucose using transmission-FTIR with those obtained using ChemDetect (see Tables 4.6 and 4.8), it was evident that all the values obtained with the QCL system were superior, meaning that significant improvements in sensitivity could be achieved due to the higher spectral power density allowed by the QCL and, thus, larger path-lengths. While the detection of glucose and lactate was possible in their entire physiological range, the detection of pyruvate below 0.2 mM remains a challenge although further improvements and increased acquisition times may enable this in future. Although this study was a critical part of the study and by itself conclusive, the translation of the QCL system to clinical microdialysate sample measurements is likely to affect the values obtained here to some extent since it will involve complex samples, and thus, potential compound interference. The study of patient microdialysate-samples will be discussed in Section 4.7.

4.7 Discrete clinical-sample measurements

As mentioned throughout this Chapter, the current microdialysate analyser (ISCUS Flex), measures the different concentrations of glucose, lactate and pyruvate, via enzymatic assays, and requires a particular amount of sample volume (minimum 10 μL) in order to do so. The required amount of microdialysate is generated approximately every hour, and thus, the current method only allows hourly readings at best. In cases where the samples cannot be immediately transferred to the analyser (e.g. if the NCCU is under-staffed, or during a critical situation with another patient), these readings may only happen every several hours. Microdialysis samples, taken consecutively from the same patient in intervals of approximately 1 hour, were collected for subsequent measurement on both the ISCUS Flex and ChemDetect Analyzer. The first question to be answered from this study was whether the previously identified compound-specific peaks (in Section 4.4) were clearly visible in spectra obtained from more complex cerebral microdialysates and if any of these peaks could be detected directly from the spectra. The second question was related to the extent of the spectral changes between each consecutive measurement and over longer time-periods. Analysing the data from one patient was thought to be a first step towards gaining further insight on these aspects. Since the ISCUS Flex requires the entire sample volume provided by one vial, approximately 3 (sometimes 4) consecutive samples were pooled together to achieve sufficient volume for measurements on both instruments, yielding a total of 16 samples. These were then split equally into two separate vials: one to be measured on the

ISCUS and the other to be measured on the ChemDetect. All samples were labelled in consecutive order and immediately frozen at -75^{o}C until just before measurements. Both sets of measurements were carried out simultaneously in order to avoid any discrepancies between identical samples, for instance, due to sample evaporation. The ISCUS Flex measurements were carried out by Dr Susan Giorgi-Coll. MIR absorbance spectra were acquired on the ChemDetect, as described in Section 4.6.1 for small sample volumes, using a 127 μm path-length and 80 averaged sweeps.

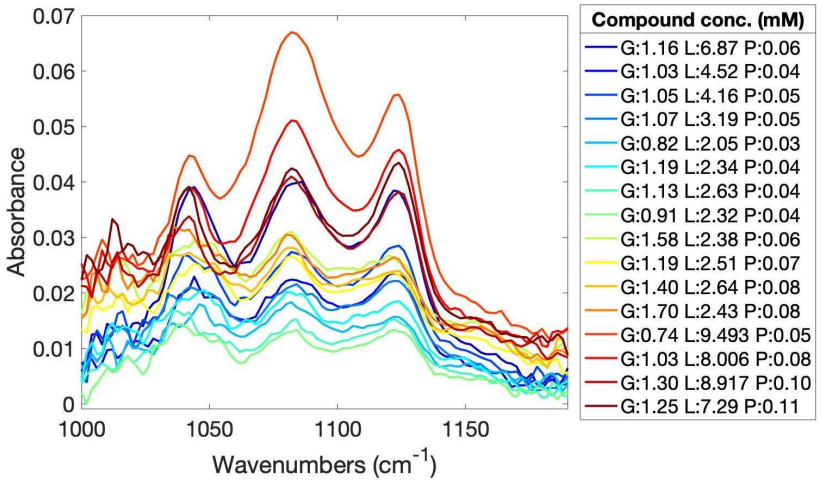

(a)

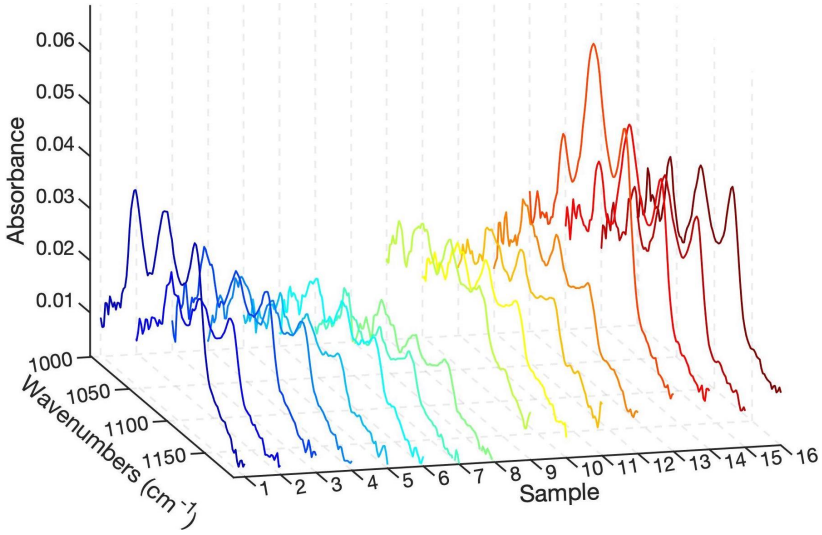

(b)

Fig. 4.27 (a) Absorbance spectra of 16 consecutively pooled clinical samples and corresponding compound concentrations for each sample, measured separately on the standard microdialysate analyser (ISCUS Flex); (b) Observed spectral changes between consecutive clinical samples over a period of approximately 48 hours. As a result of sample pooling, each spectrum corresponds to the average concentration over approximately 3 hours.

Figure 4.27a shows the spectra from all 16 samples as well as the corresponding concentrations of each compound obtained from the ISCUS Flex analysis. Three strong peaks were observed in all spectra at 1042 cm^{-1}, 1080 cm^{-1}, and 1124 cm^{-1}. An immediate analysis suggests that these correspond to the C-O stretches of lactate (1124 cm^{-1} and 1042 cm^{-1}) and glucose (1080 cm^{-1}). However, since the glucose peak at 1080 cm^{-1} is prominent compared to its usually stronger peak at 1036 cm^{-1}, which is not seen in the spectra, it is possible that there is a large contribution from the weak lactate peak at 1086 cm^{-1}. The fact that the lactate concentrations in these particular samples are far greater than those of glucose also contributes to this assumption. Moreover, it was seen previously in Section 4.4 that, when glucose and lactate are present in equimolar concentrations, the glucose and lactate peaks at 1036 cm^{-1} and 1042 cm^{-1} respectively, result in a mixture peak at 1038 cm^{-1}, which is not the case for these samples.

Given the exceptionally low concentration of glucose compared to lactate in this particular case, it was possible to assume that the changes in the main lactate peak at 1124 cm^{-1} may reflect the actual concentration changes during this time-period. To verify this, the lactate relative peak intensities at 1124 cm^{-1} and the lactate concentrations provided by the ISCUS flex for each sample were plotted against each other, as shown in Figure 4.28.

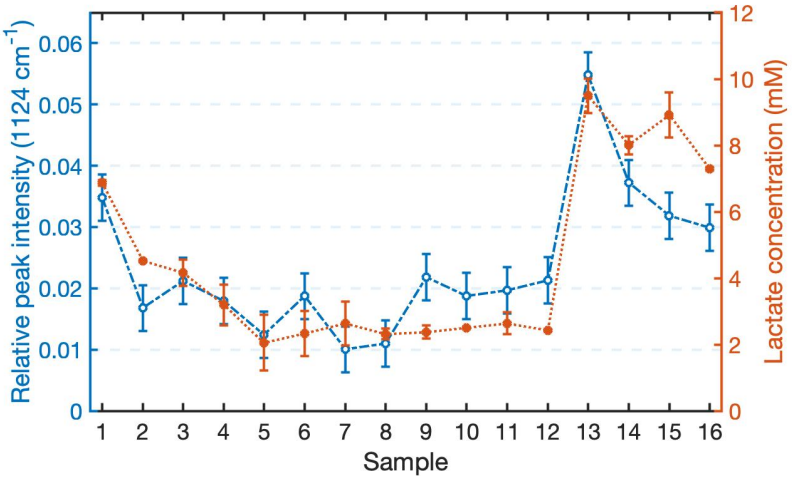

Fig. 4.28 Correlation between relative lactate peak intensities at 1124 cm^{-1} and corresponding lactate concentrations (measured on the ISCUS flex Analyser) for each consecutive sample. Error bars of relative peak intensities reflect the spectral baseline average noise level while the error bars for the lactate concentrations reflect the standard deviation for each measured concentration provided by the ISCUS Flex.

Although this was a crude comparison, and only possible given the comparably low glucose concentrations, one can observe a clear correlation between the lactate absorbance

peak changes with the lactate concentration changes. While the measured spectral range covers the region of the strong specific pyruvate peak at 1176 cm^{-1}, such a peak was not observed in any of the spectra, due to its very low concentration in comparison to glucose and lactate, and also to its LoQ between 0.2-0.4 mM using the ChemDetect, as determined previously.

Figure 4.27b shows the 16 samples in consecutive order (as they were collected and pooled), which reflect the chemical concentration changes in the brain over a period of approximately 48 hours. Since each sample results from a mixture of around 3 consecutive samples, these measurements actually represent an average concentration over a 3 hour period, rather than a particular concentration at a specific time point. This means that any significant and spontaneous change in any of the metabolites were averaged and therefore not identifiable. This same logic applies to samples collected over 1 hour, where only the slow global changes are seen and any rapid compound concentration change or spike occurring within that hour will be filtered out. Even with this being the case and bearing the latter in mind, the spectra showed notable changes over time, which indicates that there were significant dynamic changes in the patient's brain chemistry.

4.7.1 Conclusions

This section has shown that a MIR QCL-based system has great potential to be used to detect compounds of interest within clinical microdialysis. While compound specific peaks were identifiable from the spectra, given the concentration disparities in this case, the spectral interference between compounds (particularly glucose and lactate) when they are at similar concentrations will not allow direct spectral identification, and therefore, compound quantification should be carried out by the implementation of multivariate-analysis methods. Although the detection of pyruvate was not feasible in this instance, given its presence in the measured microdialysates at concentrations below its previously determined LoQ using the specified QCL system, concentrations above its LoQ should be detectable in microdialysates and there may be room for system alterations and improvements or further data processing which could enable its detection. Finally, the discrete analysis of samples collected over one or more hours (as is done in classical microdialysis monitoring) translates into the loss or dampening of any variations that may occur between these consecutive measurements, meaning that only the global changes over one or more hours are monitored, which is unfavourable and insufficient for optimal patient management and treatment. This fact points once again towards the great potential benefit of continuous monitoring, which will be discussed in the following sections.

4.8 System optimisation and clinical simulation

Before carrying out clinical studies using this novel continuous microdialysate monitoring technique, it was crucial to first assess the QCL-system in performing continuous microdialysate monitoring in conjunction with the clinically used standard microdialysis catheter and pump. Moreover, it was vital to study and address issues which may arise during patient monitoring, as well as to gain a better understanding of required sensor performance in the NCCU. The main aspects studied in this section were the following:

1. The response time (time between sampling and analysis);
2. The continuous monitoring performance and detector stability over extended periods of time (i.e. several hours/days);
3. Compound relative recovery (described in Subsection 4.2.1.1: discrepancy between compound concentration in the microdialysate and the actual concentration inside the medium of interest, i.e. artificial ECF).

4.8.1 Laboratory setup

In order to study each of the above aspects with the highest precision, a laboratory setup was created to mimic clinical monitoring, as shown in the schematic and image of Figure 4.29. Here, an external standard (ES) solution (i.e. artificial extracellular brain fluid) was prepared using PF with 5 μg/mL human serum albumin (HAS, 126658, $\geq$ 95%, Sigma Aldrich) and 0.05 % w/v sodium azide (S2002, $\geq$ 99.5%, Sigma Aldrich) (optional)[†] to make a total solution of approximately 15-20 mL, which was added to a 50 mL falcon tube. Depending on the nature of the experiment, a desired amount of any or all metabolites (glucose, lactate and pyruvate) at physiological concentrations can be added at the beginning or throughout the experiment in order to track changes. A small magnetic stirrer was added to the ES in the falcon tube, after which a 20 cm^2 of cling film was folded into a 4-layer square and used to cover the top of the open tube, secured by a rubber band. The cling film was then gently pierced and a standard triple-bolt (Integra Neuroscience, Plainsboro, NJ, USA) typically used to connect the monitoring probes/catheters to patients was inserted into the pierced hole so that it sat firmly suspended in the cling film and aligned with the top lip of the centrifuge tube. A bench-top stand and clamp were used to hold the falcon tube within a glycerol (G9012, $\geq$ 99.5%, Sigma Aldrich) bath on a thermostatically-controlled hotplate-stirrer (97042-754,

[†]Depending on the duration of the experiment, sodium azide can be used as a preservative for preventing microbial growth in the buffer.

VWR, USA) at 37^{o}C, with the stirrer speed set to 60 rpm. A standard MD catheter (8010320, CMA 71 High Cut-Off Brain Microdialysis Catheter, M Dialysis AB, Sweden), with 100 kDa MWCO and a 10 mm membrane length was placed into the ES through the triple bolt.

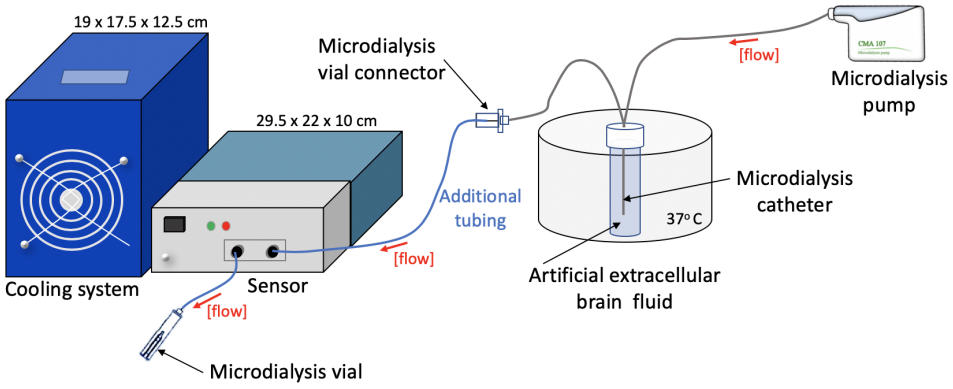

(a)

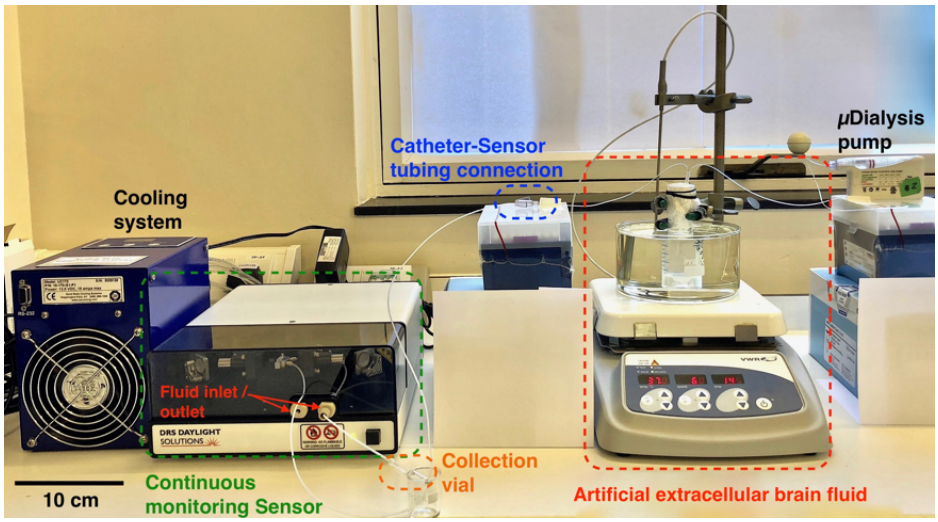

(b)

Fig. 4.29 (a) Schematic diagram of laboratory setup used to assess QCL-system performance prior to clinical studies; (b) Image of laboratory setup.

While up to three catheters can be inserted into the ES simultaneously, the experiments in this study only required one catheter at a time. The catheter inlet tubing was connected to a standard MD pump (P000127, CMA 107 Microdialysis Pump, M Dialysis AB, Sweden) with a syringe loaded with 1.5 mL PF, which perfused fluid through the catheter at the CMD standard flow-rate: 0.3 μmL/min. It was found that exceeding 2 mL PF in the syringe may cause the pump to fail and best pump performance was achieved with 1.5 mL or less. The catheter outlet tubing was connected to the inlet tubing of the flow-cell of the ChemDetect using specified tubing and connectors, as later described in Subsection 4.8.2. Once the pump,

catheter and flow-cell were connected, masking tape was used to tape down the tubing in certain locations to keep it in place during measurements. Since the sample is not consumed during measurements, it can be re-used for further analysis if desired. For this, standard MD vials can be added to sensor outlet tubing by making a small (approx. 1.6 mm) hole in the vial rubber stopper and threading through a few millimetres of tubing for a snug fit. The outlet sample can then be collected and stored (at -75 ^{o}C) for future analysis.

4.8.2 Response time

One of the most important aspects in TBI monitoring is to detect brain-chemistry changes as quickly as possible. Therefore, the time response of the sensing system is critical. Since the QCL-system acquisition time is only a few seconds, here, the response time refers to the time it takes for the sample to reach the sensor from the moment it leaves the catheter outlet. The time delay between sampling and analysis depends mainly on two factors: (1) the perfusate flow-rate; and (2) the dimensions (ID and length) of the tubing used to connect the MD catheter outlet to the sensor. The standard CMD flow-rate of 0.3 μL min^{-1} is well established and any increase would result in a decreased concentration of metabolites in the microdialysate, which in turn is harder to detect. Therefore, the only option to decrease the response time is to minimise the tubing dimensions. One straightforward approach to minimise the length of the tubing would be miniaturisation of the sensing system so that it can sit as close to the patients' head as possible (i.e. on the pillow). However, the QCL-system being tested here was not small enough to be placed on the patients' bed and therefore needed to be placed on a bedside trolley. Since sensor miniaturisation was beyond the scope of this work, focus was drawn towards using tubing with the smallest possible ID and positioning the sensor as close as possible to the catheter outlet. A safe distance from catheter outlet to the sensor inlet was established at 40 cm, although slightly longer tubing (up to 60 cm) may be required in instances where the sensor trolley has to sit further away from the patient in the NCCU (i.e. due to other clinical equipment or frequent clinical intervention), although a minimum distance was always aimed for.

Initially, a 40 cm segment of the 0.3 mm ID tubing was used to connect the MD catheter outlet, directly to the sensor inlet, as it was readily available. This was done by slight modification of the piece that is traditionally used as the vial holder of the catheter, where its plastic ends were bent back or removed in order to slide the tubing directly onto the catheter outlet needle, as shown in Figure 4.30a. Great care must be taken here to ensure that the needle does not puncture or get stuck in the tubing. However, after a first round of experimentation, it was realised that using a 40 cm tubing of 0.3 mm ID in combination with a 0.3 μL min^{-1} flow-rate would yield a time response of approximately 1.5 hours,

which is far greater than what would be required. Therefore, since the tubing cannot be shortened further and without sensor miniaturisation, the remaining option was to decrease the tubing ID. The tubing with the smallest ID available was a 0.15 mm ID PEEK tubing (18115659, 1/16", GE Healthcare Life Sciences, UK). Given the smaller ID, this tubing could not be directly connected to the MD catheter outlet and so it was used in conjunction with a small segment (3 - 4 cm) of 0.3 mm ID tubing (to connect the catheter needle), along with a 3-piece connector (742 Union ZDV PEEK 10-32, 1/16", 0.01" Thru-hole, Kinesis, UK), of 0.07μL internal volume, which allows the connection of tubing of the same OD (1/16") but different ID. The connection between the 0.15 mm ID and 0.3 mm ID tubing, and subsequent connection to the MD catheter outlet is shown in Figure 4.30b. The substitution with smaller tubing would result in a response time of approximately 29 minutes (taking into account the internal volume of the adaptor and the segment of 0.3 mm ID tubing). To achieve a total length of 40 cm, 30 cm of 0.15 mm ID tubing was used in conjunction with the 4 cm of 0.3 mm ID tubing and the 6 cm adaptor. Although the sensor is able to acquire readings every few seconds, the response time of the sensor system used here was limited by the connector-tubing dimensions since it had to be placed on a bedside trolley. Therefore, with the current QCL-system, the minimum achievable response time would be approximately 29 minutes. However, future work may focus on methods for speeding up the sample flow to the sensor and/or sensor miniaturisation for placement as close to the patient as possible.

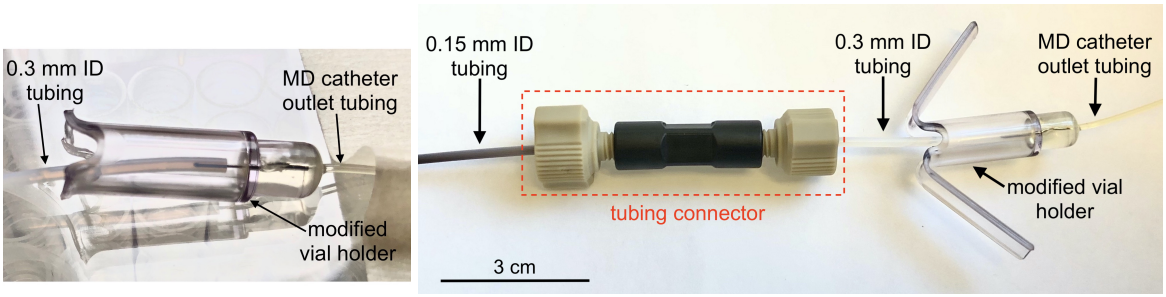

(a) (b)

Fig. 4.30 Connection from MD catheter outlet to sensor system inlet. (a) Direct connection with 0.3 mm ID tubing; (b) Connection with 0.15 mm ID tubing (in conjunction with 0.3 mm ID tubing and a 3-piece tubing connector) to improve response time.

4.8.3 Continuous monitoring of chemical changes in artificial extracellular brain fluid

In this section, the continuous monitoring performance of the sensor in conjunction with the MD catheter and pump was assessed. For this, two main experiments were carried out. The

first was to assess the continuous monitoring performance and stability over several days in order to determine any potential issues, such as unexpected spectral changes or shifts and whether a routine calibration of the detector would be required. The second was to monitor the spectral changes corresponding to analyte concentration in the artificial brain ECF and to study the profile of these changes over time. Both experiments were performed by following the laboratory setup and methods described in Section 4.8.1, where the initial concentration of compounds in the artificial ECF before measurements was 0 mM. The MD catheter was perfused with sterile PF (CNS perfusion fluid, CMA Microdialysis AB, Solna, Sweden) using the standard MD pump, which performs an automatic 5-minute flush cycle at 15 μL min^{-1} once its lid is closed, followed by an automatic decrease to the standard operation rate of 0.3 μL min^{-1}. A baseline spectrum of the sterile PF was taken immediately after the flush cycle, which was used for baseline subtraction in the subsequent spectra.

The first experiment started with 14 hours of continuous monitoring of artificial ECF with no compounds added, where only baseline spectra were acquired. After 14 hours, glucose and lactate were added to the artificial ECF, to achieve a concentration of 5 mM of each, and continuous monitoring was carried out for another two days at the same concentrations in order to observe any instabilities and/or unexpected spectral variations. Spectra were acquired every 15 seconds throughout the entire time-period and with an average of 1 sweep. Figure 4.31a shows the absorbance of the glucose peak at 1080 cm^{-1} during the entire experiment. This peak was chosen since it is the least affected by the absorbance of lactate, although a small contribution is expected, as previously shown in Section 4.4.

During the initial 14 hours, a good baseline stability was observed. Approximately 30 minutes after the addition of glucose and lactate, an increase in the 1080 cm^{-1} peak absorbance was seen, reflecting an increase in the concentration of glucose (and lactate, to some extent). A gradual increase was observed as opposed to an immediate transition, which was thought to be caused by a slight dilution of the small quantity of dialysate immediately adjacent to the pure ECF. The top-left inset of the figure shows selected absorbance spectra acquired over this time, highlighting the glucose peak at 1080 cm^{-1}. After approximately 24-hours, an unexpected upward shift in absorbance was observed (highlighted by a red arrow in the figure). The exact cause for this is unknown, but one explanation could be a variation in flow-rate provided by the pump. A decrease in flow-rate below 0.3 μL min^{-1} could allow an increased recovery of lactate in the dialysate (glucose recovery is already approximately 100 % at this flow-rate), and therefore a slight increased absorbance would be seen at 1080 cm^{-1} due to the small lactate contribution at equimolar concentrations. Apart from this shift, the remaining spectra showed good stability over the entire monitoring period. From the long-term absorbance-stability measurement, it was also possible to determine the

integration time for maximum absorbance resolution that the QCL-system is able to achieve by performing an analysis of the Allan variance, $\sigma_y^2(\tau)$, using the Allan variance function in Matlab (MathWorks Inc., USA) over a 24-hour period (top-right inset of Figure 4.31a).

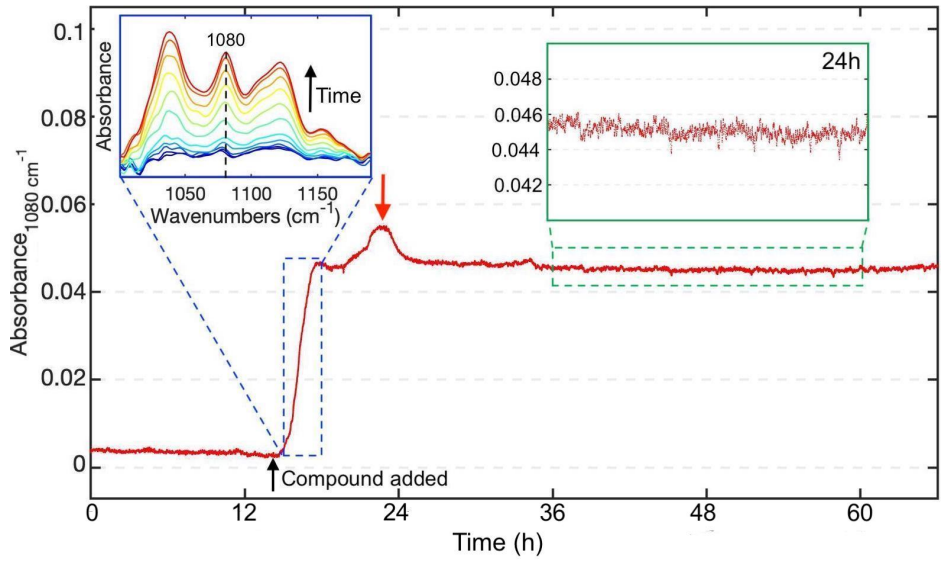

(a)

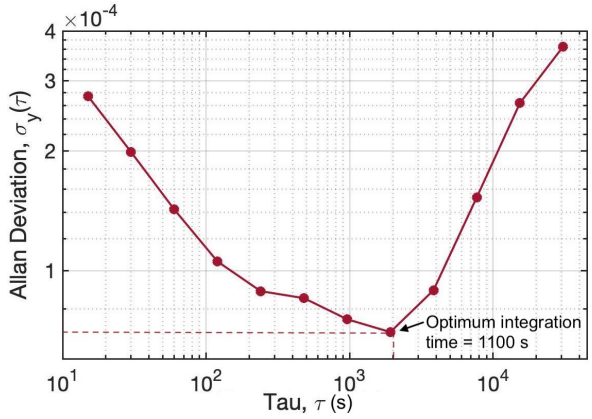

(b)

Fig. 4.31 (a) Absorbance values of the 1080 cm^{-1} glucose peak during a long-term stability measurement where microdialysate resulting from artificial ECF was continuously monitored every 15 seconds over two and a half days. After 14 hours, glucose and lactate were added to the artificial ECF to obtain a concentration of 5 mM of each, after which an increase in the 1080 cm^{-1} glucose peak was observed. The top-left inset shows select spectra during the increase in absorbance. The top right inset shows the peak absorbance over a 24-hour period. (b) Allan deviation plot over the highlighted 24-hour period with an integration time of 15 seconds, showing an optimum integration time of 1100 seconds (slope = 0).

The Allan variance is commonly used as a tool to measure the frequency stability of oscillation for a sequence of data in the time domain. It can also be used to determine the intrinsic noise in a system as a function of the integration time and to determine the resolution (smallest detectable change) of an instrument [92, 93]. Figure 4.31b shows the Allan deviation ($\sigma_y(\tau)$, square-root of the Allan variance) computed as a function of the integration time, τ. The analysis of the characteristic regions and logarithmic-scale slopes of the curve showed that the optimum integration time for maximum stability and resolution was τ = 1100 seconds (slope = 0). From here, the minimum detectable change in absorbance achieved with an integration time of 1100 seconds (18 minutes) was $7\text{x}10^{-5}$, while the minimum detectable change in absorbance for an integration time of 5 minutes, the maximum ideal integration time for this particular application, was approximately $8.8\text{x}10^{-5}$. By correlating these values with the linear calibration curve equations ($y = mx + b$) obtained for each of the pure compounds in Section 4.6.3, where y is the absorbance, x is the concentration (mM), m is the gradient, and b the y-intercept, the resolution of the QCL-system for each compound could be determined. With $b \approx 0$, and using the previously determined gradients, m, for each compound (Table 4.8), the resolution for glucose, lactate and pyruvate for a 5 minute integration time were determined as 0.013 mM, 0.031 mM and 0.015 mM, respectively. Although the optimum integration time of 18 minutes would yield higher resolutions of 0.01 mM, 0.025 and 0.012 mM for glucose, lactate and pyruvate, respectively, this difference is not significant and a reduced integration time is more favourable for this particular application. Overall, it was shown that the QCL-system provides a good stability over a long period of continuous microdialysis monitoring, as well as a sufficiently high resolution for each pure compound.

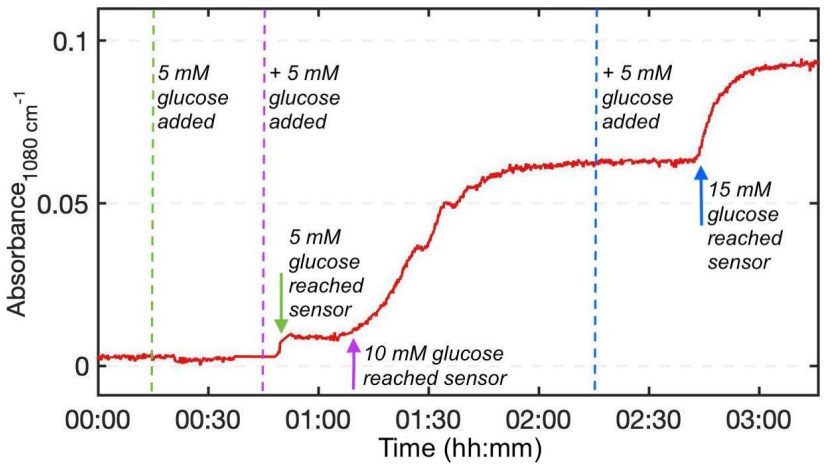

Fig. 4.32 Absorbance variations of the 1080 cm^{-1} glucose peak with increasing glucose concentrations in the artificial ECF, from 0 to 15 mM with 5 mM increments, over time.

The aim of the second experiment was to track the spectral changes corresponding to the analyte concentration in the artificial brain ECF. For this, pure glucose was added to the artificial brain ECF to achieve increasing concentrations of 5, 10 and 15 mM, and the glucose absorbance peak at 1080 cm^{-1} was monitored over time, as shown in Figure 4.32.

The additions of glucose to the artificial ECF occurred after 15 minutes, 45 minutes and 2h15 minutes. An increase in the 1080 cm^{-1} peak absorbance was expected to be seen approximately 30 minutes after the concentration increase in the artificial ECF. However, this time, it varied slightly for each case within a 27 to 37 minute window. The most logical explanation for this variation is an inconsistency in the flow-rate of fluid through the tubing. Moreover, the absorbance obtained for each concentration did not appear to be linear, as would be expected from what was previously seen in Section 4.6.3. In particular, the 5 mM glucose concentration appeared to show an absorbance at 1080 cm^{-1} which was lower than expected (between 0.02 and 0.04, as seen before), considering the normal glucose recovery at a 0.3 μl min^{-1} flow-rate. This decreased absorbance could either be due to dilution of the dialysate within the tubing or also due to flow-rate fluctuations, where an increase in flow-rate would result in less compound recovered in the dialysate, and thus, a decreased absorbance. Since the 5 mM glucose concentration was detected approximately 37 minutes after its addition, the first assumption is the most likely reason for the decreased absorbance at this concentration. On the other hand, the 1080 cm^{-1} peak absorbance for the 10 mM and 15 mM glucose concentrations were within the expected range. The non-immediate transition between the absorbance at one concentration to another and the varying transitions between concentration increments (i.e. the transition between the 5 mM and 10 mM concentrations appears to be slower than the transition between the 10 mM and 15 mM concentrations), also indicated that there may be flow-rate fluctuations and/or dialysate dilution within the tubing. Although the exact cause for the latter is unclear, this experiment suggests that an accurate control of the flow-rate is essential and that methods for preventing the dilution of the dialysate with the adjacent fluid flowing within the tubing should be considered and implemented. Other than the potential need for further control and improvements, it was shown that the QCL system in combination with the microdialysis setup was clearly able to detect changes in microdialysate concentrations over time. All the catheters used throughout the experiments were checked for any signs of damage during and after the experiments. No signs of damage were observed in any of these cases.

4.8.4 Compound relative recovery assessment

Although the relative recovery of compounds in microdialysate using the same catheter membranes used here has been studied elsewhere [71], an experiment was carried out in

order to compare the relative recovery (described in Subsection 4.2.1.1) of a select compound in the literature with that obtained using the described setup. Essentially, the aim was to compare the spectra obtained from samples extracted directly from the artificial ECF, with spectra obtained from the resulting microdialysate samples. For this experiment, the same protocol and laboratory setup as described in Section 4.8.1 were used, using a standard MD catheter and pump and an initial artificial ECF concentration of 0 mM. Lactate was arbitrarily selected as the test compound for this experiment and the concentration of the ECF was gradually increased from 5 mM to 15 mM in 5 mM increments and a spectrum of the dialysate was acquired at each concentration using an average of 55 sweeps (approximately 4 minutes) and with a baseline of sterile PF. A few minutes after each increment (to allow the fluid to homogenise with the help of the magnet stirrer), 10 μL were extracted from the ECF and stored for later analysis on the system. The analysis of the ECF samples was carried out under the same parameters (i.e. flow-rate and number of averaged sweeps) as above, with the only difference being the direct injection into the flow-cell, via the protocol described in Section 4.6. Figure 4.33a shows the absorbance spectra obtained from the microdialysate at the different lactate concentrations overlapped with the spectra obtained from the artificial ECF sample measurements.

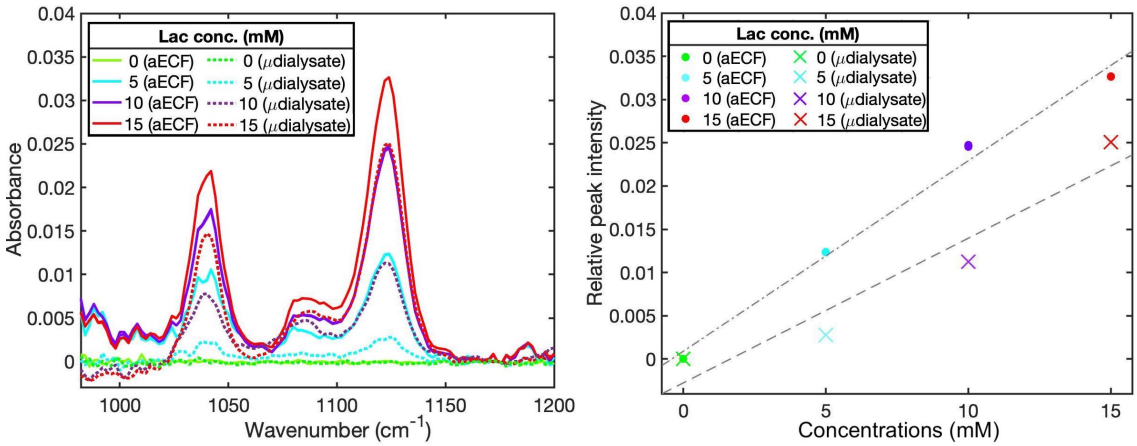

(a) (b)

Fig. 4.33 (a) Absorbance spectra of artificial ECF samples containing lactate at 0 mM, 5 mM, 10 mM and 15 mM, overlapped with the absorbance spectra of the microdialysate resulting from microdialysis in the same artificial ECF. (b) Relationship between the different lactate concentrations and corresponding relative peak intensities at 1124 cm^{-1} measured in the artificial ECF and in the resulting microdialysate.

From direct observation of the spectra and of the relative lactate peak intensities (at 1124 cm^{-1}) for each concentration shown in Figure 4.33b, it was evident that a higher lactate

absorbance, and therefore concentration, was seen in the samples extracted directly from the artificial ECF compared to those seen for the microdialysate, with exception of the 0 mM concentration. By dividing the peak absorbance values obtained for the microdialysate over the peak absorbance values obtained for the artificial ECF samples at each concentration, the mean relative recovery of lactate was estimated as 48 %. This value is almost half of the lactate relative recovery of 88.3 % determined in a previous study [71] using the same catheter and flow-rate as used here. This discrepancy may only be explained, once again, by a potentially inconsistent flow-rate provided by the pump and/or microdialysate dilution in the catheter/sensor connection tubing. While confirming the dilution of microdialysate in the tubing was challenging, an experiment to test the standard CMA 107 pump used in this experiment was carried out to determine whether this was a contributing factor to the decreased recoveries observed here. For this, an empty microdialysis vial was initially weighed and connected to the output tubing of the QCL system and the pump was set to pump at 0.3 μL min^{-1}. The vial containing accumulated sample was weighed each hour for a period of five hours. By calculating the difference in weight after each hour, the average flow-rate within each time period was determined. Figure 4.34 shows the obtained flow-rates over the 5-hour time period. Although the flow-rate is relatively consistent over the 5 hours, it lies between 0.48 and 0.53 μL min^{-1}, which is higher than the 0.3 μL min^{-1} flow-rate setting to which the pump was set. While very small variations in flow-rate over time may not cause significant variations in the final molecular concentration in the dialysate, studies have shown that an increased flow-rate causes a decreased recovery of molecules in the dialysate [71], which could easily explain the decreased relative recovery of lactate determined in the previous experiment. While the particular pump used in this and the previous experiments showed higher than expected flow-rates, it is unlikely that this is the case for all other pumps since they are required to accurately pump at specified flow-rates. However, this study showed that it is crucial to check each pump either before carrying out measurements to ensure a correct and consistent flow-rate is being provided.

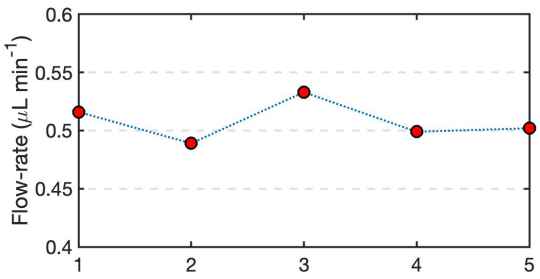

Fig. 4.34 Calculated flow-rate provided by a CMA 107 microdialysis pump set to 0.3 μL min^{-1} over a period of 5 hours.

4.8.5 Conclusions

This section described a range of experiments which were carried out to assess the QCL-system for continuous monitoring of microdialysate in combination with the standard MD catheter and pump used in the clinic. For this, a setup for mimicking the cerebral microdialysis technique was developed and combined with the sensor system. The first set of experiments was aimed at determining the response time of the sensor, here defined as the time between sample generation (at the catheter output) and sample analysis, which is primarily dependent on tubing dimensions, since the flow-rate for cerebral microdialysis is fixed at 0.3 μL min^{-1}. By using tubing with an inner diameter of 0.15 mm and a length of around 40 cm, which was determined to be the average adequate distance between a patient and sensor system in the NCCU, the time between sampling and analysis was 29 minutes, meaning that the spectra acquired will represent an occurrence in the brain from 29 minutes before. Although this is not the ideal case, it is a significant improvement from the current system not only due to the reduced delay time (currently 1 hour at best), but also because it does not require the hourly manual collection and substitution of vials. Moreover, miniaturisation of the sensor system would allow its placement at a shorter distance from the patient, and consequently the use of shorter tubing would result in significantly lower response times.

A further set of experiments were performed to study the long-term stability of the QCL-system and the maximum resolution provided by the system for each of the pure compounds, as well as its response to compound concentration variations in artificial ECF. It was shown that the sensor allows a very good stability over several days, meaning that, although a regular baseline calibration is advised, the system performs well for several hours and even days without it. Although the sensor also showed a good response to variations in artificial ECF concentrations, particular spectral behaviours were observed which indicate the possibility of either partial dialysate dilution within the tubing in the regions adjacent to concentration changes and/or inconsistencies in the flow-rate. These issues naturally affect the final output of the sensor and data acquired, and therefore, further work may be required to study these in more depth.

Finally, a study to determine the relative compound recovery obtained using the developed setup was carried out in order to compare it to the relative compound recovery obtained in the literature. Lactate was selected as the test compound in this case and a relative recovery of 48 % was achieved, in contrast to the 88.3 % recovery described in the literature. Since this disparity could be due to either the flow-rate provided by the MD pump or dilution of dialysate in the connector tubing, a study of the pump was carried out in order to rule out this option. It was found that the same pump used in the relative recovery experiment provided an average flow-rate of approximately 0.5 μL min^{-1} when set to pump at a 0.3 μL min^{-1}

flow-rate. This finding meant that the flow-rate could very well have been a contributing factor to the decreased relative recovery observed previously. Moreover, it made clear that before any set of experiments, it is crucial to first check that the pump being used is in good working order.

Overall, apart from a few issues relating to the flow-rate and potential dispersion of microdialysate in the tubing, which can potentially be corrected and/or accounted for during measurements, the QCL system showed a good performance and stability for continuous microdialysate monitoring over both short and long periods of time, and thus eliminating the need for manual labour.

4.9 Clinical procedures and studies

Continuous monitoring of TBI patients was carried out in the NCCU of Addenbrooke's Hospital, Cambridge, UK, using the QCL system described throughout this chapter. The following sections describe the clinical aspects and protocols implemented in this study, as well as the results obtained from one of the clinical studies, to demonstrate the performance of the QCL system for continuous TBI-patient monitoring.

4.9.1 Clinical aspects

Patients with TBI were defined as those who had cranial trauma with consistent computed tomography scan findings and who required invasive intracranial monitoring as part of their clinical management. Placements of microdialysis catheters in patients with TBI were into white matter not close to focal lesions. Patients were treated following local TBI-management protocols (including the following in all patients: endotracheal intubation, ventilation, sedation, and muscular paralysis) [51]. Exclusion criteria were deranged coagulation parameters and/or low platelet count preventing the placement of a microdialysis catheter. The protocol for this study was approved by the Health Research Authority (HRA) and Health and Care Research Wales (HCRW) (REC Reference No. 17/EE/0321). Assent was obtained from the relatives of the TBI patients. The study was performed in conformation with the spirit and the letter of the Declaration of Helsinki.

4.9.2 Protocol and methodologies

For each patient, new sterile tubing was prepared to the desired length of approximately 40-50 cm and with the required connectors, as previously described in Section 4.8.1. It was then connected to the inlet of the QCL system's flow-cell and sterile PF was injected

through the tubing and flow-cell for several minutes at a controlled flow-rate to ensure there were no signs of leakages or blockages throughout the fluid-carrying components. In the NCCU, the sensor was placed on a separate elevated trolley positioned as close as possible to the patient's head, typically behind the bed, while all the other equipment (including the laptop for data acquisition and cooling system) were placed on another trolley further away, given the confined environment of hospital wards. As a requirement for non-standard hospital equipment, a transformer and UPS were used to supply the QCL, cooling system and laptop, to prevent equipment damage and/or data loss in case of a power outage. For the continuous microdialysate monitoring, a sterile clinical microdialysis catheter (8010320, CMA 71, 10 mm membrane length, 100 kDa Cut-Off Brain Microdialysis Catheter, M Dialysis AB, Sweden) was introduced into the brain of the patient by a medical professional through a hole drilled into the skull bone. The outlet of the catheter now inserted into the patient's brain, which traditionally connects to a microdialysis vial, was connected to the prepared tubing leading to the flow-cell of the QCL system. If desired, modified MD vials can be placed at the output of the flow-cell to collect the analysed microdialysate for further testing, which can be collected and stored in the NCCU freezer as they fill up. The catheter inlet was connected to a CMA 107 MD pump containing a syringe with sterile CNS PF. The microdialysis catheter, connector tubing and flow-cell were perfused with the sterile PF during the automatic 5-minute flush cycle at a 15 μL min^{-1} flow-rate until the automatic decrease of flow-rate to 0.3 μL min^{-1}, at which point the baseline spectrum of the PF was acquired to be used for baseline subtraction in the subsequent spectra. Depending on the length of the tubing, a second flush may be required for the PF to reach the flow-cell for the baseline acquisition. With an acquired baseline and a flow-rate of 0.3 μL min^{-1}, the continuous spectral acquisition can begin using the ChemDetect software. While spectra can be acquired every second, in order to avoid an overload of data over long time-periods, it is preferable to acquire spectra every several seconds or minutes, anywhere between 10 seconds and 5 minutes, depending on the estimated overall measurement time. The ChemDetect software displays the continuously acquired microdialysate spectra, and all the data were collected and saved to the laptop for further analysis.

4.9.3 Continuous monitoring

To demonstrate the QCL system's performance for continuous patient microdialysate monitoring in the NCCU, clinical studies were carried out, where a total of eleven TBI patients were monitored. Due to circumstances which were out of our control, such as resuscitation procedures, patient disconnection for surgical interventions or CT scans and accidental disconnections from the microdialysis probe overnight, not all clinical studies were carried

out over sufficiently long periods of time and some were interrupted shortly after their start. Moreover, in some cases, a newly-introduced type of CNS PF containing an additional compound, dextran, was used in the NCCU without our knowledge, which strongly affected the acquired absorbance spectra. The ultimate effect of dextran on the acquired spectra and whether its use can be overcome or avoided when using this sensor system is yet to be determined and therefore will not be discussed here in further detail. On account of the above-mentioned reasons, only results for three of the carried out clinical studies were deemed coherent. In this section, continuously acquired data of one of the clinical studies is presented and discussed. The results of the two other clinical studies can be found in Appendix B. An image of the QCL sensor system connected to the outlet of a cerebral MD catheter inserted into the brain of a TBI patient for continuous monitoring, is shown in Figure 4.35.

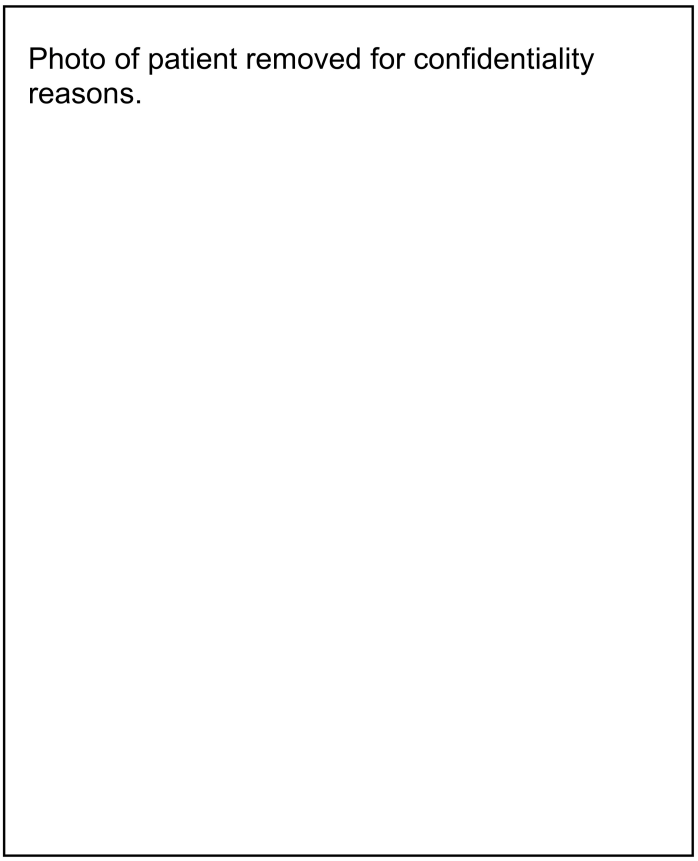

Fig. 4.35 Continuous monitoring of TBI patient microdialysate in the neurocritical care unit via the QCL-system, which is connected to the outlet of the microdialysis catheter. The data are continuously acquired and stored to a laptop for further spectral analysis.

Figure 4.36 shows the spectral data acquired from the continuous monitoring of a patient over a 24-hour period, with spectra being acquired every 60 seconds. Spectral acquisition started from the moment a baseline of PF was taken. Figure 4.36a shows a 3D view of the variation of the absorbance spectra as a function of time, while figure 4.36b shows the 2D pseudocolour plot of the evolution of the absorbance spectra, both highlighting the glucose peak at 1080 cm^{-1} with a dashed line.

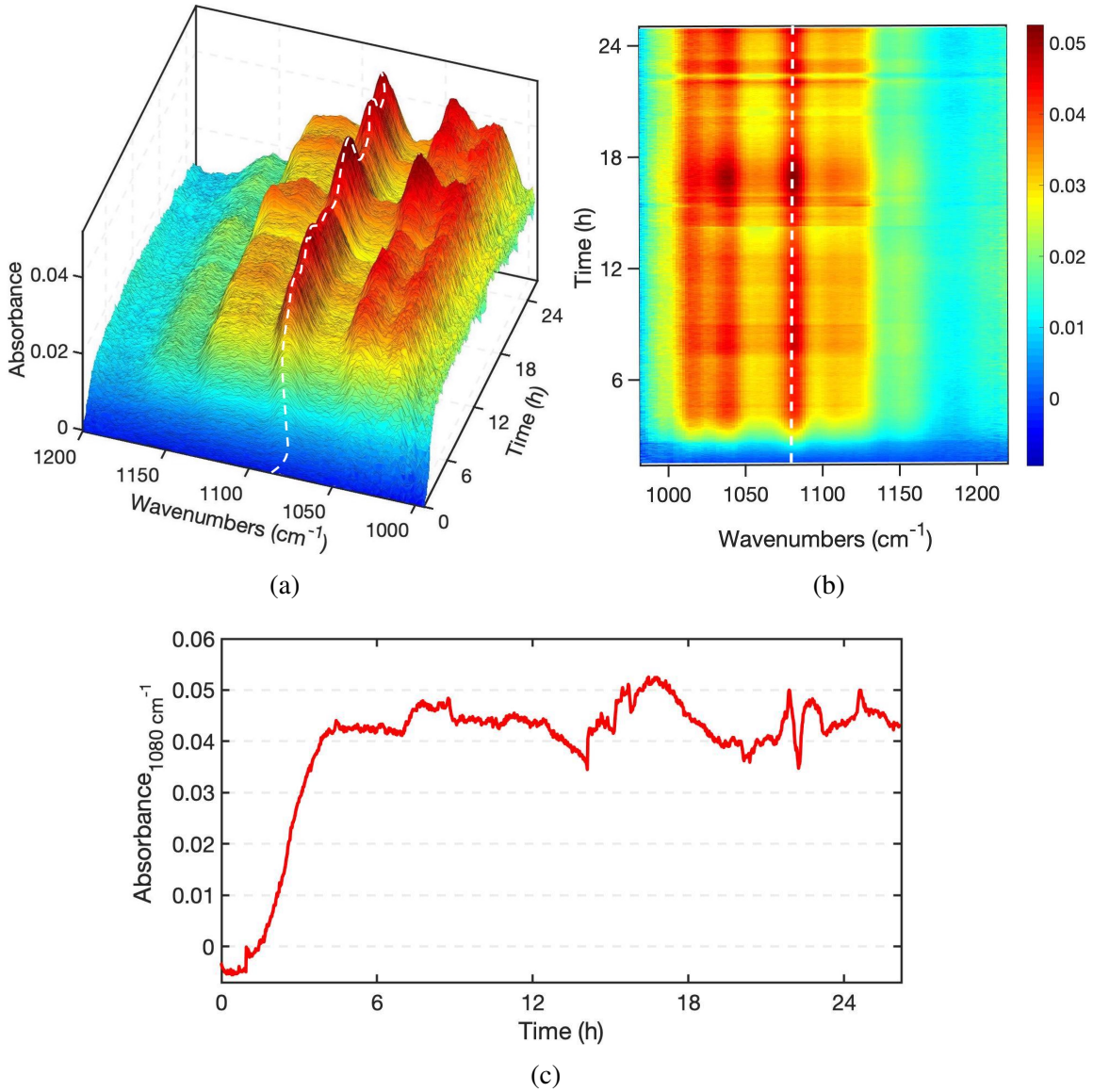

Fig. 4.36 Spectral information acquired from continuous microdialysate monitoring of a TBI patient in the NCCU over a 24-hour period. (a) 3D view of the variation of absorbance spectra over time with 1 minute spectral acquisitions, highlighting the glucose peak at 1080 cm^{-1}; (b) 2D pseudocolour plot showing a clear evolution of the absorbance spectra over the monitoring time; (c) Absorbance of the glucose peak at 1080 cm^{-1} as a function of time.

An initial increase of the overall absorbance intensity was observed from the moment the enriched microdialysate reached the flow-cell, which can clearly be seen in the 2D and 3D plots. For a more clear visualisation of the absorbance variations corresponding to concentration changes in the microdialysate, the glucose peak absorbance at 1080 cm^{-1} was plotted as a function of time, as shown in Figure 4.36.

As seen before, although the primary contributor to the absorbance peak at 1080 cm^{-1} is glucose, if present at sufficiently high concentrations (equimolar or higher), lactate will also contribute towards this peak intensity and therefore this peak cannot be used as a direct quantifier of glucose. The time (approximately 1 hour) for the microdialysate to reach the sensor was explained by the fact that a slightly longer length of tubing of approximately 50 cm had to be used in this particular case due to the limited space surrounding the patient due to other medical equipment. Moreover, the gradual (as opposed to immediate) increase observed was likely due to microdialysate dispersion within the tubing. Although this dispersion does not inhibit the quantification of metabolites in the brain, it may smooth out any rapid sharp changes in the spectra. With the continuous flow of microdialysate through the flow-cell, clear variations in absorbance were observed, which correspond to chemical fluctuations in the brain. Overall, this methodology has shown to be promising to monitor microdialysate compound levels in TBI patients continuously, over several hours without the expense of nurses' time for hourly sample collection.

4.9.4 Conclusions

This section showed the successful continuous monitoring of TBI patient microdialysate in the NCCU using a QCL-based microfluidic system for the first time. The patient data shown here were acquired every minute over 24 hours. Throughout this time, a clear variation in the absorbance spectra was observed, which directly corresponds to dynamic chemical changes within the brain. Moreover, the need for hourly vial collection by nurses and off-line analysis by clinicians (as required for the current system) was entirely eliminated using this system. While certain issues, such as the response time and potential dispersion of microdialysate within the tubing, were observed, these can be addressed in future by sensor miniaturisation and consequently with decreased tubing lengths. However, the potential microdialysate dispersion occurring within the tubing will always be less than the microdialysate dispersion occurring in the currently implemented system, where approximately 10 μL of microdialysate are dispersed into a single vial. The effect of the use of CNS PF containing dextran is yet to be determined and is scope for future work. Other external issues such as accidental disconnections and monitoring interruptions may be addressed by miniaturisation of the

sensor, which will eliminate the need for long connector tubing, and thus decrease the disconnection risk.

4.10 Multivariate data analysis for predicting microdialysate compound concentrations

This section was aimed at the development and optimisation of a statistical model for the prediction of glucose, lactate and pyruvate in patient microdialysis samples. The analytical method used for developing the model and quantifying the predictability of the different solutions was partial least squares regression (PLSR), described briefly in Chapter 2. Firstly, given the limited number of patient samples, a model was developed using synthetic samples consisting of three-component mixtures (of glucose, lactate and pyruvate) in CNS perfusion fluid within a range of clinically-relevant concentrations. This model was then used to predict the concentrations of glucose, lactate and pyruvate in patient microdialysates, which were compared against measurements obtained separately using the standard microdialysis analyser (ISCUS Flex Microdialysis Analyser).

4.10.1 Synthetic sample preparation and analysis

Given the scarcity of patient microdialysis samples at the time of this study, it was decided that synthetic samples be used for developing the regression model for subsequent use in predicting patient-sample compound concentrations. It was important to ensure that the synthetic samples used to develop the model were as relevant as possible to the clinical context and, therefore, samples were prepared to closely follow the ranges of concentrations typically found in microdialysates of TBI patients based on studies presented in the literature [53]. From the analysis of typical concentrations of each compound found in the microdialysates of 223 TBI patients [53], a simple uniform selection algorithm with reject sampling developed by a collaborator, Mr Dan Hutter, was used to generate a list of 50 samples containing different combinations of glucose, lactate and pyruvate concentrations within ranges and at relative amounts considered the most relevant to TBI monitoring. The list of samples obtained from this analysis can be found in Figure C.1 of Appendix C, and the minimum, maximum, mean and standard deviation values of concentrations of each compound are summarised in Table 4.9. The histograms in Figure 4.37 indicate the frequency at which the various concentrations of glucose, lactate and pyruvate were observed in the generated list of samples. All values are presented in micromolar (μM) concentrations for simplicity.

Table 4.9 Summary of the minimum, maximum, mean and standard deviation values of concentrations of glucose, lactate and pyruvate in the list of 50 samples generated from typical TBI-patient microdialysate compound concentrations found in literature.

	Glucose (μM)	**Lactate (μM)**	**Pyruvate (μM)**
Minimum	20	500	20
Maximum	5000	8000	300
Mean	2387.02	4487.23	172.02
Std. Dev.	1533.30	2052.69	68.27

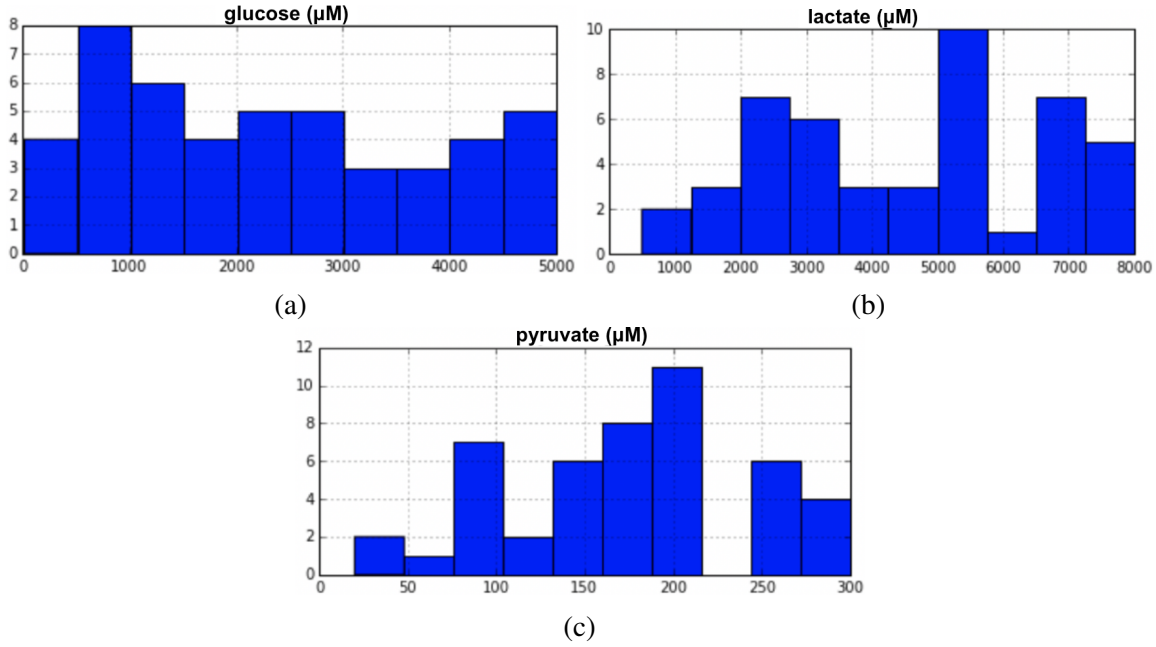

(a) (b)

(c)

Fig. 4.37 Histograms summarising the frequency with which various concentrations of glucose, lactate and pyruvate were observed in the analysis generated from TBI-patient data. Figures adapted from plots generated by Mr Dan Hutter.

The 50 samples containing different concentrations of glucose, lactate and pyruvate (Figure C.1, Appendix C) were prepared in sterile perfusion fluid by Ms Emma Gould. They were subsequently analysed using the ChemDetect QCL-system following the protocol described in Section 4.6.1, using a 127 μm path-length and 80 averaged sweeps. Figure 4.38a shows all the 50 absorbance spectra obtained for each sample plotted in the entire available spectral range, between 982 and 1258 cm^{-1}. Three outliers were determined (dashed lines in figure) and were therefore excluded for the generation of the regression model. The remaining 47 spectra used to generate and test the model are shown in Figure 4.38b, where peaks for glucose, lactate and pyruvate are clearly visible.

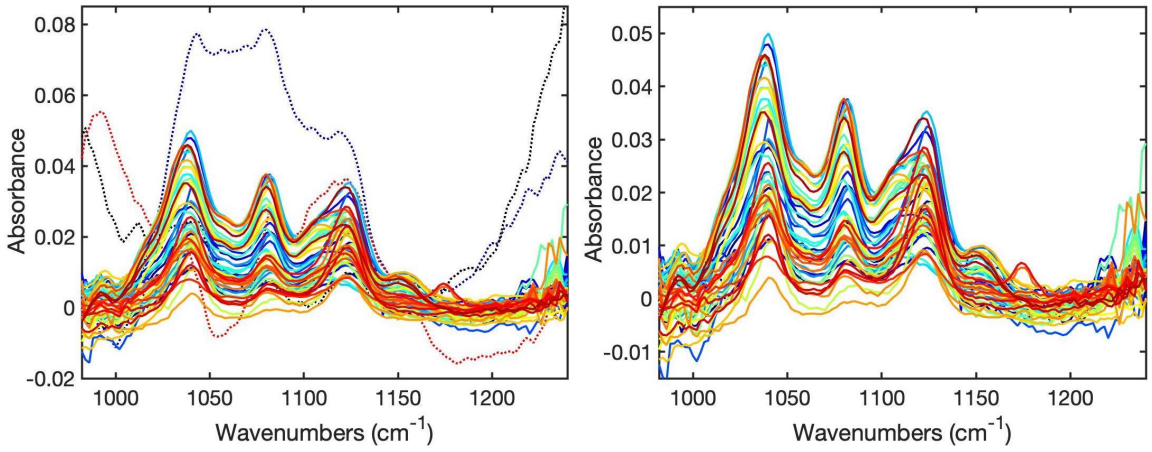

(a) (b)

Fig. 4.38 Absorbance spectra of 50 synthetic samples acquired on QCL-system. (a) All spectra including outliers (dashed lines); (b) Spectra used for developing the PLSR model (the three outliers were excluded).

4.10.2 Development, evaluation & optimisation of the PLSR model

The PLSR model used in this study was developed by Mr Dan Hutter. The model was built, optimised and the number of PLSR components was calibrated based on *k*-fold cross-validation, where the spectral data were randomly split into the following sub-sample sets: the in-sample set, comprising of 20 spectra; the out-sample set comprising of 13 spectra; and the test sample set, comprising of the remaining 14 spectra. Here, a single sub-sample (test sample) was retained as the final validation for testing the model. Using the in-sample and out-sample, the optimum number of PLSR components (i.e. that gave the lowest RMSE, Equation 2.16) was determined to be 3. To improve upon the base model, the spectra were pre-processed by limiting the spectral range to the main region of interest, between 1000 to 1200 cm^{-1} (to remove the noise from both ends of the spectra), and also by performing a baseline correction. The baseline correction was implemented by shifting all spectra to a baseline point at 1200 cm^{-1}. The performance of the model applied to each compound was then characterised by the RMSEP from applying the model to the test set. Table 4.10 summarises the RMSEP values generated using the raw absorbance spectra, the absorbance spectra within a limited spectral range and the absorbance spectra both within a limited spectral range and with baseline correction applied. It could be seen that the RMSEP is indeed better for all three compounds when both a limited spectral range and a baseline correction are implemented.

Table 4.10 RMSEP values for glucose, lactate and pyruvate obtained from applying the PLSR model to the test set using the raw absorbance spectra, absorbance spectra within a limited spectral range and absorbance spectra, both within a limited spectral range and with baseline correction applied.

	RMSEP (μM)		
Absorbance spectra	**Glucose**	**Lactate**	**Pyruvate**
Raw spectra	479.49	808.60	78.04
Limited spectral range	479.83	739.33	79.34
Limited spectral range & baseline correction	454.87	620.86	77.43

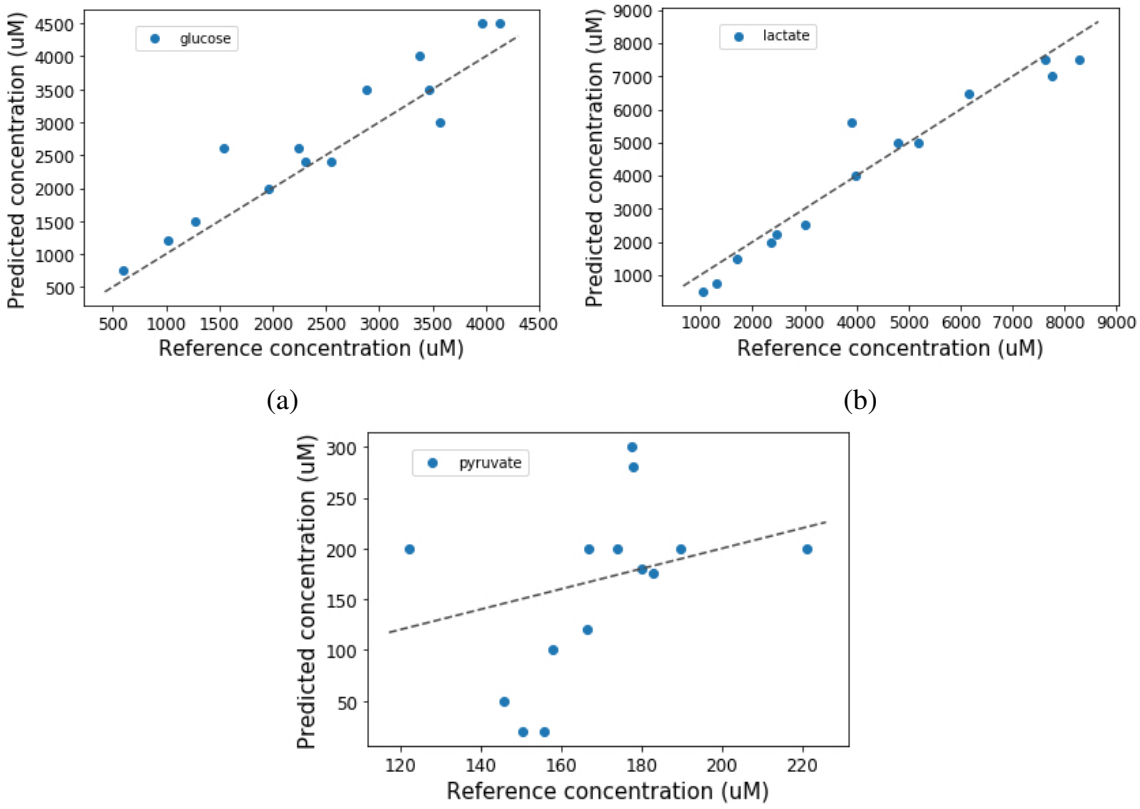

(a) (b)

(c)

Fig. 4.39 Predicted concentration levels in the 14 test samples plotted against reference concentrations for (a) glucose, (b) lactate and (c) pyruvate. Predicted values were derived from applying the PLSR model to the test set. Dashed lines represent a linear regression fit. Figures generated by Mr Dan Hutter.

Figure 4.39 shows the performance of the improved PLSR model (including a limited spectral range and baseline correction) applied to the test set spectra for each compound. A good correlation between the predicted and reference concentrations can be seen for glucose and lactate. However, for pyruvate, the model did not perform well enough for this particular application. The main reason for this was that the concentrations of pyruvate in the samples were an order of magnitude lower than for the other two compounds and the specific pyruvate peak (at 1176 cm^{-1}) was only detectable for concentrations above 200 - 400 μM, as previously determined in Subsection 4.6.3. Therefore, the pyruvate data were actually modelled using a very small number of spectra that had a detectable peak (specifically two, from analysis from the data presented in Figure 4.38), resulting in a high RMSE. In order to achieve a lower RMSE for pyruvate using the current system, a larger number of samples with pyruvate concentrations above the detectable limit would have to be used. However, this would only allow accurate predictions of pyruvate at levels concentrations above 200 - 400 μM.

4.10.3 PLSR prediction of glucose, lactate and pyruvate concentrations in patient microdialysates

Here, the main aim was to determine whether the PLSR model developed using synthetic samples could be used to accurately predict the concentrations of the relevant compounds in patient microdialysis samples. For this, the optimised PLSR model developed in the previous subsection (4.10.2) was used to predict the concentrations of glucose, lactate and pyruvate in 27 patient microdialysis samples, which were compared against reference concentration measurements obtained separately using the standard microdialysis analyser (ISCUS Flex Microdialysis Analyser). The reference measurements were acquired by Dr. Núria García and the respective concentrations obtained for each sample are provided in Figure C.2 of Appendix C. The 27 patient samples were measured using the QCL-system following the protocol described in Section 4.6.1 and using a 127 μm path-length and 80 averaged sweeps. Figure 4.40 shows the absorbance spectra obtained for each sample, plotted in the most relevant spectral range, between 1000 and 1200 cm^{-1}.

For the implementation of the PLSR model on the patient sample spectra, the spectra were limited to the 1000 - 1200 cm^{-1} spectral range and were baseline-corrected as before (all spectra were shifted to a baseline point at 1200 cm^{-1}). Figure 4.41 shows the predicted glucose, lactate and pyruvate concentrations for the 27 patient microdialysis samples, generated by applying the PLSR model developed in Subsection 4.10.2. The respective RMSEP values for each compound are presented in Table 4.11.

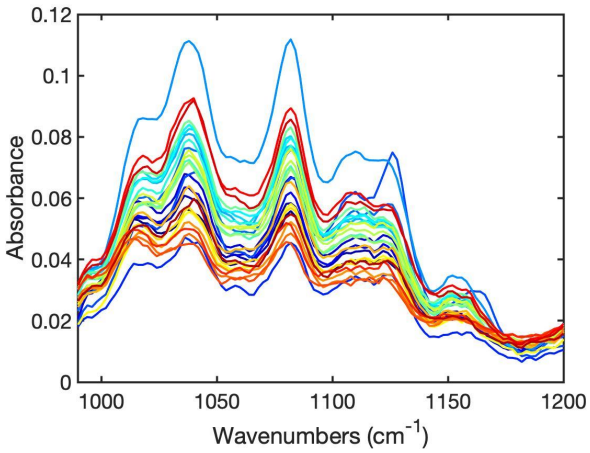

Fig. 4.40 Absorbance spectra of 27 patient microdialysis samples acquired on the QCL-system.

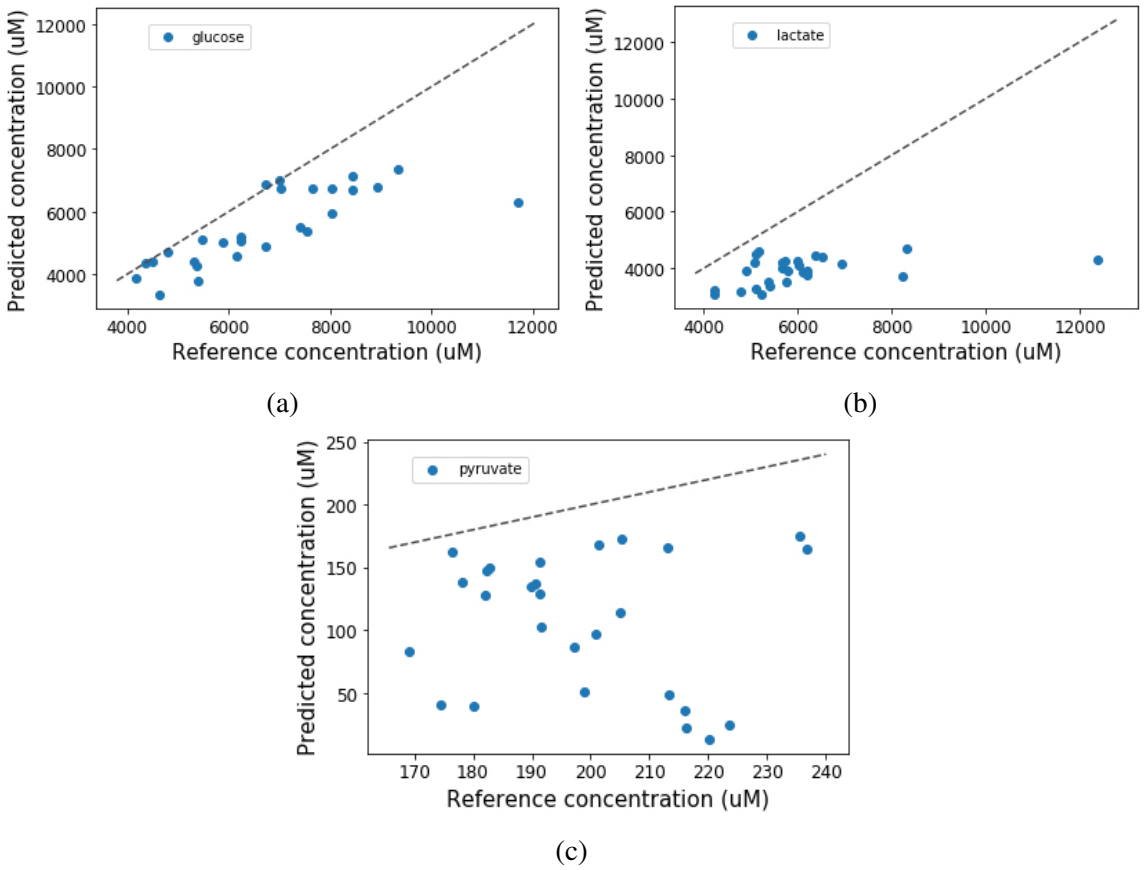

Fig. 4.41 Predicted concentration levels in 27 patient microdialysis samples plotted against reference concentrations for: (a) glucose; (b) lactate; and (c) pyruvate. Predicted values were derived from applying the PLSR model to the absorbance spectra of the patient samples. Dashed lines represent a linear regression fit. Figures generated by Mr Dan Hutter.

Table 4.11 RMSEP values obtained from the predicted versus reference concentrations of glucose, lactate and pyruvate in the 27 patient microdialysis samples.

	Glucose	**Lactate**	**Pyruvate**
RMSEP (μM)	1647	2548	108

With the exception of a few points, the predicted concentrations for glucose and lactate showed a relatively linear behaviour in relation to the reference concentrations. It was seen that the compound concentrations in the measured patient samples were confined to a lower concentration range for both glucose (between 334 and 735 μM) and lactate (between 308 and 468 μM), according to the reference measurements (Figure C.2 Appendix C), which is likely to have contributed to the relatively high RMSEP values observed.

It is expected that, for a more diverse set of patient data containing higher glucose and lactate concentrations, the PLSR model would provide a lower RMSEP. On the other hand, the predicted pyruvate concentrations showed low correlation with the corresponding reference concentrations compared to glucose and lactate. This was expected from what was observed in the previous section: the PLSR model was not good enough for modelling the pyruvate data, yielding a RMSEP value too high to allow the accurate prediction of pyruvate. Moreover, from analysis of the pyruvate concentrations obtained via the reference measurements of the microdialysates, it was seen that the higher pyruvate concentration was 175.6 μM, which lies below the quantifiable limit for pyruvate (200 - 400 μM) determined for the QCL-system. Therefore, even if the developed PLSR model had shown good results for modelling pyruvate data, its implementation on this particular set of patient microdialysate data, would be unlikely to result in a good correlation at this stage.

4.10.4 Conclusions

This chapter demonstrated an attempt to determine glucose, lactate and pyruvate concentrations in patient microdialysis samples using a PLSR model developed on microdialysate-mimicking synthetic samples containing relevant concentrations of all three compounds. The developed PLSR model was optimised by limiting the spectral interval to cover the most relevant range: 1000 - 1200 cm^{-1}, which minimised the RMSE. The model was further optimised by applying a baseline correction, where all the spectra were shifted to a baseline point at 1200 cm^{-1}, which further minimised the RMSE. When applied to the test samples, a good correlation between the predicted vs. reference concentrations of glucose and lactate was observed. However, given the order of magnitude difference between the concentrations of these and the concentration of pyruvate, the correlation between predicted

vs. reference concentrations of pyruvate was not ideal and resulted in a high RMSE. The optimised model was then used to predict the concentrations of the three compounds in patient microdialysis samples and compared to reference measurements acquired using the standard microdialysate-analysing instrument. While some correlation was seen between the predicted and reference concentrations of glucose and lactate, the poor correlation observed for pyruvate was mainly due to the pyruvate concentrations being below the quantifiable limit (200 - 400 μM) and the fact that the developed PLSR model showed an RMSEP for pyruvate which was too high to perform accurate enough predictions for this application.

Overall, the prediction of glucose, lactate and pyruvate concentrations in patient microdialysate samples by implementation of a PLSR model developed using synthetic samples has proved to be feasible. However, further improvements to the model (e.g. using larger data-sets and samples of concentrations covering a broader range) as well as the potential implementation of additional spectral pre-processing methods (e.g. using first derivative spectra) may be required. An alternative, but less practical approach, would be to use actual patient microdialysate samples to develop the model, as opposed to synthetic samples. For this, however, a sufficiently large number of samples covering an adequately broad range of the three compound concentrations would be required. Whether developing the model using real patient samples is a more accurate approach and provides higher predictive ability compared to using synthetic samples (which may lack relevant information on the nature of the samples) is yet to be determined. However, since patient microdialysate samples essentially comprise enriched perfusion fluid, it is expected that the use of synthetic samples in this case, in addition to being more practical, will also provide sufficient accuracy.

4.11 Conclusions and future work

Achieving continuous monitoring of the brain chemistry of TBI patients is incredibly challenging. However, there is no doubt that its success will heighten our understanding of the dynamic chemical processes in the injured human brain and contribute significantly to improved patient outcome due to a timely response and tailored treatment. Not only is it a challenge to achieve sufficient detection limits in order to accurately detect and quantify the cerebral molecules of interest, but also to build a system that is compatible with the current microdialysis technique and that is sufficiently compact to fit in the confined spaces of a ward without causing inconvenience. Moreover, parameters, such as a good response time, stability, accuracy, ease of use and practicality all require extensive optimisation and effort to achieve. It was demonstrated during this work that the use of transmission MIR spectroscopy in combination with microfluidics shows great potential in achieving such a system. Efforts

were made towards achieving high limits of quantification using a high spectral power density light source (i.e. a QCL), as an alternative to standard FT-IR techniques, and by optimisation of a range of parameters, such as the optical path-length and spectral acquisition times. By doing so, limits of quantification (LoQs) between 0.1 and 0.2 mM were achieved for two of the three main compounds of interest, glucose and lactate, which allow coverage of their physiological range and were comparable to the LoQs of the standard ISCUS Analyser (0.10 mM for glucose and 0.20 mM for lactate [82]). The third compound, pyruvate, was more challenging to quantify at the lower end of its physiological range, given its presence at concentrations an order of magnitude lower than the others. Moreover, the LoQ achieved for pyruvate (0.2-0.4 mM) was found to be significantly higher than that achievable by the ISCUS Analyser (0.016 mM [82]). Therefore, while pyruvate is still quantifiable in most of its physiological range, future efforts will be made to improve its detection.

Real-time microdialysate measurements were the ultimate goal. However, this was limited not only by the microdialysis technique, which requires a particularly reduced flow-rate for acquiring cerebral microdialysis samples, but also by the connector tubing which transports the microdialysate to the sensor system. In this work, a lag time of 29 minutes was achieved when using tubing of a small inner-diameter and an appropriate length. While it is already an improvement from the currently implemented system, which only allows hourly microdialysate analysis at best, efforts to minimise the response time will be a priority in future work. This may include the miniaturisation of the sensor such that it can be placed close to or on the patient, as opposed to on an external trolley, which will allow significant reduction of the tubing dimensions. Sensor miniaturisation will also decrease the risk of accidental patient disconnection from the microdialysis probe, which was sometimes seen during clinical studies, due to its positioning on an external trolley and the longer tubing required. Finally, a shorter length of tubing will minimise microdialysate dispersion within the tubing, which was thought to be observed in some cases, although to a considerably smaller extent compared to the current system, where larger volumes of microdialysate are dispersed into vials, resulting in an average over long periods and a dampening of any fast and large changes. The ongoing technological developments towards novel QCL light sources and detectors holds promise for facilitating the development of miniature, robust and highly sensitive sensor systems.

Here, it was shown for the first time that the brain chemistry of acutely injured TBI patients could be continuously monitored using MIR spectroscopy techniques. It was also shown that this technique allows continuous and stable monitoring over several days, without the need for consumables/reagents or frequent sensor calibration. Moreover, the implementation of this system successfully eliminates the need for a nurse to collect and

substitute microdialysate vials on an hourly basis. This is a particular advantage, specially in cases where the NCCU is understaffed, for example, during night shifts or other emergencies.

In an attempt to accurately quantify the compounds of interest from the MIR spectra of patient microdialysates, multivariate analysis (PLSR) was carried out. Given the limited availability of patient microdialysates at the point of the study, synthetic samples of the three compounds were prepared in perfusion fluid and used to build a PLSR model to predict compound concentrations. When the model was applied to spectra of patient microdialysates, although some correlation was seen between the predicted and reference concentrations (measured using a standard microdialysate analyser), particularly for glucose and lactate, it is clear that feeding the model with more suitable and improved spectra is required in order to obtain accurate quantitative information. This may be achieved by increasing the number of samples used to build the model and expanding their compound concentration ranges, in addition to performing additional spectral pre-processing methods (e.g. improving SNR and/or using first derivative spectra).

In addition to what was mentioned regarding detection improvements and sensor miniaturisation, future tasks will undoubtedly involve clinical-translational methods to allow clinicians to easily access the information provided by the sensor and make decisions accordingly. Further work will be carried out to investigate the possibility of integrating the information provided by this system with ICM+, a pioneering clinical research software that allows real-time data analysis from multiple bedside monitor sources to facilitate personalised medicine for TBI patients.

The work carried out in this chapter demonstrated, for the first time, the potential of using a sensor system based on MIR spectroscopy for the continuous monitoring of dynamic chemical changes in the brain of TBI patients. Although further improvements are required to improve and optimise the system, its final implementation will enable clinicians to provide rapid and tailored treatment to patients as well as to track the effect of particular treatments (i.e. drugs) as they are administered and to rapidly detect patient deterioration, which will lead to an overall improved patient outcome.

Chapter 5

MIR evanescent-field fibre-optic sensor with enhanced sensitivity for VOCs[‡]

5.1 Introduction and literature review

Volatile organic compounds (VOCs) are a hazardous group of carbon-based chemical compounds which are prone to evaporate under ambient conditions and may cause damage to humans with chronic exposure [94]. The detection, monitoring and analysis of VOC gases is crucial for many applications, such as industry, agriculture, health monitoring, security, and scientific research [95]. There is a strong need to detect toxic gases and traces of explosives, as well as to monitor indoor and outdoor air quality. Studies have shown that the inhalation of excess VOCs and their degradation products is linked to respiratory-system damage and even cancer [96]. In addition, human safety is potentially threatened by the toxicity, high flammability and explosivity of certain VOCs. Besides human health and safety, VOCs may also be related to major environmental problems, such as global warming, stratospheric ozone depletion and photochemical ozone formation [94]. Therefore, the development of new technologies that can enable highly effective sensors to monitor VOC gases in various application fields is of great importance, and the increasing awareness of the harsh environmental and health risks associated with air pollution has placed VOC sensors in high demand. Currently available low-cost sensors for VOCs are based on the use of metal-oxide semiconductors and photo-ionization principles [97]. These detectors are only capable of measuring the total VOC concentration, without any ability to differentiate between different VOCs. For any specific and selective VOC detection and classification, bulky systems (such

[‡]F. Alimagham, M. Platkov, J. Prestage, S. Basov, G. Izakson, A. Katzir, S. R. Elliott and T. Hutter, **Mid-IR evanescent-field fiber sensor with enhanced sensitivity for volatile organic compounds**, *RSC Advances*, 9, 21186, **2019**

as gas-chromatography mass-spectrometry) and complex sample preparation are required, making them unsuitable for real-time, in-line and *in situ* VOC monitoring [98, 99]. Given the advantages of MIR spectroscopy, previously highlighted in Chapter 1, it has emerged as an attractive alternative for a wide range of applications, including environmental monitoring and analysis. The development and miniaturization of advanced MIR light-source technologies, such as QCLs, has improved performance of evanescent-field based sensors, including attenuated total reflectance (ATR) crystals, optical fibres and waveguides [22]. Fibre-optic-based evanescent-wave spectroscopy (FEWS) sensors are often considered an improvement on standard ATR-based sensors since their sensitivity can be enhanced by the increased number of internal reflections provided by the fibre's geometry and also by tapering or bending the fibre [6]. Further details, including common MIR fibre-optic materials, are provided in Chapter 2. In this chapter, the development of a novel sensor design and method for increased selectivity and sensitivity of VOCs based on MIR evanescent-wave fibre-optic spectroscopy is presented and described. The sensing principle is based on MIR evanescent-wave fibre-optic spectroscopy, where a porous cladding, formed by porous silicon (PSi), was used to concentrate volatile molecules near the surface of a tapered (U-bent) optical fibre, thus increasing the number of molecules interacting with its emanating evanescent light field. A conceptual schematic of this principle is presented in Figure 5.1.

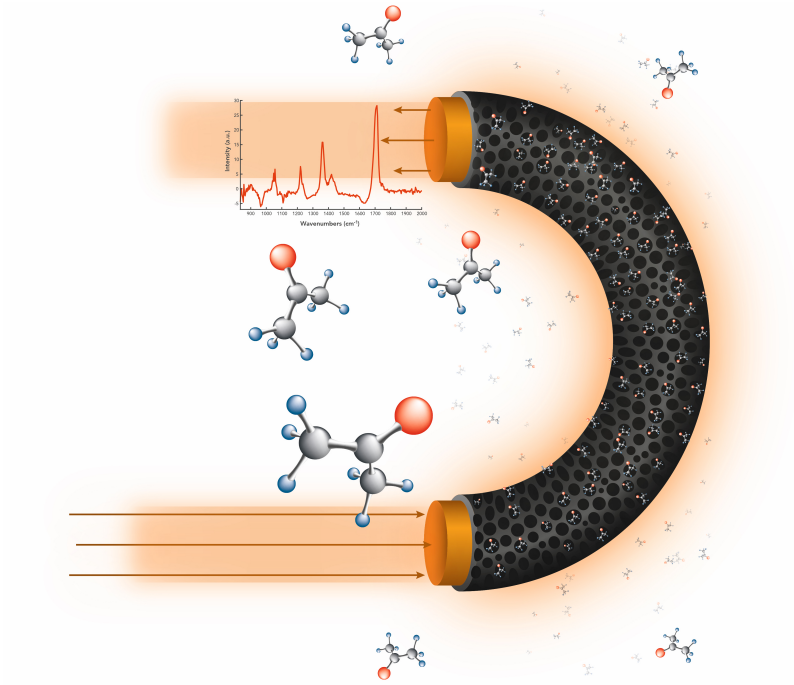

Fig. 5.1 Schematic principle of a U-bent optical fibre sensor coated with a porous cladding, capable of concentrating volatile molecules near its surface in order to increase the number of molecules interacting with the emanating evanescent light field.

To ascertain the effectiveness and performance of the sensor, different VOCs were measured, and the enhanced sensitivity was analysed using a custom-built gas cell. According to the results, this VOC sensor showed a significantly increased sensitivity compared to that of an uncoated fibre. The processes regarding the preparation of the sensor (i.e. fabrication of the U-bent fibre and PSi microparticle coating) are described in detail in section 5.2, followed by the optimisation and analysis of the sensor performance in section 5.3.

5.1.1 MIR evanescent field for VOC sensing

Several MIR evanescent-field based sensors with enhancement coatings for measuring compounds in aqueous solutions have been extensively explored and developed [100–108]. However, the detection of VOCs in the gas phase in air (or in other gases) through evanescent-field sensing still remains a great challenge. The reason for this is that gas is a low-density matrix (approximately three orders of magnitude lower in density than liquid or solid matrices), resulting in a small number of molecules at the fibre surface, at any given time, and consequently causing a low efficiency for these sensors operating in the gas phase. Therefore, evanescent-field-based MIR detection of VOCs in the gas phase is uncommon and particularly challenging. A recent study has demonstrated evanescent-field detection of ethanol at the C-H absorption band, using a single-mode chalcogenide waveguide [109]. Although this work shows the principle of selective evanescent-field detection in the gas-phase, the microfabrication process is complex and single-mode operation limits the spectral range of the measurement. Functionalized coatings have been used to adsorb and concentrate VOCs from the gas phase to enable better detection for monitoring refractive-index changes [95, 110–112]. Although sensitive measurement of refractive-index changes was successfully achieved by some of these methods, they do not allow for molecular specificity. Porous materials, such as porous silicon (PSi), have been shown to be highly useful in adsorbing and condensing VOCs due to capillary action in the pores of the PSi [113–115].

5.1.2 Porous silicon

Porous silicon (PSi) is typically obtained through the formation of pores in bulk crystalline silicon by electrochemical etching. Its porous sponge-like structure provides it with a large specific surface area, up to 1000 m^2cm^{-3}, making it an excellent candidate for a wide range of sensing applications, in particular, for the detection of vapours, liquids, and biochemical molecules [116, 115]. On exposure to chemical substances, several of its physical parameters, such as the refractive index, electrical conductivity and photoluminescence, change drastically due to its very effective interaction with various substances through adsorption and capillary

condensation. In addition, the surface of the porous silicon can be chemically modified so as to be sensitive to a specific analyte [117]. Moreover, PSi is a widely-available, low-cost material, compatible with standard silicon-based processing technologies and thus it can be easily integrated with smart sensing devices and microsystems. In the past few years, extensive experimental work has been carried out showing its successful use in optical sensors for chemical and biological sensing [118, 119].

5.1.2.1 Capillary Condensation

The phenomenon of capillary condensation occurs when a fluid, which is a gas in a macroscopic volume at a lower pressure than the saturation value, condenses into a dense liquid-like state inside narrow capillaries or nano-size pores [115]. Typically, the number of molecules that can be adsorbed by a porous layer depends on the total pore volume. Moreover, the curved surfaces of the pores enhance the attraction for molecules of wetting substances due to van der Waals interactions, resulting in their adsorption and capillary condensation [120]. Capillary condensation is regulated by the Kelvin equation [121]:

$$N_A k_B T ln(\frac{P}{P_{sat}}) = -\frac{2M\gamma cos\theta}{r\rho} \tag{5.1}$$

where N_A is the Avogadro constant, k_B is the Boltzmann constant, T is the absolute temperature, M is the molecular weight, ρ is the liquid density, θ is the contact angle, γ is the liquid-gas surface tension, P/P_{sat} is the relative pressure of a gas in equilibrium with a liquid in a cylindrical pore of radius r, and P_{sat} is the pressure value at saturation. Accordingly, the smaller the pore radius, the lower the relative vapour pressure at which the capillary condensation occurs, at a given temperature. During the capillary-condensation process, the air in the voids is replaced by condensed vapour. The extent of adsorption and capillary condensation are both influenced by the affinity of the surface of the porous matrix, which can be tailored by chemical modifications [122]. The use of capillary condensation in chemical-sensing applications, in particular for vapour sensing, has been widely proposed in the literature [115, 116, 121, 123, 124] . These sensors are typically designed to detect different vapours through changes in the electrical or optical properties of the PSi layer, such as the capacitance, conductivity and refractive index [123].

5.1.2.2 Optical properties of porous silicon

Due to the presence of air in the pores, the refractive index of PSi is lower than that of bulk silicon, and it decreases with increasing porosity. This porosity can be controlled and is proportional to the applied current density during the etching process [125]. The

possibility of modulating the PSi porosity and having control of the interface between layers of different porosities, allows the fabrication of a wide range of interesting structures, such as interferometers, high-reflectivity Bragg reflectors and optical waveguides, which have shown high optical-sensing capabilities [116]. Reversible changes in the refractive index of porous silicon upon interaction (adsorption and/or condensation processes) with specific gas species have been demonstrated through quantitative monitoring of the variation of different parameters (e.g. photoluminescence spectrum; reflected, transmitted, and diffracted optical power) as a function of the gas concentration [123]. When a PSi layer is exposed to vapours, the substitution of air ($n = 1$) in the pores by its molecules ($n > 1$) causes peak shifts in wavelength, which correspond to a change in the optical path-length nd (n being the average refractive index of the layer and d the film thickness). Since the thickness is fixed by the physical dimension of the PSi matrix, the observed variation is due to changes in the refractive index. By measuring the peak shifts in the reflection spectrum of the PSi after exposure to vapours, various chemical substances can be detected [113, 126] and binary mixture compositions can quantitatively be characterised [127]. A quantitative model taking into account the optical path increase (as a consequence of the condensed vapours in the material pores) can be realised by applying the Bruggemann effective-medium approximation theory, assuming that, after exposure at equilibrium, the chemical vapours fill a fraction V of the pore volume p according to the following equation [121]:

$$(1-p)\left(\frac{\varepsilon_{Si}-\varepsilon_{PSi}}{\varepsilon_{Si}+\varepsilon_{PSi}}\right)+(p-V)\left(\frac{\varepsilon_{air}-\varepsilon_{PSi}}{\varepsilon_{air}+2\varepsilon_{PSi}}\right)+V\left(\frac{\varepsilon_{ch}-\varepsilon_{PSi}}{\varepsilon_{ch}+2\varepsilon_{PSi}}\right)=0 \tag{5.2}$$

where p is the layer porosity, V is the liquid fraction of the condensed vapour and ε_{Si}, ε_{air}, ε_{ch} and ε_{PSi} are the dielectric constants of the silicon, air, chemical substance and porous silicon, respectively [121].

5.2 Preparation of the sensor

This section describes in detail all the experimental steps carried out to fabricate the MIR evanescent-wave fibre-optic sensor. First, a MIR optical fibre was modified by creating a U-bend in order to enhance the penetration depth of the evanescent field in the bent region. This step was followed by the formation of PSi microparticles through sonication of a fabricated PSi membrane and coating the U-bent region of the fibre with the PSi microparticles through physisorption.

5.2.1 Fabrication of the U-bent optical fibre

This work was carried out using uncladded cylindrical silver-halide fibres of composition $AgCl_{0.3}Br_{0.7}$, provided by our collaborators at the research group of Prof. Abraham Katzir (University of Tel Aviv, Israel). The exact fabrication procedure, as well as the mechanical properties of these fibres are discussed in detail in the literature [128, 129]. In brief, a single crystal is first grown from a hot melt of silver chloride (AgCl) and silver bromide (AgBr) at a predefined concentration of each constituent, which is then extruded through a die, to form polycrystalline fibres of a desired diameter. In this case, the provided fibre segments (of approx. 30 cm in length) had a diameter of 700 μm, a refractive index of 2.1 and typical losses of 1 dB/m. Given the malleable nature of AgBrCl fibres, a U-bend with a radius of approximately 0.5 cm was easily prepared by bending the fibre gently around a small cylinder. In order to protect the uncladded fibre from excessive exposure to visible and UV radiation (which have been shown to degrade silver halides [128]) as well as accidental damage, a black polyethylene (PE) jacket was threaded onto each side of the bent fibre, leaving the bent region exposed for sensing. It is worth noting that whenever the fibre was not in use for sensing, the bent region was also covered by a PE protective sleeve. The fibre jacket is held in place by jacket holders, placed on the fibre extremities, and by epoxy glue near the sensing region. SMA connectors are fitted onto the other end of the jacket holders to allow easy coupling to a FT-IR spectrometer. Finally, epoxy putty is used to secure the fibre holders in place for a more robust system. Figure 5.2 shows the final U-bent fibre setup, with a total length of approximately 15 cm.

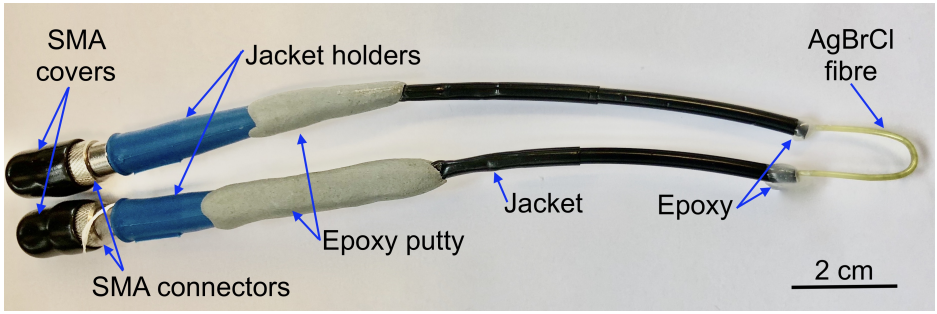

Fig. 5.2 Picture of the U-bent optical fibre.

5.2.2 Fabrication of the PSi membrane and microparticles

Nanoporous silicon membranes of 15 mm diameter were fabricated by electrochemical etching of boron-doped (p-type) silicon wafers (Pi-Kem) with a (100) crystal orientation. The silicon wafers were initially cleaned using a lint-free tissue and ethanol and subsequently

dried with a stream of nitrogen. A standard electrochemical etching setup, as shown in Figure 5.3, was used to perform the etching process, where a silicon wafer was mounted into the Teflon etch cell, making sure the aluminium back-contact is in place in the bottom of the cell. The desired mixture of 48% hydrofluoric acid (HF) and ethanol (EtOH) was added to fill to just below the spout hole of the etch cell. The platinum (Pt) electrode was immersed into the electrolyte so that it was just below the surface of the solution. The etching process was then initiated at the required current density using the Iviumsoft software. After the completion of the etch, the formed membrane was detached by applying a constant high current of 500 mA for 30 seconds. Following the membrane lift-off, the cell was washed out with EtOH (twice for three minutes) and pentane. The Si wafer was carefully removed from the cell and tweezers were used to lift the membrane off from the substrate.

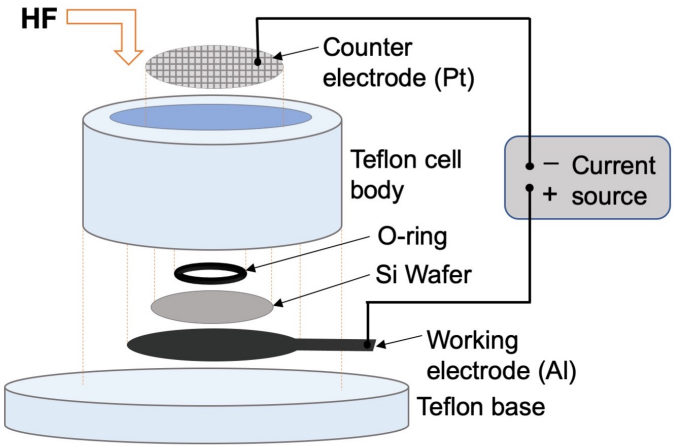

Fig. 5.3 Electrochemical etching setup for porous-silicon fabrication.

Three PSi membranes were fabricated using the etch conditions presented in Table 5.1. Membranes M1 and M2 were produced with a thickness of 50 and 200 μm, respectively. Membrane M3, produced under the same conditions as M2 and also with a 200 μm thickness, was thermally oxidised in a Lenton furnace under a flow of oxygen gas*. An image of the 50 μm-thick PSi membrane (M1) is shown in Figure 5.4.

All membranes were characterized by IR spectroscopy in order to evaluate and compare their IR optical properties. IR measurements were performed using a Bruker Vertex 70 FT-IR spectrometer. To obtain measurements within the MIR spectral range, the following standard optical components were used: a KBr beamsplitter, a liquid-nitrogen-cooled MCT detector and a MIR source, sensitive in the region from 7500 to 800 cm^{-1}.

*This process was carried out by another member of the research group.

Table 5.1 Electrochemical etching conditions used to produce the PSi membranes M1, M2 and M3.

M	Thickness (μm)	Wafer resistivity (Ω cm)	HF:EtOH ratio	Current density (mA cm^{-2})	Etch time (mins)	Oxidation
1	50	0.01-0.02	3:7	25	50	N/A
2	200	0.01-0.02	1:1	120	38	N/A
3	200	0.01-0.02	1:1	120	38	thermal

These parameters were established and optimised by another member of the research group.

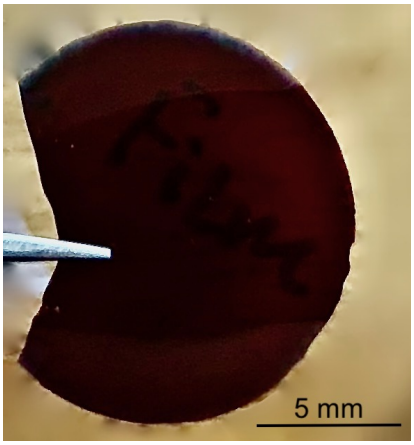

Fig. 5.4 Picture of the 50 μm-thick PSi membrane.

The membranes were carefully stuck to a sheet of aluminium foil with a small hole for the light to transmit though and this set was placed onto the Standard QuickLock Transmittance sample mount within the sample compartment. The sample compartment lid was shut and each spectrum was acquired via the OPUS software interface with an average of 32 scans to increase the signal-to-noise ratio. Figure 5.5 shows the IR spectra of the three PSi membranes. The spectra of the non-oxidised membranes (M1 and M2) show two main absorption bands in the following frequency regions: $\approx$ 915 cm^{-1} and 2070-2170 cm^{-1}, which correspond to the Si-H_2 scissors bending vibration and the SiH_x (x = 1,2,3) stretching vibrations, respectively [130]. The spectrum of the thicker (200 μm) membrane (M2) shows a larger overall absorbance and indications of spectral saturation were observed for the SiH_x vibration peak. The broad band in the spectral region between 1000-1400 cm^{-1} corresponds to the Si-O-Si vibrational stretch mode and is seen for all membranes to a smaller or larger degree, depending on the extent of oxidation. For the non-oxidised membranes, a smaller absorption in this region is seen due to involuntary post-oxidation during the sample drying process which depends on the surrounding environment. For the oxidized membrane (M3),

the Si-O-Si absorption peak is far more prominent, producing a saturated spectral band in this region.

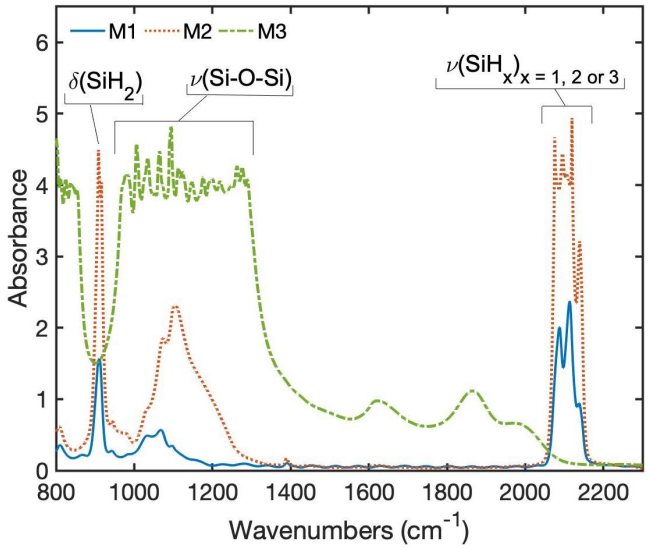

Fig. 5.5 IR spectra of the produced porous-silicon membranes: a non-oxidised 50 μm-thick membrane (M1); a non-oxidised 200 μm-thick membrane (M2) and a thermally oxidised 200 μm-thick membrane (M3).

The spectrum of the oxidised membrane also shows the decrease in intensity and disappearance of the SiH_2 scissoring and SiH_x stretching modes [131]. While the peak seen at 800 cm^{-1} for M3 corresponds to a O_nSiH_x deformation, the assignment of the small peaks observed at 1630 and 1870 cm^{-1} are unclear, although literature suggests that they could be caused by O_nSiH_x vibrations [130–132]. Overall, the oxidised membrane showed the highest absorbance in the observed MIR spectral range. Ideally, the PSi fibre coating should not significantly reduce the optical MIR transmission or evanescent field of the fibre, otherwise the optical losses will be high and the sensor performance will be compromised. Therefore, it was essential to minimize absorption by the PSi enhancement coating. As a proof-of-concept, the non-oxidised 50μ-thick membrane (M1) was chosen to fabricate the PSi microparticles for the fibre coating. The PSi microparticles were made by breaking up the selected PSi membrane into microparticles via sonication in 100 μL of a 80% solution of EtOH in deionized (DI) water for 10 minutes at room temperature, which resulted in a concentrated suspension of microparticles.

5.2.3 Coating of the fibre

The previously prepared U-bent fibre (described in Section 5.2.1) was coated with the prepared PSi microparticles of Section 5.2.2. For this, the microparticle suspension resulting from the sonicated PSi membrane was pipetted onto the U-bent region of the fibre and heated at a distance of $\approx$ 10 cm above a hot-plate held at 120^{o}C until all of the ethanol-DI water solution evaporated, leaving behind the PSi microparticles physisorbed onto the fibre-surface. During the heating process, a rotating motion was manually applied to the fibre to evenly distribute the PSi particles across its surface. This coating process, including the microparticle deposition and solvent evaporation, can be repeated more than once to ensure a full and uniform coverage of the U-bent region of the fibre. A field-emission scanning electron microscope (FEG-SEM, TESCAN MIRA3, X-Max, Oxford Instruments) was used to take images of the PSi-coated fibre, which were processed using ImageJ software to obtain information on the coverage, dimensions and morphology of the PSi microparticles. Figure 5.6a shows an SEM image of the PSi microparticle coating adhering to the surface of the U-bent region of the fibre, with microparticle dimensions ranging from 20 to 200 μm. The dimensions are likely to be highly dependent on the membrane sonication time. For longer sonication times, particles of smaller dimensions would be expected. The microparticle coverage of the fibre was controlled by the number of coating cycles applied and rotation speed. Figure 5.6b shows a zoomed-in SEM image of a single PSi microparticle, illustrating the pores, with dimensions ranging between 10 and 500 nm.

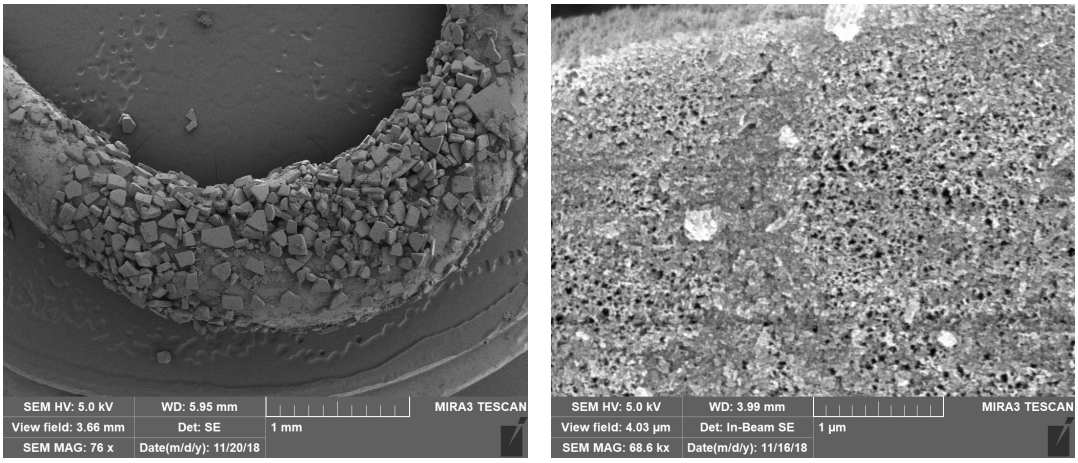

(a) (b)

Fig. 5.6 SEM images of PSi-microparticle coating on U-bent optical fibre surface. (a) U-bent region; (b) single PSi microparticle.

5.3 Optimisation and operation of the sensor

The first step in optimising the sensor and testing its performance was to select different VOCs for the sensor to be exposed to, as described in subsection 5.3.1. In order to carry out the VOC measurements, an optical setup was custom-made (subsection 5.3.2) to expose the sensor to the selected VOCs at varying concentrations. The following subsection (5.3.3) describes the optimisation process of the developed sensor by determining the most favourable number of PSi coatings. Once the optimum number of coatings was determined, a comparative study between a coated and uncoated fibre-optic sensor was carried out (subsection 5.3.4) followed by a study of the sensors' performance in simultaneous detection of different compounds within a mixture (5.3.5).

5.3.1 VOCs and specific peak selection

In order to optimise the sensor performance and test the operation of the sensor, the following three VOCs with boiling-point ranges between 50-100 and 240-260 ^{o}C were selected: acetone, ethanol and isopropyl alcohol (IPA). To identify the characteristic peaks of each compound prior to the above-mentioned experiments, MIR measurements of each individual compound were taken using a MIR fibre-coupled FT-IR spectrometer (FT-IR-FC-4TE Rocket, ArcOptix Switzerland), coupled to a U-bent MIR optical fibre sensor (from the A. Katzir research group), which was dipped into diluted (50% (v/v) in DI water) solutions of each compound. Figure 5.7 shows the spectra of each compound and their peak assignments are shown in table 5.2.

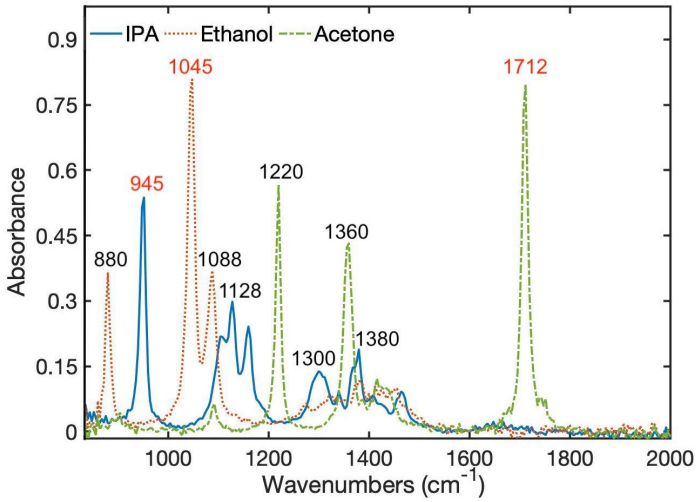

Fig. 5.7 IR spectra of 50% (v/v) solutions of IPA, ethanol and acetone in water, measured using a MIR U-bent optical fibre-sensor.

Specific peaks are seen for each compound and the strongest peak for each one, namely 945, 1045 and 1712 cm^{-1} for IPA, ethanol and acetone (highlighted in red in Figure 5.7), respectively, were used for compound identification and quantification in the following subsections.

Table 5.2 Spectral peak assignments associated to the spectrum of 50% (v/v) solutions of IPA, ethanol and acetone in water [44, 133, 134].

Compound	Peak position (cm^{-1})	Description	Assignment
IPA	945	strong	C-H bend
	1128	medium	C-C stretch
	1300	weak	O-H in-plane bend
	1380	weak	CH_3 deformation (sym.)
Ethanol	880	medium	C-C stretch
	1045	strong	C-O stretch (sym.)
	1088	medium	C-O stretch (asym.)
Acetone	1220	medium	C-C stretch (asym.)
	1360	medium	CH_3 deformation (sym.)
	1712	strong	C=O stretch

5.3.2 Experimental setup for optical measurements

For accurately controlling the amount of VOCs exposed to the fibre-optic sensor during optical measurements, a custom-built gas flow-cell was designed and fabricated, as shown in the CAD model of Figure 5.8a. The 26 x 20 x 8 mm flow-cell comprised of two polyether ether ketone (PEEK) parts, each with a 15 x 15 x 2.5 mm internal cavity. The two compartments of the flow-cell were sealed together using four bolts with the U-bent fibre inside, ensuring that the sensitive portion of the fibre was suspended within the gas compartment of an internal volume of approximately 1.1 cm^3. A photo of the sensing region of the U-bent fibre placed inside the internal cavity of the unassembled flow-cell is shown in Figure 5.8b. Lateral holes on either side of the cell were used as the inlet and outlet for VOCs, flowing in one direction. The VOCs flow through the gas cell was obtained by bubbling pure air through bottled VOC liquids on a temperature-controlled plate (Torrey Pines Scientific, Ecotherm). The resulting vapour was directed through the outlet of the sealed bottle into the inlet of the gas cell (containing the U-bent fibre) via PTFE connector tubing of 0.3 mm ID and 1.6 mm OD (Cole Parmer). The flow of air and VOCs were controlled using flow controllers (Alicat Scientific). Schematic diagrams of the experimental setups used in this

work are shown in Figure 5.9. The setup of Figure 5.9a was designed for measurements involving the detection of pure VOCs at varying concentrations. Here, a 4-point valve was used to switch between pure air and air containing VOCs at their saturated vapour pressure, flowing through the cell. Depending on the flow-rate of each one of these (controlled by the flow-controllers), VOC-air mixtures of varying concentrations can be achieved. This setup was used for determining the ideal number of PSi coatings for optimum VOC sensitivity, as well as to compare the sensitivity of an uncoated U-bent fibre with that of the same fibre coated with PSi microparticles, as later described in subsections 5.3.3 and 5.3.4. The setup of Figure 5.9b allowed the simultaneous flow control of two different VOCs through the gas cell. It was therefore used for testing the qualitative sensing capabilities of the developed sensor by conducting simultaneous measurements of two different VOCs at varying concentrations, as described in detail in subsection 5.3.5. In this case, the relative concentration of each VOC was controlled by their flow-rate through the gas cell at room temperature. Here, a T-junction valve was used to mix the two different VOCs at different flow-rates, varying from 0 to 500 sccm (standard cubic cm per minute), resulting in different VOC mixtures.

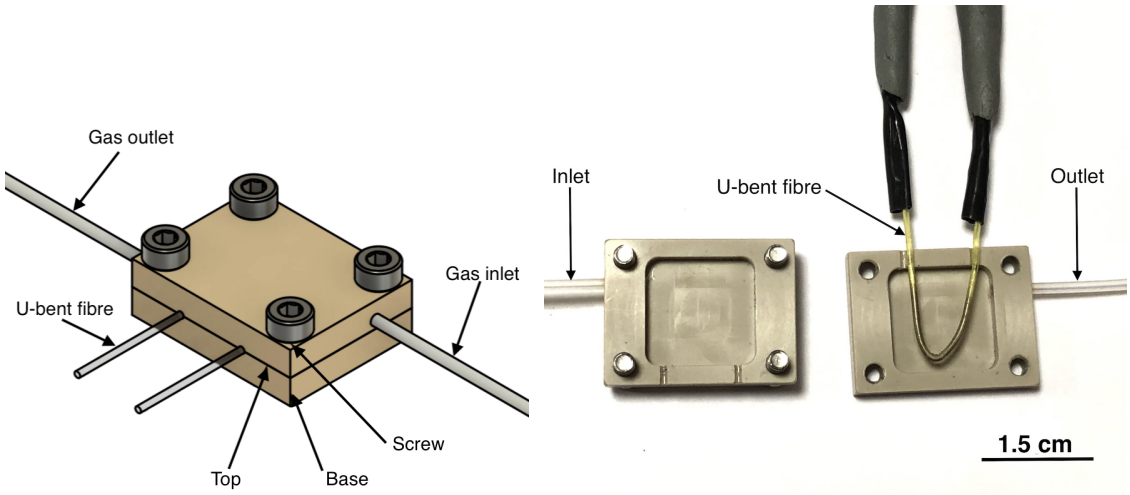

(a) (b)

Fig. 5.8 Schematic illustration of the custom-built gas flow-cell for controlled VOC measurements. (a) CAD model of the assembled gas flow-cell; (b) picture of the unassembled gas flow-cell with the sensing region of the PSi-coated U-bent fibre inserted into its internal cavity.

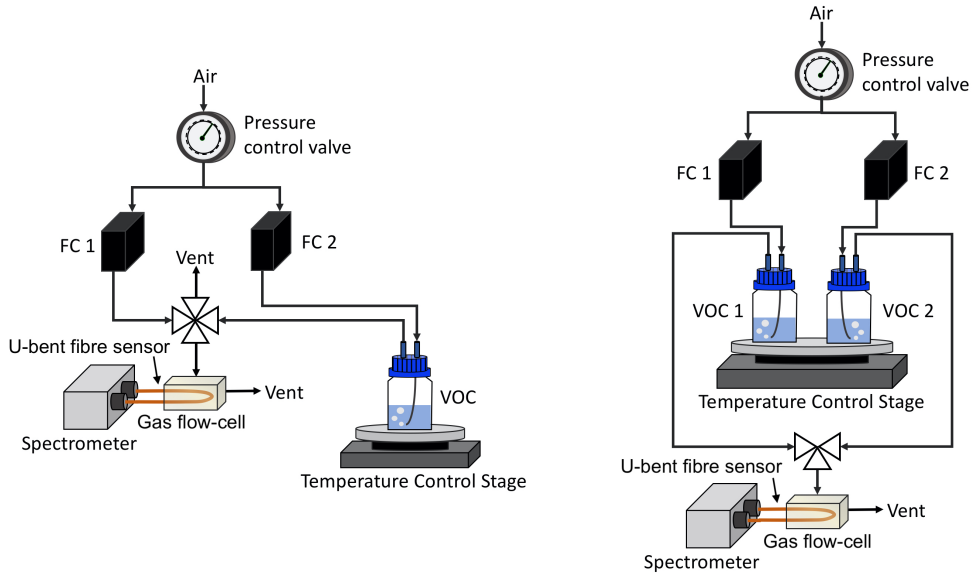

(a) (b)

Fig. 5.9 Schematic illustration of the experimental setup for VOC sensing. (a) Setup for detection of pure VOCs at different concentrations); (b) setup for simultaneous detection of two VOCs at varying concentrations. In both cases, the gas flow rate is controlled by two flow controllers, FC1 and FC2.

5.3.3 Optimisation of the number of coatings

To determine the effect of the PSi coating on the transmission and the light attenuation of MIR radiation of the U-bent fibre, 5 iterations of fibre coatings were performed and the transmitted spectrum was measured in air, as shown in Figure 5.10. These spectra show the effect of increased absorbance upon adding PSi layers on the fibre, as well as peaks associated with the PSi microparticles themselves, the silver-halide fibre, atmospheric absorption, and absorption by the components of the FT-IR spectrometer [128]. The raw measured spectrum of the PSi-coated fibre shows a slight overall decrease in intensity compared to the uncoated fibre, and a prominent absorption band of a coated fibre at 1070 cm^{-1}, corresponding to a Si-O-Si stretch, pointing to oxidized PSi microparticles [135–138]. In fact, it was expected that the microparticles oxidize far more rapidly than bulk Si due to the larger surface area. Compared to the uncoated fibre, the overall fibre transmission decreased by 5% and 38% for 1 and 5 coating-layers, respectively. To study the effect of the number of coatings on the acquired IR absorbance spectra, both the uncoated and coated fibres were exposed to saturated acetone vapour using the experimental setup of Figure 5.9a and a flow-rate of 200 sccm at room temperature. The resulting spectra are shown in Figure 5.11a. It was clearly

observed that there was an increase in the absorbance peak intensity for the coated fibre compared to the uncoated fibre.

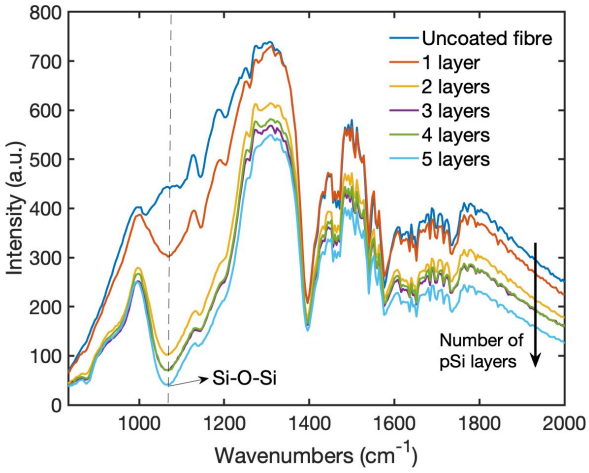

Fig. 5.10 Single-beam spectra of a U-bent silver-halide fibre with no coating and with one to five coating layers of PSi microparticles.

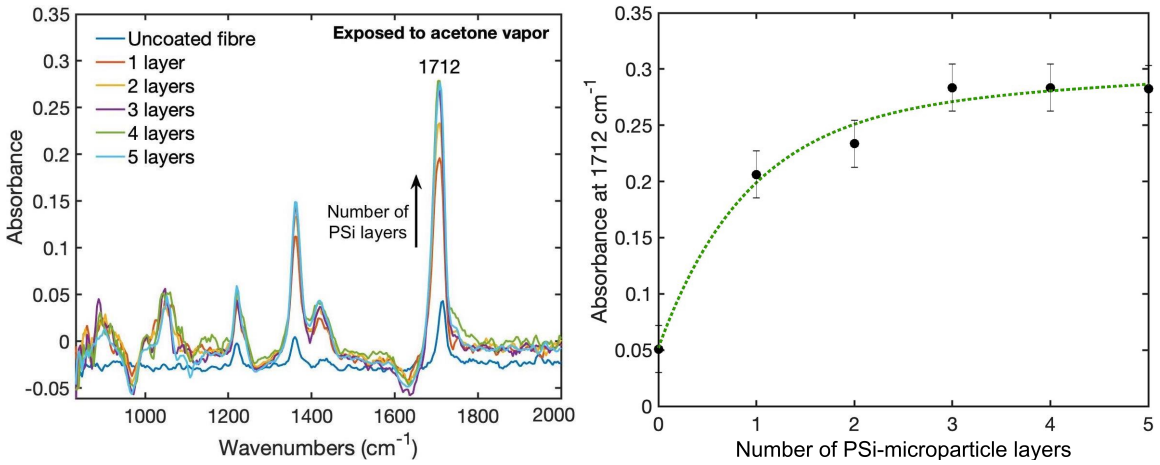

(a) (b)

Fig. 5.11 (a) Absorbance spectra for the uncoated and coated fibre, with increasing layers of PSi microparticles, exposed to acetone vapour; (b) absorbance intensity of the C=O acetone stretch peak at 1712 cm^{-1} as a function of the number of PSi microparticle layers.

Moreover, the peak intensity increased with increasing number of PSi-coating layers. The peak intensity at 1712 cm^{-1}, corresponding to the acetone carbonyl C=O stretch, is plotted as a function of the number of layers in Figure 5.11b. The absorbance is seen to increase with the number of PSi microparticle layers until a saturation point is reached after the third layer.

This saturation may be due to a reduction of analyte penetration close to the fibre through the increasingly thick set of PSi layers. Therefore, it was determined that the optimum number of PSi microparticle layers to coat the fibre was three. Although coating with additional layers did not affect the sensor performance, it is more laborious and time-consuming.

5.3.4 Operational sensitivity: uncoated versus coated fibre

Once the optimal number of PSi coatings was established using acetone, the detection sensitivity of the coated versus uncoated fibres was also assessed for the other VOCs (IPA and ethanol) using the setup of Figure 5.9a. The resulting spectra of IPA and ethanol measured using the uncoated and coated fibres are shown in Figure 5.12. Similarly to what was observed for acetone, a clear increase in absorbance of both compounds was seen for the coated fibre.

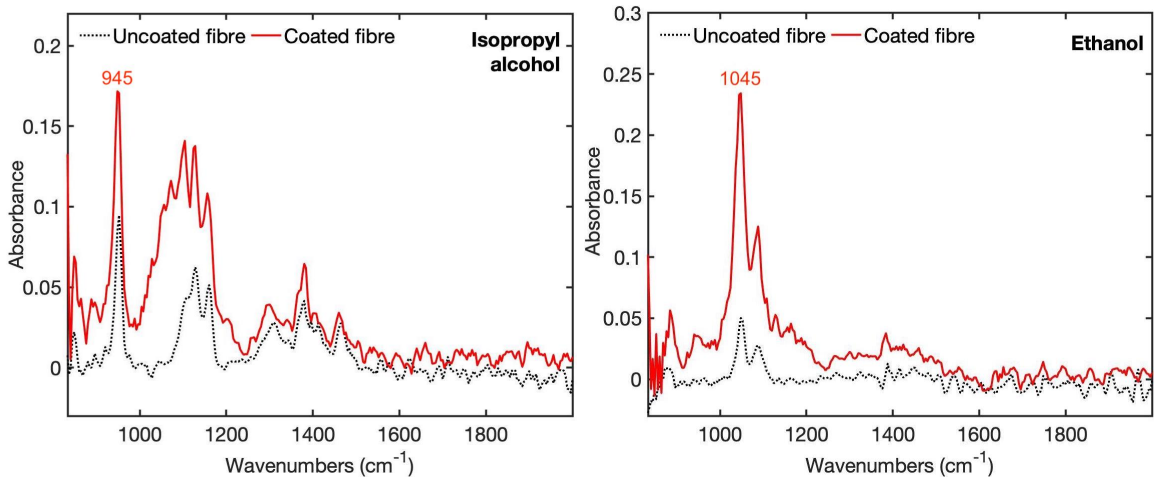

Fig. 5.12 Spectra acquired with coated and uncoated fibres exposed to: (a) isopropyl alcohol; and (b) ethanol.

Figure 5.13 shows the enhancement in sensitivity of the coated fibre, compared to the uncoated fibre, for all three compounds, according to the absorbance peak intensities (at 945 cm^{-1}, 1045 cm^{-1} and 1712 cm^{-1} for IPA, ethanol and acetone). Based on these results, the sensitivity enhancement factors ($Abs_{coated}/Abs_{uncoated}$) for acetone, ethanol and IPA were determined to be 12.7, 10.5 and 9.6 respectively, demonstrating an order-of-magnitude in sensitivity enhancement using this method. The determined enhancement is not quite the same for the three measured compounds, probably because the VOCs' adsorption onto the

porous matrix is highly dependent on the analyte properties, such as its affinity to the surface and the analyte vapour pressure.

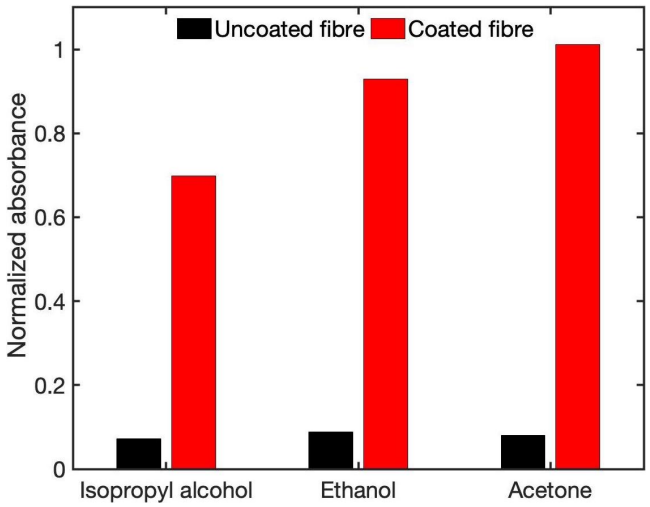

Fig. 5.13 Normalised absorbance peak intensities of isopropyl alcohol (945 cm^{-1}), ethanol (1045 cm^{-1}) and acetone (1712 cm^{-1}) for uncoated and coated fibres.

In addition to the enhancement in the sensor sensitivity, other performance characteristics, such as the kinetic response and recovery times, were studied. In order to demonstrate the reversibility of the sensor's response, time-dependent measurements were conducted by repeatedly exposing the sensor to acetone vapour. Each spectrum was integrated over one minute, meaning that the time resolution of the sensor is one minute. Figure 5.14 shows the absorbance intensity at 1712 cm^{-1} for acetone, when switching from air to saturated acetone vapour three times. It can be seen that the absorbance signal returns to the original baseline level throughout, meaning that the sensor shows good reversibility. Moreover, the response and recovery times appear to be around one minute.

In order to test and compare the uncoated and coated fibres' response to different VOC concentrations, the acetone absorbance peak was measured for both cases as a function of VOC concentration, again, using the setup of Figure 5.9a. Figure 5.15 shows the results of gradually increasing concentrations of acetone through the gas flow-cell from 0 to 100%, for both uncoated and coated fibres. An increase in the absorbance can be observed with an increase of acetone concentration for both fibres. This increase is significantly larger for the coated fibre. The plateau response of the coated fibre, visible at the high concentrations, could be due to pore saturation. The error bars were calculated by taking into account the changes in the intensity at a specific wavelength over time and calculating the respective standard deviation.

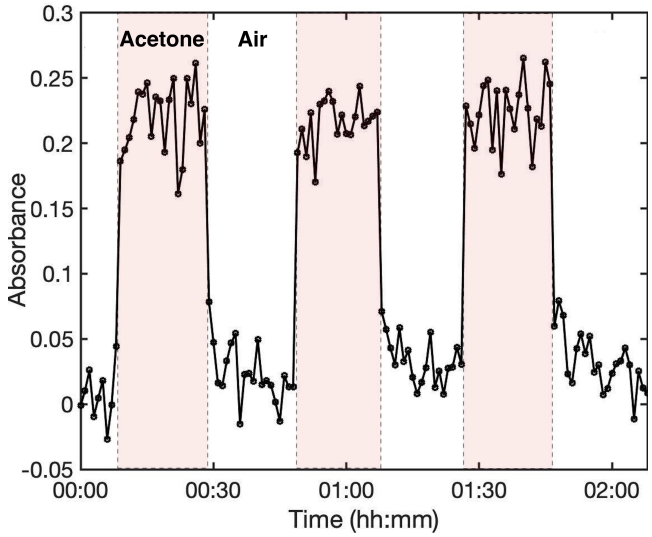

Fig. 5.14 Reversibility test for the sensor upon exposure to saturated acetone vapour three times. The absorbance corresponds to a specific acetone peak at 1712 cm^{-1}.

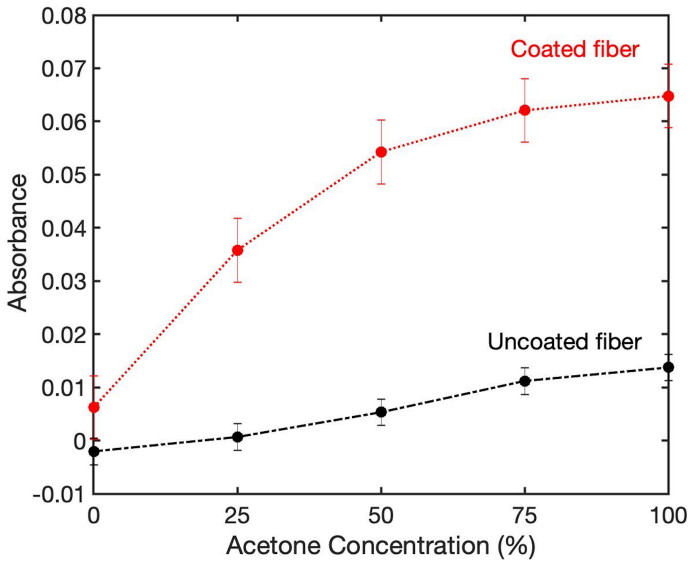

Fig. 5.15 Absorbance of the C=O acetone stretch at 1712 cm^{-1} as a function of acetone concentration for uncoated and coated fibres.

5.3.5 Mixtures

To demonstrate the developed sensors' capability for simultaneous detection of different VOCs, the coated PSi fibre was exposed to a mixture of ethanol and acetone using the experimental setup of Figure 5.9b. The relative concentrations of ethanol and acetone were simultaneously varied between 0 and 100%, as shown in table 5.3.

Table 5.3 Flow-controller flow-rates to achieve different mixtures of VOC_1 and VOC_2 flowing through gas chamber.

FC1 flow-rate (sccm)	**VOC_1**	**FC2 flow-rate (sccm)**	**VOC_2**
500	100	0	0
400	75	100	25
250	50	250	50
100	25	400	75
0	0	500	100

The absorbance spectra of 100% acetone, 100% ethanol and a 50%:50% mixture are shown in Figure 5.16, highlighting the characteristic peaks at 1045 cm^{-1} and 1712 cm^{-1} for ethanol and acetone, respectively. Figure 5.17 shows the absorbance variation at the selected wavelengths for acetone and ethanol, as a function of relative vapour concentrations. It was seen that the signal for acetone increases with the increasing relative acetone concentration, and the signal for ethanol decreases with the decrease in relative ethanol concentration. For acetone, a similar plateau response as previously described was observed, while for ethanol the response appears to be linear over the measured range. This can be attributed to the difference between the saturated vapour pressures of acetone and ethanol at 20^oC: 184 mmHg vs. 43.7 mmHg, respectively. Therefore, we may conclude that a high vapour concentration of acetone saturates the pores of the PSi.

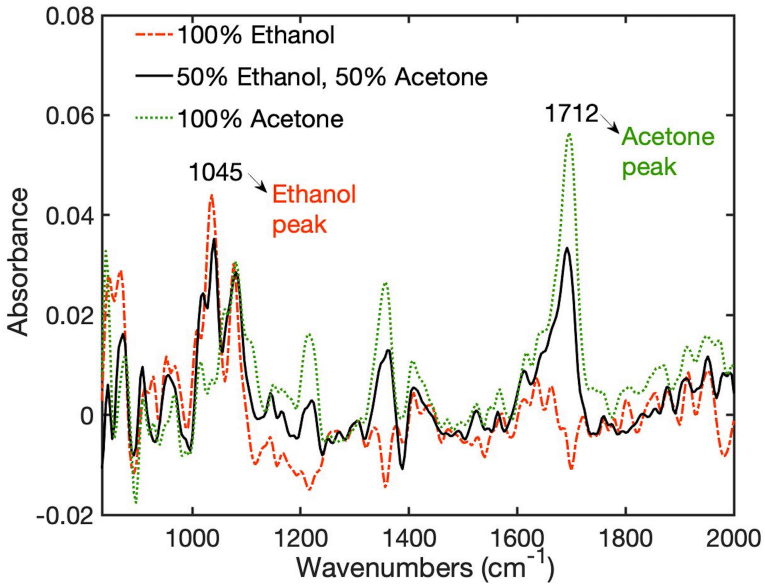

Fig. 5.16 Absorbance spectra of 100% acetone, 100% ethanol and a 50%:50% mixture using a PSi microparticle-coated fibre.

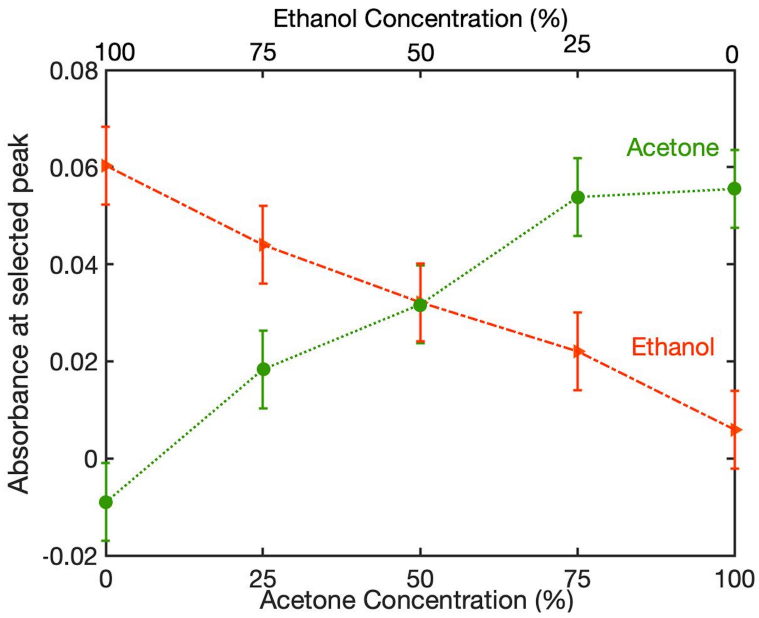

Fig. 5.17 Relative peak intensities at wavelengths of 1045 cm^{-1} and 1712 cm^{-1} for ethanol and acetone, respectively, for varying binary-mixture concentrations.

5.4 Conclusions

A novel fibre-optic evanescent-wave spectroscopy method was found to enhance the sensitivity for detecting VOCs. Porous silicon, an attractive material for use in sensing applications due to its porous nature and large surface area, was used to coat the surface of a silver-halide MIR-transmitting U-bent fibre. The infiltration of solvents or vapours into the material pores can efficiently be detected by monitoring the changes in light propagation inside the PSi structures. In this work, it was shown that the porous silicon cladding on the optical fibres' surface concentrated the VOCs inside it, thus enabling a larger number of molecules to interact with the evanescent field of the fibre sensor. The effect of the PSi microparticles on the optical IR transmission spectrum of the fibre was studied. While an increasing number of PSi microparticle layers on the fibre surface caused a gradual decrease in transmission, an increase in sensitivity to VOCs was observed with an increase in the number of layers up to 3, at which a saturation point was reached. It was shown that the PSi-coated U-bent fibre exhibited a significantly higher sensitivity for the three measured VOCs, isopropyl, ethanol and acetone, compared to the uncoated fibre. In addition to the increased sensitivity to pure VOCs, the simultaneous detection of different relative concentrations of acetone and ethanol was also demonstrated. This arrangement can be further improved in enabling better sensitivity and selectivity by functionalising the surface of the PSi and hence changing the affinity

of the different VOCs to the porous surface. Moreover, the sensitivity could potentially be improved and optimised by varying the dimensions and density of microparticles as well as the dimensions of the porous silicon pores. The homogeneity of the PSi coating may also be improved by a more controlled variation of the size of the coated region of the fibre and by exploring different coating methods which will not interfere with the transmission of the fibre and evanescent field. Future work will focus on exploring these possibilities.

Chapter 6

Bioprocess monitoring using MIR spectroscopy

6.1 Introduction and literature review

Biotechnological processes (bioprocesses) are vital in the development of any economy worldwide and include a vast range of sectors, including pharmaceutical, beverage production, agro-food and waste treatment [139]. Apart from distinct main objectives and price ranges of the end products, all bioprocesses include the cultivation of microorganisms under controlled conditions which form a complex combination of chemical, physical and biological events [139]. As complex and multi-variable systems, bioreactor operation involves the consumption of substrates and the generation of products and intermediate metabolites in the presence of live cells [139, 140]. These cells are typically suspended in the bioreactor medium in concentrations ranging from very low to constituting a major solid phase, and their presence can strongly interfere with the most frequently used analytical tools. Currently, the chemical constituents of bioreactor media (i.e. substrates, intermediates and products) are mostly monitored off-line* by methods requiring sample preconditioning steps, such as biomass separation [141]. One example of a well-established technique which is widely used for analysis of complex mixtures is high-performance liquid chromatography (HPLC). As well as sampling and sample preconditioning issues, off-line analytical methods are time-consuming and retrospective, and thus do not provide real-time information on the conditions affecting the bioprocess. In order to effectively control bioprocesses for increased productivity, efficiency and reproducibility, as well as for improved quality control and environmental pollution reduction, real-time monitoring of bioreactors is indispensable.

*The definitions of off-line, at-line, on-line and in-line monitoring are given in Subsection 6.1.1.

Great effort has been made in recent years to develop more efficient bioprocess-monitoring techniques, including the development of chemical sensors, bio-sensors, and optical sensors [142–144]. Although the developed sensors for on-line bioprocess monitoring show improved performance and reliability, they are costly, frequently limited to single-compound analysis and require frequent maintenance, which reduce their appeal and applicability, both in industry and research. Sensors for real-time bioreactor monitoring should ideally be rapid, non-destructive, sensitive, robust and also generate multi-analyte data without analyte consumption. Moreover, they should not interfere with culture metabolism and should be resistant to harsh, sterile and agitated environments [145]. Taking this into account, optical spectroscopy techniques are especially suitable for bioreactor monitoring and many of these, often coupled to optical fibres, have been implemented in a wide range of different *in-situ* applications. Depending on the wavelength range used, such as UV–Vis, NIR, MIR, Raman, and fluorescence spectroscopy, different properties can be investigated [141]. In addition to quantifying media components and desired products, these techniques can also be used to detect unwanted by-products and determine the cause of their production. Moreover, real-time knowledge can allow the identification of deviations from the expected process so that appropriate adjustments can be made promptly, before the production of by-products. Of the above-mentioned optical techniques, MIR spectroscopy provides molecular-specific information of the sample of interest as each molecule leads to a unique absorption pattern. Moreover, it requires little to no sample preparation and allows fast and simultaneous determination of several analytes. Its use for the determination of bioreactor media components has been extensively reported and typically involves the implementation of statistical data-analysis methods to retrieve quantitative information [146, 147]. The reported studies are an explicit indication of the applicability and potential of on-line and in-line MIR spectroscopy for bioprocess monitoring. Different in-line bioprocess monitoring techniques by MIR spectroscopy have been developed and successfully implemented in monitoring media components in a range of fermentations, mainly via ATR [148–150] or fibre-optic probes [151], although fibre-optic probes have not been implemented as widely. In-line ATR and fibre-optic probes are commercially available from various companies, such as Art Photonics GmbH, Germany, and a specialised real-time ATR-based process analyser (IRmadillo) has been developed by Keit spectrometers, UK.

The aim of this work was to carry out a preliminary exploration of the capability and associated challenges of using fibre-optic-based MIR spectroscopy for in-line monitoring of a particular bioprocess by using a simple and relatively low-cost configuration and set-up. The bioprocess studied in this work was for the production of microbial biosurfactants, namely sophorolipids (SLs), where the goal was to monitor SLs production and other media

components as well as to identify the two commonly produced types of SLs (acidic and lactonic). While SLs have been previously studied by IR spectroscopy [152, 153], to the best of the author's knowledge, the continuous in-line monitoring of SLs in bioreactors has not yet been reported. As a first approach, bioreactor samples were measured on standard FT-IR equipment for proof-of-principle and to study the spectra of the compounds of interest. This was followed by the preliminary development of a sensor comprising of a U-bent MIR optical fibre and assessing its performance for real-time in-line analysis of bioreactor media. This work was carried out in collaboration with our collaborators at Holiferm Ltd. (Manchester, UK), a fermentation technology company, who provided insight for the need and requirements of such a sensor, as well as all of the bioreactor samples used in this study.

The following subsections provide further insight into the general bioprocess monitoring methods, as well as into the particular fermentation and its compounds studied in this work. Section 6.2 explains the general requirements for an in-line bioprocess monitoring sensor according to the needs of bioreactor companies. Section 6.3 describes the initial work carried out to assess the feasibility of using standard MIR spectroscopy (ATR-FTIR, based evanescent-field) for measuring fermentation samples and detecting the bioprocess compounds of interest. Section 6.4 describes the development of a preliminary fibre-optic probe and system, as well as its assessment for bioprocess sample monitoring. Finally, Section 6.5 discusses the overall conclusions and future work.

6.1.1 Bioprocess monitoring methods

The quality of the product of a given bioprocess can be ensured by monitoring vital process parameters using process analytical technology (PAT) tools [139]. This is a particular advantage in processes where the raw materials are subject to change, where by knowing the relationship between the raw materials and the product, the process parameters (e.g. the temperature, amount of raw material added, etc.) can be chosen according to the desired product quality. In order to measure process parameters, suitable sampling methods from the process line or vessel need to be selected. Bioprocess monitoring is typically performed by the following methods:

- **Off-line analysis:** A sample is withdrawn from the process and analysed by a laboratory equipment located at a physical distance from the process environment after a suitable sample-preparation process. Although high selectivity and sensitivity is usually achieved, there is always a delay in obtaining results, making it of little to no use for process control but potentially valuable for process understanding;

- **At-line analysis:** A sample is withdrawn from the process and analysed in close proximity to the process line/vessel after suitable sample preparation. Here, the analysers typically need to be more robust and compact than standard laboratory analysers, which often results in compromised selectivity and sensitivity;
- **On-line analysis:** A sample is automatically withdrawn, prepared and transported to the analyser, allowing monitoring in continuous-mode or at small time-intervals. The analysed sample can then be fed back into the process or discarded if sample preparation was required;
- **In-line** or ***in situ*** **analysis:** A probe is directly inserted into the bioreactor vessel in contact with the sample and measurements are taken of the unaltered process medium, allowing rapid and real-time measurements. However, robustness, long-term stability, aseptic design and cleaning-in-place (CIP) or steam-in-place (SIP) capability are required [145, 154].

Figure 6.1 shows the four above-mentioned bioprocess-monitoring methods. On-line and in-ine analyses are preferable to off-line and at-line analyses since rapid measurements are of major importance in most bioprocesses. While some chemical and physical parameters, such as pH, temperature and gas composition, are already monitored on-line and in-line during fermentation, there are a number of other chemical parameters, such as product concentrations, substrate composition and metabolic information, which are typically monitored off-line or at-line [155].

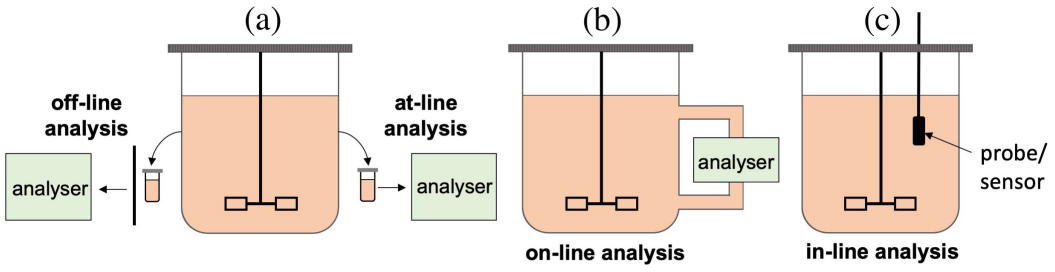

Fig. 6.1 Different bioprocess-analysis methods. (a) Off-line analysis, with analyser at a distance from the bioprocess laboratory environment, and at-line analysis, with analyser in the bioprocess environment; (b) on-line analysis; and (c) in-line or *in-situ* analysis.

While the currently observed bioreactor parameters are typically based on experience rather than on an understanding of underlying phenomena, there is still a need for developing appropriate bioprocess-monitoring tools to enable real-time acquisition of biological and chemical information during fermentation processes. The use of optical fibres for spectroscopic techniques is highly attractive for in-line process monitoring since they allow guidance

of light from one point to another without line-of-sight propagation. Moreover, they allow remote analysis to be carried out, as well as the use of a single analyser for performing measurements at several points in the bioprocess using a multiplexer.

6.1.2 Bioreactor process and compounds of interest

In this thesis, a particular bioreactor fermentation process, for the production of sophorolipids (SLs), was studied. SLs are one of the most promising microbially generated biosurfactants nearing large-scale commercialization, which are mainly produced by yeasts such as *Candida bombicola* in industrial bioreactor processes [156, 157]. They are industrially produced by a number of companies, who typically use them in cleaning products, due to their detergent and low-foaming properties. However, there are a number of studies that have shown potential therapeutic and medical applications of SL properties, such as antimicrobial, antiviral, antifungal, and anticancer properties. Moreover, the emulsifying and taste sensory properties of SL, make them potentially useful in applications within the food industry [156–158]. SLs are a type of glycolipid composed of a long-chain hydroxy fatty acid linked to a glucose sophorose, and thus, their production involves two kinds of substrates: a sugar (i.e. glucose) and a lipid source (i.e. oil), which are fed into the fermentation broth. There are two forms of SLs: lactonic SLs, where the fatty acid is joined by an ester bond to the second glucose monomer, and acidic SLs, where the fatty acid is only joined to one glucose monomer, which result in a range of different structures and properties. Figure 6.2 represents two common structures of lactonic and acidic SLs typically produced via *C. bombicola*. The lactonic forms are more hydrophobic and have been reported to have enhanced properties for anticancer, spermicide, cytotoxic and pro-inflammatory activities, while the acidic forms are better foaming agents with a higher water solubility, and have been reported to have better use in the food industry, cosmetics and bioremediation [159].

The fermentation medium is composed of different phases. Initially (at time zero of the fermentation), there is an oil phase and a broth phase, which is then inoculated with cells, forming another (solid) phase. However, since the cells are suspended in the broth phase, there is no apparent additional phase. The broth phase typically contains glucose, some residual oil, cells, and cellular by-products (e.g. carboxylic acids). After a period of time, SLs are produced, forming another phase (SL phase), containing approximately 50% SLs and 50% water. These two phases are then separated using appropriate separation methods, described elsewhere [157]. The concentration of glucose, oil and SLs vary naturally throughout the course of the fermentation. Since a prerequisite for an efficient fermentation process and SL production is real-time and dynamic monitoring of all or at least some of these compounds, the development of tools which enable this are of utmost importance.

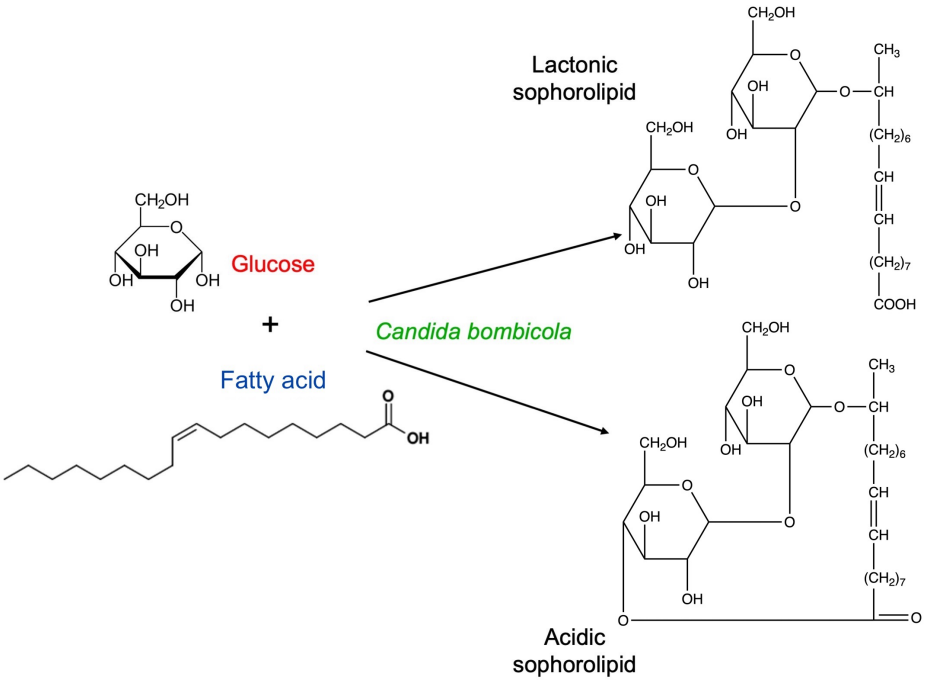

Fig. 6.2 Sophorolipid molecular structure in common lactonic and acidic forms produced by yeast *C. bombicola*, using glucose and a fatty acid as substrates. The lactonic sophorolipid has a lactonic bond joining the fatty-acid chain to the second glucose monomer of the sophorose, while the acidic sophorolipid has a free carboxylic acid terminating its fatty acid chain. Adapted from [157].

6.2 Device requirements and considerations

Real-time in-line sensors for monitoring non-ideal complex media, such as bioreactor media, are probably among the most challenging types of sensors to develop. A few requirements for such a sensor have previously been mentioned, such as rapid acquisition times, sensitivity, robustness, multi-analyte detection, non-destructive, and non-interfering with the fermentation process. Another important factor to consider is that the developed sensor should resist the harsh environments of bioprocesses, which often constitutes high-viscosity media, sterilisation and constant agitation. The sensor should also be able to perform measurements over extended periods of time (i.e. for the duration of the bioprocess, which can range from several hours to several days). Ideally, the sensing element itself should be robust and of sufficiently small dimensions to easily allow its insertion into the bioreactor via an appropriate insertion channel. Moreover, the analyser (comprising of a light source and detector), to which the fibre sensor is coupled, should be compact and relatively portable. The overall cost of such sensor should also be considered and kept to a minimum. For this, the

use of readily available materials, easy and simple fabrication processes and spectrometers with sufficient specifications should be prioritised. In terms of compound identification for the particular fermentation studied in this thesis, the developed sensor should ideally: (1) detect the product (SL) concentration in solution; (2) distinguish between lactonic and acidic SLs and determine the ratio between them in solution; (3) determine the oil concentration in solution; (4) detect the glucose concentration in solution; and (5) potentially detect other impurities in solution, such as proteins and cells.

6.3 ATR-FTIR spectroscopy of bioprocess compounds and samples

The aim of this section was to perform a preliminary study to assess the suitability of MIR spectroscopy for bioprocess monitoring by measuring the pure compounds of interest, as well as samples extracted from bioreactor processes using standard FT-IR spectroscopy and analysing their spectral features. Since the end goal was to develop a MIR fibre-optic sensor based on evanescent-field sensing, this preliminary work was carried out using a standard spectroscopy method, ATR-FTIR spectroscopy, which is equally based on evanescent-field sensing.

6.3.1 Analysis of individual bioreactor compounds

Here, the focus was drawn towards the analysis of unique MIR spectral features of each of the fermentation compounds of interest, namely the substrates, glucose and rapeseed oil, as well as the produced SLs, in order to determine the specific peaks for each of these and potential peak contributions. The ATR-FTIR measurements of the pure samples were carried out using a Perkin Elmer Spectrum 100 FT-IR spectrometer in conjunction with a Specac Heated Golden Gate ATR Accessory containing a single-reflection diamond ATR crystal. The spectrometer was operated via the Perkin Elmer 'Spectrum' Software and was equipped with a SiC hot-spot stabilised IR light source and a liquid nitrogen-cooled mercury cadmium telluride (MCT) detector. Before each set of experiments and between samples, the surface of the diamond was cleaned thoroughly using deionised (DI) water and a lint-free wipe in order to avoid contamination from any previous samples or solvents. Liquid samples were loaded by depositing 20 μL of sample directly onto the diamond surface, so that it is completely covered, using a pipette. The anvil provided by the accessory was left in an upright position for all liquid sample spectra acquisitions. MIR ratio spectra were generated via the accumulation of 150 scans with a resolution of 4 cm^{-1} using a background of water,

which was acquired before each set of measurements. The sugar and lipid source used in the particular fermentation studied in this work were glucose and rapeseed oil, respectively. Figure 6.3 shows the FTIR-MIR spectra of a 100 mM glucose solution in DI water, pure rapeseed oil and a pure SL sample as a product of these, between 800 and 1800 cm^{-1}, which was the region containing the main spectral features. Table 6.1 presents the main peak assignments associated with each of the compounds. The main glucose peaks are located between 950 cm^{-1} and 1200 cm^{-1}, corresponding to the C-O vibrations at 1036 and 1080 cm^{-1} and the C-C vibrations at 994, 1108 and 1152 cm^{-1} [83]. The spectrum of rapeseed oil presents its most prominent peak at 1744 cm^{-1}, assigned to the C=O stretching of the aliphatic esters. The peaks at 1162 cm^{-1} and 1235 cm^{-1} were assigned to the ester C-O stretching. Lastly, the peaks at 1375 cm^{-1} and 1461 cm^{-1} were assigned to the methyl C-H bending and the methylene C-H bending, respectively [160].

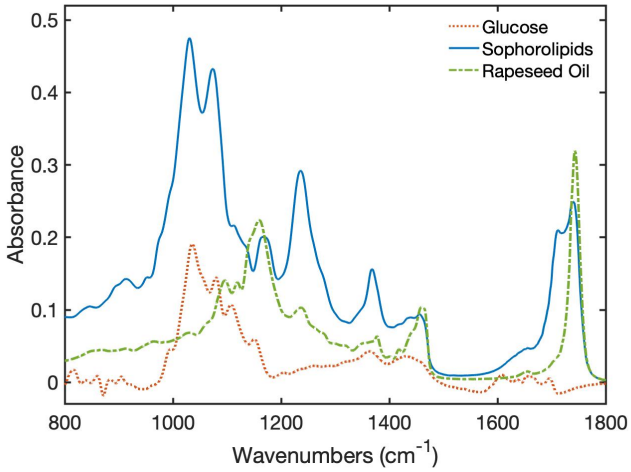

Fig. 6.3 ATR-FTIR spectra of glucose, rapeseed oil and of the produced SLs.

The SL absorption peaks observed at 1030 and 1074 cm^{-1} were associated with the C-O stretches from the C-O-H groups of the glucose (sophorose moiety), while the C-O stretches of the C(=O)-O-C group in lactones and acetyl esters appear at 1170 cm^{-1} and 1236 cm^{-1}, respectively. The peak at 1368 cm^{-1} was attributed to the CH_3 bending of the acetyl group and the weak peak at 1454 cm^{-1} corresponded to the C-O-H in-plane bend of the carboxylic acid (-COOH). The weak peak occurring at 1654 cm^{-1} was associated with the stretching vibration of the unsaturated alkene group (-CH=CH-) present in the fatty-acid chain. Finally, the strong absorption peak at 1740 cm^{-1} could be attributed to the C=O stretching from lactone esters or acids [152]. While there are many distinct peaks between the glucose and rapeseed oil spectra, most of the peaks between these and the SL spectra overlap, as expected, given that SLs derive from the combination of glucose and rapeseed oil.

Table 6.1 Peak assignments associated with the spectra of a 100 mM solution of glucose in DI water, rapeseed oil and SLs, shown in Figure 6.3 [83, 160, 152].

Compound	Frequency (cm^{-1})	Strength	Assignment
Glucose	994	medium	C-C (alicyclic) vibration
	1036	strong	C-O stretch
	1080	strong	C-O stretch
	1108	medium	C-C (alicyclic) vibration
	1152	medium	C-C (alicyclic) vibration
	1364	medium	C-O-H bend
	1432	medium	CH_2 bend
Rapeseed oil	1162	medium	C-O stretch (asym.)
	1235	medium	C-O stretch (sym.)
	1375	weak	CH_3 bend
	1461	medium	CH_2 bend
	1744	strong	C=O stretch (esters)
Sophorolipids	1030	strong	C-O stretch (glucoses)
	1074	strong	C-O stretch (glucoses)
	1170	medium	C-O stretch (lactones)
	1236	medium	C=O stretch (acetyl esters)
	1368	medium	CH_3 bend (acetyl group)
	1454	weak	C–O–H in-plane bend (acids)
	1654	weak	C=C stretch (fatty acid)
	1740	strong	C=O stretch (lactones, esters or acids)

6.3.2 Sophorolipid detection

One of the aims of this work was to distinguish between the broth and sophorolipid phases, mainly so that the production of SLs can be monitored within the broth phase during fermentation, which is kept at a constant high agitation. For this, the MIR spectra of a sample of the fermentation broth phase, as well as of the resulting produced SL phase, was obtained via ATR-FTIR spectroscopy, as previously described in Section 6.3.1. A background of air was used in this case in order to observe the significance of the water content in both samples. The broth-phase and SL-phase MIR spectra are shown in Figure 6.4. The spectrum of the SL phase shows identical peaks to the SL sample measured in Section 6.3.1, with the only difference of having a prominent peak at 1635 cm^{-1}, corresponding to the water O-H-O scissor bending, due to the fact that a background of air was used. The broth phase

spectrum presents low-intensity peaks corresponding to the previously assigned glucose peaks (between 950 cm^{-1} and 1200 cm^{-1}) as well as the water peak at 1635 cm^{-1}. The higher water peak observed for the broth phase confirms that there is a higher water content in this phase than in the SL phase.

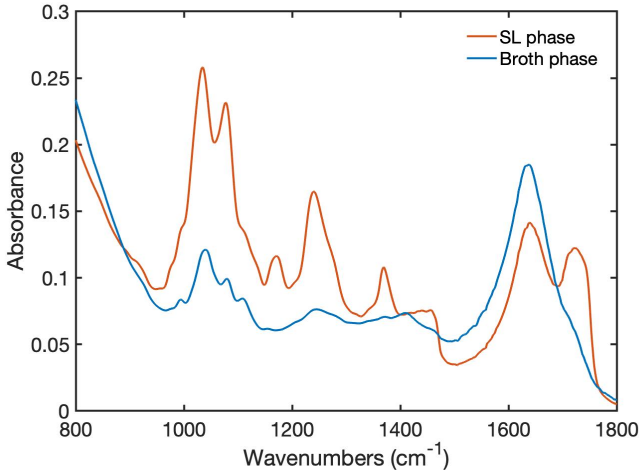

Fig. 6.4 ATR-FTIR spectra of broth-phase and SL-phase samples.

Since the initial broth phase typically contains a known value of glucose and oil, it is possible to use the initial fermentation medium as a background in order to subtract the contributions from these and to facilitate the detection and monitoring of the SL production during fermentation. MIR spectra of samples of fermentation broth containing different concentrations of SLs were measured using the initial broth phase as a background. Since the sophorolipid phase quickly separates from the broth phase when no agitation is applied, each sample was vortexed for 5 seconds before each measurement, and measurements were taken as quickly as possible to minimise phase separation. Figure 6.5a shows the acquired spectra of SLs in the broth phase at concentrations ranging from 0 to 160 g/L. An increase for all the the SL absorbance peaks was seen with increasing SL concentrations, apart from the peak at 1635 cm^{-1}, corresponding to the water peak, which indicates a decrease in the overall water content from the initial broth with the increase in SL concentration. This correlates with the fact that the broth has a higher water content than the SL phase, as was previously seen. Figure 6.5b shows the relative peak intensity of the SL peak at 1070 cm^{-1}, corresponding to the C-O glucose peak, as a function of increasing concentrations, where an almost linear trend was observed. The slightly non-linear behaviour could be explained by potential phase separation of the sample during measurements.

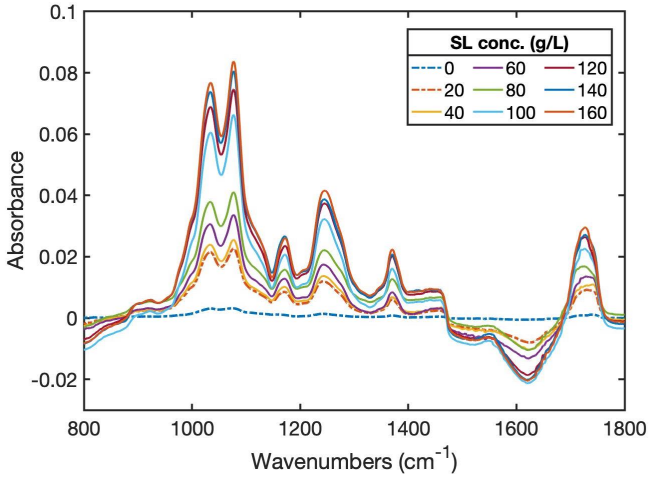

(a)

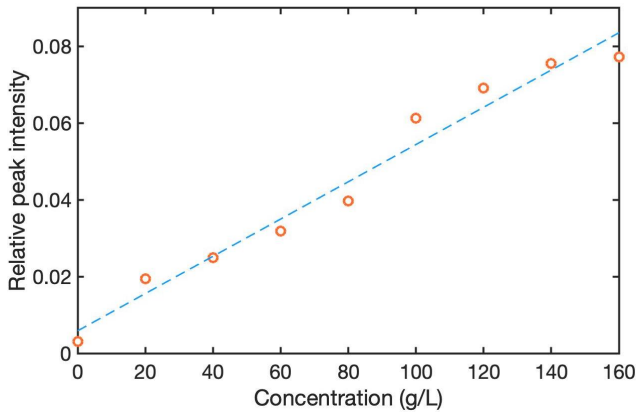

(b)

Fig. 6.5 (a) ATR-FTIR spectra of SLs at increasing concentrations in fermentation broth, from 0 to 160 g/L. (b) Relationship between different SL concentrations and the corresponding relative peak intensities at 1070 cm^{-1}. Dashed line represents the linear regression fit, with slope 0.00049 and intercept 0.0058. Note: spectra normalised to a baseline point at 1790 cm^{-1}.

6.3.3 Identification of sophorolipid type

As previously highlighted, SLs are produced as a mixture of lactonic and acidic sophorolipids, which have structural differences impacting their biological and physiochemical properties, and thus making them more or less suitable for different applications. It has been shown that the ratio of lactonic and acidic types produced depends on different fermentation parameters and can be tweaked according to the requirements [161]. The accurate identification of each type of SL within a fermentation process is essential for most SL producers, and therefore, the aim of this section was to determine MIR spectral features specific to each SL type via

ATR-FTIR spectroscopy. For this, samples of 20% (w/v) lactonic SL and 20% (w/v) acidic SL were prepared in DI water from crystallised lactonic SLs (powder form) and purified acidic SLs, prepared and supplied by a collaborating biosurfactants company, Allied Carbon Solutions Co., Ltd., Japan. ATR-FTIR measurements were then acquired, as previously described in Section 6.3.1, using air as background. Figure 6.6 shows the MIR spectra of the laconic and acidic SL types, which present a number of common peaks between them, as well as a number of peaks unique to each structure.

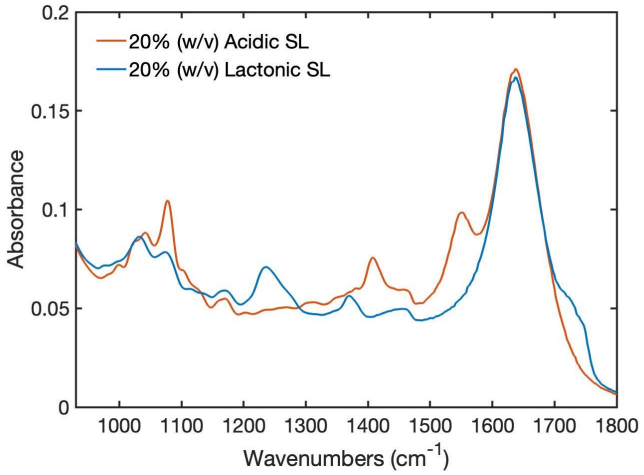

Fig. 6.6 Comparison of ATR-FTIR spectra of lactonic and acidic SLs.

The C-O stretch from the C-O-H groups of glucose were observed between 1030 cm^{-1} and 1078 cm^{-1} for both lactonic and acidic SLs. The small peak at 1170 cm^{-1} corresponded to the C-O stretching of the lactones. The peak at 1236 cm^{-1} was associated with the C=O stretch in the lactonic sample, confirming the presence of acetate groups. This peak became very weak or disappeared in the case of the acidic sophorolipid, which confirms the evidence of deacetylation of the acetyl esters [162]. The peak at 1368 cm^{-1} observed for the lactonic SL corresponds to the CH_3 bending of the acetyl group, which indicates the presence of acetylated sophorose moieties. The weak peaks at 1406 and 1454 cm^{-1} correspond to the C-O-H in-plane bending of the carboxylic acid (-COOH) structure for both SL types. The peak observed at 1550 cm^{-1} for the acidic SL corresponds to the stretching of the -CH=CH- of the fatty-acid chain. The corresponding peak for the lactonic SL would typically be shifted to around 1650 cm^{-1} due to the opening of the lactone ring, but was not observed due to the prominent water peak at 1635 cm^{-1} (since a background of air was used for these measurements). Finally, the lactonic SL presents a shoulder at 1740 cm^{-1}, corresponding to the C=O lactone carbonyl. Spectral differences between the two types of SLs were clearly observed, allowing the structural identification of each type of SL.

6.3.4 Bioreactor sample monitoring

As well as monitoring the production of SLs during fermentation, in order to optimise and maximise production, it is also of great importance to monitor the substrates (i.e. glucose and oil) which are consumed. The aim of this section was to study the MIR spectral variations corresponding to different compounds in samples collected at different time-points within a 72-hour period of a fermentation process carried out at Holiferm, Ltd. Exact time points and details of the actual fermentation process have been omitted for confidential purposes. Glucose-concentration measurements of each sample were taken separately and offline using a standard glucose meter for correlation with the acquired spectra. MIR spectra were acquired via ATR-FTIR spectroscopy, as described in Section 6.3.1, and a spectrum of the initial fermentation broth (already containing some glucose and oil) was used as a background. Each sample was vortexed for 5 seconds prior to measurements to avoid phase separation. Glucose and oil were added to the fermentation broth upon collection of sample 1 and sample 9. Figure 6.7a shows the MIR absorbance spectra of each sample collected at different time-points, numbered according to the order in which they were collected. Characteristic spectral features of glucose were predominant at first (samples 2 and 3, bands at 1036, 1080, 1108 and 1152 cm^{-1}) followed by a gradual depletion of glucose and a superposition of the SL sugar peaks which are present within the same region as those of glucose, but slightly shifted (i.e. the 1080 cm^{-1} glucose peak is shifted to 1070 cm^{-1} in the SL). Samples 4 and 5 clearly indicate the depletion of glucose with the simultaneous production of SLs, after which the glucose depletion continues, as observed by the increasingly negative absorbance. The decrease in absorbance at 1361 cm^{-1} and 1450 cm^{-1} indicate the consumption of oil throughout the process, while the decrease in absorbance between 1560 and 1690 cm^{-1} indicates a decrease in the water content in some of the samples. The variation in absorbance between 1720 and 1740 cm^{-1} corresponds to the C=O stretch of lactones, esters or acids, indicating the presence of the produced SLs. In order to observe the correlation between the measured glucose concentrations and the spectral variations of glucose, the relative glucose peak intensities (at 1036 cm^{-1}) were calculated and plotted for each sample, together with the measured concentrations, as shown in Figure 6.7b. It was seen that the variation of the relative glucose peak intensity over time is closely correlated to the variation of measured glucose concentrations, where an initial increase in glucose was followed by its gradual depletion as it was consumed to form SLs. A small increase in glucose was then observed after glucose feeding at the same time-point as sample 9 collection. This close correlation indicates that, despite the challenges to accurately quantify analytes independently due to their simultaneous depletion/production, it may be possible to track and monitor the changes of particular analytes. Although a more accurate quantification and analysis is likely

achievable with the implementation of multivariate-analysis methods, the analysis presented here may be sufficient for this particular application or for some companies since, rather than requiring accurate concentration values, the concentration trends are often considered equally as important and useful.

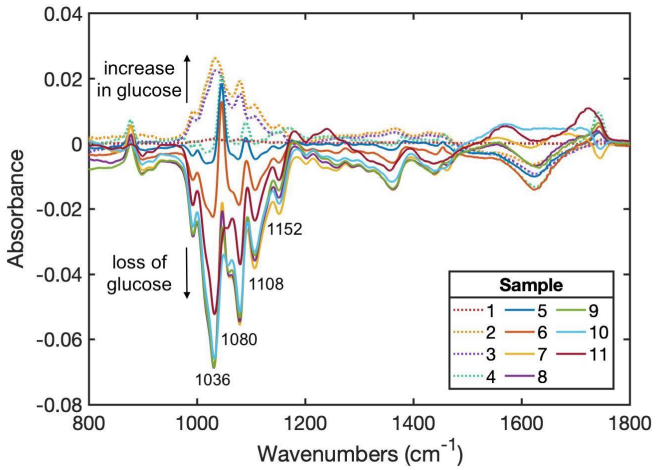

(a)

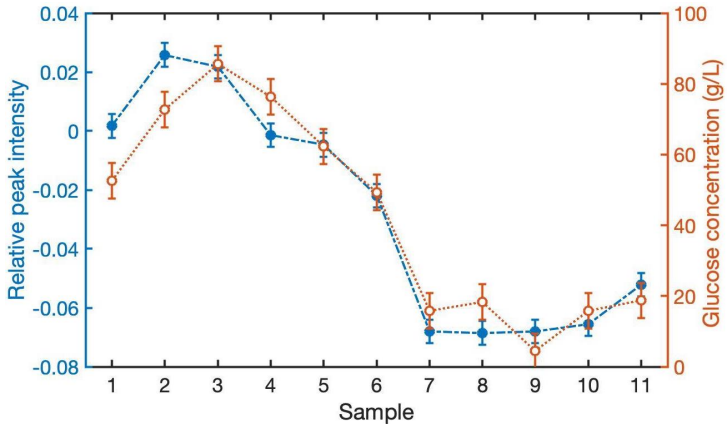

(b)

Fig. 6.7 (a) ATR-FTIR spectra of 11 bioreactor samples collected consecutively over a 72-hour period. (b) Correlation between relative glucose peak intensities variation at 1036 cm^{-1} and corresponding glucose concentration changes (measured using a standard glucose meter) for each consecutive sample. The error bars of the relative peak intensities reflect the spectral baseline average noise levels, while the error bars for the glucose measurements reflect the standard deviation of the glucose meter.

6.4 Optical-fibre sensor for bioprocess monitoring

Based on the preliminary work carried out in the previous section using ATR-FTIR spectroscopy, this section was aimed at developing a MIR fibre-optic sensor prototype for in-line bioprocess monitoring and assessing its performance. The initial stage involved the fabrication of a simple U-bent optical fibre and preparation of a laboratory set-up to carry out MIR measurements. This was followed by spectral acquisition of bioprocess samples using the developed optical-fibre probe and analysis of the results.

6.4.1 Sensor fabrication and laboratory set-up

The optical-fibre sensor was fabricated from uncladded cylindrical silver-halide fibres of composition $AgCl_{0.3}Br_{0.7}$, diameter 700 μm, a refractive index of 2.1 and typical attenuation of 1 dB/m, supplied by collaborators at the research group of Prof. Abraham Katzir (Tel Aviv University, Israel). The detailed fibre-fabrication procedure, as well as the mechanical properties of these fibres, are discussed in detail elsewhere [128, 129]. A U-bend (with radius of approximately 0.5 cm) was gently prepared in the fibre using a small cylinder, in order to increase the penetration depth, d_p, of the evanescent field and thus increase the sensitivity of the fibre probe, as described in Chapter 2. The final total length of the fibre-optic sensor was approximately 15 cm. The U-bend portion of the fibre was the only part left exposed, while the remaining fibre was covered with a polyethylene jacket. The extremities of the jacket closest to the U-bent fibre were sealed with epoxy glue to prevent the sample from entering the space between the fibre and jacket. SMA connectors were fitted onto the other end of the jacket holders to allow coupling to an FT-IR spectrometer. For bioreactor-sample measurements, the U-bent fibre was coupled to a MIR fibre-coupled FT-IR spectrometer (FT-IR-FC-4TE Rocket, ArcOptix Switzerland), which was selected for in-line bioprocess-monitoring experiments since it is compact, portable and allows fibre-coupling. Spectrometer control and data recording were handled by the dedicated ArcOptix software, and spectra were acquired with a resolution of 4 cm^{-1}. The samples were placed inside an open container (i.e. beaker) containing a small magnet and placed on a magnetic stirrer (FB15001 Heating magnetic stirrer, Fisher Scientific) in order to maintain a constant agitation of the samples to avoid phase separation. The spectrometer was placed onto a height-adjustable stand so that the fibre could be easily lowered/retracted into/from the sample. Figure 6.8 shows a schematic of the general laboratory setup used to carry out the sample measurements in this section. For the measurements, the fibre probe was carefully lowered into the sample ensuring total submersion of the U-bent sensing region.

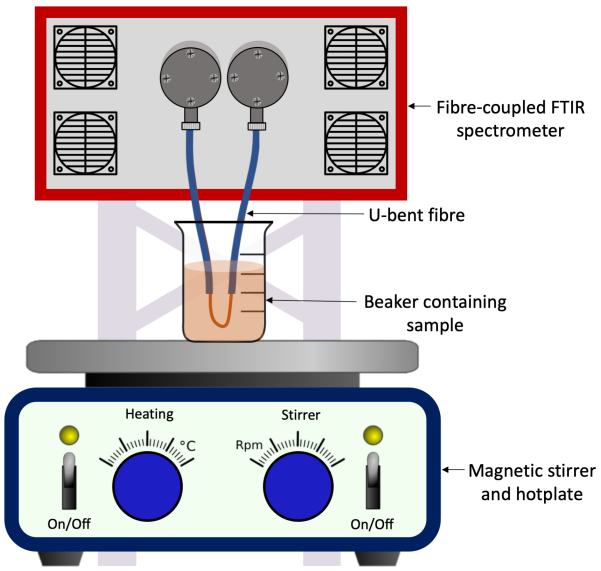

Fig. 6.8 Schematic of laboratory setup used to perform bioprocess-sample measurements, including a compact and portable fibre-coupled FT-IR spectrometer (dimensions: 180 x 160 x 80 mm), to which the developed fibre-optic sensor prototype is connected, a beaker containing the sample (into which the bent portion of the fibre sensor is immersed), and a magnetic-stirrer plate, to keep the sample under constant agitation during measurements, to prevent phase separation.

To provide insight into the accessible wavenumber ranges and the general transmission characteristics of the respective set-up, single-beam spectra (i.e. the raw intensity that reaches the detector at each wavenumber) when no sample is present (i.e. the fibre is in air), and when the fibre is submerged in the initial fermentation broth, were taken using the described setup and are presented in Figure 6.9. Here, the general shape and wavenumber regions where very little light reaches the detector (i.e. where the intensity becomes very low or reaches zero), can be analysed. Two key things are evident from the single-beam spectra of the set-up in air and in the fermentation broth: (1) the accessible wavenumber range is governed by the IR-transmission characteristics of the silver halide fibre, where the spectral range above 2300 cm^{-1} is unusable since there is no IR-transmission; and (2) there is an overall decrease in transmission when fermentation broth is used as a sample, due to the increased absorption of this medium compared to air. Despite this decrease in transmission, there is still sufficient transmission available for absorbance-spectra acquisition.

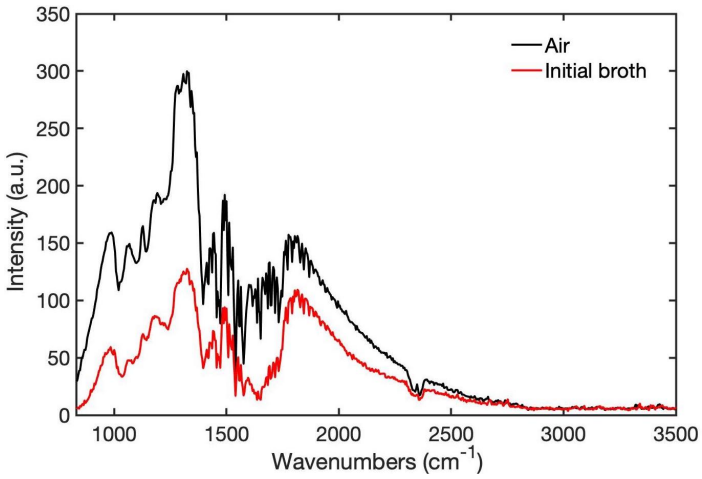

Fig. 6.9 Single-beam spectra recorded with the FT-IR ArcOptix spectrometer coupled to the U-bent fibre in air (black line) and submerged in the initial fermentation broth.

6.4.2 Performance: fibre-optic probe & ATR-FTIR

The aim of this section was to compare the performance between both spectroscopic systems: the developed fibre-optic probe coupled to a compact and portable spectrometer, and the single-bounce ATR element using a standard FT-IR spectrometer. For this, measurements of bioprocess broth-phase and SL-phase samples were acquired using the fibre-optic probe setup and compared to the previously acquired (in Section 6.3.2) ATR-FTIR spectra of the same samples, as shown in Figure 6.10. Both sets of measurements were taken using 150 scans, with a background of air and a resolution of 4 cm^{-1}. A significant increase in absorbance was seen for the fibre-optic probe measurements compared to the ATR measurements, which can be explained by the multiple internal reflections occurring within the fibre as opposed to the single reflection provided by the ATR element, leading to a larger interaction with the sample, and consequently, a larger absorbance. While the ATR element of approximately 500 μm^2 only allows interaction with a small sample volume, pipetted onto its surface, the fibre-probe allows sample interaction throughout the entire surface and length of its U-bent region, which is suspended and fully submerged in the sample of interest. It was also noted that the spectra acquired using the fibre-optic probe exhibited slightly higher noise levels compared to the standard ATR spectra, which could be explained by the likely decreased raw transmission provided by the fibre due to its inherent fibre-optic attenuation. Despite the differences in absorbance and noise levels between both sets of spectra, they presented identical spectral features, as previously identified in Section 6.3.2. This study showed that the developed fibre-optic probe had an ideal, if not superior, performance for bioprocess-sample measurements compared to the standard single-bounce ATR-FTIR spectroscopy, with the added advantages

of allowing higher sample interaction and complete insertion into the bioreactor medium, as well as its very simple fabrication. The possibility of direct insertion of the probe into the bioprocess medium means that the acquired measurements are more representative of real compound concentrations since there is little to no risk of phase separation due to the constant agitation of the fermentation medium, compared to the static sample measurements performed using standard ATR-FTIR spectroscopy.

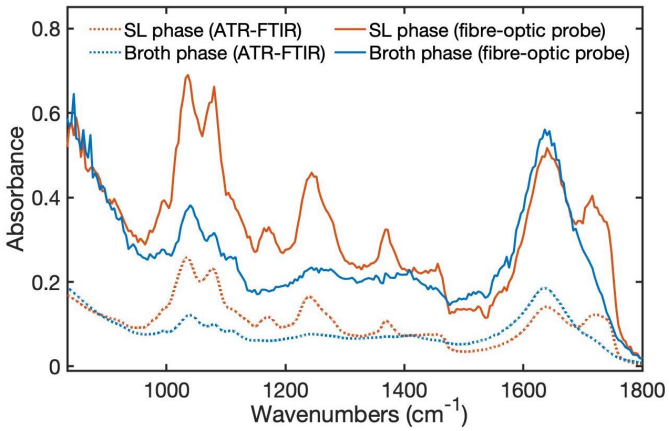

Fig. 6.10 Absorbance spectra of broth-phase and SL-phase samples acquired using the developed fibre-optic probe (solid blue and orange lines, respectively) and using standard ATR-FTIR spectroscopy with a single-bounce ATR element (dotted blue and orange lines, respectively).

6.4.3 Continuous sophorolipid monitoring

In this section, an experiment was carried out to assess the performance of the developed fibre-optic probe for continuous bioprocess monitoring. To achieve this, the setup described in Section 6.4.1 was used to measure bioreactor samples with increasing concentrations of SLs over time. The fibre probe was carefully lowered into the beaker, which at first contained initial fermentation-broth (containing some glucose and oil but no SLs), so that total submersion of the U-bent region was achieved. The background was acquired in the initial fermentation-broth sample with the probe in its final position in the beaker, which was used as the background for the subsequent absorbance spectra. SLs were gradually added to the fermentation broth every 5 minutes over a period of 1 hour and 45 minutes to achieve increasing known SL concentrations in the beaker at different time-points, ranging from 0 to 210 g/L. Measurements were acquired approximately every 5 minutes, once the SLs were sufficiently dispersed by the help of the magnetic stirrer. Figure 6.11a shows the spectra of increasing concentrations of SLs in the fermentation broth, where the expected characteristic spectral features of SLs are clearly visible (at 1030, 1074, 1170, 1236, 1368,

1454 and 1740 cm^{-1}) and an increase in absorbance was seen for all peaks with the increase in SL concentration. A decrease in absorbance is seen between 1470 and 1684 cm^{-1}, which indicates a depletion of the water content as the broth phase becomes enriched with SLs. Figure 6.11b shows the relative peak intensities of the SL's sugar peak at 1070 cm^{-1} as a function of the increase in SL concentration.

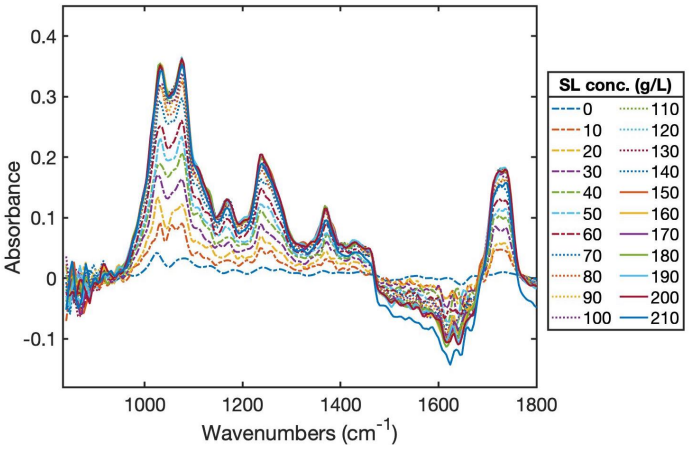

(a)

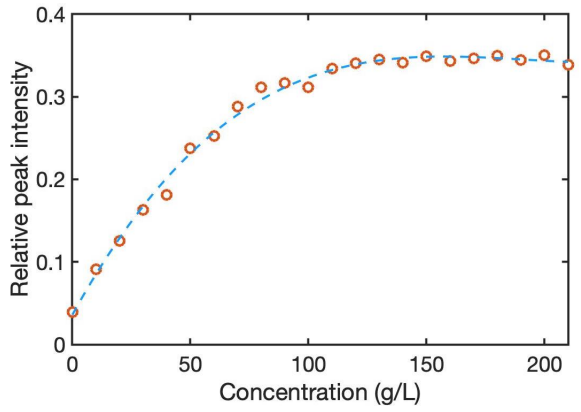

(b)

Fig. 6.11 (a) Absorbance spectra of SLs at increasing concentrations in fermentation broth, from 0 to 210 g/L. (b) Relationship between increasing SL concentrations and the corresponding relative peak intensities at the SL sugar peak (1070 cm^{-1}). Dashed line represents a cubic polynomial regression fit. Note: spectra normalised to a baseline point at 950 cm^{-1}.

While a practically linear increase in absorbance was observed up until a SL concentration of approximately 80 g/L, above this concentration, the absorbance did not increase further and reached saturation. This could be explained by the potential accumulation of SLs, which have a honey-like viscous consistency, on the surface of the fibre-optic probe and within the depth of the evanescent field, thus preventing the detection of further changes in the surrounding medium. This could be confirmed in two ways. Firstly, by comparison with previous results

(Figure 6.5 of Section 6.3.2) which showed that, for an increase in SL concentration in broth, measured using the standard ATR-FTIR element, the absorbance continued to increase linearly up until 160 g/L. In this case, only small (20 μL) samples were placed onto the element and replaced with a new sample each time, preventing the accumulation of substance on the surface. Secondly, by visual inspection of the fibre after measurements, where an accumulation of residual substance on the surface of the fibre was evident. Although the fibre-optic probe allowed continuous SL monitoring, the accumulation of substance on the fibre surface would undoubtedly be an issue for long-term bioreactor monitoring, and therefore, methods to prevent this from happening would need to be implemented, such as a routine cleaning cycle and/or probe retraction between measurements.

6.4.4 Identification of sophorolipid type

In this section, measurements of pure samples of the different types of SLs (lactonic and acidic), as previously achieved in Section 6.3.3 using standard ATR-FTIR spectroscopy, as well as of binary mixtures of these at different concentrations, were acquired using the developed fibre-optic probe. The aim of this was to assess not only its performance at identifying the different SL structures independently in pure solutions but also within mixtures of the two at varying concentrations, as they are typically produced during a normal fermentation process. For this, aqueous solutions containing 20% (w/v) of each type of SL were prepared, as described in Section 6.3.3, along with mixtures of these solutions at different concentrations (% v/v), as shown in Table 6.2. The measurements were carried out, once again, using the setup described in Section 6.4.1 and in this case, a background of water was taken in order to eliminate any water interference. Figure 6.12a shows the absorbance spectra of the pure lactonic and acidic SL forms as well as of the binary mixtures of these.

Table 6.2 Prepared mixtures of different concentrations of acidic and lactonic SL solutions.

SL concentrations (% v/v)	
Lactonic	**Acidic**
0	100
15	85
30	70
50	50
70	30
85	15

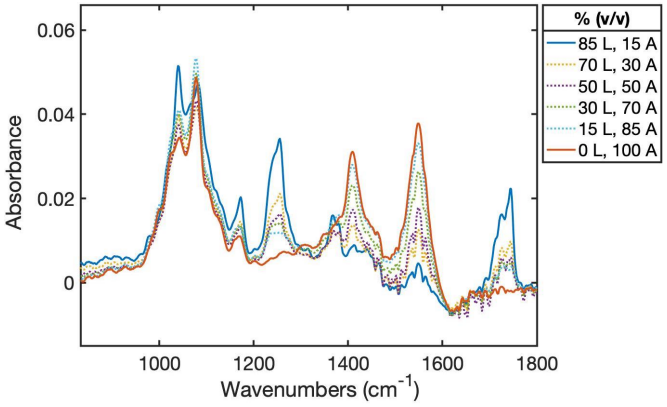

(a)

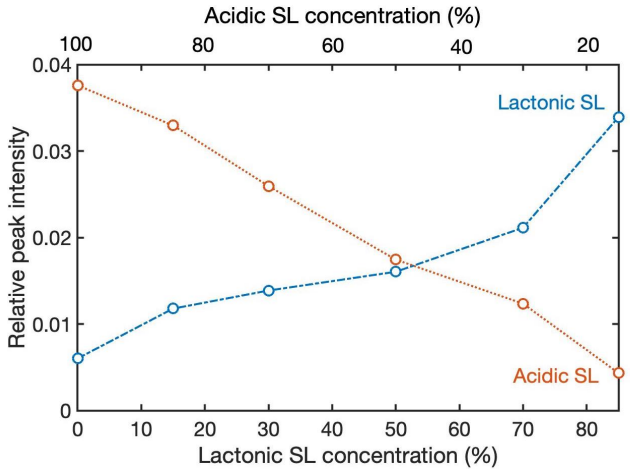

(b)

Fig. 6.12 (a) Absorbance spectra of pure lactonic and acidic SL samples and of binary mixtures of these at different concentrations (shown in Table 6.2). (b) Relationship between the different lactonic/acidic SL concentrations and the corresponding relative peak intensities at 1236 cm^{-1} and 1550 cm^{-1} for the lactonic and acidic SLs, respectively. Note: spectra normalised to a baseline point at 1790 cm^{-1}.

The previously identified peaks for both SL structures were clearly observed in the spectra: the peaks at 1030 and 1070 cm^{-1} for both structures, corresponding to the C-O stretches of the SL glucoses; the 1170 cm^{-1} peak associated with the lactone C-O stretch; the C=O absorption peak at 1236 cm^{-1} of the acetyl esters; the lactonic peak at 1368 cm^{-1} of the methyl groups of the acetyl esters (confirming acetylated sophorose moieties); the 1406 cm^{-1} peak of the carboxylic-acid structure; the prominent acidic SL peak at 1550 cm^{-1} of the -CH=CH- of the fatty-acid chain; and finally, the C=O lactone carbonyl peak at 1740 cm^{-1}. The absence of the broad water peak at 1635 cm^{-1} seen in the lactonic and acidic ATR-FTIR spectra in Section 6.3.3 and the decreased overall absorbance was due to the fact that water was used as a background in this case. Figure 6.12b shows the relative peak intensities for

the different concentrations at selected peaks for the lactonic SL (at 1236 cm^{-1}) and the acidic SL (at 1550 cm^{-1}), where an increase in lactonic/acidic SLs was clearly observed for increasing lactonic/acidic SL concentrations. This confirms that the optical-fibre probe is capable of not only detecting varying concentrations of overall SLs but also identifying the ratio of lactonic/acidic SLs that are being produced during a fermentation.

6.5 Conclusions and future work

To date, several different approaches have been carried out in order to achieve continuous real-time bioprocess monitoring for bioprocess optimisation. However, the standard methods for bioreactor-compound analysis currently implemented in many, if not in most, bioreactor companies are off-line and require the extraction of samples and sample pre-treatment. These are not only labour intensive but also only provide delayed results, which is less than ideal if the intention is to optimise a particular process in real time. One reason for this is the limited availability of sensors capable of real-time monitoring of such environments, and another is the elevated cost of the sensors that are able to achieve this.

The work described in this chapter focused on the exploration of fibre-optic MIR spectroscopy for the development of a simple, easy-to-fabricate and relatively low-cost sensor (based on evanescent-field sensing) for in-line, real-time bioprocess monitoring, where a particular fermentation process for sophorolipid (SL) production was studied. In the first section (Section 6.3), the use of standard ATR-FTIR spectroscopy (also based on evanescent-field sensing) was studied for bioreactor-sample measurements and bioreactor-compound identification, using a single-bounce ATR element. It was shown that both fermentation substrates (glucose and rapeseed oil) as well as the fermentation product (SLs) had unique spectral features in the MIR region, allowing their identification and quantification within a fermentation broth. Moreover, the two structurally different types of SLs (lactonic and acidic) could also be distinguished via ATR-FTIR spectroscopy. The second section (Section 6.4), described the development of a preliminary fibre-optic sensor prototype. A comparison between bioreactor-sample measurements acquired via ATR-FTIR and via the fibre-optic probe showed that the fibre-optic probe allowed a higher sample interaction due to its increased length and increased number of total internal reflections. The fibre-optic probe successfully performed continuous measurements of increasing concentrations of SLs in fermentation broth up until a certain concentration of SLs (approximately 80 g/L), after which an accumulation of residue on the fibre surface hindered the subsequent measurements. This finding proved that, for future long-term bioprocess measurements, the implementation of methods for routine cleaning of the fibre-surface and/or for the prevention of sample build-up would

be required. The fibre-optic probe was successfully able to distinguish between lactonic and acidic SLs in their pure form, as well as in binary mixtures of these at different concentrations. The work carried out here, although explorative and preliminary, demonstrated the feasibility of using a simple MIR fibre-optic probe for bioprocess monitoring. The easy fabrication of the probe could yield high throughput, large-scale fabrication at a reduced cost. The final cost of the sensor could potentially be relatively low-cost, depending mostly on the quality of the spectrometer (which typically determines the achievable sensitivity). Moreover, the possibility of using a multiplexing system in combination with the spectrometer would allow more than one fibre-optic probe to be used at once, meaning that several reactors could be monitored simultaneously using a single spectrometer (as opposed to requiring one system per reactor).

Future work may include the implementation of multivariate analysis for quantitative measurements and the simultaneous detection of several compounds. Moreover, further developments of the sensor system to allow routine cleaning and to withstand the harsh environment of bioreactors, which typically involve sterilisation (at 120^{o}C), varying pHs and constant agitation, could be implemented.

Chapter 7

Conclusions and future perspectives

This thesis details the work carried out towards the development and assessment of different sensor systems for the detection of chemical compounds with applications in the medical, environmental and industrial sectors, all of which were based on the same fundamental technique: mid-infrared (MIR) spectroscopy.

The growing technological advancements of MIR light sources, detection schemes and transducer materials and structures has drastically improved the sensing capabilities of MIR spectroscopy, enabling high sensitivity and selectivity as well as the development of robust and miniaturised sensing devices. Given this, and in addition to other inherent advantages of this technique (e.g. label-free, reagent-less analysis and fast acquisition times), it is no surprise that MIR spectroscopy has been considered an attractive alternative to standard sensing techniques and its use in solving different sensing problems has escalated in recent years. This thesis focused on applying MIR spectroscopy to explore alternative and improved sensing solutions for four different applications.

In Chapter 3, IR spectroscopy was combined with microfluidics using optical fibres to develop sensing platforms ideal for continuous microlitre liquid sample analysis. Many applications require the on-chip analysis of continuously flowing samples in real-time, from biofluid monitoring to the analysis of catalytic and biochemical processes. In this thesis, four microfluidic devices (three in transmission-mode and one transflection-mode configuration) were developed and coupled to optical fibres, which were used to guide IR light to and from the device's sensing regions. These were then assessed in terms of their hardware and liquid-sensing performance. The three transmission-mode devices (devices 1, 2 and 3), were fabricated out of different materials (PTFE, PEEK and stainless-steel, respectively), and with different specifications (i.e. optical path-lengths, channel volume, fibre-coupling methods) in order to compare their performance. Device 3 showed the overall best performance and was able to successfully monitor varying levels of glucose in aqueous solutions over time, down

to the physiologically relevant concentration of 1.5 mM. A fourth device (device 4) was fabricated in transflection-mode in an attempt to achieve a more compact and robust system through coupling (both the illumination and detection) fibres from the same side (as opposed to in transmission-mode configurations). However, this resulted in additional challenges, such as light scattering and absorption from the required additional MIR components and increased fibre losses due to the longer fibres needed in this case. Although glucose in aqueous solutions could be detected using this system, the spectra exhibited high noise levels compared to those of device 3. Out of all the fabricated systems, device 3 was considered the most robust and suitable for continuous liquid monitoring. Future work may focus on improvements to the sensitivity, potentially by using a more sophisticated light source and detector, and subsequently testing this sensor system for particular continuous online sample-monitoring applications.

Chapter 4 involved the study and implementation of MIR spectroscopy for the continuous, reagent-free monitoring of the dynamic changes in the brain chemistry of traumatic brain injury (TBI) patients via the microdialysis sampling technique. This work was carried out in collaboration with the Department of Clinical Neurosciences, Addenbrooke's Hospital and University of Cambridge. The currently-implemented method for TBI patient monitoring, based on enzymatic assays, requires frequent manual sample collection and only allows hourly monitoring at best, meaning that any rapid changes in brain chemistry are lost. Studies have shown that detecting and responding to these rapid changes could significantly improve patient outcome. In this work, the continuous monitoring of clinically relevant compounds (glucose, lactate and pyruvate) was assessed using a sensor system comprising of QCL light source and a micro flow-cell. This system was extensively tested and optimised for clinical monitoring, where the outlet of a clinically-approved microdialysis catheter was coupled to the inlet of the sensor system's flow-cell, allowing the continuous flow and spectral acquisition of sample. Clinical studies were then carried out on TBI patients, where continuous microdialysate monitoring over several hours was successfully achieved. Multivariate data-analysis methods were implemented in order to quantify compound concentrations in patient microdialysates. Despite the promising results, further improvements are needed before such a system can be considered for routine clinical use. Future work may involve improving the detection of pyruvate, which may be possible through system optimisation (e.g. laser intensity, optical path-length, etc.). Another challenge will be to improve the response time (currently 29 minutes) caused primarily by the connector tubing dimensions. Although better response times than the current system were achieved, for maximum benefits, it is important to decrease this further. This may be achieved by increasing the flow-rate at the catheter outlet, or by modifying the sensor system so that the sensing element can be placed closer to

the patient, and consequently shorten the tubing. Future work will also focus on improving compound quantification via multivariate analysis. While up until now, the optimisation of the sensor system for clinical performance was prioritised, improving the multivariate model is essential. This may be achieved by using a larger number of samples of compound concentrations covering a sufficiently broad range, as well as the implementation of spectral pretreatment methods. This project has received an NIHR Invention for Innovation (i4i) product development Award for a further 3-years funding to continue the development of the MIR-based continuous metabolite monitoring sensor.

The work carried out in Chapter 5 was aimed at the development of a novel sensor based on fibre-optic evanescent-wave spectroscopy (FEWS) to detect particular compounds that are increasingly affecting people's health around the world: volatile organic compounds (VOCs). This work was carried out in collaboration with the research group of Professor A. Katzir (Tel Aviv University, Israel). The sensor was fabricated by applying a porous silicon (PSi) coating to a U-bent optical fibre, in order to capture and condense VOCs within the emanating evanescent field. Upon exposure to three different VOCs, the fibre sensor showed significantly increased sensitivity for all VOCs compared to a fibre without a PSi coating. The sensor was also able to perform simultaneous detection of varying concentrations of different VOCs in binary mixtures. Future work may involve the optimisation of the PSi coating (i.e. optimising the porosity and dimensions of the PSi microparticles) for increased sensitivity and improving the robustness of the sensor. Moreover, the PSi surface could be functionalised to adjust the affinity towards particular VOCs.

Finally, in Chapter 6, the development of a fibre-optic sensor system for real-time, continuous bioprocess monitoring was explored. While real-time monitoring is essential for the optimisation of any bioprocess, standard monitoring methods are typically carried out off-line, time-consuming and labour-intensive, and the commercially-available real-time sensors are currently limited and costly. Here, work was carried out in collaboration with bioreactor companies to develop a simple and relatively low-cost alternative for in-line continuous chemical compound monitoring of a particular bioprocess for sophorolipid (SL) production. Varying concentrations of SLs were successfully monitored continuously in bioreactor broth using the developed fibre-optic sensor prototype. Moreover, it was able to distinguish between the two types of produced SLs (acidic and lactonic) within varying mixtures of the two. Since an accumulation of residue on the fibre surface was seen after certain SL concentrations, which affected subsequent measurements, future work may involve the implementation of methods for routine cleaning and/or the prevention of sample build-up. Another important future step will be to increase the robustness of the sensor to withstand the harsh bioreactor environments (i.e. sterilisation, agitation, etc.) for extended time-periods.

Finally, although the observation of trends may be sufficient for some, less complex processes, the implementation of multivariate analysis methods will be required for extracting accurate quantitative information on several bioreactor compounds.

The research presented in this thesis has revealed the versatility of MIR spectroscopy, which can be implemented in a range of different setups and configurations in order to accommodate the requirements of particular applications. This technique can be used not only as an improved alternative to currently implemented sensor systems but also opens doors to a varied range of novel sensing applications.

References

[1] J. Haas and B. Mizaikoff, "Advances in mid-infrared spectroscopy for chemical analysis," *Annual Review of Analytical Chemistry*, vol. 9, no. 1, pp. 45–68, 2016.

[2] J. Haas, R. Stach, M. Sieger, Z. Gashi, M. Godejohann, and B. Mizaikoff, "Sensing chlorinated hydrocarbons: Via miniaturized GaAs/AlGaAs thin-film waveguide flow cells coupled to quantum cascade lasers," *Analytical Methods*, vol. 8, no. 36, pp. 6602–6606, 2016.

[3] N. Picqué and T. W. Hänsch, "Mid-IR spectroscopic sensing," *Optics & Photonics, The Optical Society*, pp. 26–33, 2019.

[4] A. Perro, G. Lebourdon, S. Henry, S. Lecomte, L. Servant, and S. Marre, "Combining microfluidics and FT-IR spectroscopy: Towards spatially resolved information on chemical processes," *Reaction Chemistry and Engineering*, vol. 1, no. 6, pp. 577–594, 2016.

[5] V. Sablinskas, "Instrumentation," in *Handbook of Spectroscopy*, vol. 126, ch. 4, pp. 48–69, Weinheim, FRG: Wiley-VCH Verlag GmbH & Co. KGaA, jan 2005.

[6] F. Alimagham, M. Platkov, J. Prestage, S. Basov, G. Izakson, A. Katzir, S. R. Elliott, and T. Hutter, "Mid-IR evanescent-field fiber sensor with enhanced sensitivity for volatile organic compounds," *RSC Advances*, vol. 9, no. 37, pp. 21186–21191, 2019.

[7] M. Baker, C. S. Hughes, and K. A. Hollywood, "Infrared spectroscopy," in *Biophotonics: Vibrational Spectroscopic Diagnostics*, ch. 2, pp. 1–14, IOP Publishing, 2016.

[8] B. H. Stuart, "Chapter 1," in *Infrared Spectroscopy: Fundamentals and Applications*, vol. 8, pp. 1–11, Sydney, Australia: John Wiley & Sons, Inc., 2004.

[9] M. El-Azazy, "Infrared spectroscopy - A synopsis of the fundamentals and applications," in *Infrared Spectroscopy - Principles, Advances, and Applications*, pp. 2–11, Intech Open, 2019.

[10] C. U. Ritter, "Functionalization of Mesoporous Covalent Organic Frameworks," tech. rep., Ludwig-Maximilians-University, 2011.

[11] P. R. Griffiths and J. A. Haseth, "Introduction to vibrational spectroscopy," in *Fourier Transform Infrared Spectrometry*, ch. 1, pp. 1–18, Hoboken, New Jersey: John Wiley & Sons, Inc., 2nd ed., 2007.

[12] K. Hashimoto, V. R. Badarla, A. Kawai, and T. Ideguchi, "Complementary vibrational spectroscopy," *Nature Communications*, vol. 10, no. 1, pp. 1–6, 2019.

[13] K. Hsieh, G. Zhao, and T.-h. Wang, "Applying biosensor development concepts to improve preamplification-free CRISPR/Cas12a-Dx," *The Analyst*, 2020.

[14] P. R. Griffiths and J. A. Haseth, "Attenuated total reflection," in *Fourier Transform Infrared Spectrometry*, ch. 15, pp. 321–347, Hoboken, New Jersey: John Wiley & Sons, Inc., 2nd ed., 2007.

[15] A. Ghatak and K. Thyagarajan, "Introduction to fiber optics," in *Fundamentals of photonics*, ch. 1.7, pp. 249–292, Cambridge: Cambridge University Press, 1998.

[16] P. J. Melling and M. Thompson, "Handbook of vibrational spectroscopy," in *Fiber-Optic Probes for Mid-Infrared Spectrometry* (J. M. Chalmers and P. R. Griffiths, eds.), ch. 2, pp. 1–10, Chichester, UK: John Wiley & Sons, Ltd, dec 2002.

[17] T. Schädle and B. Mizaikoff, "Mid-infrared waveguides: A perspective," *Applied Spectroscopy*, vol. 70, no. 10, pp. 1625–1638, 2016.

[18] M. Karlowatz, M. Kraft, E. Eitenberger, B. Mizaikoff, and A. Katzir, "Chemically tapered silver halide fibers: An approach for increasing the sensitivity of mid-infrared evanescent wave sensors," *Applied Spectroscopy*, vol. 54, no. 11, pp. 1629–1633, 2000.

[19] B. D. Gupta, H. Dodeja, and A. K. Tomar, "Fibre-optic evanescent field absorption sensor based on a U-shaped probe," *Optical and Quantum Electronics*, vol. 28, no. 11, pp. 1629–1639, 1996.

[20] S. Korposh, S. W. James, S.-W. Lee, and R. P. Tatam, "Tapered optical fibre sensors: current trends and future perspectives," *Sensors*, vol. 19, no. 10, p. 2294, 2019.

[21] D. King, W. B. Lyons, C. Flanagan, and E. Lewis, "Interpreting complex data from a three-sensor multipoint optical fibre ethanol concentration sensor system using artificial neural network pattern recognition," *Measurement Science and Technology*, vol. 15, no. 8, pp. 1560–1567, 2004.

[22] Y. Raichlin and A. Katzir, "Fiber-optic evanescent wave spectroscopy in the middle infrared," *Applied Spectroscopy*, vol. 62, no. 2, pp. 55A–72A, 2008.

[23] M. Azkune, L. Ruiz-Rubio, G. Aldabaldetreku, E. Arrospide, L. Pérez-Álvarez, I. Bikandi, J. Zubia, and J. L. Vilas-Vilela, "U-shaped and surface functionalized polymer optical fiber probe for glucose detection," *Sensors*, vol. 18, no. 1, 2018.

[24] S. Wold, M. Sjöström, and L. Eriksson, "PLS-regression: A basic tool of chemometrics," *Chemometrics and Intelligent Laboratory Systems*, vol. 58, no. 2, pp. 109–130, 2001.

[25] A. De Juan and R. Tauler, "Chemometrics applied to unravel multicomponent processes and mixtures: Revisiting latest trends in multivariate resolution," *Analytica Chimica Acta*, vol. 500, no. 1-2, pp. 195–210, 2003.

[26] D. E. Booth, "Chemometrics: data analysis for the laboratory and chemical plant," *Technometrics*, vol. 46, no. 1, pp. 110–110, 2004.

[27] J. A. Westerhuis, H. C. Hoefsloot, S. Smit, D. J. Vis, A. K. Smilde, E. J. Velzen, J. P. Duijnhoven, and F. A. Dorsten, "Assessment of PLSDA cross validation," *Metabolomics*, vol. 4, no. 1, pp. 81–89, 2008.

[28] S. Turker-Kaya and C. W. Huck, "A review of mid-infrared and near-infrared imaging: Principles, concepts and applications in plant tissue analysis," *Molecules*, vol. 22, no. 1, pp. 1–20, 2017.

[29] D. Li, "Microfluidics based microsystems: fundamentals and applications," in *Microfluidic Lab-on-a-Chip Devices for Biomedical Applications* (S. Kakac, B. Kosoy, D. Li, and A. Pramuanjaroenkij, eds.), pp. 305–376, Dordrech, Netherlands: Springer, 2009.

[30] K. L. Chan, S. Gulati, J. B. Edel, A. J. De Mello, and S. G. Kazarian, "Chemical imaging of microfluidic flows using ATR-FTIR spectroscopy," *Lab on a Chip*, vol. 9, no. 20, pp. 2909–2913, 2009.

[31] A. V. Ewing, G. S. Clarke, and S. G. Kazarian, "Attenuated total reflection-Fourier transform infrared spectroscopic imaging of pharmaceuticals in microfluidic devices," *Biomicrofluidics*, vol. 10, no. 2, pp. 1–13, 2016.

[32] J. Hu, V. Tarasov, A. Agarwal, L. Kimerling, N. Carlie, L. Petit, and K. Richardson, "Fabrication and testing of planar chalcogenide waveguide integrated microfluidic sensor," *Optics Express*, vol. 15, no. 5, p. 2307, 2007.

[33] Y. C. Chang, P. Wägli, V. Paeder, A. Homsy, L. Hvozdara, P. Van Der Wal, J. Di Francesco, N. F. De Rooij, and H. Peter Herzig, "Cocaine detection by a mid-infrared waveguide integrated with a microfluidic chip," *Lab on a Chip*, vol. 12, no. 17, pp. 3020–3023, 2012.

[34] K. Choi, J. M. Mudrik, and A. R. Wheeler, "A guiding light: spectroscopy on digital microfluidic devices using in-plane optical fibre waveguides," *Analytical and bioanalytical chemistry*, vol. 407, no. 24, pp. 7467–7475, 2015.

[35] C. Vranić, A. Fomichova, N. Gretz, C. Herrmann, S. Neudecker, A. Pucci, and W. Petrich, "Continuous glucose monitoring by means of mid-infrared transmission laser spectroscopy in vitro," *Analyst*, vol. 136, no. 6, pp. 1192–1198, 2011.

[36] S. Liakat, *Development of a noninvasive in vivo glucose sensor based on mid-infrared quantum cascade laser spectroscopy*. PhD thesis, Princeton University, 2015.

[37] B. L. Mojet, S. D. Ebbesen, and L. Lefferts, "Light at the interface: the potential of attenuated total reflection infrared spectroscopy for understanding heterogeneous catalysis in water," *Chemical Society Reviews*, vol. 39, no. 12, p. 4643, 2010.

[38] V. H. Highland, *A Sensor for Metabolic Profiling of Traumatic Brain Injury*. PhD thesis, University of Cambridge, 2018.

[39] A. M. Díez-Pascual, M. Naffakh, C. Marco, G. Ellis, and M. A. Gómez-Fatou, "High-performance nanocomposites based on polyetherketones," *Progress in Materials Science*, vol. 57, no. 7, pp. 1106–1190, 2012.

[40] J. Bayly, V. Kartha, and W. Stevens, "The absorption spectra of liquid phase H2O, HDO and D2O from 0·7 μm to 10 μm," *Infrared Physics*, vol. 3, no. 4, pp. 211–222, 1963.

[41] N. Kakuta, H. Yamashita, D. Kawashima, K. Kondo, H. Arimoto, and Y. Yamada, "Simultaneous imaging of temperature and concentration of ethanol-water mixtures in microchannel using near-infrared dual-wavelength absorption technique," *Measurement Science and Technology*, vol. 27, no. 11, pp. 115–401, 2016.

[42] A. Beganović, V. Moll, and C. W. Huck, "Comparison of Multivariate Regression Models Based on Water- and Carbohydrate-Related Spectral Regions in the Near-Infrared for Aqueous Solutions of Glucose," *Molecules*, vol. 24, no. 20, p. 3696, 2019.

[43] W. Kaye, "Near-infrared spectroscopy. I. Spectral identification and analytical applications," *Spectrochimica Acta*, vol. 6, no. 4, pp. 257–287, 1954.

[44] J. Coates, "Interpretation of Infrared Spectra, A Practical Approach," in *Encyclopedia of Analytical Chemistry*, pp. 10815–10837, Chichester, UK: John Wiley & Sons, Ltd, sep 2006.

[45] V. A. Saptari, *A spectroscopic system for near infrared glucose measurement*. PhD thesis, Massachusetts Institute of Technology, 2004.

[46] A. K. Amerov, J. Chen, and M. A. Arnold, "Molar absorptivities of glucose and other biological molecules in aqueous solutions over the first overtone and combination regions of the near-infrared spectrum," *Applied Spectroscopy*, vol. 58, no. 10, pp. 1195–1204, 2004.

[47] H. Von Lilienfeld-Toal, M. Weidenmüller, A. Xhelaj, and W. Mäntele, "A novel approach to non-invasive glucose measurement by mid-infrared spectroscopy: The combination of quantum cascade lasers (QCL) and photoacoustic detection," *Vibrational Spectroscopy*, vol. 38, no. 1-2, pp. 209–215, 2005.

[48] F. Bonnier, H. Blasco, C. Wasselet, G. Brachet, R. Respaud, L. F. C. Carvalho, D. Bertrand, M. J. Baker, H. J. Byrne, and I. Chourpa, "Ultra-filtration of human serum for improved quantitative analysis of low molecular weight biomarkers using ATR-IR spectroscopy," *Analyst*, vol. 142, no. 8, pp. 1285–1298, 2017.

[49] T. Lawrence, A. Helmy, O. Bouamra, M. Woodford, F. Lecky, and P. J. Hutchinson, "Traumatic brain injury in England and Wales: Prospective audit of epidemiology, complications and standardised mortality," *BMJ Open*, vol. 6, no. 11, pp. 1–8, 2016.

[50] D. J. Davies, Z. Su, M. T. Clancy, S. J. Lucas, H. Dehghani, A. Logan, and A. Belli, "Near-Infrared Spectroscopy in the Monitoring of Adult Traumatic Brain Injury: A Review," *Journal of Neurotrauma*, vol. 32, no. 13, pp. 933–941, 2015.

[51] A. Helmy, M. Vizcaychipi, and A. K. Gupta, "Traumatic brain injury: Intensive care management," *British Journal of Anaesthesia*, vol. 99, no. 1, pp. 32–42, 2007.

[52] C. Kwasnica, A. W. Brown, E. P. Elovic, S. Kothari, and S. R. Flanagan, "Congenital and Acquired Brain Injury. 3. Spectrum of the Acquired Brain Injury Population," *Archives of Physical Medicine and Rehabilitation*, vol. 89, pp. S15–S20, mar 2008.

[53] I. Timofeev, K. L. Carpenter, J. Nortje, P. G. Al-Rawi, M. T. O'Connell, M. Czosnyka, P. Smielewski, J. D. Pickard, D. K. Menon, P. J. Kirkpatrick, A. K. Gupta, and P. J. Hutchinson, "Cerebral extracellular chemistry and outcome following traumatic brain injury: A microdialysis study of 223 patients," *Brain*, vol. 134, no. 2, pp. 484–494, 2011.

[54] P. J. Hutchinson, I. Jalloh, A. Helmy, K. L. Carpenter, E. Rostami, B. M. Bellander, M. G. Boutelle, J. W. Chen, J. Claassen, C. Dahyot-Fizelier, P. Enblad, C. N. Gallagher, R. Helbok, L. Hillered, P. D. Le Roux, S. Magnoni, H. S. Mangat, D. K. Menon, C. H. Nordström, K. H. O'Phelan, M. Oddo, J. Perez Barcena, C. Robertson, E. Ronne-Engström, J. Sahuquillo, M. Smith, N. Stocchetti, A. Belli, T. A. Carpenter, J. P. Coles, M. Czosnyka, N. Dizdar, J. C. Goodman, A. K. Gupta, T. H. Nielsen, N. Marklund, A. Montcriol, M. T. O'Connell, M. A. Poca, A. Sarrafzadeh, R. J. Shannon, J. Skjøth-Rasmussen, P. Smielewski, J. F. Stover, I. Timofeev, P. Vespa, E. Zavala, and U. Ungerstedt, "Consensus statement from the 2014 International Microdialysis Forum," *Intensive Care Medicine*, vol. 41, no. 9, pp. 1517–1528, 2015.

[55] K. L. Carpenter, A. M. Young, and P. J. Hutchinson, "Advanced monitoring in traumatic brain injury," *Current Opinion in Critical Care*, vol. 23, no. 2, pp. 103–109, 2017.

[56] M. A. Booth, S. A. Gowers, C. L. Leong, M. L. Rogers, I. C. Samper, A. P. Wickham, and M. G. Boutelle, "Chemical Monitoring in Clinical Settings: Recent Developments toward Real-Time Chemical Monitoring of Patients," *Analytical Chemistry*, vol. 90, no. 1, pp. 2–18, 2018.

[57] M. L. Rogers, C. L. Leong, S. A. Gowers, I. C. Samper, S. L. Jewell, A. Khan, L. McCarthy, C. Pahl, C. M. Tolias, D. C. Walsh, A. J. Strong, and M. G. Boutelle, "Simultaneous monitoring of potassium, glucose and lactate during spreading depolarization in the injured human brain - Proof of principle of a novel real-time neurochemical analysis system, continuous online microdialysis," *Journal of Cerebral Blood Flow and Metabolism*, vol. 37, no. 5, pp. 1883–1895, 2017.

[58] S. A. Gowers, M. L. Rogers, M. A. Booth, C. L. Leong, I. C. Samper, T. Phairatana, S. L. Jewell, C. Pahl, A. J. Strong, and M. G. Boutelle, "Clinical translation of microfluidic sensor devices: Focus on calibration and analytical robustness," *Lab on a Chip*, vol. 19, no. 15, pp. 2537–2548, 2019.

[59] S. A. N. Gowers, I. C. Samper, D.-S. R. K. Murray, G. K. Smith, S. Jeyaprakash, M. L. Rogers, M. Karlsson, M. H. Olsen, K. Møller, and M. G. Boutelle, "Real-time neurochemical measurement of dynamic metabolic events during cardiac arrest and resuscitation in a porcine model," *The Analyst*, vol. 145, no. 5, pp. 1894–1902, 2020.

[60] H. M. Heise, U. Damm, M. Bodenlenz, V. R. Kondepati, G. Köhler, and M. Ellmerer, "Bedside monitoring of subcutaneous interstitial glucose in healthy individuals using microdialysis and infrared spectrometry," *Journal of Biomedical Optics*, vol. 12, no. 2, p. 024004, 2007.

[61] H. M. Heise, L. Cocchieri, T. Vahlsing, D. Ihrig, and J. Elm, "Monitoring of interstitial buffer systems using micro-dialysis and infrared spectrometry," in *Optical Diagnostics and Sensing XVII: Toward Point-of-Care Diagnostics* (G. L. Coté, ed.), vol. 10072, p. 100720E, 2017.

[62] T. Vahlsing, S. Delbeck, J. Budde, D. Ihrig, S. Leonhardt, and H. M. Heise, "Reliable glucose monitoring by ex-vivo blood microdialysis and infrared spectrometry for patients in critical care," in *Optical Diagnostics and Sensing XVII: Toward Point-of-Care Diagnostics* (G. L. Coté, ed.), vol. 10072, p. 100720D, feb 2017.

[63] M. C. Dewan, N. Mummareddy, J. C. Wellons III, and C. M. Bonfield, "Epidemiology of global pediatric traumatic brain injury : qualitative review," *World Neurosurgery*, vol. 91, pp. 497–509, 2016.

[64] A. I. Maas, N. Stocchetti, and R. Bullock, "Moderate and severe traumatic brain injury in adults," *The Lancet Neurology*, vol. 7, no. 8, pp. 728–741, 2008.

[65] B. Roozenbeek, A. I. Maas, and D. K. Menon, "Changing patterns in the epidemiology of traumatic brain injury," *Nature Reviews Neurology*, vol. 9, no. 4, pp. 231–236, 2013.

[66] C. Werner and K. Engelhard, "Pathophysiology of traumatic brain injury," *British Journal of Anaesthesia*, vol. 99, no. 1, pp. 4–9, 2007.

[67] R. A. Stocker, "Intensive care in traumatic brain injury including multi-modal monitoring and neuroprotection," *Medical Sciences*, vol. 7, no. 3, p. 37, 2019.

[68] S. Jones, G. Schwartzbauer, and X. Jia, "Brain monitoring in critically neurologically impaired patients," *International Journal of Molecular Sciences*, vol. 18, no. 1, pp. 1–17, 2017.

[69] J. Ghajar, "Traumatic brain injury," *The Lancet*, vol. 356, no. 9233, pp. 923–929, 2000.

[70] D. Roh and S. Park, "Brain multimodality monitoring: updated perspectives," *Current Neurology and Neuroscience Reports*, vol. 16, no. 6, pp. 1–17, 2016.

[71] A. Helmy, K. L. H. Carpenter, and P. J. Hutchinson, "Microdialysis in the human brain and its potential role in the development and clinical assessment of drugs," *Current Medicinal Chemistry*, vol. 14, no. 14, pp. 1525–1537, 2007.

[72] C. Mahajan and G. Rath, "Cerebral microdialysis," *Journal of Neuroanaesthesiology and Critical Care*, vol. 02, no. 03, pp. 232–239, 2015.

[73] M. M. Tisdall and M. Smith, "Cerebral microdialysis: Research technique or clinical tool," *British Journal of Anaesthesia*, vol. 97, no. 1, pp. 18–25, 2006.

[74] M. De Lima Oliveira, A. C. Kairalla, E. T. Fonoff, R. C. R. Martinez, M. J. Teixeira, and E. Bor-Seng-Shu, "Cerebral microdialysis in traumatic brain injury and subarachnoid hemorrhage: State of the art," *Neurocritical Care*, vol. 21, no. 1, pp. 152–162, 2014.

[75] P. Mergenthaler, U. Lindauer, G. A. Dienel, and A. Meisel, "Sugar for the brain: the role of glucose in physiological and pathological brain function," *Trends in Neurosciences*, vol. 36, no. 10, pp. 587–597, 2013.

[76] E. P. Thelin, K. L. Carpenter, P. J. Hutchinson, and A. Helmy, "Microdialysis monitoring in clinical traumatic brain injury and its role in neuroprotective drug development," *AAPS Journal*, vol. 19, no. 2, pp. 367–376, 2017.

[77] P. Reinstrup, N. Ståhl, P. Mellergård, T. Uski, U. Ungerstedt, and C. H. Nordström, "Intracerebral microdialysis in clinical practice: Baseline values for chemical markers during wakefulness, anesthesia, and neurosurgery," *Neurosurgery*, vol. 47, no. 3, pp. 701–710, 2000.

[78] E. Rostami, "Glucose and the injured brain-monitored in the neurointensive care unit," *Frontiers in Neurology*, vol. 5, pp. 1–8, 2014.

[79] L. Carteron, P. Bouzat, and M. Oddo, "Cerebral microdialysis monitoring to improve individualized neurointensive care therapy: an update of recent clinical data," *Frontiers in Neurology*, vol. 8, pp. 1–10, 2017.

[80] A. F. Revzin, K. Sirkar, A. Simonian, and M. V. Pishko, "Glucose, lactate, and pyruvate biosensor arrays based on redox polymer/oxidoreductase nanocomposite thin-films deposited on photolithographically patterned gold microelectrodes," *Sensors and Actuators, B: Chemical*, vol. 81, no. 2-3, pp. 359–368, 2002.

[81] G. Gauglitz, "Analytical evaluation of sensor measurements," *Analytical and Bioanalytical Chemistry*, vol. 410, no. 1, pp. 5–13, 2018.

[82] Y. Tholance, G. Barcelos, I. Quadrio, B. Renaud, F. Dailler, and A. Perret-Liaudet, "Analytical validation of microdialysis analyzer for monitoring glucose, lactate and pyruvate in cerebral microdialysates," *Clinica Chimica Acta*, vol. 412, pp. 647–654, mar 2011.

[83] G. Socrates, "Infrared Characteristic Group Frequencies: Tables and Charts," *Journal of Chemical Education*, vol. 72, no. 4, p. A93, 1995.

[84] C. Petibois, A. M. Melin, A. Perromat, G. Cazorla, and G. Déléris, "Glucose and lactate concentration determination on single microsamples by Fourier-transform infrared spectroscopy," *Journal of Laboratory and Clinical Medicine*, vol. 135, no. 2, pp. 210–215, 2000.

[85] A. Helmy, K. L. Carpenter, D. K. Menon, J. D. Pickard, and P. J. Hutchinson, "The cytokine response to human traumatic brain injury: Temporal profiles and evidence for cerebral parenchymal production," *Journal of Cerebral Blood Flow and Metabolism*, vol. 31, no. 2, pp. 658–670, 2011.

[86] H. M. Heise and T. Vahlsing, "Influence of spectral bandwidth limitations of tuneable external-cavity based quantum cascade laser systems for clinical biofluid analysis," in *Optical Diagnostics and Sensing XIV: Toward Point-of-Care Diagnostics* (G. L. Coté, ed.), vol. 8951, p. 895108, 2014.

[87] I. L. Jernelv, K. Strøm, D. R. Hjelme, and A. Aksnes, "Infrared spectroscopy with a fiber-coupled quantum cascade laser for attenuated total reflection measurements towards biomedical applications," *Sensors*, vol. 19, no. 23, p. 5130, 2019.

[88] K. Isensee, N. Kröger-Lui, and W. Petrich, "Biomedical applications of mid-infrared quantum cascade lasers-a review," *Analyst*, vol. 143, no. 24, pp. 5888–5911, 2018.

[89] M. Brandstetter, L. Volgger, A. Genner, C. Jungbauer, and B. Lendl, "Direct determination of glucose, lactate and triglycerides in blood serum by a tunable quantum cascade laser-based mid-IR sensor," *Applied Physics B: Lasers and Optics*, vol. 110, no. 2, pp. 233–239, 2013.

[90] A. Schwaighofer, M. R. Alcaráz, C. Araman, H. Goicoechea, and B. Lendl, "External cavity-quantum cascade laser infrared spectroscopy for secondary structure analysis of proteins at low concentrations," *Scientific Reports*, vol. 6, pp. 1–10, 2016.

[91] T. Vahlsing, H. Moser, M. Grafen, K. Nalpantidis, M. Brandstetter, H. M. Heise, B. Lendl, S. Leonhardt, D. Ihrig, and A. Ostendorf, "Mid-infrared spectroscopic characterisation of an ultra-broadband tunable EC-QCL system intended for biomedical applications," in *Optics InfoBase Conference Papers* (J. Q. Brown and V. Deckert, eds.), vol. 953713, p. 953713, 2015.

[92] D. W. Allan, "Time and frequency characterization estimation and prediction of precision clocks and oscillators Allan IEEE transaction on ultrasonics ferroelectrics.pdf," *Ieee Transactions on Ultrasonics, Ferroelectrics and Frequency Control.*, vol. 34, no. 4, pp. 647–654, 1987.

[93] N. A. Zaidi, M. W. Tahir, M. Vellekoop, and W. Lang, "Using Allan variance to determine the resolution of ethylene gas chromatographic system," in *IEEE SENSORS*, pp. 1–3, IEEE, oct 2017.

[94] O. M. S. Ismail and R. S. A. Hameed, "Environmental effects of volatile organic compounds on ozone layer," *Pelagia Research Library Advances in Applied Science Research*, vol. 4, no. 1, pp. 264–268, 2013.

[95] J. Tang, J. Fang, Y. Liang, B. Zhang, Y. Luo, X. Liu, Z. Li, X. Cai, J. Xian, H. Lin, W. Zhu, H. Guan, H. Lu, J. Zhang, J. Yu, and Z. Chen, "All-fiber-optic VOC gas sensor based on side-polished fiber wavelength selectively coupled with cholesteric liquid crystal film," *Sensors and Actuators B: Chemical*, vol. 273, pp. 1816–1826, nov 2018.

[96] M. Kampa and E. Castanas, "Human health effects of air pollution," *Environmental Pollution*, vol. 151, no. 2, pp. 362–367, 2008.

[97] B. Szulczyński and J. Gębicki, "Currently commercially available chemical sensors employed for detection of volatile organic compounds in outdoor and indoor air," *Environments*, vol. 4, no. 1, p. 21, 2017.

[98] H. Kataoka, Y. Ohashi, T. Mamiya, K. Nami, K. Saito, K. Ohcho, and T. Takigaw, "Indoor air monitoring of volatile organic compounds and evaluation of their emission from various building materials and common products by gas chromatography-mass spectrometry," in *Advanced Gas Chromatography - Progress in Agricultural, Biomedical and Industrial Applications*, ch. 9, pp. 162–183, Intech Open, 2012.

[99] N. Watson, S. Davies, and D. Wevill, "Air monitoring: New advances in sampling and detection," *The Scientific World Journal*, vol. 11, pp. 2582–2598, 2011.

[100] R. Lu, G. Sheng, W. Li, H. Yu, Y. Raichlin, A. Katzir, and B. Mizaikoff, "IR-ATR chemical sensors based on planar silver halide waveguides coated with an ethylene/propylene copolymer for detection of multiple organic contaminants in water," *Angewandte Chemie - International Edition*, vol. 52, no. 8, pp. 2265–2268, 2013.

[101] G. Roy and J. A. Mielczarski, "Infrared detection of chlorinated hydrocarbons in water at ppb levels of concentrations," *Water Research*, vol. 36, no. 7, pp. 1902–1908, 2002.

[102] Y. Luzinova, B. Zdyrko, I. Luzinov, and B. Mizaikoff, "Detecting trace amounts of water in hydrocarbon matrices with infrared fiberoptic evanescent field sensors," *Analyst*, vol. 137, no. 2, pp. 333–341, 2012.

[103] R. Lu, W. W. Li, B. Mizaikoff, A. Katzir, Y. Raichlin, G. P. Sheng, and H. Q. Yu, "High-sensitivity infrared attenuated total reflectance sensors for in situ multicomponent detection of volatile organic compounds in water," *Nature Protocols*, vol. 11, no. 2, pp. 377–386, 2016.

[104] E. Baudet, A. Gutierrez-Arroyo, M. Baillieul, J. Charrier, P. Němec, L. Bodiou, J. Lemaitre, E. Rinnert, K. Michel, B. Bureau, J. L. Adam, and V. Nazabal, "Development of an evanescent optical integrated sensor in the mid-infrared for detection of pollution in groundwater or seawater," *Advanced Device Materials*, vol. 3, no. 2, pp. 23–29, 2017.

[105] R. Lu, B. Mizaikoff, W. W. Li, C. Qian, A. Katzir, Y. Raichlin, G. P. Sheng, and H. Q. Yu, "Determination of chlorinated hydrocarbons in water using highly sensitive mid-infrared sensor technology," *Scientific Reports*, vol. 3, pp. 1–6, 2013.

[106] C. Heath, M. Myers, and B. Pejcic, "The effect of pressure and temperature on mid-infrared sensing of dissolved hydrocarbons in water," *Analytical Chemistry*, vol. 89, no. 24, pp. 13391–13397, 2017.

[107] B. Mizaikoff, Göbel, R. Krska, K. Taga, R. Kellner, M. Tacke, and A. Katzir, "Infrared fiber-optical chemical sensors with reactive surface coatings," *Sensors and Actuators B*, vol. 29, pp. 58–63, 1995.

[108] M. Karlowatz, M. Kraft, and B. Mizaikoff, "Simultaneous quantitative determination of benzene, toluene, and xylenes in water using mid-infrared evanescent field spectroscopy," *Analytical Chemistry*, vol. 76, no. 9, pp. 2643–2648, 2004.

[109] T. Jin, J. Zhou, H.-Y. G. Lin, and P. T. Lin, "Mid-infrared chalcogenide waveguides for real-time and nondestructive volatile organic compound detection," *Analytical Chemistry*, vol. 91, no. 1, pp. 817–822, 2019.

[110] P. Wang, S. Caron, C. Paré, F. Picard, S. Dubus, N. Le Bouch, P. Paradis, and S. Chen, "Fiber optic volatile organic compounds sensor based on polymer coated FBG refractometer," *Photonics and Optoelectronics Meetings 2011: Optoelectronic Sensing and Imaging*, vol. 8332, p. 83320E, 2012.

[111] X. Ning, C. Zhao, F. Shi, and S. Jin, "Multipoint chemical vapor measurement by zeolite thin film-coated Fresnel reflection-based fiber sensors with an Array-Waveguide Grating," *Sensors and Actuators, B: Chemical*, vol. 227, pp. 533–538, 2016.

[112] J. C. Echeverría, P. de Vicente, J. Estella, and J. J. Garrido, "A fiber-optic sensor to detect volatile organic compounds based on a porous silica xerogel film," *Talanta*, vol. 99, pp. 433–440, 2012.

[113] J. Gao, T. Gao, and M. J. Sailor, "Porous-silicon vapor sensor based on laser interferometry," *Applied Physics Letters*, vol. 77, no. 6, pp. 901–903, 2000.

[114] I. A. Levitsky, "Porous silicon structures as optical gas sensors," *Sensors*, vol. 15, no. 8, pp. 19968–19991, 2015.

[115] L. Moretti, L. De Stefano, and I. Rendina, "Quantitative analysis of capillary condensation in fractal-like porous silicon nanostructures," *Journal of Applied Physics*, vol. 101, no. 2, p. 024309, 2007.

[116] L. De Stefano, L. Moretti, A. Lamberti, O. Longo, M. Rocchia, A. Rossi, P. Arcari, and I. Rendina, "Optical sensors for vapors, liquids, and biological molecules based on porous silicon technology," *IEEE Transactions On Nanotechnology*, vol. 3, no. 1, pp. 49–54, 2004.

[117] A. M. Tinsley-Bown, L. T. Canham, M. Hollings, M. H. Anderson, C. L. Reeves, T. I. Cox, S. Nicklin, D. J. Squirrell, E. Perkins, A. Hutchinson, M. J. Sailor, and A. Wun, "Tuning the pore size and surface chemistry of porous silicon for immunoassays," *Physica Status Solidi (A) Applied Research*, vol. 182, no. 1, pp. 547–553, 2000.

[118] M. Hecini, A. Khelifa, B. Bouzid, N. Drouiche, S. Aoudj, and H. Hamitouche, "Study of formation, stabilization and properties of porous silicon and porous silica," *Journal of Physics and Chemistry of Solids*, vol. 74, no. 9, pp. 1227–1234, 2013.

[119] D. Nichols, T. Jordan, and N. Kerr, "Chemical and physical properties of lipids," in *Chemical and Functional Properties of Food Lipids*, vol. 4, pp. 23–33, CRC Press Inc., 2 ed., 2010.

[120] G. Dolino, D. Bellet, and C. Faivre, "Adsorption strains in porous silicon," *Physical Review B - Condensed Matter and Materials Physics*, vol. 54, no. 24, pp. 17919–17929, 1996.

[121] L. De Stefano, K. Malecki, F. G. Della Corte, L. Moretti, I. Rea, L. Rotiroti, and I. Rendina, "A microsystem based on porous silicon-glass anodic bonding for gas and liquid optical sensing," *Sensors*, vol. 6, no. 6, pp. 680–687, 2006.

[122] T. Gao, J. Gao, and M. J. Sailor, "Tuning the response and stability of thin film mesoporous silicon vapor sensors by surface modification," *Langmuir*, vol. 18, no. 25, pp. 9953–9957, 2002.

[123] G. Barillaro, "Porous Silicon Gas Sensing," in *Handbook of Porous Silicon*, vol. 2-2, pp. 1251–1262, Cham: Springer International Publishing, 2018.

[124] B. H. King, A. M. Ruminski, J. L. Snyder, and M. J. Sailor, "Optical-fiber-mounted porous silicon photonic crystals for sensing organic vapor breakthrough in activated carbon," *Advanced Materials*, vol. 19, no. 24, pp. 4530–4534, 2007.

[125] M. J. Sailor, "Fundamentals of porous silicon preparation," in *Porous Silicon in Practice*, ch. 1, pp. 1–42, Weinheim, Germany: Wiley-VCH Verlag GmbH & Co. KGaA, jan 2012.

[126] M. A. Anderson, A. Tinsley-Bown, P. Allcock, E. A. Perkins, P. Snow, M. Hollings, R. G. Smith, C. Reeves, D. J. Squirrell, S. Nicklin, and T. I. Cox, "Sensitivity of the optical properties of porous silicon layers to the refractive index of liquid in the pores," *Physica Status Solidi (A) Applied Research*, vol. 197, no. 2, pp. 528–533, 2003.

[127] L. De Stefano, L. Moretti, I. Rendina, and A. M. Rossi, "Quantitative optical sensing in two-component mixtures using porous silicon microcavities," *Physica Status Solidi (A) Applied Research*, vol. 201, no. 5, pp. 1011–1016, 2004.

[128] C. A. Damin and A. J. Sommer, "Characterization of silver halide fiber optics and hollow silica waveguides for use in the construction of a mid-infrared attenuated total reflection fourier transform infrared (ATR FT-IR) spectroscopy probe," *Applied Spectroscopy*, vol. 67, no. 11, pp. 1252–1263, 2013.

[129] M. Saito and K. Kikuchi, "Infrared optical fiber sensors," *Optical Review*, vol. 4, no. 5, pp. 527–538, 1997.

[130] Y. H. Ogata, "Characterization of porous silicon by infrared spectroscopy," in *Handbook of Porous Silicon*, vol. 1-2, pp. 705–712, Cham: Springer International Publishing, 2018.

[131] D. B. Mawhinney, J. A. Glass, and J. T. Yates, "FTIR study of the oxidation of porous silicon," *The Journal of Physical Chemistry B*, vol. 101, no. 7, pp. 1202–1206, 1997.

[132] F. Wang, T. J. Barnes, and C. A. Prestidge, "Controlling and predicting the dissolution kinetics of thermally oxidised mesoporous silicon particles: towards improved drug delivery," *Pharmaceutics*, vol. 11, no. 12, p. 634, 2019.

[133] S. Corsetti, F. M. Zehentbauer, D. McGloin, and J. Kiefer, "Characterization of gasoline/ethanol blends by infrared and excess infrared spectroscopy," *Fuel*, vol. 141, pp. 136–142, 2015.

[134] J. J. Max and C. Chapados, "Infrared spectroscopy of acetone-water liquid mixtures. Ii. Molecular model," *Journal of Chemical Physics*, vol. 120, no. 14, pp. 6625–6641, 2004.

[135] B. Arkles, "Silicon Compounds, Silanes," in *Kirk-Othmer Encyclopedia of Chemical Technology*, no. 215, pp. 1 – 592, Hoboken, NJ, USA: John Wiley & Sons, Inc., 3 ed., 2000.

[136] N. Arad-Vosk and A. Sa'ar, "Radiative and nonradiative relaxation phenomena in hydrogen- and oxygen-terminated porous silicon," *Nanoscale Research Letters*, vol. 9, no. 1, pp. 1–6, 2014.

[137] W. Salcedo, F. R. Fernandez, and E. Galeazzo, "Structural characterization of photoluminescent porous silicon with FTIR spectroscopy," *Brazilian Journal of Physics*, vol. 27, no. 4, pp. 158–161, 1997.

[138] G. Mattei, E. V. Alieva, J. E. Petrov, and V. A. Yakovlev, "Quick oxidation of porous silicon in presence of pyridine vapor," *Physica Status Solidi (A) Applied Research*, vol. 182, no. 1, pp. 139–143, 2000.

[139] N. D. Lourenço, J. A. Lopes, C. F. Almeida, M. C. Sarraguça, and H. M. Pinheiro, "Bioreactor monitoring with spectroscopy and chemometrics: A review," *Analytical and Bioanalytical Chemistry*, vol. 404, no. 4, pp. 1211–1237, 2012.

[140] J. Gomes, V. Chopda, and A. S. Rathore, "Monitoring and control of bioreactors: basic concepts and recent advances," in *Bioprocessing Technology for Production of Biopharmaceuticals and Bioproducts* (C. Komives and W. Zhou, eds.), ch. 6, pp. 201–227, Hoboken, NJ, USA: John Wiley & Sons, Inc., 2018.

[141] R. Ulber, D. Sell, T. Becker, B. Hitzmann, K. Muffler, R. Pörtner, K. Reardon, and F. Stahl, "White Biotechnology," in *Advances in Biochemical Engineering/Biotechnology*, vol. 105, pp. 249–293, Berlin, Heidelberg: Springer, 2007.

[142] A. Rudnitskaya and A. Legin, "Sensor systems, electronic tongues and electronic noses, for the monitoring of biotechnological processes," *Journal of Industrial Microbiology and Biotechnology*, vol. 35, no. 5, pp. 443–451, 2008.

[143] O. S. Wolfbeis, "Fiber-optic chemical sensors and biosensors," *Analytical Chemistry*, vol. 74, no. 12, pp. 2663–2677, 2002.

[144] P. Harms, Y. Kostov, and G. Rao, "Bioprocess monitoring," *Current Opinion in Biotechnology*, vol. 13, no. 2, pp. 124–127, 2002.

[145] M. Pohlscheidt, S. Charaniya, C. Bork, M. Jenzsch, T. L. Noetzel, and A. Luebbert, "Bioprocess and fermentation monitoring," in *Encyclopedia of Industrial Biotechnology*, pp. 1469–1492, Hoboken, NJ, USA: John Wiley & Sons, Inc., 2013.

[146] P. Roychoudhury, L. M. Harvey, and B. McNeil, "The potential of mid infrared spectroscopy (MIRS) for real time bioprocess monitoring," *Analytica Chimica Acta*, vol. 571, no. 2, pp. 159–166, 2006.

[147] R. Ulber, J. G. Frerichs, and S. Beutel, "Optical sensor systems for bioprocess monitoring," *Analytical and Bioanalytical Chemistry*, vol. 376, no. 3, pp. 342–348, 2003.

[148] P. Fayolle, D. Picque, and G. Corrieu, "On-line monitoring of fermentation processes by a new remote dispersive middle-infrared spectrometer," *Food Control*, vol. 11, no. 4, pp. 291–296, 2000.

[149] D. J. Pollard, R. Buccino, N. C. Connors, T. F. Kirschner, R. C. Olewinski, K. Saini, and P. M. Salmon, "Real-time analyte monitoring of a fungal fermentation, at pilot scale, using in situ mid-infrared spectroscopy," *Bioprocess and Biosystems Engineering*, vol. 24, no. 1, pp. 13–24, 2001.

[150] A. Bogomolov, M. Heßling, U. Wenzel, S. Princz, T. Hellmuth, M. J. Bernal, T. Sakharova, I. Usenov, V. Artyushenko, and H. Meyer, "Development and testing of mid-infrared sensors for in-line process monitoring in biotechnology," *Sensors and Actuators, B: Chemical*, vol. 221, pp. 1601–1610, 2015.

[151] H. M. Heise, L. Küpper, and L. N. Butvina, "Bio-analytical applications of mid-infrared spectroscopy using silver halide fiber-optic probes," *Spectrochimica Acta - Part B Atomic Spectroscopy*, vol. 57, no. 10, pp. 1649–1663, 2002.

[152] V. Bajaj, A. Tilay, and U. Annapure, "Enhanced Production of Bioactive Sophorolipids by Starmerella bombicola NRRL Y-17069 by Design of Experiment Approach with Successive Purification and Characterization," *Journal of Oleo Science*, vol. 61, no. 7, pp. 377–386, 2012.

[153] V. K. Bajaj and U. S. Annapure, "Castor Oil as Secondary Carbon Source for Production of Sophorolipids using Starmerella bombicola NRRL Y-17069," *Journal of Oleo Science*, vol. 64, no. 3, pp. 315–323, 2015.

[154] T. Redman and D. O. Grady, "Improve products and processes with inline particle analysis," Tech. Rep. August, American Institute of Chemical Engineers (AIChE), 2017.

[155] C. Koch, *Advances in Bioprocess Monitoring by Mid-Infrared Spectroscopy*. PhD thesis, TU Wien, 2015.

[156] S. Roelants, D. Solaiman, R. Ashby, S. Lodens, L. Van Renterghem, and W. Soetaert, "Production and applications of sophorolipids," in *Biobased Surfactants*, ch. 3, pp. 65–119, Elsevier Inc, 2nd ed., 2019.

[157] B. M. Dolman, C. Kaisermann, P. J. Martin, and J. B. Winterburn, "Integrated sophorolipid production and gravity separation," *Process Biochemistry*, vol. 54, pp. 162–171, 2017.

[158] M. A. Díaz De Rienzo, I. M. Banat, B. Dolman, J. Winterburn, and P. J. Martin, "Sophorolipid biosurfactants: Possible uses as antibacterial and antibiofilm agent," *New Biotechnology*, vol. 32, no. 6, pp. 720–726, 2015.

[159] M. R. Oliveira, A. Magri, C. Baldo, D. CAmiliou-Neto, T. Minucelli, and M. A. P. C. Celligoi, "A Review: sophorolipids a promising biosurfactant and its applications," *International Journal of Advanced Biotechnology and Research*, vol. 6, no. April, pp. 161–174, 2018.

[160] Y. Lu, C. Du, Y. Shao, and J. Zhou, "Characterization of rapeseed oil using FTIR-ATR spectroscopy," *Journal of Food Science and Engineering*, vol. 4, no. May, pp. 244–249, 2014.

[161] K. Kim, D. Yoo, Y. Kim, B. Lee, D. Shin, and E. K. Kim, "Characteristics of sophorolipid as an antimicrobial agent," *Journal of Microbiology and Biotechnology*, vol. 12, no. 2, pp. 235–241, 2002.

[162] A. Jasmin, *Synthesis and Characterisation of Novel Sophorolipids and Their Applications*. PhD thesis, University of Huddersfield, 2016.

Appendix A

Engineering drawings of device 1, device 2 and device 3

Engineering drawings of device 1 (Figure A.1), device 2 (Figure A.2) and device 3 (Figure A.3). These were drawn by Mr. Oliver Norris, Engineer at the the Department of Chemistry workshop, University of Cambridge.

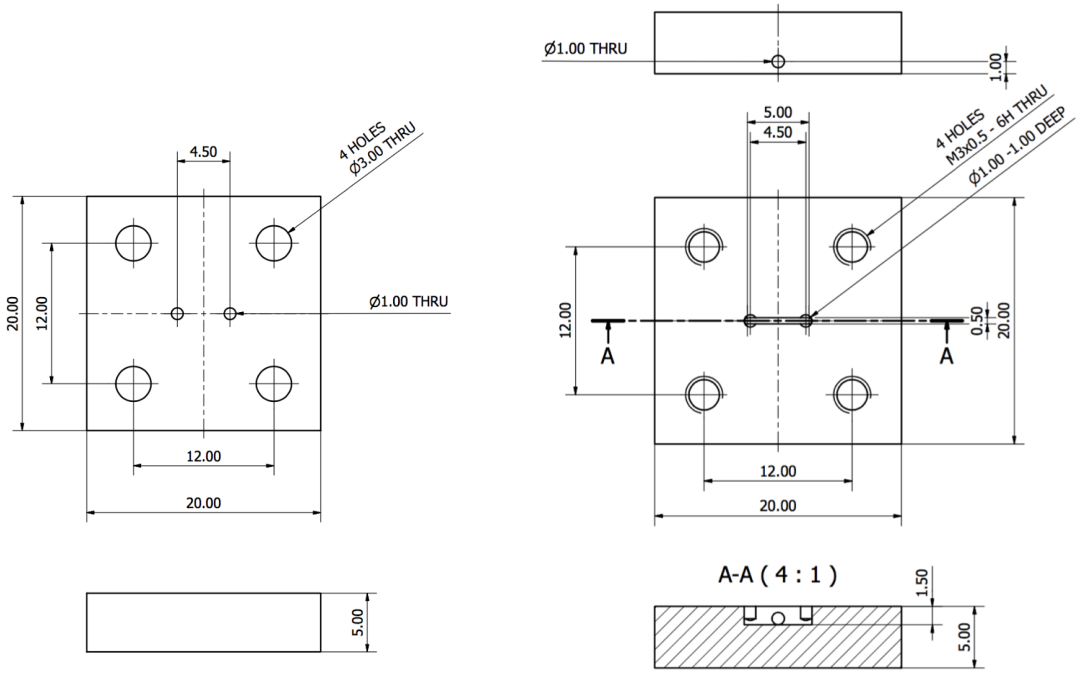

(a) (b)

Fig. A.1 Engineering drawings of device 1. (a) Top layer; (b) Bottom layer. Dimensions are in millimetres.

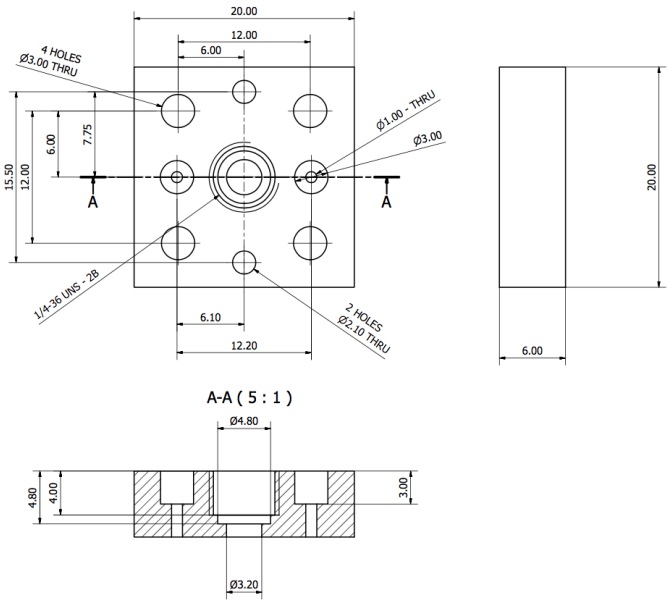

(a)

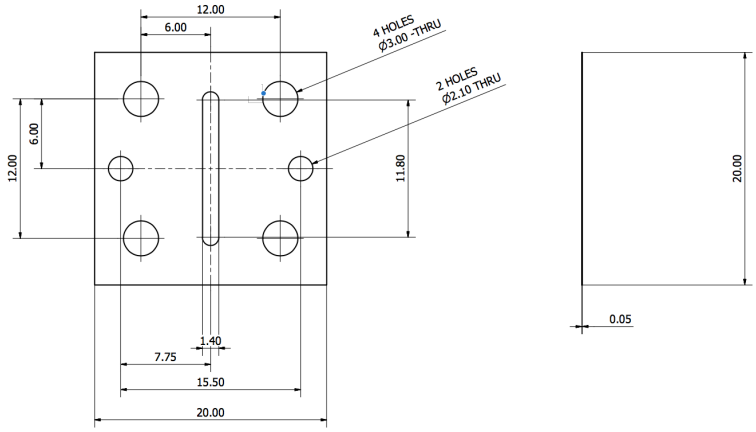

(b)

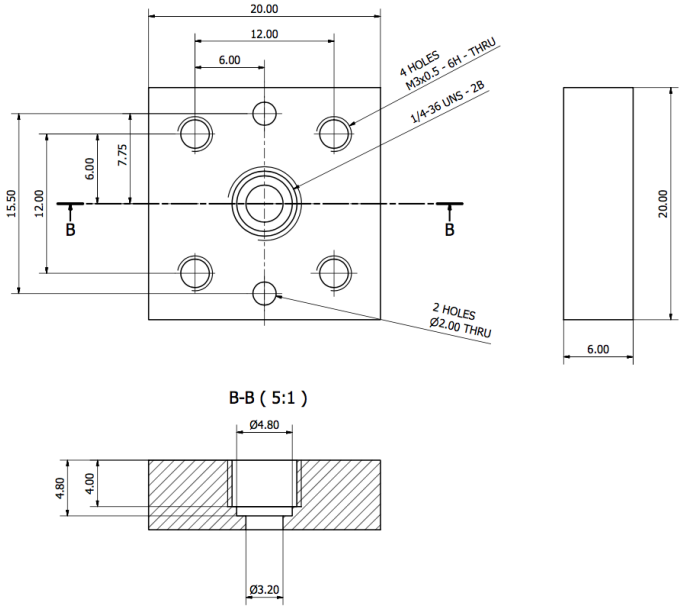

(c)

Fig. A.2 Engineering drawings of device 2. (a) Top layer; (b) Middle layer (50 μm stainless-steel shim); (c) Bottom layer. Dimensions are in millimetres.

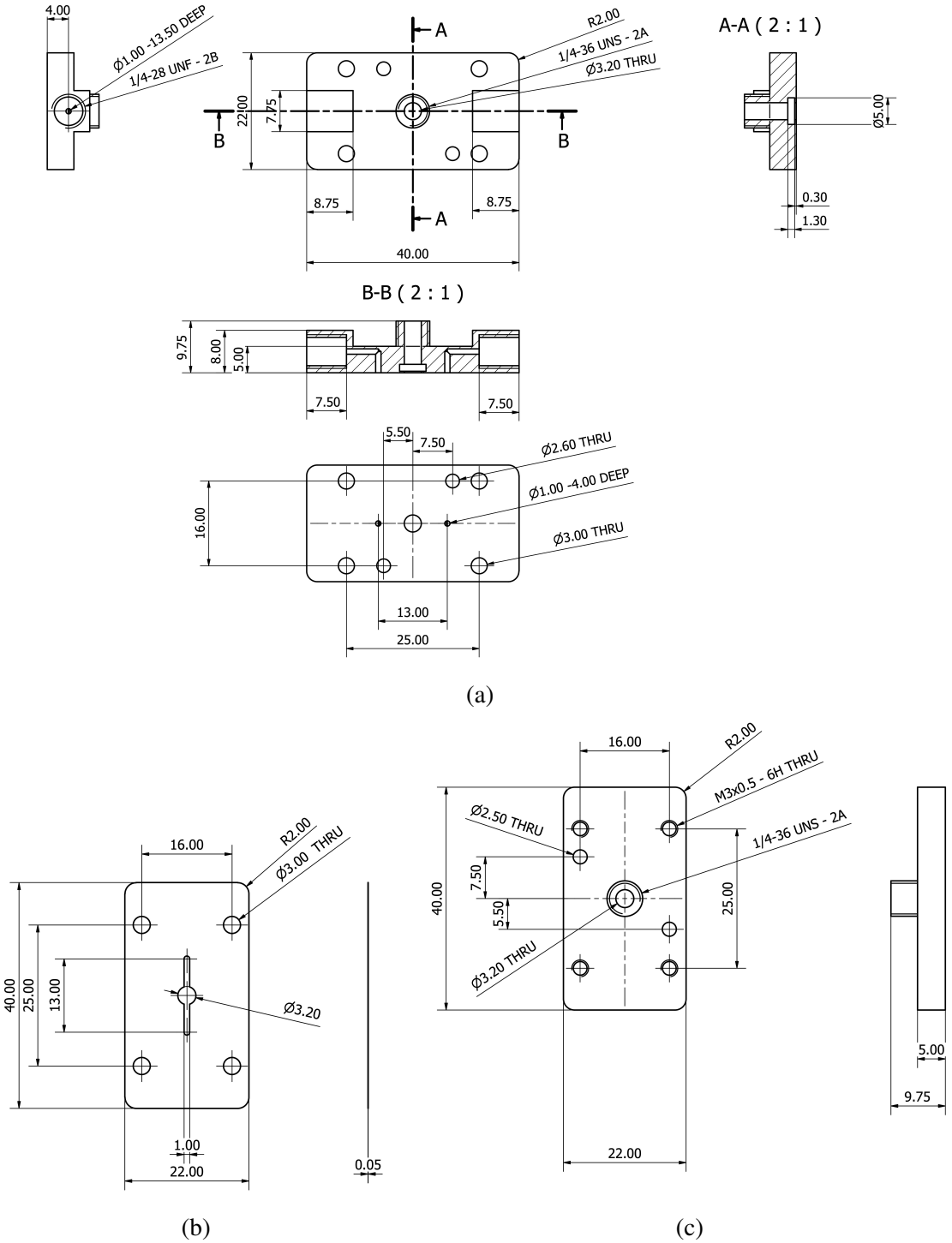

Fig. A.3 Engineering drawings of device 3. (a) Top layer; (b) Middle layer (PTFE gasket); (c) Bottom layer. Dimensions are in millimetres.

Appendix B

Clinical study results (additional)

B.1 Clinical study 2

The results of a second clinical study carried out in the NCCU of Addenbrooke's Hospital are shown in Figure B.1, where the absorbance spectra of continuously-flowing TBI-patient microdialysate were acquired every minute over a period of two hours.

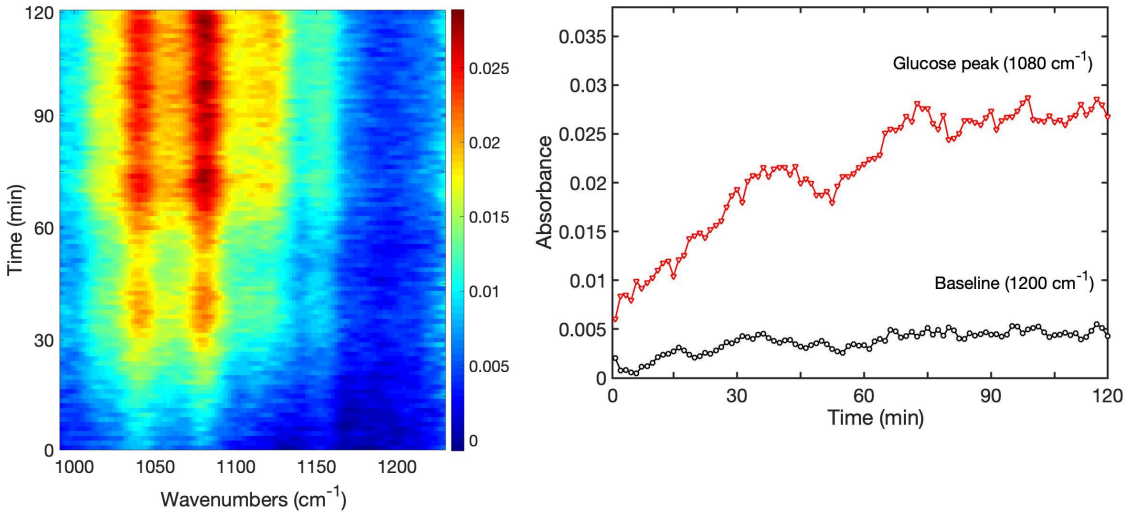

(a) (b)

Fig. B.1 Spectral information acquired during clinical study 2, where a TBI patient was continuously monitored for 2 hours. (a) 2D pseudocolour plot showing evolution of the absorbance spectra over the monitoring time; (b) Absorbance of the glucose peak (at 1080 cm^{-1}) and the baseline (at 1200 cm^{-1}) as a function of time. Spectra were acquired with 1 minute intervals.

B.2 Clinical study 3

The results of a third clinical study carried out in the NCCU of Addenbrooke's Hospital are shown in Figure B.2, where the absorbance spectra of continuously-flowing TBI-patient microdialysate were acquired every 30 seconds over a period of two hours and ten minutes.

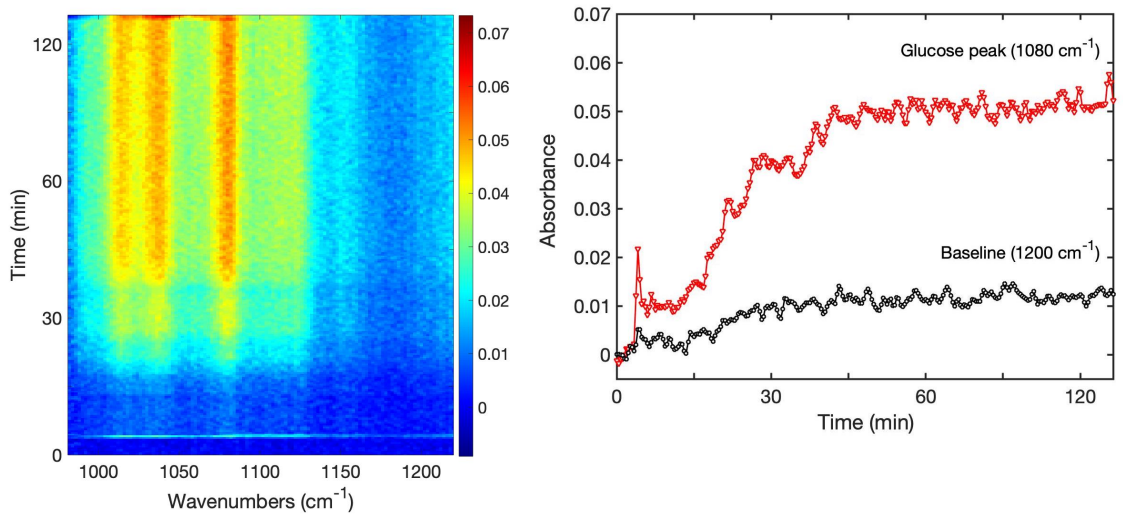

(a) (b)

Fig. B.2 Spectral information acquired during clinical study 3, where a TBI patient was continuously monitored for 2 hours and 10 minutes. (a) 2D pseudocolour plot showing evolution of the absorbance spectra over the monitoring time; (b) Absorbance of the glucose peak (at 1080 cm^{-1}) and the baseline (at 1200 cm^{-1}) as a function of time. Spectra were acquired with 30 second intervals.

Appendix C

Synthetic-sample and microdialysate compound concentrations

C.1 Synthetic sample compound concentrations

The concentrations of glucose, lactate and pyruvate in each of the prepared synthetic samples, used for building the PLSR model, are shown in Figure C.1.

Sample no.	glucose (µM)	lactate (µM)	pyruvate (µM)
1	3600	2600	200
2	2500	1750	120
3	1200	3000	175
4	1200	7200	280
5	4000	6500	175
6	4800	3600	250
7	800	7800	250
8	2200	3250	80
9	4500	5000	100
10	4800	5600	180
11	4500	5000	280
12	1800	3250	140
13	2400	3500	200
14	2400	750	20
15	3500	2000	100
16	800	5600	200
17	4000	5000	140
18	4000	7200	250
19	120	6500	250
20	1800	2500	100

(continued on next page)

Fig. B.1 Concentrations of glucose, lactate and pyruvate in each of the prepared synthetic samples used for building the PLSR model.

Sample no.	glucose (µM)	lactate (µM)	pyruvate (µM)
21	2000	2800	140
22	20	3250	200
23	2600	4000	120
24	750	2250	200
25	3000	2500	200
26	4500	2500	200
27	3500	1500	50
28	550	5600	280
29	4800	1750	80
30	1000	4000	300
31	2200	7500	200
32	4000	4500	100
33	700	3250	250
34	1200	7000	200
35	800	6500	175
36	800	4500	250
37	5000	4000	80
38	3000	5600	150
39	1200	5000	100
40	2500	6500	140
41	500	2500	200
42	2500	5600	175
43	1500	5000	280
44	1500	8000	175
45	4800	7500	140
46	2000	500	20
47	450	6000	175
48	650	7000	250
49	3500	4500	180
50	4400	7500	200

Fig. C.1 Concentrations of glucose, lactate and pyruvate in each of the prepared synthetic samples used for building the PLSR model.

C.2 Patient microdialysate compound concentrations

The concentrations of glucose, lactate and pyruvate in each of the collected cerebral microdialysates, measured using the standard microdialysis analyser (ISCUS Flex Microdialysis Analyser), are shown in Figure C.2. These were used as reference values for the predicted values obtained via PLSR.

Sample no.	glucose (µM)	lactate (µM)	pyruvate (µM)
1	735.303	408.438	40.50334757
2	680.196	439.617	40.01788747
3	512.507	401.488	22.53024313
4	428.305	354.131	25.088629
5	502.032	388.304	13.562807
6	489.743	417.241	35.81840244
7	518.562	445.299	49.32894368
8	440.128	338.337	51.62421268
9	507.837	431.317	114.3954131
10	537.727	468.899	86.98931198
11	629.663	369.332	83.66143693
12	593.461	393.113	97.01208234
13	667.735	378.048	103.1748011
14	676.148	423.003	128.9438523
15	675.785	424.341	149.8771541
16	699.903	420.529	128.5006059
17	714.159	389.402	147.9230369
18	688.629	447.537	135.4826372
19	675.13	460.143	138.3977699
20	550.729	420.154	162.9697063
21	377.321	308.036	137.4262157
22	438.354	392.337	168.4892182
23	457.353	328.433	154.9175675
24	469.569	308.276	173.2034389
25	435.848	321.431	165.4541204
26	385.715	319.237	175.6009834
27	334.726	350.686	165.0359813

Fig. C.2 Concentrations of glucose, lactate and pyruvate in collected cerebral microdialysates, measured using the ISCUS Flex Microdialysis Analyser.